

UNIVERSITÀ DEGLI STUDI DI PADOVA

Sede Amministrativa: Università degli Studi di Padova

Dipartimento di Scienze Chimiche

SCUOLA DI DOTTORATO DI RICERCA IN SCIENZE MOLECOLARI

INDIRIZZO SCIENZE CHIMICHE

CICLO XX

MODELING OF DYNAMIC SOLVATION EFFECTS

Direttore della Scuola: Ch.mo Prof. Maurizio Casarin

Supervisore: Prof. Antonino Polimeno

Dottoranda: Silvia Carlotto

DATA CONSEGNA TESI

31 gennaio 2008

"... and if again I say that to talk every day about virtue and the other things [...] and examining myself and others is the greatest good man, and that the unexamined life is not worth living, you will believe me still less.¹"

(Plato, *Apology*)

"Nor ought we obey those who enjoin that a man should have man's thoughts and a mortal the thoughts of mortality, but we ought so far as possible to achieve immortality, and do all that man may to live in accordance with the highest thing in him...²"

(Aristotle, *Nicomachean Ethics*)

¹"...Ancor meno mi crederete se dico che il più grande bene dato all'uomo è proprio questa possibilità di ragionare quotidianamente [...] sui vari temi su cui mi avete sentito discutere o esaminare me stesso e altri: una vita senza ricerca non è degna, per l'uomo, di essere vissuta."

²"Ma non bisogna dar retta a coloro che consigliano all'uomo, poichè uomo e mortale, di limitarsi a pensare cose umane e mortali; anzi, al contrario, per quanto è possibile, bisogna comportarsi da immortali e far di tutto per vivere secondo la parte divina che è in noi..."

Modeling of dynamic solvation effects

Abstract

Reactivity of molecular and supramolecular systems is greatly modified by the surrounding environment, often a fluid medium, and an active area of research is nowadays the study of the influence of a solvent structure on the static and dynamic properties of photo-active and paramagnetic probes, varying solvent properties, sample geometry and external perturbations. Standard continuum solvent theories are based on crude representations of the probe. Solvation processes depend in a specific way upon the structure of the solute, and in particular on molecular features as shape, flexibility, distribution of charges and anisotropy of the polarizability. Augmented solvent continuum approaches have been developed to interpret chromophore dynamics to account for persistent solvent local structures. Description of collective solvent modes is also necessary to understand relaxation processes affecting dynamics at longer times, in complex fluid environments: phase transitions in supercooled liquids, rheological properties of emulsions and colloids, confinement effects and finally micro and nano-probes dynamics. The inclusion of solvent effects is of great importance, in order to understand the physical mechanisms responsible of the tuning of the optical properties and therefore to the ultimate possibility to design nanomaterials with specific optical response. Theoretical methodologies based on stochastic and hydrodynamic modeling have proven over the years to be a powerful approach, especially when coupled with advanced quantum mechanical treatments, to describe effectively the dynamical aspects of solvation. The relationship between spectroscopic measurements and molecular properties can be gathered only indirectly, that is, structural and dynamic molecular characteristics can be inferred by the systematic application of modeling and numerical simulations to interpret experimental observables. A straightforward way to achieve this goal is the employment of spectroscopic evidence as the "target" of a fitting procedure of molecular, mesoscopic and macroscopic parameters entering the model. A more refined methodology is based on the combination of quantum mechanical calculations of structural parameters possibly including environmental and fast vibrational and librational averaging, and direct feeding of calculated molecular parameters into dynamic

models based on molecular dynamics, coarse grain dynamics, and above all stochastic modeling or a combination of the three. Our main objective in this PhD work has been to discuss the degree of progress of advanced theoretical models are explored, aimed at clarifying the influence of solvent-driven relaxation processes on optic, magnetic and rheological observables. In particular we have developed integrated computational approaches to the interpretation of fluorescence emission of organic molecules in solvated environments, CW-ESR spectroscopy and rheological properties of ordered systems via combination of advanced quantum mechanical approaches, stochastic modeling of relaxation processes, and, in the last case, macroscopic models. In the first period we have shown that the model proposed is able to reproduce the spectral position and shape of the emission spectra. In particular the model reproduces the red shift expected for TICT excited states when the dielectric constant of the solvent increases. We developed a stochastic approach to the interpretation of the emission fluorescence of 4-(N,N-dimethylamino) benzonitrile (DMABN). Then we proceed by extending the modeling approach, in which internal degrees of freedom are coupled with an effective solvent relaxation variable. The extension of the model is applied to the simulation of the emission spectra of DMABN-Crown5, a DMABN derivative. Evaluation of potential energy surfaces using advanced QM approach and estimates of dissipative parameters based on hydrodynamic arguments are discussed. Emission fluorescence is calculated by solving a diffusion/sink/source equation for the stationary population of excited states, and compared to experimentally measured emission fluorescence of DMABN and DMABN-Crown5. Next we developed the complete a priori simulation of the ESR spectra of complex systems in solution. The usefulness and reliability of the method are demonstrated on the very demanding playground represented by the tuning of the equilibrium between 3_{10} - and α -helices of polypeptides by different solvents. The starting point is good agreement between computed and X-ray diffraction structures for the 3_{10} -helix adopted by the double spin-labeled heptapeptide Fmoc-(Aib-Aib-TOAC)₂-Aib-OMe. Next, density functional computations, including dispersion interactions and bulk solvent effects, suggest another energy minimum corresponding to an α -helix in polar solvents, which, eventually, becomes the most stable structure. Computation of magnetic and diffusion tensors provides the basic ingredients for the

building of complete spectra by methods rooted in the Stochastic Liouville Equation (SLE). The remarkable agreement between computed and experimental spectra at different temperatures allowed us to identify helical structures in the various solvents. The generality of the computational strategy and its implementation in effective and user-friendly computer codes pave the route toward systematic applications in the field of biomolecules and other complex systems. Finally, the purpose of the last part of the PhD period has been to analyze the dynamical behavior of a low viscosity nematic liquid crystals in presence of micro-size probe. We present a study of the translational friction coefficients of spherical and ellipsoidal probes moving in nematic liquid crystalline fluids, by solving numerically the constitutive hydrodynamic equations of nematic. The evaluation of the translational friction coefficients is based on a numerical solution of Leslie-Ericksen constitutive equations for the case of incompressible nematic fluids. The nematic medium is described by a vector field which specifies the director orientation in each point and by the velocity vector field. Simulation of director dynamics surrounding the moving probe are presented, and the dependence of translational diffusion upon liquid crystal viscoelastic parameters is discussed. The time evolution of director field, described by Leslie-Ericksen equations, is studied in the presence of an orienting magnetic field in two characteristic situations: director of motion parallel and perpendicular to field.

Modellizzazione di effetti di solvatazione dinamica

Sommario

La reattività dei sistemi molecolari e supramolecolari è fortemente influenzata dall'ambiente di reazione, quindi un'area di ricerca di grande attualità è lo studio dell'influenza della struttura del solvente sulle proprietà statiche e dinamiche di probe fotoattivi o paramagnetici al variare delle proprietà del solvente o della geometria del campione. Le teorie standard che descrivono il solvente come un mezzo continuo (continuum solvent approaches) sono basate su una rappresentazione poco raffinata del probe. Al contrario i processi di solvatazione dipendono dalla specifica struttura del soluto e, in particolare, dalle caratteristiche molecolari come la forma, la flessibilità, la distribuzione di cariche e l'anisotropia della polarizzabilità. All'interno di questa classe di approcci sono state sviluppate nuove metodologie per l'interpretazione della dinamica di cromofori che tengano debitamente in considerazione la struttura locale del solvente. La descrizione dei modi collettivi per il solvente è anch'essa necessaria per una corretta comprensione dei processi di rilassamento che influenzano la dinamica su lunghe scale temporali in ambienti descritti da fluidi complessi. Tali fluidi complessi possono rappresentare transizioni di fase in liquidi sovraraffreddati, proprietà reologiche di emulsioni e colloidali, effetti di confinamento e dinamiche di probe micro e nano-metrici. L'inclusione degli effetti solvente si rivela di enorme importanza per comprendere i meccanismi fisici responsabili della modulazione delle proprietà ottiche e offre quindi un aiuto basilare nel design di nanomateriali dotati di specifici responsi ottici. Negli anni le metodologie teoriche basate su modellizzazione stocastica e idrodinamica si sono dimostrate un valido approccio nell'effettiva descrizione degli aspetti di solvatazione dinamica, specialmente quando vengono accoppiate con avanzati trattamenti quantomeccanici. Dal momento che la relazione tra le misure spettroscopiche e le proprietà molecolari può essere dedotta solo in modo indiretto le caratteristiche molecolari strutturali e dinamiche possono essere desunte dall'applicazione sistematica di modellizzazioni e simulazioni numeriche per interpretare gli osservabili sperimentali. Una strada diretta per ottenere questo obiettivo è l'utilizzo di evidenze spettroscopiche come "target" delle procedure di fitting dei parametri molecolari, mesoscopici e macro-

scopici che compaiono nel modello. Una metodologia più raffinata è basata sulla combinazione di calcoli quantomeccanici per i parametri strutturali con l'inserimento diretto di parametri molecolari calcolati all'interno di modelli dinamici e, soprattutto, modelli stocastici. L'obiettivo principe del lavoro di Dottorato è stato la discussione e lo sviluppo di modelli teorici avanzati atti a chiarire l'influenza dei processi di rilassamento guidati dal solvente sugli osservabili ottici, magnetici e reologici. In particolare si sono sviluppati degli approcci computazionali integrati per l'interpretazione degli spettri di emissione di fluorescenza di molecole organiche in ambienti solvatati, per le spettroscopie CW-ESR e per le proprietà reologiche di sistemi ordinati. Tali approcci prevedono la combinazione di avanzati metodi di calcolo quantomeccanico, modelli stocastici per i processi di rilassamento e, nell'ultimo caso, modelli macroscopici. Nel primo periodo si è mostrato che il modello proposto è in grado di riprodurre la posizione e la forma di uno spettro di emissione. In particolare il modello riproduce lo spostamento a frequenze minori (red-shift) atteso per gli stati eccitati che presentano il fenomeno del trasferimento di carica intramolecolare legato all'incremento della costante dielettrica del solvente. Si è sviluppato un approccio stocastico per l'interpretazione dello spettro di emissione di fluorescenza del 4-(N,N-dimethylamino) benzonitrile (DMABN). Si è poi proceduto ad estendere il modello, nel quale i gradi di libertà interna sono accoppiati con una variabile di rilassamento per il solvente, a sistemi di complessità maggiore. L'applicabilità del modello è stata quindi estesa alla simulazione dello spettro di emissione di un derivato del DMABN, il DMABN-Crown5. Si sono poi presentate le valutazioni delle superfici di energia potenziale ottenute mediante approcci QM e si sono stimati i parametri dissipativi mediante argomenti idrodinamici. Gli spettri di emissione di fluorescenza sono stati calcolati risolvendo un'equazione diffusione/bagno termico/sorgente per la popolazione stazionaria degli stati eccitati ed i risultati ottenuti sono stati comparati con gli spettri di emissione del DMABN e del DMABN-Crown5 misurati sperimentalmente. Successivamente si è sviluppata una simulazione *a priori* degli spettri ESR di sistemi complessi in soluzione la cui esattezza e l'utilità sono state evidenziate in un banco di prova di notevole complessità rappresentato dalla modulabilità dell'equilibrio tra l'elica 3_{10} e l'elica α di polipeptidi in diversi solventi. Il punto di partenza è il buon accordo tra la struttura ottenuta mediante calcoli quantistici

e quella ricavata dalle misure ai raggi X per la conformazione ad elica 3_{10} adottata dall'eptapeptide Fmoc-(Aib-Aib-TOAC)₂-Aib-OMe doppiamente marcato con radicali nitrossido. I calcoli quantistici effettuati tramite la teoria del funzionale densità, che includono le interazioni di dispersione e gli effetti di bulk, suggeriscono la presenza di un altro minimo di energia corrispondente ad un'elica α in solventi protici. La maggiore stabilità di una conformazione secondaria rispetto all'altra è legata alle caratteristiche del solvente. La simulazione dello spettro ESR del peptide è stata possibile risolvendo l'equazione stocastica di Liouville (SLE) la quale necessita, oltre dei dati ottenuti mediante calcoli quantistici, del calcolo del tensore di diffusione e del tensore magnetico di interazione dipolare. Il notevole accordo tra gli spettri sperimentali e gli spettri simulati a diverse temperature permette di stabilire la percentuale delle due conformazioni secondarie nei vari solventi. L'universalità della strategia computazionale e la sua implementazione in codici computer *user-friendly* tracciano la strada verso un'applicazione sistematica nel campo delle biomolecole e di altri sistemi complessi. Infine, lo scopo del lavoro svolto nell'ultima parte del periodo di dottorato è l'analisi del comportamento dinamico di cristalli liquidi nematici a bassa viscosità in presenza di un probe di dimensioni micrometriche. Tale indagine permette di evidenziare gli effetti del solvente sulle proprietà reologiche di sistemi ordinati. Si presenterà in particolare uno studio dei coefficienti di attrito traslazionale di un probe sferico o ellissoidale in movimento in un cristallo liquido nematico risolvendo numericamente le equazioni idrodinamiche per i nematici. La valutazione dei coefficienti di attrito traslazionale è basata sulla soluzione numerica delle equazioni di Leslie-Ericksen per il caso di un fluido nematico incomprimibile. Il nematico che funge da solvente è descritto da un vettore di campo che specifica l'orientazione del direttore in ogni punto e da un vettore velocità. In questa parte del lavoro viene presentata la simulazione della dinamica del moto del direttore del nematico che circonda un probe in movimento. Nello specifico si considera la dipendenza della diffusione traslazionale dai parametri viscoelastici tipici di ogni cristallo liquido. L'evoluzione temporale del direttore, descritto dalle equazioni di Leslie-Ericksen, è studiata in presenza di un campo magnetico orientante in due situazioni caratteristiche: moto del direttore parallelo e perpendicolare al campo esterno applicato.

Index

1	Theoretical methods	25
1.1	Introduction	25
1.2	Molecular Approaches	29
1.2.1	Density Functional Theory	30
1.2.2	Molecular Dynamics	32
1.3	Mesosopic Approaches	37
1.3.1	The QM/MM methods	38
1.3.2	Polarizable Continuum Model	41
1.3.3	Dissipative Particle Dynamics	43
1.3.4	Stochastic Methods	44
1.4	Macroscopic Approaches	49
1.4.1	Hydrodynamics/Continuum Approaches	50
1.4.2	Smoothed Particle Hydrodynamics	54
1.4.3	Hydrodynamics Approaches/Stochastic Methods	55
1.5	A critical overview on the different approaches	58
1.6	Work-Plane	60
2	An integrated approach for the fluorescence spectra of DMABN	63
2.1	Introduction	63
2.2	An integrated approach for the fluorescence spectra of DMABN	66
2.2.1	The model	70
2.2.2	Hydrodynamic model for the diffusion tensor	75
2.2.3	The model treatment	78
2.2.4	Parameters	81

2.2.5	The simulated fluorescence spectra of DMABN	87
2.3	Extension of the model to a DMABN derivative: DMABN-Crown5 . . .	89
2.3.1	The model extension	93
2.3.2	Parameters	97
2.3.3	The simulated fluorescence spectra of DMABN-Crown5	101
2.4	Conclusions	104
3	<i>Ab-initio</i> computational modeling of CW-ESR spectra of a double labeled peptide	107
3.1	Introduction	107
3.2	A brief introduction to the ESR technique	110
3.3	<i>Ab-initio</i> modeling of a double spin labeled peptide in a polar solvent .	112
3.3.1	Peptide Synthesis, X-ray Diffraction and ESR Characterization .	114
3.3.2	The Stochastic Liouville Equation	116
3.3.3	Magnetic tensor	120
3.3.4	Structure and diffusion properties	123
3.3.5	Results	126
3.4	Unraveling solvent-driven equilibria between α and 3_{10} helices through an integrated computational approach	129
3.4.1	Modeling	132
3.4.2	Structure, magnetic and diffusion properties	133
3.4.3	Results	141
3.5	Conclusions	145
4	Evaluation of translational friction coefficients of macroscopic probes in Nematic Liquid Crystals	149
4.1	Introduction	149
4.2	Nematic Liquid Crystals	151
4.3	The model	154
4.3.1	Isotropic fluid	154
4.3.2	Leslie-Ericksen equations	156
4.4	Computational methodology	158

4.5	Results	162
4.5.1	Axially symmetric case	162
4.5.2	Shape probe dependence	164
4.5.3	Viscoelastic parameters dependence	169
4.5.4	Comparison with experimental data	170
4.6	Conclusions	171
5	Conclusions	175
A	The time dependent emission fluorescence signal	177
B	Analysis of the translational and rotational motions	181
C	The dipole-dipole magnetic tensor	185

List of Figures

1-1	Scheme of the different theoretical methods used for described a system: macroscopic approaches (left), mesoscopic approaches (center) and molecular approaches (right).	28
1-2	Schematic comparison of time- and length-scale, accessible to different types of simulation techniques (quantum simulations (QM), molecular dynamics (MD), stochastic approaches (SA) and hydrodynamics/fluid dynamics (HD)).	29
1-3	Typical examples for potential terms as used in common force-fields. Figure from ref. [12].	34
1-4	Different applications of QM/MM methods: material science (left) and bioscience (right).	39
1-5	Schematic representation of the partition of a system in a condensate phase.	40
1-6	Representation of the DPD approaches in the multiscale approaches.	43
1-7	Lateral view of the carbon nanotube (left) and the gramicidin A channel (right) systems.	47
2-1	The twisted intramolecular charge-transfer (upper panel) and planar (lower panel) state model. Figure from ref. [158].	67
2-2	Structures of N,N dimethylamino-benzonitrile (DMABN).	72
2-3	Scheme for the evaluation of diffusion tensor of a flexible N -fragments systems; the molecular frame MF is fixed on the second fragment.	76
2-4	Schematic drawings of selected molecular orbitals (HOMO and LUMO) for DMABN at ground state geometry.	82

2-5	(a) Ground (g in green) and low-lying singlet excited states (LE state in blue and TICT state in red) potential energy surfaces (PES) of DMABN <i>in vacuo</i> as a function of the torsional angle (in degrees). The energy (in eV) is relative to the minimum of the ground state. (b) Ground and low-lying singlet excited states dipole moment curves of DMABN <i>in vacuo</i> as a function of the torsional angle (in degrees). Dipole moment are in debye.	85
2-6	Schematic representation of the DMABN in the hydrodynamic approach.	86
2-7	Experimental (a) and simulated (b) emission spectra for DMABN in: DMSO (purple), acetonitrile (red), <i>n</i> -butylchloride (orange), diethylether (dark yellow), dibutyl ether (blue), benzene (cyan), cyclohexane (olive) and <i>n</i> -hexane (black).	89
2-8	Structure of 4-(1-aza-4,7,10,13-tetraoxacyclododecyl) benzonitrile (DMABN-Crown5).	94
2-9	Relevant degrees of freedom for modeling DMABN-Crown5 fluorescence. Orientation is given by a set of Euler angles $\mathbf{\Omega}$; relative orientation of donor-acceptor groups are described by the torsional angle φ ; a stochastic vector coordinate \mathbf{X} represents the solvent relaxation.	95
2-10	Structure of DMABN-Crown5 local minima.	98
2-11	Potential energy surfaces (left) and dipole moments (right) for the five conformers (a)-(e) of DMABN-Crown5 as a function of the dihedral angle φ in the ground (green), LE (blue) and TICT (red) electronic state.	99
2-12	Experimental (a) and simulated (b) fluorescence emission spectra of DMABN-Crown5 in acetonitrile (red), DMSO (purple), dichloromethane (blue) and cyclohexane (olive).	102
3-1	Chemical structure of Fmoc-(Aib-Aib-TOAC) ₂ -Aib-OMe (heptapeptide 1).	114
3-2	Reference frame employed in the Stochastic Liouville Equation (SLE).	119

3-3	View of the π^* orbital containing the unpaired electron of TOAC radical. In particular we show a sketch of SOMO (A) and SOMO-1 (B) of TOAC (R1=-COOH, R2=-NH2).	121
3-4	Trend in $ T^{(2,0)} $ versus distance calculated with the approximated expression (dash line) and the exact treatment (solid line).	122
3-5	Optimize structure of heptapeptide 1 : (a) View along the helix axis (b) View orthogonal to the helix axis.	123
3-6	Representation of heptapeptide 1 used in the hydrodynamic model for the calculation of the diffusion tensor.	126
3-7	Comparison of the CW-ESR experimental spectrum of heptapeptide 1 (black line) at 310 K and the calculated spectra in the optimized 3_{10} -helix conformation (red line) and in a hypothetical α -helix structure (blue line).	127
3-8	Experimental (solid line) and theoretical (dashed line) CW-ESR spectra of heptapeptide 1 in MeCN at temperatures 330, 310, 290 and 270 K.	128
3-9	X-Ray diffraction structure of heptapeptide 1 . Intramolecular H-bonds are represented by dashed lines.	133
3-10	Optimized structure of heptapeptide 1 : View along (right) and orthogonal (left) the helix axis of the (a) 3_{10} -helix and (b) α -helix secondary structure.	135
3-11	Structures of the TOAC-solvent complexes: twist conformation with CHCl_3 (A1); twist conformation with methanol (A2). R = peptide chain.	137
3-12	Trend of $ T^{(2,0)} $ versus distance calculated with the point dipole (dashed line) and localized quantum mechanical (solid line) approaches.	140
3-13	Experimental (solid line) and theoretical (dashed line) CW-ESR spectra of heptapeptide 1 in methanol at temperatures 320, 310, 300 and 280 K.	142
3-14	Experimental (solid line) and theoretical (dashed line) CW-ESR spectra of heptapeptide 1 in toluene at temperatures 350, 340, 330, 320, 310, 300, 290, 280 and 270 K.	144

3-15	Experimental (solid line) and theoretical (dashed line) CW-ESR spectra of heptapeptide 1 in chloroform at temperatures 290, 280, 270, 260 and 250 K.	145
3-16	Experimental (left) and simulated α -helix (center) and 3_{10} (right) CW-ESR spectra of heptapeptide 1 in toluene (A) and methanol (B) at temperature 310 K.	146
3-17	Chart of the integrated computational approach to the simulation of the CW-ESR spectra in solution. Steps (2) and (3) are based on the optimized geometry and electronic structure obtained in step (1). . . .	148
4-1	Pictorial representation of a nematic liquid crystal.	152
4-2	Polar coordinates for the position vector \mathbf{r} and for the director \mathbf{n} for the ellipsoidal case.	160
4-3	Adimensional Stokes coefficients versus δ parameter, for the case of a spherical probe in MBBA, calculated according to Eq. 4.32 for weak anchoring (dot line) and compared to the asymptotic value obtained from Eq. 4.38 (full line).	164
4-4	Time evolution of director field, for a spherical probe in MBBA, $R/V=1$, $R=100\ \mu\text{m}$ and $\delta=0.2$: direction of motion parallel to field (red) and perpendicular (blue).	165
4-5	Stationary adimensional friction factor, in MBBA (squares), PAA (circles), 5CB (diamond) and E7 (triangle) for $\delta=0.2$ for a sphere; empty symbols are for the case of parallel magnetic field and full symbols for the case of perpendicular magnetic field.	166
4-6	Time evolution of director field, for a prolate ellipsoidal probe in MBBA, $R_{\text{eff}}/V=1$, $R_{\text{eff}}=100\ \mu\text{m}$ and $\delta=0.2$: direction of motion parallel to field (red) and perpendicular (blue).	167
4-7	Time evolution of director field, for an oblate ellipsoidal probe in MBBA, $R_{\text{eff}}/V=1$, $R_{\text{eff}}=100\ \mu\text{m}$ and $\delta=0.2$: direction of motion parallel to field (red) and perpendicular (blue).	168

4-8	Stationary adimensional friction coefficient c of a ellipsoid moving in rectilinear motion in MBBA $R_{\text{eff}}/V = 1$, $R_{\text{eff}}= 100 \mu\text{m}$ and $\delta= 2$, as function of a_3/a_1	169
4-9	Stationary adimensional friction factor c , in MBBA (squares), PAA (circles), 5CB (diamonds) (cfr. Table 4.1), for $\delta= 0.2$ for a sphere (a), a prolate ellipsoid (b) and an oblate ellipsoid (c); empty symbols are for cases of parallel magnetic field, full symbols for cases of perpendicular magnetic field.	173

List of Tables

2.1	Absorption energies (in eV) for DMABN <i>in vacuo</i> at TD-DFT level employing PBE0 functional and different basis sets. Oscillatory strength is given in parenthesis. MO main contributions for each transition are also shown.	83
2.2	Relative energy (in eV) and dipole moment (in D) of the ground state and the lower energy excited states of DMABN <i>in vacuo</i> . In parenthesis the experimental values. ^a from ref. [185]. ^b from ref. [212].	84
2.3	Physical characteristics and solvent dependent parameters for DMABN in <i>n</i> -hexane, cyclohexane, benzene, dibutyl ether, diethyl ether, <i>n</i> -butylchloride, acetonitrile and dimethylsulfoxide. The energy corrections are expressed in eV.	87
2.4	Experimental and simulated fluorescence maxima for LE and TICT bands in different solvents.	88
2.5	Characteristic of the five most stable conformers of DMABN-Crown5 with a torsional angle equal to 90°. The structures are optimized in the gas-phase at the PBE0/6-31G(d). The energy are expressed in eV and the dipole moment in debye.	100
2.6	Physical characteristics and solvent dependent parameters for DMABN-Crown5 in cyclohexane, dichloromethane, acetonitrile and dimethylsulfoxide. The energy corrections are expressed in eV. ^a from [215].	103
2.7	Experimental and simulated fluorescence maxima for LE and TICT bands in different solvents.	103

3.1	Relative stabilities (ΔE in kcal/mol) of the low-energy peptide conformations obtained by PBE0/6-31G* full geometry optimization.	124
3.2	Summary of the parameters employed in the simulations of the ESR spectra.	125
3.3	Comparison between the X-ray diffraction and computed geometrical parameters for heptapeptide 1 (distance in Å and angles in degrees. Estimated standard deviations for the crystallographically derived parameters are in the ranges 0.004-0.007 Å, 0.3-0.5° and 0.3-0.6° for bond distance, bond angles and torsional angles, respectively.	134
3.4	Comparison between X-ray diffraction and computed geometrical parameters for 1 with a particular attention to the hydrogen bonds. Distance are in Å and the estimated standard deviation is in the range 0.004-0.007 Å.	136
3.5	Gyromagnetic tensor (ppm) computed in different solvents. Value in parentheses are obtained including one specific solvent molecule for each NO moiety (see Figure 3-11).	138
3.6	Dipolar hyperfine tensor (in Gauss) computed for heptapeptide 1 in different solvent. Value in parentheses are obtained including one specific solvent molecule for each nitroxide moiety (see Figure 3-11).	138
3.7	Calculated nitrogen isotropic hyperfine coupling (in Gauss) for the optimized 3_{10} -helix of the heptapeptide 1 are compared with fitted values (best fit). The final calculated values (best calc.) include electronic values at the energy minimum (a_{iso}°), vibrational averaging (Δ_{vib}), and, for protic solvents, the contribution of a single explicit solvent molecule (Δ_{1s}). The last column reports the optimized values of the isotropic hyperfine coupling.	139
4.1	Leslie coefficients for three nematic liquid crystals phases.	162

4.2	Comparison between the calculated and experimental values for the translational diffusion coefficient for different chemical systems. A detailed description of the specific characteristic of the systems are reported in the text.	171
-----	--	-----

Chapter 1

Theoretical methods

1.1 Introduction

Models are necessary to interpret chemical phenomena. A given model is made of three basic elements: the material constituents or "building blocks" of the system, the physical rules underlying the chemical process, and the mathematical formalism required to describe such a process according to the physical problem [1]. The final objective is to develop a theoretical model describing the chemical behavior.

Quantum computational chemistry originates from the study of small systems in gas phase. New methods and increasingly powerful hardware have made possible the extension of theoretical methods to larger systems in condensed phases. Description and prediction of the interaction between solutes and solvents are of enormous significance for computational methods that describe solution-phase chemistry. Often, the knowledge of the molecular properties of the systems in gas-phases is not sufficient to predict their behavior in solution because solute-solution solvent interaction can change many observables drastically, like the reactivity and the energetic of chemical processes [2]. From a rigorous theoretical point of view the very concepts of solute and solvent are meaningless, since a solution is an ensemble of molecules which should be treated at the same level, irrespective of their nature and population. The differentiation between solute and solvent is due to practical considerations, because of the difficulty of treating correctly bulk solutions due to: (i) the large number of solvent molecules and (ii) the high level of accuracy required to describe the solute. Solvation

affects the solute structure, the thermodynamics and kinetics of chemical processes. The solvent can induce a notable change in the molecular structure, both in terms of nuclear and electronic distributions. Change in the nuclear configuration may arise from the tendency of polar solvents to stabilize structure with large charge separation. But the best known solvent effect is the modulations of chemical reactivity [3]. This effect is especially relevant in water where it can invert the sign of the free energy change for a chemical reaction in gas phase. The solvent has three major effects on chemical reactivity: (i) the modulation of the intrinsic reactive characteristic of the reactants, (ii) the introduction of viscosity effects; (iii) the direct interaction of solvent molecules with reactants, products or transition states, which may lead to a different stabilization of these species.

During the early decades of the twentieth century provided the impetus for the search of a theory that could explain chemical system properties from their atomic constituents. It was soon realized that developing such a theory was not practical, because (i) the disparity between the relevant length and time scales (ii) the enormous required computational power. The last decades of the twentieth century witnessed the development of many qualitative and semi-quantitative models that could explain the properties of systems. Some of these models are relatively simple while others must be accompanied by very extensive computations. Continuum approaches are appropriate for describing a mesoscopic and macroscopic length scales, but cannot provide any insight into properties and characteristics at molecular scale. Methods for computing the molecular properties of the chemical system at molecular scale are divided into density functional theory and its variants, the classical Molecular Dynamic (MD) simulations and the quantum molecular dynamic techniques (Car-Parrinello). In general, we should not over-use atomic-scale simulations for studying of macroscopic properties, since atomic-scale mechanisms are separated from the macroscopic behavior by a vast array of intervening scales. Mesoscopic approaches filter (average) and modulate (i.e. set the boundary conditions of driving forces for) atomic-scale phenomena [4]. Methods that consider the solvent as a part of a system can be divided into several major groups: (i) macroscopic approaches (continuum methods), (ii) molecular approaches (explicit solvent models with molecular details) and (iii) mesoscopic approaches (hy-

brids of the first two)[5]. Historically, continuum methods were among the first to consider solvent effects and they still represent very popular approaches to evaluate, for example, solvation free energies. Early applications of these methods used simple analytical functions to estimate the electrostatic interaction between a solute, represented with point charges or dipole moments and solvent, described as a polarizable continuum medium characterized by a dielectric constant [6],[7]. Onsager developed a model for the calculation of the solvation free energy for a dipole in a spherical cavity [8]. With the advances in computational techniques it became possible to use numerical methods for molecules of different shapes. Hybrid methods are obtained when different continuum approaches are incorporated into quantum mechanical methods. The most used is the Polarizable Continuum Method by Tomasi and coworkers [9]. Many of these methods add the solvent dependent potential(s) to the solute Hamiltonian, next the Schrödinger equation is solved in a self-consistent manner. The major advantage of QM approaches combined with continuum models for the solvent is that they can describe charge transfer between solute and solvent. Among the hybrids/mesoscopic methods we would like to mention techniques which combine QM and MM approaches to calculate, for example, enzymatic reactions. These methods allow high level *ab-initio* treatment of the critical part of the system, and solvent is treated explicitly with a molecular mechanical approach. The last group of methods use the explicit solvent in combination with statistical mechanics. Solvent effects are represented by pair-wise interaction terms: electrostatic and van der Waals. These methods include DFT or molecular dynamics methods. The fundamental difference between the molecular and the continuum solvent models is not that one has solvent and the other does not. Rather, the difference is that the continuum model employs a homogeneous medium to represent the solvent where molecular model use atomistically represented molecules. While the latter choice is clearly more realistic, the practical limitations imposed by molecular representation hint that it is not necessarily the best choice for a given problem [10]. Figure 1-1 shows a scheme of the different approaches. Continuum models are based on the assumption that the relevant fields that describe the state of the system vary only at the macroscopic scale and are derived by averaging the system's properties at the smaller length scale. It is therefore clear that continuum theories can

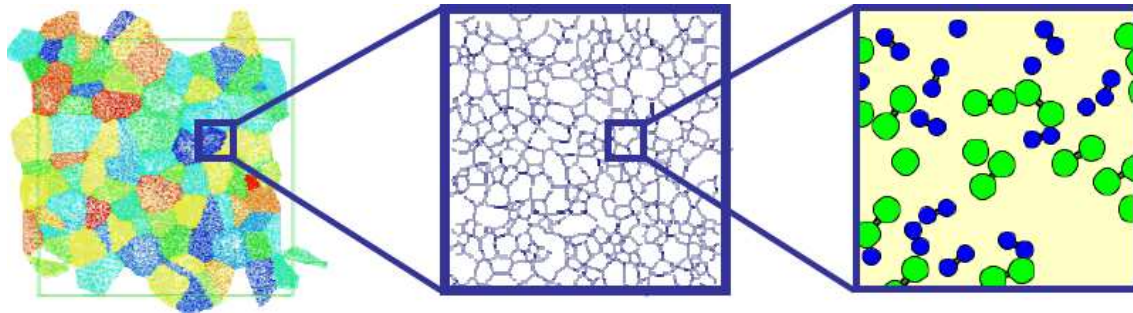


FIGURE 1-1: Scheme of the different theoretical methods used for describing a system: macroscopic approaches (left), mesoscopic approaches (center) and molecular approaches (right).

be enriched by incorporating additional information and that atomistic and continuum models need and reinforce each other. Each class of models has its own strengths and weaknesses, dictated by the domain of temporal and spatial phenomena for which they are valid [11]. The spatial domains of applicability range from the extent of individual atomic librations, characteristic of short time fluctuations, to the essentially infinite extent characteristic of macroscopic phase boundaries. Time scales similarly range from intramolecular vibrations to scales associated with net mass and heat transport. An important issue of simulation studies is the accessible time- and length scale covered by molecular simulations. Figure 1-2 shows a schematic representation for different types of simulations in length-time-diagram. It is clear that the more detailed a simulation technique is the smaller is the accessibility of long times and large length scales. Therefore quantum simulations, where fast motion of electrons are taken into account, are located in the lower left corner of the diagram and typical length time scales are of order of \AA and ps. Classical and *ab-initio* molecular dynamics approximates electronic distributions in a rather coarse-grained fashion by putting either fixed partial charges on interaction sites or adding an approximate model for polarization effects [12]. In both cases, the time scale of the system is not dominated by motion electrons, but the time of intermolecular collision events, rotational motions or intramolecular vibrations, which are orders of magnitude slower than those of electron motions. Consequently, the time step of integration is larger and trajectory length are of order of ns and accessible length of order of 10-100 \AA . If one considers particles in a solvent medium, where one is not interested in a detailed description of the solvent, one can apply stochastic

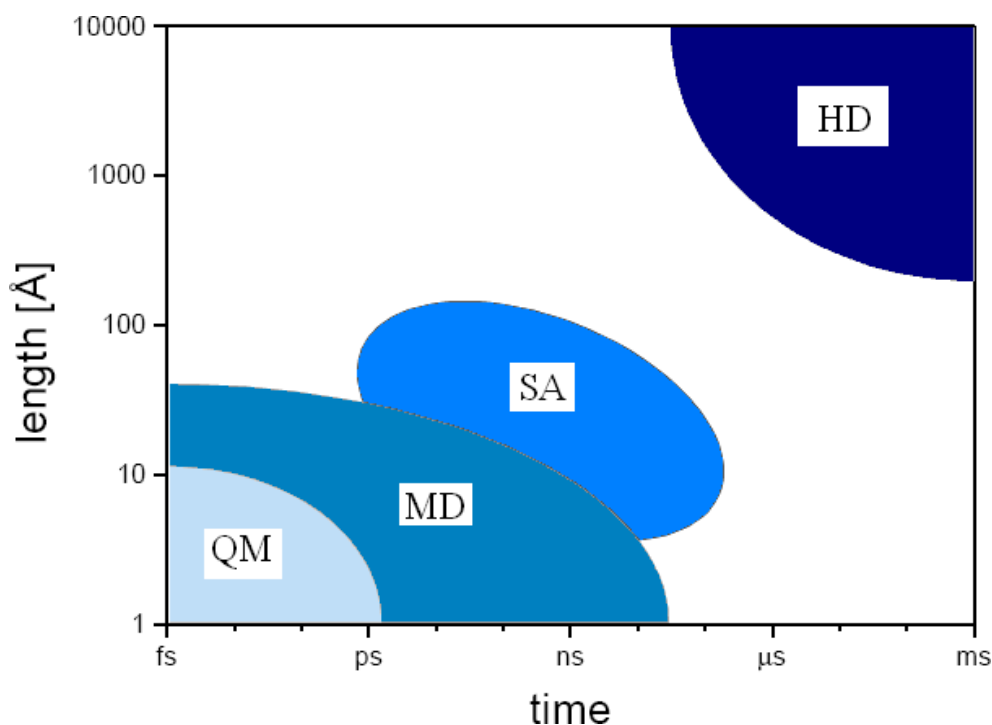


FIGURE 1-2: Schematic comparison of time- and length-scale, accessible to different types of simulation techniques (quantum simulations (QM), molecular dynamics (MD), stochastic approaches (SA) and hydrodynamics/fluid dynamics (HD)).

approaches, where the effect of the solvent is hidden in average quantities. Since the solvent is not simulated explicitly, the length scales may be increased considerably. Finally, if one is not interested in a molecular picture but in macroscopic quantities, the concepts of hydrodynamics may be applied, where the system properties are hidden in effective numbers, e.g. density, viscosity.

1.2 Molecular Approaches

At the heart of chemistry are atoms and molecules—they are the basis words in which chemical events are expressed. Description at molecular level of the solvent leads to a system characterized by an enormous number of degrees of freedom. In this Section we discuss modeling and simulation of chemical systems and their properties at the molecular scale. To achieve our goal we describe three important theoretical and computational tools that have been developed over the past three decades, namely, the

density functional theory (DFT), classical molecular dynamics (MD) simulation [13], and *ab-initio* molecular dynamics techniques (Car-Parrinello).

1.2.1 Density Functional Theory

Depending on the properties and systems of interest one can choose different theoretical approaches. For instance, when focusing on the mechanical properties of macroscopic samples, the precise arrangement of electrons is of secondary interest. On the other hand when one studies the electronic properties or the reactivity of specific molecules, one needs to include explicitly electronic degrees of freedom [14]. In the full quantum mechanical approach the solute and the solvent are considered as a supermolecule. The reliability of the theoretical prediction increases with the number of solvent molecules considered because surrounding the solute with a sufficient number of molecules simulating the bulk solvent generally requires an enormous amount of computer time. The Density Functional Theory (DFT) is the most used model employed to describe a solute/solvent system within a molecular approach. The modern formulation of the DFT is due to Hohenberg and Kohn in 1964 [15]. The fundamental tenet of the DFT is the special role that can be assigned to the density of particles in the ground state of a quantum many-body system. The density can be considered as a "basic variable" and all properties of the system can be considered to be unique *functionals* of the ground state density. The theorems of HK are an existence proof of such a functional, but there is no prescription on how to construct it. Unfortunately we do not know the exact form of the energy functional. It is necessary to use approximations regarding parts of the functional dealing with kinetic energy and exchange and correlation energies of the system of electrons [16]. The simplest approximation is the local density approximation (LDA) which leads to a Thomas-Fermi [17],[18] term for the kinetic energy [19],[20],[21] and the Dirac [22] term for the exchange energy. In general for an atom or molecule, the energy of the system can be written considering: the kinetic energy of the nuclei, the kinetic energy of the electrons, the interaction energy of nuclei (Coulombic repulsion), the external potential (the electrostatic potential coming from nuclei, with which electrons interact) and the electrostatic repulsion between electrons. Since nuclei are much heavier than electrons, they have much larger inertia than electrons,

and we can consider that electrons will adjust their positions instantly whenever nuclei move. We can separate the movement of the electrons and nuclei, and assume that movement of electrons depends on the positions of nuclei in a parametric way. This is the well-known Born-Oppenheimer approximation. It allows us to use the electronic energy related to the hamiltonian, and add the components of energy coming from nuclei at the end of calculations. In this approach the total energy of the many-body electronic system can be expressed as:

$$E_{el}[\rho(\mathbf{r})] = T_{el}[\rho(\mathbf{r})] + E_{ee}[\rho(\mathbf{r})] + E_{en}[\rho(\mathbf{r})] \quad (1.1)$$

where $E_{el}[\rho(\mathbf{r})]$ is the total electronic energy, $T_{el}[\rho(\mathbf{r})]$ is the electronic kinetic energy, $E_{ee}[\rho(\mathbf{r})]$ is the contribution to the total energy from electron-electron interactions, and $E_{en}[\rho(\mathbf{r})]$ is the contribution from the electron-nuclear interactions. The form of $E_{en}[\rho(\mathbf{r})]$ is generally expressed as $\int \nu(\mathbf{r})\rho(\mathbf{r})d\mathbf{r}$, where $\nu(\mathbf{r})$ is the nuclear potential, generally taken to be a Coulombic interactions. Finding accurate functional form for $T[\rho(\mathbf{r})]$ and $E_{ee}[\rho(\mathbf{r})]$ is a continuing challenge [23]. The KH theorems provide a prescription of minimizing energy by changing corresponding density. Unfortunately, the expression relating to the kinetic energy of the density is not known with satisfactory accuracy. The solution come from considering the the kinetic energy is easily calculated from the wave function, provided that it is known. Khon and Sham [24] gave an ingenious method of marrying wave function and density approach. First implementations of the Kohn-Sham method were based on local approximations to the exchange correlation energy. DFT provides excellent results for the calculation of the molecular geometry, vibrational frequencies, ionization potentials, electron affinities and proton affinities [16],[25],[26],[27],[28],[29],[30]. Recently, there is much interest in using DFT for high spin species or for the calculation of parameters for NMR and ESR spectroscopy, diamagnetic properties, polarizabilities an other. In particular it is possible for example to apply the DFT methods to the computations of NMR parameters for transition-metal complexes [31]. The DFT consider in the correct way the strong influence of electron correlation in particular for the $3d$ metals [32],[33].

1.2.2 Molecular Dynamics

Molecular dynamics methods are concerned with simulating motion of molecules to gain a deeper understanding of chemical reactions, fluid flow, phase transitions, droplet formation, and other physical phenomena that derive from molecular interactions. These studies include not only the motion of many molecules as fluid, but also the motion of single large molecules consisting of hundreds or thousands of atoms, as in proteins. Molecular dynamics (MD) is probably the most important and most widely used particle method in computational chemistry. MD was first used in thermodynamics and physical chemistry studies to calculate thermodynamical properties of various physical systems including gases, liquids, and solids.

There are two basic assumptions made in *standard* MD simulations: (i) molecules or atoms are described as a system of interacting material points, whose motion is described dynamically with a vector instantaneous positions and velocities. The atomic interaction has a strong dependence on the spatial orientation and distances between separate atoms. (ii) No mass charges in the system. Equivalently, the number of atoms in the system remains the same. The simulated system is treated as an isolated domain system with conservative energy [34]. The two main families of the molecular dynamic simulations are classical molecular dynamics and *ab-initio* Car-Parrinello molecular dynamics.

Classical Molecular Dynamics

Classical molecular dynamics methods are applied to a large ensemble class of problems, e.g. properties of liquids, defects in solids, fracture, surface properties, friction, molecular clusters, polyelectrolytes and biomolecules [12]. They are based on atomistic simulation methods where: (i) each atom is treated as a point of mass, (ii) simple force rules describe the interactions between atoms, (iii) Newton's equations are integrated to advance the atomic positions and velocities and (iv) thermodynamic statistics are extracted from atomic (molecular) positions. In a molecular dynamics simulation, one wishes to explore the macroscopic properties of a system through microscopic simulations, for example, to calculate changes in the binding free energy of a particular drug

candidate, or to examine the energetics and mechanisms of conformational change. The connection between microscopic simulations and macroscopic properties is made via statistical mechanics which provide the rigorous mathematical expressions that relate macroscopic properties to the distribution and motion of the atoms and molecules of the N-body system; molecular dynamics simulations provide the means to solve the equation of motion of the particles and evaluate these mathematical formulas. With molecular dynamics simulations, one can study both thermodynamic properties and/or time dependent (kinetic) phenomenon. Models of particle systems are characterized by the nature of the interactions between particles. Molecular dynamics simulation consists of numerical, step-by-step, solution of the classical equations of motion (Newton's second law), which for a simple atomic system may be written

$$\begin{aligned}
 M_I \ddot{\mathbf{R}}_I &= \mathbf{F}_I \\
 \mathbf{F}_I &= -\frac{\partial}{\partial \mathbf{R}_I} \mathcal{U}
 \end{aligned}
 \tag{1.2}$$

We need able to calculate the forces \mathbf{F}_I acting on the atoms, which usually derived from a potential energy \mathcal{U} . From a knowledge of the forces acting on each atom, it is possible to determine the acceleration of each atom in the system. Integration of the equations of motion then yields a trajectory that describes the positions, velocities and accelerations of the particles as they vary with time. From this trajectory, the average values of properties can be determined. The method is deterministic; once the positions and velocities of each atom are known, the state of the system can be predicted at any time in the future or the past. All simulated objects are defined within a model description. In classical simulations *objects* are most often described by point-like centers which interact through pair- or multibody interaction potentials. The highly complex description of electron dynamics is abandoned and an effective picture is adopted where the main feature like the hard core of a particle, electric multipoles or internal degrees of freedom of a molecules are modeled by a set of parameters and analytical functions. Since the parameters and functions give a complete information of the system's energy as well as the force acting on each particle. The combination of parameters and functions is called a force fields Figure 1-3. Different types of force field were developed

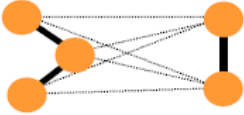
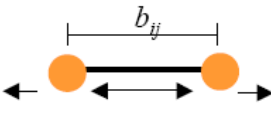


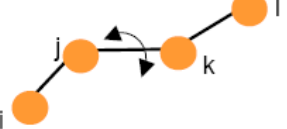
6-9 van der Waals		$u_{ij}(r_{ij}) = 4\epsilon_{ij} \left(\left(\frac{\sigma_{ij}}{r_{ij}} \right)^9 - \left(\frac{\sigma_{ij}}{r_{ij}} \right)^6 \right)$
6-12 van der Waals		$u_{ij}(r_{ij}) = 4\epsilon_{ij} \left(\left(\frac{\sigma_{ij}}{r_{ij}} \right)^{12} - \left(\frac{\sigma_{ij}}{r_{ij}} \right)^6 \right)$
Electrostatic		$u_{ij}(r_{ij}) = \frac{q_i q_j}{r_{ij}}$
Quadratic bond-stretching		$u_{ij}^s(r_{ij}) = \frac{1}{2} k_{ij} (r_{ij} - b_{ij})^2$
Morse bond-stretching		$u_{ij}(r_{ij}) = k \left(1 - e^{-a(r_{ij} - r_0)} \right)^2$
Bond-bending		$u_{ij}^b(\vartheta_{ijk}) = \frac{1}{2} k_{ijk} (\vartheta_{ijk} - \vartheta_{ijk}^0)^2$
Improper dihedrals		$u_{ij}^{id}(\xi_{ijkl}) = \frac{1}{2} k_{ijkl} (\xi_{ijkl} - \xi_0)^2$
Proper dihedrals		$u_{ij}^{pd}(\varphi_{ijkl}) = k_\varphi (1 + \cos(n\varphi_{ijkl} - \varphi_0))$

FIGURE 1-3: Typical examples for potential terms as used in common force-fields. Figure from ref. [12].

during the last ten years: UFF, CHARMM [35], AMBER [36], MM4. Most force fields used in chemistry are empirical and consist of a summation of bonded forces associated with chemical bonds, bond angles, and bond dihedrals, and non-bonded forces associated with van der Waals forces and electrostatic charge. These potentials contain free parameters such as atomic charges, van der Waals parameters, equilibrium bond length, angle, and dihedral; these are obtained by fitting against detailed electronic calculations or experimental physical properties such as elastic constants, lattice parameters and spectroscopic measurements. There are several different force fields for proteins and nucleic acids, differing either for the kind or analytical form used, or for the parametrization procedure. The force field typically used for proteins or nucleic acids (AMBER and CHARMM) are based on the fitting of *ab-initio* potential energy

surface (PES) for small molecules and on the reproduction of thermodynamic structural data. A drawback of this kind of approach is the limited transferability: these force fields are typically parameterized to work well for simulations at room temperature and not give accurate results at different temperatures. The first distinction is to be made between pair- and multibody potentials. In systems with no constraints, the interaction is most often described by pair potentials. A second important difference between interactions is the spatial extent of the potential, classifying it into short range and long range interactions. Short range interactions offer the possibility to take into account neighbored particles up to a certain distance for the calculation interactions. In that way a cutoff radius is introduced. A source of short range interaction is the van der Waals interaction. For neutral particles these are the London forces arising from induced dipole interactions. Fluctuations of the electron distribution of a particle give rise to the fluctuating dipole moments, which on average compensate to zero. But the instantaneous created dipoles induce also dipoles on neighbored particles which attract each other $\propto r^{-6}$. The common form of the resulting interactions is the Lennard-Jones potential. In the case of long range potentials, like the Coulomb potential, interactions between all particles in the system must be taken into account, if treated without any approximation. The Lennard-Jones and the Coulomb potentials consider the part of the potential energy representing non-bonded interactions between atoms. The bonding potentials consider the intramolecular bonding interactions. The simplest molecular model include term as bond terms, bend angle terms and torsional angle terms reported in Figure 1-3. Generally it is assumed that the forces between the particles are conservative, two-body forces; that is, energy is conserved and the total force acting on a particle due to the other particles is the sum of the forces between pairs of particles. Having specified the potential energy function the next step is to calculate the atomic forces \mathbf{F}_I . For site-site potentials is simple and it become more complicate for the intramolecular part of the potential. For solving Newton's equations of motion the favor is the Verlet algorithm.

Car-Parrinello *ab-initio* Molecular dynamics

In our discussion of classical MD presented so far, atoms are generally considered to be points which interact with other atoms by some predefined potential form. The forms of the potential can be, for examples, Lennard-Jones potentials or Coulomb potentials. The atoms are given velocities in random directions with magnitudes selected from a Maxwell-Boltzmann distribution, and then they are allowed to propagate via Newton's equations of motion according to a finite-difference approximation. At the very heart of any MD scheme is the question of how describe the interatomic interactions. The most delicate ones are systems where (i) many different atom or molecules types give rise to a myriad of different interatomic interaction that have to be parameterized and/or (ii) the electronic structure and thus the bonding pattern changes qualitatively in the course of the simulation [37]. We now discuss *ab-initio* molecular dynamics simulation (Car-Parrinello) in which quantum mechanical effects for the electronic degrees of freedom are taken into account [4]. The basic idea underlying every *ab-initio* molecular dynamics methods is to compute the force acting on the nuclei from electronic structure calculations that are performed "on-the-fly" as the molecular dynamics trajectory is generated. In this way the electronic variables are not integrated out beforehand, but are considered as active degrees of freedom. This implies that, given a suitable approximate solution of the many-electron problem, also chemically complex systems can be handled by molecular dynamics. An non-obvious approach to cut down the computational expenses of molecular dynamics which includes the electron in a single state was proposed by Car and Parrinello in 1985 [38]. The basic idea of the Car-Parrinello approach can viewed to exploit the quantum-mechanical adiabatic time-scale separation of fast electronic and slow nuclear motion. In order to achieve this goal the two-component quantum / classical problem is mapped into two component purely classical problem with two separate energy scales, at the expense of losing the explicit time-dependence of the quantum subsystem dynamics. The essential feature of the approach takes advantage of the fact that the total energy of the system of interaction nuclei and electrons is a function of both the classical variables for the nuclei and the quantum variables for the electrons. Instead of considering the motion of nuclei and

the solution of the equations for the electrons at fixed classical variables as separate problems [39]. The energy of the electronic subsystem $\langle \Psi_0 | H_e | \Psi_0 \rangle$ is evaluated with some wavefunction Ψ_0 and it is a function of the nuclear positions $\{\mathbf{R}_I\}$. But at the same time it can be considered to be a functional of the wavefunction Ψ_0 and thus of a set of one-particle orbital $\{\psi_i\}$ used to build up this wavefunction. Now, in the classical mechanics the force on the nuclei is obtained from the derivative of the Lagrangian with respect to the nuclear positions. This suggest that a functional derivative with respect to the orbitals, which are interpreted as a classical fields, might yield the force on the orbitals, given a suitable Lagrangian. Car and Parrinello postulated the following class of Lagrangians $\mathcal{L} = \sum_I \frac{1}{2} M_I \dot{\mathbf{R}}_I^2 + \sum_i \frac{1}{2} \mu_i \langle \dot{\psi}_i | \dot{\psi}_i \rangle - \langle \Psi_0 | H_e | \Psi_0 \rangle + \text{constraints}$ where μ_i is a fictitious mass associated with the electronic orbital and M_I is the actual mass of the I -th nucleus. The first and the second terms are the kinetic energy, and the third is that potential energy. The last term on the right hand side is necessary to ensure orthogonality conditions that include an overlap matrix. The corresponding Newtonian equations of the motion for the electronic states are derived from the Lagrange equations of motion $\frac{d}{dt} \left[\frac{\partial \mathcal{L}}{\partial \dot{\psi}_i^*} \right] = \frac{\partial \mathcal{L}}{\partial \psi_i^*}$. The equations of motion for the nuclei read $M_I \ddot{\mathbf{R}}_I = -\frac{\partial}{\partial \mathbf{R}_I} E_{tot}$. To summarize the Car-Parrinello techniques is actually based upon three ideas: (i) the force are calculated during the simulation (without evaluating all the single-particle energies) and only for those configurations which are actually visited. (ii) The electronic structure can be determined by minimizing the energy using an arbitrary minimization method. Car and Parrinello choose the molecular dynamics methods for this purpose, but other methods can be employed, and (iii) we can accelerate simulations by not requiring the electrons to relax to the minimum energy before each nuclear displacement. With respect to the molecular dynamic methods based on classical potential the Car-Parrinello methods determine properties of the systems with a few fitted parameters.

1.3 Mesoscopic Approaches

Having identified some problems connected with molecular approaches it seems an obvious step to decrease gradually the molecular detail in the description of chemical

system. Mesoscopic approaches include less degrees of freedom respect to the molecular approaches; the solvent is described as a continuum medium but the solute maintains its molecular structure. For instance, to the extent first-solvation-shell effects are qualitatively different from those deriving from the bulk, one might choose to include the first solvation shell explicitly and model the remainder of the system with a continuum [10]. But this approach shows some problems. A typical first shell of solvent for a small molecule may be composed by a dozen or so solvent molecules. The resulting supermolecular cluster is be characterized by a large number of accessible structures and the QM part requires a strong computational investment.

Here, we present different mesoscopic approaches: the hybrids quantum mechanical/molecular mechanical methods, the polarizable continuum models, the dissipative particles dynamics and the stochastic methods.

1.3.1 The QM/MM methods

Theoretically *ab-initio* quantum mechanical (QM) methods are able to use for calculations of systematic intermolecular interactions in solution and for generate the necessary energetic and the structural data. In practice it is impossible to well reproduce a total system in condensate phases with quantum mechanic calculations because the calculation time is too higher for the faster computer too. In general it is possible to use empirical functions for the potential energy but they are difficult to associate with the molecular mechanics (MM) force field. The problems raise because it is impossible to describe explicitly the electronic structure, the MM force fields are inadequate for reproduce experimental data and the empirical functions that describe the potential (and consequently the simple molecular dynamic methods) are insufficient for describe chemical reactions that involve with the formation or the break of a chemical bond. Systems of chemical interest in the computational biology or in the catalysis are systems in condensate phase composed by hundreds and hundreds of atoms so studies [40]. The QM/MM methods have several applications (Figure 1-4) and they are principally in the protein modeling area [41],[42],[43],[44],[45]. Only recently Morokuma [46] has applied these methods to metallorganic reactions. It is possible to extend the application area to solvation studies [47], spectroscopic properties in condensate phases [48],

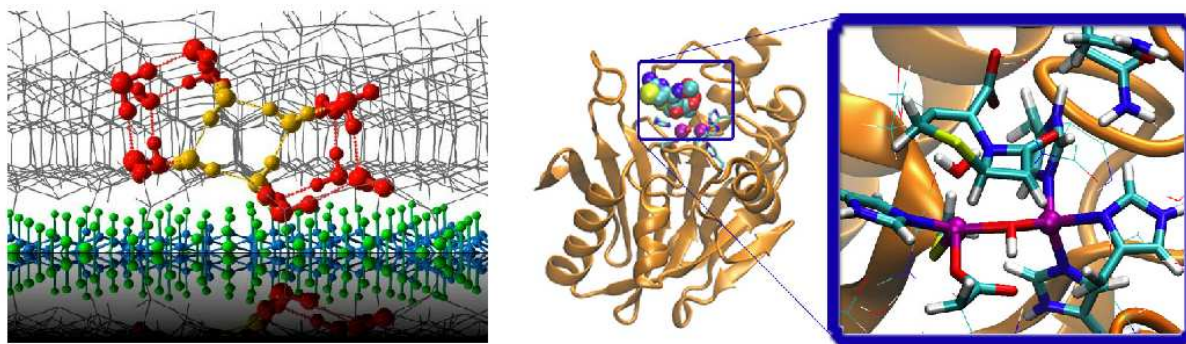


FIGURE 1-4: Different applications of QM/MM methods: material science (left) and bioscience (right).

conformational flexibility studies [49], chemical reactions and enzymes [50] and DNA [43]. Consequently the theoretical and computational chemistries develop adapted software (CHARMM) for the implementation of these kind of systems. The alternative approach of the hybrid QM/MM methods consist to divide the entire system in two parts one part is describe with QM methods and the other part is describe with a classical MM methodology. The develop of QM/MM methods begin with the pioneer studies of Warshel and Levitt [51] and of Singh and Kollman [52]. They adopted as general line the idea that a chemical system (compose by hundreds or thousands of atoms) can divide (Figure 1-5) into an electronically important region (describe with a quantum mechanical treatment) and the remainder region that act in a perturbative way. It can be describe with a classical methodology. In this way the reaction system (or the active site in an enzyme) is describe explicitly with a QM methodology while solvent molecules, that represent the reaction habitat (or the near amino-acids), are tract with MM *force field standard*. They are the heaviest part of the computational calculations. The hybrid methods are a good way for combine the classical approaches and the quantum one. The quantum part permits the calculation of the properties of the ground and excited electronic states. It requires an absent (*ab-initio* methods) or limited (semiempirical methods) parametrization. The success of the classical force field MM depends strongly on the calibration of an high number of parameters respect to the experimental data. The classical part gives an appreciable computational efficient. The electronic structure is involved in the reaction and the solute-solvent

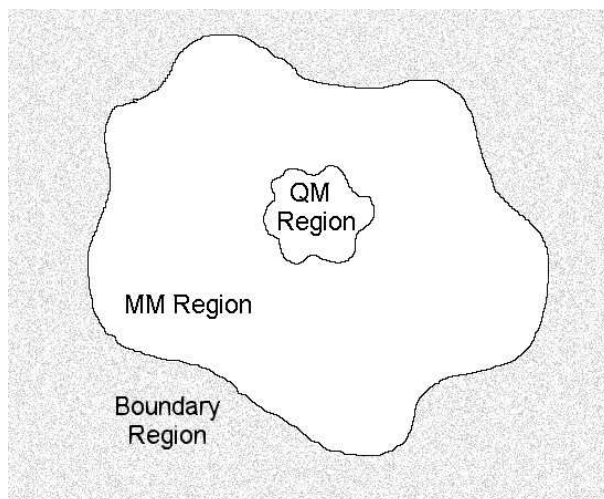


FIGURE 1-5: Schematic representation of the partition of a system in a condensate phase.

interactions are obtained by quantum calculations. For these reasons the QM/MM procedures raise a lot of interest for the study of chemical reactions. Polarization effects of the solvent on the solute are included in QM calculations by a model that describe the solvent as a continuum dielectric and calculate the solvation energy using the Onsager reaction field. These type of models have the advantage to be efficient for electrostatic long-range contributions in the solvation but they do not consider specific solute-solvent interactions. Instead in many case it is necessary to include in an explicit way these interactions. Consequently it is possible to develop a model in which the solute is treated with few solvent molecules with QM calculations and the solvent is treated with classical models as described by Warshel [53] in the Empirical Valence Bond theory (EVB). Another problem is the explicit inclusion in the quantum mechanical calculation of the solvent effects, namely the treatment of the region between the QM region and the MM region. In theory the division between two regions is simple and clear but it is rarely possible to define the total energy of the system as the sum of two subsystem. Often interactions between two regions are very strong, with the obvious case of a generic chemical bond. The last aspect to consider is the description of the confine region, i.e the region after the MM region. This region participates to the total energy of the system because it imposes some constraints in the external part of the MM region that permit to maintained the molecular structure. The total

energy of the system can be defined in a simple mode as:

$$E = E(QM) + E(MM) + E(QM/MM) + E(\text{confine}) \quad (1.3)$$

where $E(QM)$ represents the QM region energy as for an isolate system; the term $E(MM)$ gives the MM region energy, $E(QM/MM)$ in the interactions energy between QM and MM regions. This energy depends by the definition on the system in this complicate region. $E(QM/MM)$ includes all the coupling terms between regions: van der Waals interactions and modifications of QM Hamiltonian cause by the MM region as for example electrostatic perturbations, do not neglected in presence of link-atoms. At the end $E(\text{confine})$ is the energetic term cause by the constrainment in the external part of the MM region.

1.3.2 Polarizable Continuum Model

The electrostatic interaction of a solute with the solvent depends sensitively upon the charge distribution and polarizability of the solute. The latter is important because the solute and the solvent relax self-consistently to each other's presence [54]. The ability of solvent to polarize under equilibrium conditions is encapsulated by its dielectric constant, but solutes, being the primary interest, are allowed to have more components. Ultimately, the charge distribution of a solute is determined by quantum mechanics. The critical physical concept for treating solute polarization in solute is the reaction field. The reaction field is the electric field exerted on the solute by the solvent that it has polarized. The most popular of these type of methods is the Polarizable Continuum Model (PCM) developed primarily by the Pisa group of Tomasi [9],[55]. The PCM model, in its original form, is based on a description of the solvent as a macroscopic continuum medium having suitable properties (dielectric constant, thermal expansion coefficient, etc...) [56]. In this procedure the solute molecule is embedded in a cavity in the dielectric medium which is defining in terms of interlocking spheres centered on the solute nuclei and is studied *ab-initio*; solute-solvent interactions are described in terms of the reaction field due to the present of the dielectric medium. The latter acts as a perturbation on the Hamiltonian of the solute through its reaction potential. The solvation free energy of a solute molecule can be written as

the sum of the electrostatic, Pauli repulsion, and dispersion interactions, respectively, between the solute and the implicit solvent molecules [57]. Another term that contributed in the definition represents the reversible work required to create a cavity of the molecular shape of the solute. The cavity is defined in terms of spheres having radii determined empirically; the most popular choice for most atoms is typically 1.2 times the atomic van der Waals radius of Bondi [58]. The electrostatic components tends to be the dominant contribution in solvation free energies and contains both the electrostatic interactions between electrons and nuclei in the solute and between solute and solvent. The polarization of the solvent by the solute charge distribution induces a surface charge distribution on the solute-solvent interface. The solute-solvent interface is divided into N elements (tesserae) small enough to consider the charge distribution constant inside the them. Thus the continuum charge distribution of apparent point charges. The evaluation of the charge density in different surface elements is performing by solving the Laplace equation dependent on the reaction potential of the solvent. The repulsion forces (Pauli repulsion) between two interacting molecules originate mainly from the Pauli exclusion principles, increasing with the overlap of the two distributions and being related to the density of electron with the same spin. The chemical applications of the PCM model rapidly increasing in number and variety. A first general application of interest is the study of chemical reactions and it regards the chemical equilibrium conditions. The most extensively studies equilibria regard tautomeric processes, isomerizations, acid-base equilibria, and condensation reactions. Another interest aspect in the study of reaction mechanisms to derive quantitative information of chemical interest such as the reaction rate or the simulation of IR and CD spectra [59]. The model can be applied to anisotropic dielectric too [60]. The PCM model is inserted in the mesoscopic approaches considering the natural evolution in which a quantum mechanical description is used for the molecular structure. The merging was initiated when it was recognized that QM description of the electrostatic potential generated by the charge distribution of the molecule could represent a valid analytic and interpretative tool to study intermolecular interactions [61].

1.3.3 Dissipative Particle Dynamics

The most famous particle model that allows to simulate complex fluids at mesoscopic scale is the Dissipative Particle Dynamics (DPD) in Figure 1-6. The DPD model was initially devised by Hoogerbrugge and Koelman [62] as a simulation methods to capturing hydrodynamic time and space scales much larger than those available with Molecular Dynamics. The model consists of a set of point particles that move off-lattice interacting each other through a set of prescribed forces [63]. These forces are of three

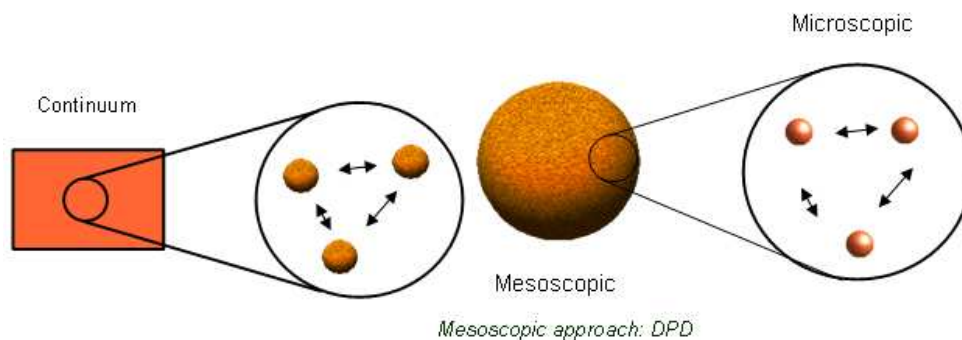


FIGURE 1-6: Representation of the DPD approaches in the multiscale approaches.

types: a purely repulsive conservative force, a dissipative force and a stochastic force directed along the line joining the center of the particles. The amplitude of this forces is dictated by a Fluctuation-Dissipation theorem. The DPD model captures the essentials of mass and momentum conservation which are the responsible for the hydrodynamic behavior of a fluid at large scale [64], [65], [66], [67]. From a physical point of view, each dissipative particle is regarded not as a single molecule but rather as a collection of molecules that move in a coherent fashion. DPD can be understood as a *coarse-graining* of molecular dynamics. The conservative forces oblige the fluid particles to be as evenly distributed in space as possible result of certain "pressure" among them, the friction force represent viscous resistances between different part of fluid, whereas the stochastic forces represent the degrees of freedom that have been eliminated from the description in the coarse-graining process. One of the most attractive feature of the model is its enormous versatility in order to construct simple models for complex fluids. In DPD the Newtonian fluid is made complex by adding additional interactions between

the fluid particles. By changing the conservative interactions one can easily describe polymers and colloids. Dissipative particle dynamics has been shown to produce the correct macroscopic (continuum) theory; that is, for a one-component DPD fluid, the Navier-Stokes equations emerge in the large scale limit, and the fluid viscosity can be computed. DPD appeared as a quick way of getting hydrodynamics suitable for mesoscale.

In the DPD methodology, the fundamental particles are "beads" that represent small regions of fluid material rather than the atoms and molecules familiar from MD simulations. All degrees of freedom smaller than a bead radius are assumed to have been integrated out leaving only coarse-grained interactions between beads. There are three types of force between pairs of beads, each of which conserves both bead number and linear momentum: an harmonic conservative interaction, a dissipative force representing the viscous drag between moving beads (i.e., fluid elements), and a random force to maintain energy input into the system in opposition to the dissipation. All forces are short-ranged with a fixed cut-off radius. By a suitable choice of the relative magnitudes of these forces, a system can be shown to evolve to a steady-state that corresponds to the Gibbs Canonical ensemble. Integration of the equations of motion for the beads generates a trajectory through the system's phase space from which all thermodynamic observables (e.g., density fields, order parameters, correlation functions, stress tensor, etc) may be constructed from suitable averages. An advantage over conventional Molecular Dynamics and Brownian Dynamics simulations is that all forces are "soft" allowing the use of a much larger time-step and correspondingly shorter simulation times.

1.3.4 Stochastic Methods

The QM/MM and the PCM mesoscopic approaches describe with different degrees of accuracy the static part of the molecular system (solute and solvent). It is important to consider that some solvent effects are not correctly reproduced without the dynamic part. Molecular dynamic provides a most powerful approach to gain information about dynamical properties of large assemblies of particles with known interactions. The primary objects of these methods are the trajectories of the considered system. The

mutual interactions of the solute with the solvent is required to simulate the time evolution of the full system [68]. A less detailed description that capture the relevant aspects of the problem can be achieved by the theory of stochastic processes. The dynamics of the solvent is modeled in some crude manner that reflects the statistical behavior of many collisions between solute and solvent but not the detailed process of a single molecular encounter. The forces of the solvent on the solute are divided into a friction force and a fluctuating force. For small velocities of the solute relative to the average motion of the solvent the Stokes' law describes the friction force while the fluctuating force is modeled by Gaussian white noise, the strength of which is related to the temperature of the solvent and to the friction constant, according to Einstein's formula. In a simulation only few stochastic differential equation describing the dynamics of the relevant degrees of freedom have to be solved in contrast with the MD in which a huge number of Newton's equations of motion for all microscopic degrees of freedom. Both methods rely on statistical mechanics: in MD the initial condition are drawn from a distribution of points in phase space describing the system in a particular thermodynamic state. In stochastic approaches the statistical properties of the random forces are dictated by relations from statistical mechanics.

Stochastic processes are sequence of random variables generated by probabilistic laws. The word "stochastic" comes from the Greek and means "random" or "chance" [69]. The most known application of the stochastic approaches is the interpretation of the Brownian motion. The Roman Lucretius's poem "De Rerum Natura" (c. 60 BC) has a remarkable description of Brownian motion of dust particles (though their movement happens to be mostly due to air currents). He uses this as a proof of the existence of atoms: "*Observe what happens when sunbeams are admitted into a building and shed light on its shadowy places. You will see a multitude of tiny particles mingling in a multitude of ways... their dancing is an actual indication of underlying movements of matter that are hidden from our sight... It originates with the atoms which move of themselves [i.e. spontaneously]. Then those small compound bodies that are least removed from the impetus of the atoms are set in motion by the impact of their invisible blows and in turn cannon against slightly larger bodies. So the movement mounts up from the atoms and gradually emerges to the level of our senses, so that those bodies*

are in motion that we see in sunbeams, moved by blows that remain invisible.”

Nevertheless Brownian motion is traditionally regarded as discovered by the botanist Robert Brown in 1827 while studying the plant life of the South Seas. In this study, he dealt with the transfer of pollen into the ovulum of plant. He examined aqueous suspensions of pollen grains under a microscope and found that the pollen grains were in *rapid oscillatory motion* [70]. Following Brown’s work Einstein explained Brownian movement essentially by combining the elementary stochastic process known as the random walk with the Maxwell-Boltzmann distribution. His idea may be summarized in this case: if a particle in a fluid without friction receives a blow due to a collision with a molecule, then the velocity of a particle changes. If the fluid is very viscous, the change in velocity is quickly dissipated and the net result is a change in the displacement of the particle. He assumed that the cumulative effect of collisions is to produce a random jump in the position of a particle; the particle performs a kind of random walk. At the microscopic level of description the particle is in constant interaction with the constituent of the fluid, which comprise a heat bath. The heat bath is in equilibrium at fixed temperature [71]. The mathematical formulation of Brownian motion consists of a stochastic differential equation, the *Langevin equation*, for the momentum of the particle. This equation is driven by random force, simulating the effect of the collision between the solute and the particle of the heat bath. In 1908 Langevin began by simply writing the equation of motion of the Brownian particle according to Newton’s laws under the assumption that the Brownian particle experiences two forces: (i) a systematic force (viscous drag) $-\zeta\dot{x}(t)$ which represents the dynamical friction experienced by the particle. x is the displacement and ζ is the coefficient of friction. (ii) A rapidly fluctuating force $F(t)$ which is again due to the impact of the molecules of the solvent on the particle now called white noise. This equation, according to Newton’s second law of motion, is:

$$m\frac{d^2x(t)}{dt^2} = -\zeta\frac{dx(t)}{dt} + F(t) \tag{1.4}$$

The friction term $\zeta\dot{x}$ is assumed to be governed by Stokes’s law which states that the frictional force decelerating a spherical particle of a radius a and mass m is $\zeta\dot{x} = 6\pi\eta a\dot{x}$,

where η is the viscosity of the fluid. The fluctuating part consider that $F(t)$ is independent of x and varies extremely rapidly respect to the variation of $x(t)$. This is the first example of a stochastic differential equation. Each solution of the Langevin equation

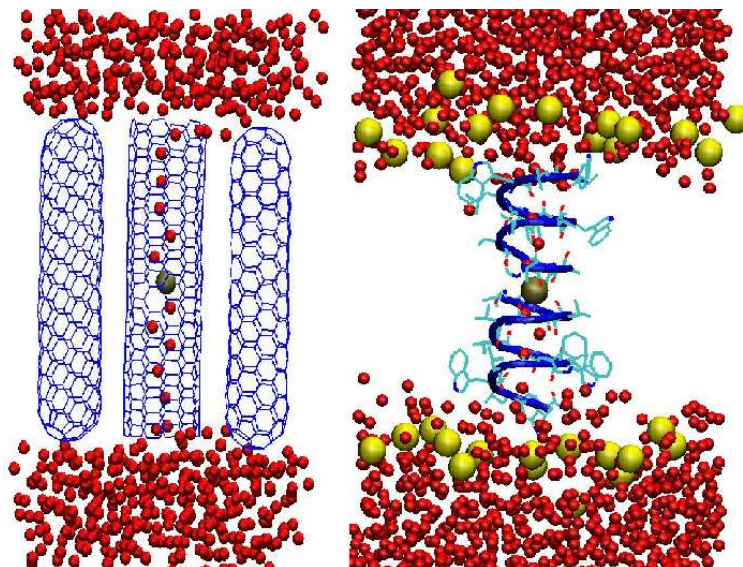


FIGURE 1-7: Lateral view of the carbon nanotube (left) and the gramicidin A channel (right) systems.

represent a different random trajectory and measurable results can be derived. The Figure 1-7 presents a biological application of the Langevin equation in which the solution of the equation allows to simulating conductance of ions across membrane channels. In the particular case a carbon nanotube across the membrane and the gramicidin A. An equivalent approach is to formulate an evolution equation for the time-dependent probability distribution in the phase space of the system. This equation is referred to as the *Fokker-Planck*(FP) or Smoluchowski equation in different contests. The FP equation describes the time evolution of the probability density function P of position and velocity of a particle, but it can be generalized to any other observable, too [72]. It is an equation for the evolution of the distribution function of fluctuating macroscopic variables. The main use of the FP equation is an approximate description for any Markov process in which the individual jumps are small. The Markov process is a process that has no memory, save the memory of the last observable point. Considering the conditional probability, the restriction to Markov process and the Taylor

expansion of the expression that define a diffusive process it is possible to obtain the FP equation:

$$\begin{aligned}\frac{\partial P}{\partial t} &= -\hat{\Gamma}P \\ \hat{\Gamma} &= -\sum_{i=1}^N \frac{\partial}{\partial x_i} D_i^1 - \frac{1}{2} \sum_{i,j} \frac{\partial^2}{\partial x_i \partial x_j} D_{ij}^2\end{aligned}\quad (1.5)$$

This is the FP equation for a one dimensional Markov process. D^1 is called the drift coefficient and D^2 the diffusion coefficient. The two coefficients may be calculated using the Langevin equation. In the most part of the applications the process is stationary and the FP equation assumes the canonical form:

$$\begin{aligned}\frac{\partial P}{\partial t} &= -\hat{\Gamma}P \\ \hat{\Gamma} &= -\sum_{ij} \frac{\partial}{\partial x_i} \Xi P_{eq} \frac{\partial}{\partial x_j} \Xi P_{eq}^{-1}\end{aligned}\quad (1.6)$$

where the equilibrium distribution is $P_{eq} = \exp[V/k_B T] / \langle \exp[V/k_B T] \rangle$ and V is the potential. The FP equation has become a very useful tool for treating noise in quantum optics as for example a laser that is the most important device in quantum optics [73]. The Smoluchowski equation is a special form of the FP equation. In particular, Smoluchowski considered the problem of the Brownian movement of a 1D particle under the influence of an external force. In this case the conditional probability is given by:

$$\begin{aligned}\frac{\partial P(r, p, t)}{\partial t} &= -\hat{\Gamma}P(r, p, t) \\ \hat{\Gamma} &= pm^{-1} \frac{\partial}{\partial r} - \frac{\partial U}{\partial r} \frac{\partial}{\partial p} - k_B T \frac{\partial}{\partial p} \xi P_{eq}(r, p) \frac{\partial}{\partial p} P_{eq}^{-1}(r, p)\end{aligned}\quad (1.7)$$

where p is the conjugated momentum. The first part of the equation is the streaming operator. It describes the deterministic drift that dependent only on the conservative, deterministic forces derived by the potential V . The second part is the collision operator; it describes the drift caused by the fluctuation-dissipations and depends on the friction ξ . The Smoluchowski equation is the high-friction limit of the FP equation. Specifically, it is obtained by assuming that the momentum relaxation is instantaneous,

and it is valid on diffusive time scale [74]. It is possible obtained the motion equation for the probability function P :

$$\begin{aligned}\frac{\partial P(r, t)}{\partial t} &\approx -\hat{\Gamma}P(r, t) \\ \hat{\Gamma} &= -\frac{\partial}{\partial r}DP_{eq}(r)\frac{\partial}{\partial r}P_{eq}^{-1}(r)\end{aligned}\quad (1.8)$$

where the diffusion tensor is defined by the Einstein law $D = k_B T \Xi^{-1}$. The chemical application of these type of methods are enormous because they consider the dynamical aspects that the other methods do not consider. In the recent years the generalized Smoluchowski equation has been presented to describe the diffusion and time-dependent fluorescence of a solute in a nanoconfined solvent [74]. The Langevin equation is applied to study the effects of fluid inertia [75], the diffusion in the convective boundary layer [76], to different physical phenomena [77], chemical reaction in condensed phases [78], loss processes in dielectric and ferrofluids, superparamagnetism, nonlinear relaxation processes [70], polymer or polymeric fluid. The FP equation is applied to study dusty plasma and active particles (e.g. cells in biological systems) [79], the intramolecular hydrogen transfer reaction dynamics [80] or self-organized molecular machine [81]. Other applications of these approaches are in the biological area with the explanation of the equilibrium fluctuation of the distance between an electron transfer donor and acceptor pair within a protein [82] or to study the Brownian motion of DNA [83]. In general these stochastic approaches permit to describing different dynamic processes, diffusion and solvation dynamics, and ultimately reaction dynamics in a wide variety of solvent system.

1.4 Macroscopic Approaches

This Section is concerned with the macroscopic/continuum models for solvation effects. The assumption underlying macroscopic/continuum approaches is that one may remove the huge number of the individual solvent molecules from the model, as long as one modifies the space those molecules used to occupy so that, modeled as a continuous medium, it has properties consistent with those of the solvent itself. Two advantage

are evident. The first is a reduction in the system's number of degrees of freedom and the second is that these techniques provide a very accurate way to treat the strong, long-range electrostatic forces that dominate many solvation phenomena. An important application of continuum models is in biosciences area. These models have been used to study biomolecular function over 80 years, starting with work by Born on ion solvation, Lang and Tanford and Kirkwood on protein titration, and Flanagan on hemoglobin dimer assembly [84]. In the 1980's, with increasing of the computer power and the availability, robust numerical model are introduced for described biomolecular geometries. The first one was introduced by Warwicker and Watson [85], who described the numerical solution of the Poisson-Boltzmann equation to obtain the electrostatic potential in the active site of an enzyme. The main macroscopic approaches are: hydrodynamic/continuum approaches, the smoothed particles dynamics and then we introduced a new approach that connect the hydrodynamic and the stochastic model.

1.4.1 Hydrodynamics/Continuum Approaches

The hydrodynamic/continuum label for chemistry approaches can be considered principally in two different way. From a part we can highlight the dependence on the density, the velocity or the viscosity of the solvent and from the other part we can focus on dielectric part of the solvent. At the most elementary level, many collective phenomena involve large numbers of individual, but interacting, objects. However, methodologists do not attempt to trace the motion of individual molecules, but consider average properties as temperature, pressure, etc... They use macroscopic or continuum theories - theories dealing with quantities averaged over very many neighboring particles [86]. The simplest of continuum models involve a density, a flux vector and a balance law. A density measures the amount of some relevant attribute per unit volume surrounding a point at a time t . We describe in an explicit way the continuum models with the second point of view, the dielectric models. A continuum model in computational science can be defined as a model in which a number of degrees of freedom of the constituent particles (a large number, indeed) are described in a continuous way, usually by means of a distribution function [61]. Traditionally, continuum models of solvent were focused on dielectric models of electrostatic effects. In a dielectric model the solvent is

modeled as a continuous medium, usually assumed homogeneous and isotropic, characterized solely by a scalar, static dielectric constant [54]. The physics of the electrostatic solute-solvent interaction is simple. The charge distribution of the solute, inside the cavity, polarizes the dielectric continuum, which in turn polarizes the solute charge distribution. This definition of the interaction corresponds to a self-consistent process, which is numerically solved following an iterative procedure. The continuum electrostatic approximation is based upon the assumption that solvent polarization density of the solvent at the position \mathbf{r} in space is linearly related to the total local electric field at that position [87]. Poisson theory provides a rigorous (macroscopic) theoretical framework for formulating and calculating the electrostatic components of the free energy of solvation for a set of charges embedded in a low-dielectric cavity that is surrounded by a solvent environment represented as a dielectric continuum [88]. The Poisson equation (or Poisson-Boltzmann when salt effects are included) for macroscopic medium follows the local and linear electrostatic response of the solvent

$$-\nabla[\epsilon(\mathbf{r})\nabla V(\mathbf{r})] = 4\pi\rho_M(\mathbf{r}) \quad (1.9)$$

where $V(\mathbf{r})$ is the electrostatic potential, $\rho_M(\mathbf{r})$ the charge density of the solute and $\epsilon(\mathbf{r})$ the position-dependent dielectric constant at the point \mathbf{r} . The potential depends on the electrostatic potential generated by the charge distribution and on the reaction potential generated by the polarization of the dielectric medium. It is assumed that all of the real charge of the system are inside the cavity. The Poisson equation and the relative boundary conditions are the basic elements to use in the elaboration of solvation methods according to standard electrostatics. There are several approaches to solve the problem: (i) the apparent surface charge (ASC) methods, (ii) the multipole expansion (MPE) methods, (iii) the generalized Born approximation (GBA), (iv) the image charge (IMC) methods, (v) the finite elements (FEM) methods, and (vi) the finite difference (FDM) methods. In methods based on the apparent surface charge (ASC) the reaction field is represented in terms of an imaginary surface charge spread over the cavity, and the electrostatic free energy of solvation can be expressed in dependence of the apparent surface charge distribution, on the solute distribution,

on the solute electrostatic potential on the cavity surface and on the solvent reaction potential. The solutions are generally based on a discretization of the integral, that define the electrostatic free energy, into a finite number of elements. The cavity surface is approximated in terms of a set of finite elements (called tesserae) small enough to consider the apparent surface charge almost constant within each tessera. Methods based on multipole expansions (MPE) of the solute charge distribution are probably the simplest one. These model start from the idea of Kirkwood [7] to describe the interaction between a set of classical charges (described in terms of a multipole expansion) enclosed in a spherical cavity embedded in a structureless polarizable dielectric medium described by a macroscopic dielectric constant. The cavity, obviously, has not molecular details. During the decades the MPE method undergo to evolution. First it is consider a one-center expansion for a spherical cavity. The expression of the multipole expansion for the potential of a charge distribution placed into a sphere, immersed in a continuum. Then Rivail and co-workers [89] abandoned the spherical cavity to pass to ellipsoids. The shape of the cavity is a critical factor in continuum methods. More elaborate methods have been developed based on multipole expansions and the Generalized Born (GB) methods can be considered as an extreme case of multicenter MPE, with multipole truncated at the first term, the charge, and the centers of expansion placed on all of the nuclei. The GB [90] treats the solute as a set of monopoles (centered at nuclei), each independently solvated. Only monopoles (atomic partial charges) are employed and instead of solving the Poisson equation with this charge distribution. Earlier version of the GB approach were described in the 1994 by Still [90] and it considers a multiplicity of interacting spheres, each with a charge at its center. Still defines an empirical Coulomb operator ($1/f_{GB}$) that has to be applied to all pairs of atomic solute charges. The definition of the free energy is

$$\Delta G = - \left(\frac{\epsilon - 1}{\epsilon} \right) \sum_{i,j=1} \frac{q_i q_j}{2f_{GB}} \quad (1.10)$$

The definition of the Coulomb operator depends on the generalized Born radii. The radius of an atom characterized its degree of burial inside the solute; qualitatively it can be thought as the distance from the atom to the molecular surface. An accurate

estimation of the Born radii is critical for the GB model [91]. The GBSA (Generalized Born Surface Area) is simply GB model augmented with the hydrophobic solvent accessible surface area term. This formulation has been shown to successfully in biomolecular simulation. The GBSA have been used in protein loop prediction algorithms [92], protein-protein docking [93], the refinement of NMR structures [94] and folding of proteins [95], [96]. The use of fictitious charges with appropriate positions and values is an old device in classical electrostatics. The image charge (IMC) method come from the simplest example, that of a point charge q placed in the vacuum at the distance d from the plane surface of a semi-infinite grounded conductor. The single fictitious charge having the request properties is a charge placed at a distance $-d$. The conductor surface acts as a mirror. This approach is of wide use for electrolytes or other fluids bearing localized systems of charges near a hard wall, or confined between parallel walls. The finite difference methods (FDM) is applied to models with sharp boundaries and to salt solution where ϵ depends on \mathbf{r} through the concentration. Non linear effects, related to the ionic strength of the solution are also included. The first application is due to Warwicker [85]. The whole space, including the solute as well as solvent, is mapped in a 3D Cartesian grid. The differential equation is replaced by a set of finite difference equations for each point of the grid. FDM provides good estimates of the free energy of solvation for small molecules [97],[98] provided that the grid of points is dense enough. Otherwise, rather inaccurate results are obtained. Like the FDM, the FEM is numerical methods of differential type. The FDM replaces the differential equations by algebraic ones, valid at a set of nodes within the domain, through the approximation of derivatives by finite differences, while the FEM replaces the domain by a set of finite domains, connected through their nodes, and reproducing at the nodes in an approximate way the behavior of the function in the subdomain. The methods may be applied to surfaces as well as volumes. The use of this 3D mesh lead to a sparse system of equations that are solved iteratively. In these approaches, a discrete approximation of the governing partial PB differential equations is obtained through a volume-filling grid. Ideally, a boundary-conforming grid is preferred but it is difficult to generate for a complex molecular shape. Although this problem these methods are wide used. Methods that discretize the Poisson differential operator over

finite differences or finite elements have long been used for biopolymers having classical charge distributions [99]. Results obtained using macroscopic continuum models for biomolecular solute depends sensitively on atomic partial charges assigned to the nuclei and the location of the dielectric boundary between the solute and the solvent.

1.4.2 Smoothed Particle Hydrodynamics

Smoothed particle hydrodynamics (SPH) is a computational techniques for the numerical solution of the equations of fluid dynamics without use of a numerical mesh. This methods was developed by Lucy [100] and Monaghan [101] in 1970s to simulate astrophysical gas dynamics problem. SPH method was elaborated for hydrodynamics problems that are basically in the form of partial differential equations (PDE) of field variables such as the density, velocity, energy, etc.. Obtaining analytical numerical solutions for such a set of PDEs is not usually possible [102]. Traditional techniques for the numerical solution of a fluid governed by the equations of classical Newtonian hydrodynamics first involve the creation of a computational mesh which is used to discretise the partial differential equations describing the flow. The partial derivatives can be approximated by a number of different methods including finite difference, finite volume, or finite element schemes. The computational mesh can be either fixed in space and cover the entire fluid domain (the Eulerian method), or can be fixed to the fluid and move with the flow (the Lagrangian method). The Eulerian method often requires the construction of a very fine mesh over the whole flow domain because the location of the interesting features of the flow is not known a priori. Hence the method is often computationally expensive. Lagrangian meshes overcome these problems by attaching the mesh points to the fluid itself and allowing the points to move with the flow. The non-linear terms then no longer appear and the mesh need only be defined in the regions of space occupied by the fluid. If the motion of the fluid becomes geometrically complex however then the mesh undergoes severe distortion and the underlying numerical methods become unstable. SPH is a Lagrangian method, although the points are never linked together to create a computational mesh. Each of the fluid dynamic variables is expressed as an integral interpolant using a smoothing function and the integral is then approximated by a summation over the interpolation points. By using

this approach, the derivatives of the fluid variables can then be evaluated by calculating the derivatives of the smoothing function. The hydrodynamic equations are solved with a set of particles with prescribed interactions. The resulting algorithm is very much like molecular dynamics with additional thermodynamic variables. The large amount of algorithmic knowledge in molecular dynamic can be transferred directly to the simulation of partial differential equations. Generalizations of SPH in order to include viscosity and thermal conduction and thermal convection have been presented only recently. The basic idea in SPH is to use an interpolant function to allow one to compute spatial derivatives of the fields at a given particle location [103]. Every fluid dynamic variable is expressed as an integral interpolant. Consider a general function $A(\mathbf{r})$ expressed in the form

$$A(\mathbf{r}) = \int A(\mathbf{r}')\delta(\mathbf{r} - \mathbf{r}')d\mathbf{r}' \quad (1.11)$$

where $\delta(\mathbf{r} - \mathbf{r}')$ is the Dirac delta function and the integral is taken over the entire 3D space. The equation is exact but not useful. The idea of SPH is to approximate the delta function by a suitable continuous function. This function is called kernel and the choice of the kernel is of the central importance to the success of the SPH methods.

1.4.3 Hydrodynamics Approaches/Stochastic Methods

Continuum Models [61] have proved to be quite successful in improving the determination of molecular properties via QM/MM approaches, from ground state characteristics (geometry, charge distributions etc.), to spectroscopic parameters (e.g. magnetic tensors) to electronic excited states *in medio*. Efficient implementation of current popular continuum models has led to a wide spread of this technique, which appears nowadays a good alternative to costly explicit solvent approaches, above all in the case of large solutes typical of biochemical substrates [87]. However, standard ISM are inherently based on an equilibrium description. The problem of generalizing current continuum models-based approaches is by no means a trivial task, for a number of reasons which need to be addressed explicitly before approaching such a task. First of all, we must ask ourselves what it is our goal, i.e. what is, precisely, a "dynamic equivalent of

standard continuum models". We shall define hereafter a standard continuum models any of the current formulation of quantum treatments based on the cavity-dielectric view, in a time independent framework. We shall call "dynamic equivalent" a self-consistent definition of a phenomenological theory which includes the full description of a electro-hydrodynamic (or electro-magneto-hydrodynamic) fluid and the time dependent QM description of the solute. Notice that we want to take into account the direct effects of the solvent dynamics on the solute and *viceversa*, thus our goal is different from addressing pure solvent relaxation via the definition of a frequency dependent polarization [104]: rather we wish to describe back-flow effects on the solvent dynamics resulting from the solute dynamics. However, we wish to maintain our description at phenomenological (i.e. macroscopic) level, without resorting to microscopic (molecular) derivations in order to keep full contact with standard static continuum models formulation. To further generalize the standard approach, however, we would like to retain a specific, and very relevant character of the mesoscopic nature of the continuum approach, by recognizing and describing, at least approximately, the fluctuating behavior of local medium. Therefore, we aim to include, based on fluctuation-dissipation arguments, a coherent description of stochastic processes in our picture.

After defining, hopefully in a compact and convincing form, our basic methodology, the very serious task remain of efficiently implementing a computational methodology able to extract satisfactorily dynamic information from the model. Indeed, we shall keep in mind that any methodological formulation, however elegant, is of practical null usefulness if it is not properly implemented. Some approximations will be necessarily introduced, during the derivation and after, but our aim is to demonstrate that at least in a few simple test cases a practical implementation is achievable, at a relatively low additional computational burden if compared to current ISM implementation. This is an important point, which underline a precise question: is it worthwhile to undergo such a job? Would it not be better, after all, to simple dispense with modeling and rely on explicit dynamics solvent treatments? The derivation of non-linear hydrodynamics for field variables in complex fluids is strictly related to rational derivation of deterministic hydrodynamics. Hydrodynamics equations for ideal condensed systems based on Poisson-like algebraic structures has been presented by Thellung [105] and

Turski [106] for isotropic non-dissipative fluids. Among other authors, Dzyaloshinskii and Volovick have discussed Poisson brackets in condensed matter description [107]. The Hamiltonian formulation of ideal isotropic fluids has been further discussed, for instance, by van Saarloos, Bedeaux and Mazur [108]. More recently a systematic tool for the derivation of hydrodynamics equations in complex fluids has been provided by the GENERIC formalism [109],[110]. Sonnet and Turski have discussed the related Dirac approach to accommodate constraints in dissipative fluids dynamics [111],[112]. Systematic derivations of complex fluids constitutive equations are discussed by Anthony [113], Muschik, Papenfuss and Ehrentraut [114].

The theory on non-linear fluctuations in isotropic compressible fluid is nowadays well-founded and applied profitably to several problems, like the interpretation of phase transitions in supercooled fluids. The basic methodological procedure for defining non-linear fluctuating hydrodynamical equations (i) assumes as a starting point the deterministic hydrodynamics equations for the field variables describing the fluid, (ii) defines a proper partition of deterministic drives into conservative and dissipative contributions - usually employing Poisson-like algebraic structures to describe conservative terms - and (iii) applies standard fluctuations-dissipation equivalence to introduce multiplicative noise into the deterministic equations. The resulting generalized Langevin equations can be related to a FP formulation. Literature available on the inclusion of fluctuations in hydrodynamics is rather large, and just a few references are quoted here, which are partly representative of the field. The fluctuating approach to hydrodynamics has been pioneered by Landau and Lifshitz [115], who established linear fluctuations theory, i.e. inclusion of fluctuation dissipation in linearized hydrodynamics equations. The study of randomly stirred Navier-Stokes fluids has been discussed by Forster, Nelson and Stephen [116], [117]; formal properties of fluctuations in nonlinear irreversible dynamics are commented by Grabert and Green [118], Grabert, Graham and Green [119]. Fokker-Planck formalism for describing non-linear fluctuating fluids has been presented by Enz [120], [121], Enz and Turski [122], Saarloos, Bedeaux and Mazur [123]. Application of non-linear fluctuations theory to liquid-glass transition has been studied by Das and Mazenko [124]. The full set of fluctuating non-linear hydrodynamics equations for normal fluids has been commented by Kim and Mazenko

[125]. A general discussion on fluctuations in systems not in local equilibrium have been presented by Eyink, Lebowitz and Spohn [126]. Mazur [127] and Rubi and Mazur [128] have discussed the relation between fluctuations theory and non-equilibrium thermodynamics. Statistical interpretation of fluctuating hydrodynamics has been discussed by Grabert [129]. Microscopic derivation of a Fokker-Planck equation for non-linear hydrodynamics description of macroscopic fields has been obtained by Zubarev and Morozov [130], and its connection to Langevin formalism has been clarified by Espanol [131].

1.5 A critical overview on the different approaches

Given the variety of approaches and models described above, how can the best methods for a particular simulation be chosen? Ideally, all systems should be simulated and with a molecular approach. However, as discussed above, such models add significant complexity to the simulation and therefore become impractical for very large (or lengthy) molecular simulations [132]. *Macroscopic approaches* describe the solvent as a continuum medium and the solute without molecular details. They have widespread application in the study of biochemical systems, where efficient algorithms are necessary. However, the shortcomings of these methods have to be properly considered. In the most case non-electric contributions in the solvation energy are neglected, and a detailed treatment of the solvent-induced polarization of the solute is difficult. Indeed, the description of the solute charge distribution and the definition of the cavity may not be accurate enough. Finally, the specific solute-solvent interactions are not dealt with. Some studies are beginning to showcase examples whereby a continuum treatment alone is not sufficient to mimic all aspects of the solvent environment [88]. These include water near a membrane bilayer [133], and ion dynamics in gramicidin channel [134]. Large differences between molecular and continuum approaches are generally expected when the properties of the water molecules are substantially different from those of bulk solvent. The detailed role of solvent in mediating interactions may be required for example during the protein folding [135],[136]. The treatment of the solute-solvent system at the molecular quantum mechanical level is impossible with

the current computational resources. The cost of the molecular quantum mechanical (DFT) approaches limits the description the solvent to a few molecules to analyze the specific interactions with the solute. In the *mesoscopic approaches* the solute is treated at the quantum mechanical level, while the solvent is represented using discrete (MM) or continuum representations. The QM/MM mesoscopic approaches are very attractive from a conceptual point of view and have a wide range of applications. The QM treatment of the solute prevents the errors in the intramolecular energy terms inherent to force fields and the solute-solvent polarization effects are considered. Moreover, the solvent is represented at discrete level, allowing an analysis of the specific solute-solvent interactions. The use of these methods is, nevertheless, limited by their computational cost, which makes it necessary to use non-polarizable force-fields for the solvent and simple Hamiltonians for the solute. These simplifications may affect the accuracy of the results [1]. The approaches based on PCM methods work in the framework of quantum mechanical codes ranging from semiempirical to post Hartree-Fock levels. Because of the lack of a microscopic treatment of the solvent, which is represented by a continuum medium, the computational requirements for the study of solvation phenomena do not differ substantially from those required for an isolated molecule. Indeed, most of the codes are easily available. For example Gaussian03 [137] includes several of these methods. In the last years there is a growing interest in the mesoscopic approaches of all sorts because they are seen as the combination of the advantages of the microscopic and the macroscopic approaches; but the choice of a mesoscopic model is not intrinsically better than a molecular or macroscopic approaches. To summarize the theoretical representation of condensed phases can be achieved by a large variety of techniques. Continuum or discrete representation of the solvent can be combined with quantum or classical treatment for the solute. Each technique has its strengths and shortcomings, and the proper selection of an adequate method to be used in the study of a specific system is probably the most important decision for the study of a chemical process in solution.

1.6 Work-Plane

Reactivity of molecular and supramolecular systems is greatly modified by the surrounding environment, often a fluid medium, and an active area of research is nowadays the study of the influence of a solvent structure on the static and dynamic properties of photo-active and paramagnetic probes, varying solvent properties, sample geometry and external perturbations. Standard continuum solvent theories are based on crude representations of the probe. Solvation processes depend in a specific way upon the structure of the solute, and in particular on molecular features as shape, flexibility, distribution of charges and anisotropy of the polarizability. Augmented solvent continuum approaches have been developed to interpret chromophore dynamics to account for persistent solvent local structures. Description of collective solvent modes is also necessary to understand relaxation processes affecting dynamics at longer times, in complex fluid environments: phase transitions in supercooled liquids, rheological properties of emulsions and colloids, confinement effects and finally micro and nano-probes dynamics. The inclusion of solvent effects is of great importance, in order to understand the physical mechanisms responsible of the tuning of the optical properties and therefore to the ultimate possibility to design nanomaterials with specific optical response. Theoretical methodologies based on stochastic and hydrodynamic modeling have proven over the years to be a powerful approach, especially when coupled with advanced quantum mechanical treatments, to describe effectively the dynamical aspects of solvation. In this work, a number of applications of advanced theoretical models are explored, aimed at clarifying the influence of solvent-driven relaxation processes on optic, magnetic and rheological observables. In particular, first a stochastic approach to the interpretation of the emission fluorescence of 4-(N,N-dimethylamino) benzonitrile (DMABN) is revised and discussed. We proceed by extending a stochastic modeling approach, in which internal degrees of freedom are coupled with an effective solvent relaxation variable. Evaluation of potential energy surfaces using advanced QM approach and estimates of dissipative parameters based on hydrodynamic arguments are discussed. Emission fluorescence is calculated by solving a diffusion/sink/source equation for the stationary population of excited state, and compared to experimentally

measured emission fluorescence of DMABN. Next we discuss the complete a priori simulation of the ESR spectra of complex systems in solution. The usefulness and reliability of the method are demonstrated on the very demanding playground represented by the tuning of the equilibrium between 3_{10} - and α -helices of polypeptides by different solvents. The starting point is the good agreement between computed and X-ray diffraction structures for the 3_{10} -helix adopted by the double spin-labeled heptapeptide Fmoc-(Aib-Aib-TOAC)₂-Aib-OMe. Next, density functional calculations, including dispersion interactions and bulk solvent effects, suggest another energy minimum corresponding to an α -helix in polar solvents, which, eventually, becomes the most stable structure. Computation of magnetic and diffusion tensors provides the basic ingredients for the building of the complete spectra by methods rooted in the Stochastic Liouville Equation (SLE). The remarkable agreement between computed and experimental spectra at different temperatures allowed us to identify helical structures in the various solvents. The generality of the computational strategy and its implementation in effective and user-friendly computer codes pave the route toward systematic applications in the field of biomolecules and other complex systems. Finally, we present a study of the translational friction coefficients of spherical and ellipsoidal probes moving in nematic liquid crystalline fluids, by solving numerically the constitutive hydrodynamic equations of nematic. The evaluation of the translational friction coefficients is based on a numerical solution of Leslie-Ericksen constitutive equations for the case of incompressible nematic fluids. The nematic medium is described by a vector field which specifies the director orientation in each point and by the velocity vector field. Simulation of director dynamics surrounding the moving probe are presented, and the dependence of translational diffusion upon liquid crystal viscoelastic parameters is discussed. The time evolution of director field, described by Leslie-Ericksen equations, is studied in the presence of an orienting magnetic field in two characteristic situations: director of motion parallel and perpendicular to field. In particular, a detailed analysis is given for the case of a spherical probe in rectilinear motion in nematic MBBA (4-Methoxybenzylidene-4'-n-butylaniline), together with a comparison with other nematogens, namely PAA (4,4'-Dimethoxyazoxy benzene) and 5CB (4'-n-Pentyl-4-cyanobiphenyl).

Chapter 2

An integrated approach for the fluorescence spectra of DMABN

2.1 Introduction

In recent years, the margin of interaction between computational chemistry and most branches of experimental chemistry has increased at a fast pace. The experimental characterization of new systems relies on computational methods for the rationalization of structural, energetic, electronic and dynamic features. Theoretical interpretation *via* computational modeling of optical spectroscopy observables in solution is of fundamental importance to gather information on the stability and reactivity of molecular systems [138]. It is in fact nowadays possible to model with a relatively high accuracy physico-chemical properties of complex molecules in solution, and to link spectroscopic evidence directly to structural and dynamic properties of optically active solvated probes. For medium to large-size molecules, methods rooted in the density functional theory are paving the route toward an accurate and effective computation of structural, electric, and magnetic properties. An effective computational strategy for the study of large system in solution can be obtained using DFT approaches in mixed quantum mechanical/molecular mechanical methods including last generation mean field models (e.g. PCM) for the description of the environmental effects. A truly effective and self-consistent treatment of long range dynamic solvation effects is relatively less advanced. Relevant efforts have been made in the direction of the eval-

uation of the effects on optical observables via the application of stochastic models, which essentially model relaxation processes, like molecular tumbling, local solvent relaxation, internal conformational motions and so on in terms of suitable classical time evolution operators which depend upon phenomenological dissipative parameters. We apply these approaches to reproduce a particular optical observable: the fluorescence spectra.

Fluorescence has proven to be a versatile tool for a myriad of applications. It is a powerful technique for studying molecular interactions in analytical chemistry, biochemistry, cell biology, physiology, nephrology, cardiology, photochemistry, and environmental science. It boasts phenomenal sensitivity for the analytical chemist or the life scientist working at nanomolar concentrations. But fluorescence offers much more than mere signal-gathering capability. New developments in instrumentation, software, probes, and applications have resulted in a burst of popularity for a technique that was first observed over 150 years ago. As the theoretical underpinnings of fluorescence became more understood, a more powerful set of applications emerged that yield detailed information about complex molecules and their reaction pathways. For instance, the binding of biochemical species and dynamics of the folding of proteins can be easily studied in situ, distances within macromolecules may be measured. Concentrations of ions can be measured inside living cells, membrane structure and function may be studied with fluorescence probes. Drug interactions with cell receptors can be investigated. Minute traces of fluorescent materials can be detected and identified in mixtures. The electronic structure and dynamics of an excited state of a molecule may be elucidated. These are only a few examples of the applications of modern fluorescence techniques. Fluorescence is a luminescence phenomenon in which electron de-excitation occurs almost spontaneously, and in which emission from a luminescent substance ceases when the exciting source is removed. In fluorescent materials, the excited state has the same spin as the ground state. Usually the absorbed photon is in the ultraviolet, and the emitted light (luminescence) is in the visible range. Fluorescence is named after the mineral fluor spar (calcium fluoride), which exhibits this phenomenon [139]. The distribution of wavelength-dependent intensity that causes fluorescence is known as the fluorescence excitation spectrum, and the distribution of wavelength-dependent inten-

sity of emitted energy is known as the fluorescence emission spectrum. The observed shift in the electronic emission spectra of organic compounds induced by solvents are commonly understood as an indication of the extent of charge reorganization of solute molecules upon electronic excitation [140]. Solvent shift of emission fluorescence bands reflect the influence of equilibrium solvent arrangement around the excited solute, rearranging inertially due to the instantaneous charge redistribution upon radiative deactivation to the ground state. Solvatochromic effects on the electronic spectra may be classified as positive or negative, depending on they promoted blue or red shift, respectively. The starting point for modeling solvent effects on the electronic spectra is recognized that there are long-range dielectric polarization effects and short-range effects. For electronic spectra, the short-range effects were traditionally assumed to be dominated by the dispersion interactions, which are expected to be positive when the excited state is more polarizable than the ground state, which is usually the case [54].

There are two common theoretical methods to simulate the emission spectra of organic and inorganic materials: the quantum mechanical methods and the Monte Carlo simulations. In the quantum mechanical methods the geometry of the electronic excited state is optimized by *ab-initio* methods and the intensity distribution of the band is calculated considering the Franck-Condon approximation. There are several examples of these kind of investigations. Marian [141] has simulated the emission spectra of an organic chromophore applying the time dependent density functional gradient algorithm of Turbomole program package. A valence triple basis sets with polarization functions on all atoms (TZVP) was employed and the B3LYP functional was used. The Franck-Condon distribution of the fluorescence emission is obtained by computing transition between the initial state and the vibrational level of the electronic ground state. It is possible to apply the QM methods to large oligomer system [142]. In this example the geometry is optimized with TDDFT using the B3LYP functional while the electronic emission spectra was calculated at the ZINDO/S level. Another interesting study used the CS-INDO solvation model to describe the fluorescence spectra of cyanines and betaines that are representative of positively and negatively solvatochromic behavior [143]. The procedure is characterized by a peculiar modeling of the solvation set representing the polarized solvent surrounding the solute. The Monte Carlo simula-

tions are commonly applied to biological problems [144], [145]. It is possible extend the MC simulations of the fluorescence spectra of a dye molecule confined in nanocavities [146].

In this Chapter we focus our attention on a the twisted intramolecular charge transfer, a particular process in which the role of solvent effects is important. The strong dependence of the TICT process on the solvents has been inspired a large number of theoretical studies on solvent effects [147]. These studies can be roughly divided into two types: stochastic models and quantum mechanical methods. In the first methods the overall rate is obtained from statistical mechanical methods that incorporating the solvent effect as a friction term. The potential energy surface (PES) on which the molecule moves during the TICT is not calculated a priori in this model. The solvent hinders the twisting motion through friction, the randomness of the buffering (collisions) necessitates of statistical models. Another effect is the reorganization of the solvent dipole around the instantaneously crated polar TICT state. In this model the solvent is taken account as a continuous medium. If in the stochastic model the structure of the solute is completely neglected this is different for the quantum mechanical model. In the quantum mechanical approach the potential energy surface is first constructed using quantum mechanical methods for isolated molecule while the solvation energy is calculated and added to get the PES in the presence of the solvent. This process has been studied in a particular class of donor-acceptor molecule derived from the 4-(N,N-dimethylamino) benzonitrile (DMABN).

2.2 An integrated approach for the fluorescence spectra of DMABN

Since the seminal studies [148] on the dual fluorescent behavior of 4-(N,N-dimethylamino) benzonitrile (DMABN) in polar solvents this molecule has been the subject of several experimental [149],[150],[151] and theoretical studies [152],[153],[154],[155],[156]. The main finding of such experiments were an additional emission in polar solvents, red shifted from the normal fluorescence band. This band was called "anomalous" because

constituted an obvious exception from well-established rule by Kasha [157] stating that the fluorescence spectrum is dominated by a single band arising from emission from the single excited state. The emission spectrum of DMABN presents two fluorescence bands strongly dependent on the solvent polarity and temperature. In low-polarity solvents only a band is usually observed (locally excited, LE) at high frequency, while in highly polar solvents a second band is present at low frequency. Intermediate behaviors, where both LE and TICT bands are present, are observed in medium-polarity solvents. This phenomena has been observed in several other electron-donor compounds, but DMABN remains one of the most studied case. The relatively small dimension make the molecule an excellent prototype system. The fact that the emissive properties of these compounds can be controlled by external parameters such as solvent polarity or temperature is important for applications [158], for example as a fluorescence marker [159],[160] or in material science [161],[162]. The interest multiplied when it become clear that photoinduced intramolecular charge-transfer may play a crucial role in biological light-harvesting processes such as photosynthesis [163],[164]. The unusual behavior of DMABN and relative compounds be explained qualitatively as resulting from a twisted intramolecular charge transfer state (TICT) phenomenon describe in the Grabowski model [152],[165] which links the charge transfer reaction (LE-TICT) to a twisting motion and orbital decoupling of the phenyl acceptor ring from the electron donor group in Figure 2-1. In short, DMABN can be thought to

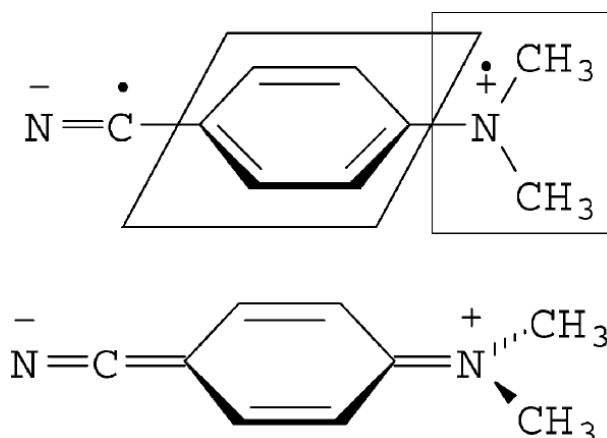


FIGURE 2-1: The twisted intramolecular charge-transfer (upper panel) and planar (lower panel) state model. Figure from ref. [158].

possess a double-minimum potential in its excited state. In the ground state the donor and the acceptor moieties are planar; the molecule in its first excited state can twist the dimethylamino group from planar to perpendicular conformation with respect to the phenyl ring. The twisting motion is accompanied by a charge transfer from donor to acceptor in the excited state. The resulting state, the TICT state is characterized by a large intramolecular charge separation and an increased dipole, and can be stabilized in polar solvent. It is the cause of the TICT band in the spectrum of DMABN. The LE state is the lowest excited singlet state of the DMABN and is the origin of the LE band (normal band) in the fluorescence spectrum. This state is the less polar where no twisting has occurred.

The dual fluorescence in DMABN arises from the two lowest singlet excited states, as each has a different geometry at which it attains a minimum. These two states have an intersection region with strong vibronic coupling which allows for transitions between LE and TICT. During the years many different hypothesis were formulated in competition with the TICT for assign the origin of the new band of DMABN. It is ascribed to an excimer [166], to a protonate species [167] or to an exciplex [168] with the solvent. But at the end the experimental evidence look to confirm the intramolecular structural charge. A quantitative description of the excited states dynamics can be obtained by considering the angle between the amino group and the aromatic plane as a relevant internal degree of freedom and adopting a stochastic description for its time evolution [156],[165],[169],[170], [171],[172],[173] in order to describe the charge-transfer process of the excited state which accompanies torsional motion. The internal coordinate is coupled to a solvent polarization coordinate defined as the stochastic reaction field in an Onsager cavity [173]. The time evolution equation for the excited state population is determined by a Smoluchowski operator modified by inclusion of sink and source terms. Basic ingredients of the model are (i) the total energy of the solute-solvent system in the two excited states and in the ground state which is given as the sum of the potential energy of the isolated molecule and a solvent correction; (ii) the diffusion coefficients for the internal motion and for the solvent relaxation. The aim of this work is to develop a general model that allow to reproduce the emission spectra of DMABN and its derivatives. Several molecules derived from DMABN exhibit

also complex fluorescence in polar solvents, and several prototype systems with similar behavior have been studied [175],[176]. The covalent attachment of the benzonitrile group to the aza group of a metal binding ionophore such as Cyclam creates a fluorescent ionophore DMABN-Cyclam [177],[178] that uniquely combines the characteristic fluorescence properties of DMABN with the metal binding properties of Cyclam. The molecule presents a triple fluorescence in ethanol that can be possibly interpreted as resulting from a LE state, a TICT state and an intramolecular exciplex (E) [179]. The LE state emission at high frequency dominates the spectrum in non polar solvents as n-hexane while polar solvents stabilize the charge-transfer states at lower frequency. Letard *et al.* [180] reported the dual fluorescence of two compounds structurally similar to DMABN-Cyclam, 4-(1-aza-4,7,10-trioxacyclododecyl) benzonitrile (DMABN-Crown4 and 4-(1-aza-4,7,10,13-tetraoxacyclododecyl) benzonitrile (DMABN-Crown5).

The fluorescence spectra of DMABN-Crown4 and DMABN-Crown5 show two bands in medium polarity solvents which can be interpreted as TICT and LE signals. The TICT/LE ratio increases with increasing solvent polarity. The relative intensity of the TICT band increases going from DMABN-Crown4 to DMABN-Crown5. There are several possible level of extension to present theoretical approaches which are worthwhile to be addressed, and which could provide a dramatic improvement in the present interpretative tools available to the physical chemist. Any true advance in the application of theoretical/computational approaches to the interpretation of optical spectroscopies in solution must be based on a combination of the statistical-thermodynamic description of the solvent and advanced determination of molecular structural properties. First of all, at a basic level on integration, it is possible to combine present state-of-art quantum mechanical and stochastic approaches in a integrated scheme. A refined computational treatment is then based on a computational approach, which combines (i) quantum mechanical calculations of structural parameters (molecular shape, dipole moments, Franck-Condon factors), including environmental and fast vibrational and librational averaging; (ii) direct feeding of calculated molecular parameter into stochastic modeling. Integration of all those building blocks define a reliable computational approach for the *ab-initio* prediction of structures, vibrations, and spectroscopic properties of organic molecule in solution. Notice that, in principle, solvent effects can

be dealt with in the determination of structural parameters, leaving to the stochastic model the description of slowly relaxing dynamics only; or structural properties can be determined *via* quantum mechanical methods *in vacuo*, allowing for semi-classical corrections in the stochastic model [138]. In this work, we are interested in defining a coarse-grained description of solvation dynamics to understand the main effects of polar media on the observed emission fluorescence of DMABN, as a prototype model which will be also employed for more complex systems. We seek a relatively simple interpretation based on macroscopic solvent properties (dielectric constants and viscosity), keeping at a minimum the number of adjustable parameters. In order to do so, we shall consider a stochastic diffusive description of the molecule internal dynamics, an explicit evaluation of dissipative properties (diffusion tensor) from a simplified hydrodynamic description of the solute molecule and a simple characterization of solvent variables. The methodology is based on a three-step procedure, namely (i) the definition of potential energy surfaces for the ground state and the two lowest energy excited states of the solute molecules *in vacuo*, (ii) coupled with a description for the roto-translational and conformational dynamics, in the presence of a (iii) stochastic polarization coordinates representing the solvent relaxation.

2.2.1 The model

We review here briefly a phenomenological approach to the calculation of emission fluorescence signal [170], [171],[172],[173] in DMABN. The (time dependent) emission fluorescence signal $I(\omega, t)$ for a generic molecular system can be in general written as an integral over excited state phase space variables

$$I(\omega, t) \propto \omega^3 \int d\mathbf{Q} \sum_n k_{n \rightarrow g}^{rad}(\mathbf{Q}) g_n[\omega - \Delta\omega_n(\mathbf{Q})] P_n(\mathbf{Q}, t) \quad (2.1)$$

here we shall denote with collective index \mathbf{Q} the coordinates (in a broad sense, to be specified later as the chosen variables describing the instantaneous solute + solvent configuration) for a given configuration. The derivation of the Eq. 2.1 is reported in Appendix A. The sum runs over excited states $n=1, \dots, N$. Quantity $\Delta\omega_n(\mathbf{Q})$ is the difference between state n and the ground state g , $\hbar\Delta\omega_n(\mathbf{Q}) = E_n(\mathbf{Q}) - E_g(\mathbf{Q})$,

$k_{n \rightarrow g}^{rad}(\mathbf{Q})$ is the radiative emission factor for state n to ground state and $g_n(\mathbf{Q})$ is an intrinsic line shape. The excited state populations $P_n(\mathbf{Q}, t)$ are described by a time evolution equation which is based on stochastic operator $\hat{\Gamma}_n$, describing internal relaxation processes affecting the excited state, source terms $S_n(\mathbf{Q}, t)$ for the creation of excited state population and kinetic terms accounting for radiative and non-radiative decay to ground state and coupling among excited states:

$$\frac{\partial}{\partial t} P_n(\mathbf{Q}, t) = -\hat{\Gamma}_n P_n(\mathbf{Q}, t) - \sum_{n'} k_{nn'}(\mathbf{Q}) P_{n'}(\mathbf{Q}, t) + S_n(\mathbf{Q}, t) \quad (2.2)$$

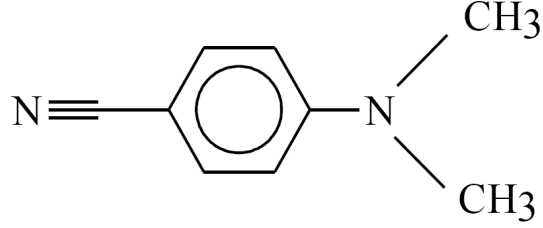
with suitable initial condition, e.g. simply $P_n(\mathbf{Q}, t) = 0$. By modeling $\hat{\Gamma}_n$, $k_{nn'}(\mathbf{Q})$ and $S_n(\mathbf{Q}, t)$ the dynamic or static emission can be reproduced. The stationary emission spectrum is obtained in particular as

$$I(\omega) \propto \omega^3 \int \mathbf{Q} \sum_n k_{n \rightarrow g}^{rad}(\mathbf{Q}) g_n[\omega - \Delta\omega_n(\mathbf{Q})] P_{st,n}(\mathbf{Q}) \quad (2.3)$$

where the stationary population for all excited states is obtained as

$$\hat{\Gamma}_n P_{st,n}(\mathbf{Q}) + \sum_{n'} k_{nn'}(\mathbf{Q}) P_{st,n'}(\mathbf{Q}) = S_n(\mathbf{Q}) \quad (2.4)$$

where $S_n(\mathbf{Q})$ is the stationary source function. To summarize, the dynamic or static fluorescence emission is in principle obtainable after defining suitable pump and kinetic term, both generic functions of the systems variables (including internal solute conformational degrees of freedom plus solvent configuration coordinates), radiative emission factors $k_n^{rad}(\mathbf{Q})$, intrinsic shape functions $g_n(\omega)$ and above all time evolution operators $\hat{\Gamma}_n$ which are defined as stochastic operator for the time evolution along the \mathbf{Q} coordinates in the n -th excited state, and is fully specified with respect to the potential energy surfaces (PES) of the excited state. We start by providing explicit forms for Eqns. 2.1-2.4 for the case of DMABN. We consider two diabatic states $n=LE, TICT$. The molecular structure is summarized in Figure 2-2. An internal coordinate describing the donor/acceptor relative orientation is introduced as the main degree of freedom describing internal conformational dynamics. The twist of the amino group not only modifies the relative energy of the two states significantly, but also enhances the



(DMABN)

FIGURE 2-2: Structures of N,N dimethylamino-benzonitrile (DMABN).

charge separation in the low-lying states due to the electronic decoupling between the amino and the phenyl ring. Therefore, the twist angle of the amino group can be served as the TICT reaction coordinates to discuss the dual fluorescence [174]. The phase space variables is described in principle as $\mathbf{Q} = (\mathbf{\Omega}_{MF}, \varphi, \mathbf{X})$, i.e. orientational coordinates $\mathbf{\Omega}_{MF}$ for the position of the molecular frame (MF) in space, plus internal coordinate φ and fluctuating solvent polarization vector \mathbf{X} , with components naturally defined in the laboratory (inertial) frame (LF) [170]. We write the PES for each state in the form

$$E_n(\mathbf{Q}) = \varepsilon_n(\mathbf{\Omega}_{MF}, \varphi) - \frac{F_\infty}{2} \mu_n^2(\varphi) - \mu_n(\mathbf{\Omega}_{MF}, \varphi) \cdot \mathbf{X} + \frac{1}{2F_{or}} X^2 \quad (2.5)$$

where $\varepsilon_n(\mathbf{\Omega}_{MF}, \varphi)$ is the *in-vacuo* energy of the n -th excited state depending upon the internal geometry; $\mu_n(\mathbf{\Omega}_{MF}, \varphi)$ is the electric dipole moment vector of the molecule in the n -th excited state, with components in LF; term $\frac{F_\infty}{2} \mu_n^2(\varphi)$ represents the solvation energy due to electric polarization while $\mu_n(\mathbf{\Omega}_{MF}, \varphi) \cdot \mathbf{X}$ derives from solute-solvent interaction due to orientational polarization. The last term $\frac{1}{2F_{or}} X^2$ accounts for the solvent coordinate fluctuations. Onsager theory in its simplest form (solute as a spherical cavity of volume V) gives us explicit estimates of F_0 , F_∞ and $F_{or}=F_0-F_\infty$:

$$F_{0,\infty} = \frac{1}{4\pi V \epsilon_{vacuo}} \frac{2(\epsilon_{0,\infty} - 1)}{2\epsilon_{0,\infty} + 1} \quad (2.6)$$

where ϵ_{vacuo} is the dielectric permittivity in vacuo [173],[175]. Time evolution operator $\hat{\Gamma}_n$ describing the molecule dynamics is defined as the diffusive operator

$$\begin{aligned} \hat{\Gamma}_n &= - \left(\hat{\mathbf{M}} \frac{\partial}{\partial \varphi} \right)^{tr} \cdot \mathbf{D}_n \cdot P_{eq,n}(\mathbf{Q}) \left(\frac{\hat{\mathbf{M}}}{\frac{\partial}{\partial \varphi}} \right) P_{eq,n}^{-1}(\mathbf{Q}) \\ &\quad - \left(\frac{\partial}{\partial \mathbf{X}} \right)^{tr} \cdot \mathbf{D}_S \cdot P_{eq,n}(\mathbf{Q}) \left(\frac{\partial}{\partial \mathbf{X}} \right) P_{eq,n}^{-1}(\mathbf{Q}) \end{aligned} \quad (2.7)$$

where $n=A, B$ and where the solute gradient operator is $\left(\hat{\mathbf{M}} \frac{\partial}{\partial \varphi} \right)$ and depends upon the rotational infinitesimal operator $\hat{\mathbf{M}}$ [181] and internal rotation $\frac{\partial}{\partial \varphi}$. Function $P_{eq,n}$ is defined as the equilibrium (Boltzmann) distribution with respect to the total energy E_n . Diffusion tensors \mathbf{D}_n and \mathbf{D}_S are defined for the solute and solvent motion. We can write the general expression for \mathbf{D}_n

$$\mathbf{D}_n = \begin{pmatrix} \mathbf{D}_{R,n} & \mathbf{D}_{RI,n} \\ \mathbf{D}_{RI,n}^{tr} & D_{I,n} \end{pmatrix} \quad (2.8)$$

where blocks $\mathbf{D}_{R,n}$, $\mathbf{D}_{RI,n}$, $D_{I,n}$ are related to purely rotational, rotational-conformational and purely conformational diffusive motion, respectively and they can be estimated using hydrodynamic arguments. Solvent polarization diffusion is described by diffusion tensor \mathbf{D}_S , which can be related to solvent relaxation times, as specified in the following paragraphs. In principle Eqns. 2.7 and 2.8 allow the description of the joint relaxation of a molecule in state n , rotating in space and subject to internal conformational dynamics, coupled to a solvent polarization vectorial coordinate. No rotational invariance has been invoked yet, and thus physical environment which are characterized by rotational anisotropy, like, for instance nematic or smectic liquid crystals, can be described. In the case of polar isotropic fluids, one can (i) average out the dependence upon rotational coordinates $\mathbf{\Omega}_{MF}$; (ii) refer the solvent coordinate vector the molecular frame MF - which is supposed to be essentially the same in all states - chosen to have one axis along internal dipole $\mu_n(\varphi) = \mu_n \mathbf{u}_n$; (iii) assume that $x = \mathbf{X} \cdot \mathbf{u}_n$, i.e. the component of solvent polarization along the dipole is the major source of coupling in Eq. 2.8 and neglect other components; (iv) assume that no significant coupling exists between internal and conformational degrees of freedom, i.e. neglect non diagonal blocks in Eq. 2.8 and residual dependence of diagonal blocks upon internal coordinate

φ ; also, to a first approximation, differences in shape in states are neglected, leading to a single dissipative parameter $D_{I,n} \approx D_I$ for internal rotation; finally (v) assume a scalar approximation for tensor $\mathbf{D}_S = D_S \mathbf{1}$. Assumptions (i) and (ii) are exact statements consequent from the assumption of rotational isotropy; (iii), (iv) and (v) are approximations based on the idea that static and dynamic properties are mainly represented by coordinates $\mathbf{Q} = (\varphi, x)$. The simplified time evolution operator is now given by

$$\hat{\Gamma}_n = -D_I \frac{\partial}{\partial \varphi} P_{eq,n}(\varphi, x) \frac{\partial}{\partial \varphi} P_{eq,n}^{-1} - D_S \frac{\partial}{\partial x} P_{eq,n}(\varphi, x) \frac{\partial}{\partial x} P_{eq,n}^{-1} \quad (2.9)$$

where $n=LE, TICT$. The final form of the operator in Eq. 2.9 is obtained in a detailed way in the Appendix B. The kinetic terms in Eq. 2.3 need yet to be defined. Assuming that both radiative and non-radiative processes are taken into account, we can write $k_{LE} = k_{LE \rightarrow TICT}^{nr} + k_{LE \rightarrow g}^{nr} + k_{LE \rightarrow g}^{rad}$, $k_{TICT} = k_{TICT \rightarrow LE}^{nr} + k_{TICT \rightarrow g}^{nr} + k_{TICT \rightarrow g}^{rad}$, $k_{LE/TICT} = -k_{TICT \rightarrow LE}^{nr}$ and $k_{TICT/LE} = -k_{LE \rightarrow TICT}^{nr}$ where $k_{LE \rightarrow g}^{nr}$ and $k_{LE \rightarrow g}^{rad}$ are kinetic coefficients (in general depending upon φ) for non-radiative and radiative decay to ground state from state LE, $k_{LE \rightarrow TICT}^{nr}$ is the kinetic coefficient for (assumed non-radiative) transition $LE \rightarrow TICT$ and so on. To summarize: for the case of fluorescence emission of DMABN, with two diabatic states LE and TICT both emitting to the g state, with one conformational degree of freedom φ , in the presence of coupling with one effective solvent coordinate x in a polar aprotic isotropic solvent, the following basic functions and model parameters are needed: dielectric constants $\epsilon_{0,\infty}$ and estimate of the molecular volume V to evaluate $F_{0,\infty}$ parameters; *in vacuo* PES $\varepsilon_n(\varphi)$ and electric dipole moment $\mu_n(\varphi)$, obtained from QM calculations, for LE, TICT, and g states; relaxation coefficients D_I (for internal dynamics) and D_S (solvent relaxation) which can be related to molecular geometry and solvent macroscopic properties; kinetic coefficients $k_{LE \rightarrow g}^{nr}$, $k_{TICT \rightarrow g}^{nr}$, $k_{LE \rightarrow TICT}^{nr}$, $k_{TICT \rightarrow LE}^{nr}$, $k_{LE \rightarrow g}^{rad}$, $k_{TICT \rightarrow g}^{rad}$. Finally, in order to evaluate the stationary emission fluorescence according to Eqn. 2.3 we need to specify functions $S_n(\varphi, x)$ and $g_n(\omega)$.

2.2.2 Hydrodynamic model for the diffusion tensor

In most cases the general problem of determining diffusion tensor value is meet considering the description of molecular probe as macroscopic objects immersed in fluid, i.e. a purely hydrodynamic view. Usually this description is sufficient to allow the determination of friction and/or diffusion tensor, by means of a relatively simple description linking the overall molecular shape directly to roto-translational (and internal) friction properties [182],[183]. The resulting friction/diffusion tensor are surprisingly-given the limits of a macroscopic description of a molecular system-close to available experimental values. The evaluation of the diffusion properties of molecular systems, with internal degrees of freedom, was based on a hydrodynamic approach. We may start from a simplified view of the molecule under investigation as an ensemble of N fragments, each formed by spheres representing atoms or group of atoms, immersed in a homogeneous isotropic fluid of know viscosity. Let us assume that the i -the fragment is composed by N_i spheres (extended atoms) and that the torsional angle θ_i defines the relative orientation of the fragments i and $i + 1$. We denote by \mathbf{u}_i the unitary vector for the corresponding bond. A total of $N - 1$ torsional angles/bonds are present - only non-cyclic and non-branched geometries are considered here - and each fragment has n_i atoms. For convenience, each \mathbf{u}_i points from an atom in fragment i to an atom in fragment $i + 1$ for $i \geq v$ and \mathbf{p} points from an atom in fragment $i + 1$ to an atom in fragment i for $i < v$. Notice that the definition of the MF in a flexible system is somewhat arbitrary, and can be essentially left to convenience arguments. For sake of simplicity we may assume that MF is fixed on generic fragment v . In Fig. 2-3 we show the schematic representation of the system, with an assumed MF fixed on the second fragment ($v=2$). By definition, in the MF, atoms of fragment v have only translational and rotational motions while atoms of all other fragments have additional internal rotational motions. Let us now associate the set of coordinates $(\mathbf{R}, \Omega, \theta)$, which describe the translational, rotational and internal torsional motions respectively, with the generalized velocities $(\mathbf{V}, \omega, \dot{\theta})$ representing the molecule's translational velocity, angular velocity around an inertial frame, and associated torsional momenta. In the presence of constraints in and among fragments, the generalized force \mathcal{F} , made of force \mathbf{F} , torque

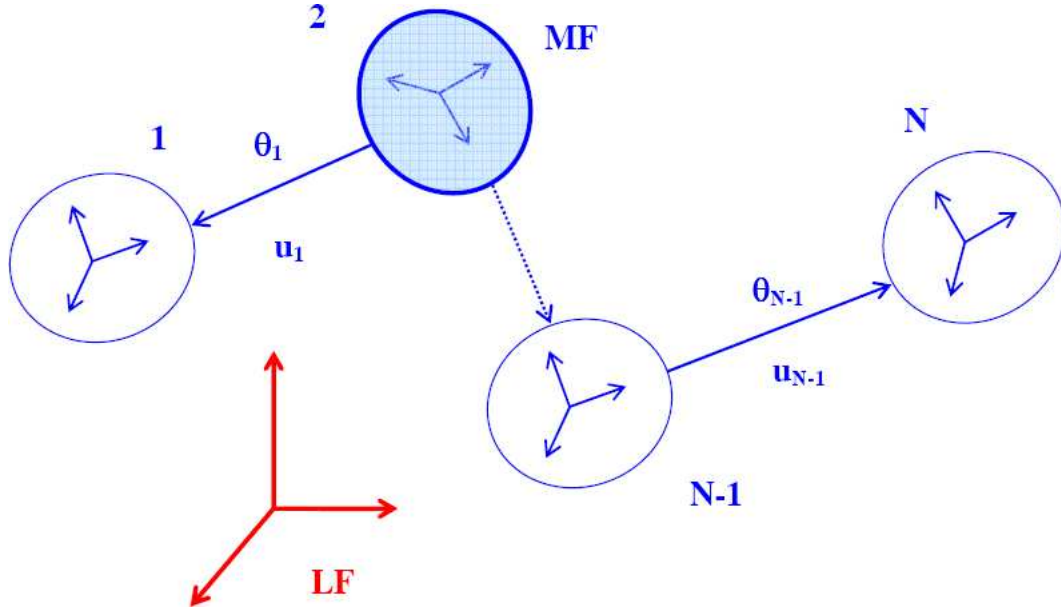


FIGURE 2-3: Scheme for the evaluation of diffusion tensor of a flexible N -fragments systems; the molecular frame MF is fixed on the second fragment.

\mathbf{N} and the internal torques \mathbf{N}^{int} , is related to the generalized velocity by the relation.

$$\mathcal{F} = -\Xi \mathcal{V}$$

$$\mathcal{F} = \begin{pmatrix} \mathbf{F} \\ \mathbf{N} \\ \mathbf{N}^{int} \end{pmatrix}, \mathcal{V} = \begin{pmatrix} \mathbf{V} \\ \omega \\ \dot{\theta} \end{pmatrix} \quad (2.10)$$

while in the absence of constrains a similar relation holds for each single extended atom between its velocity and the force acting on it, which in compact matrix form can be written

$$\mathbf{f} = -\xi \mathbf{v}$$

$$\mathbf{f} = \begin{pmatrix} \mathbf{f}_1^1 \\ \dots \\ \mathbf{f}_{n_N}^N \end{pmatrix}, \mathbf{v} = \begin{pmatrix} \mathbf{v}_1^1 \\ \dots \\ \mathbf{v}_{n_N}^N \end{pmatrix} \quad (2.11)$$

where \mathbf{f}_j^i is the force acting on j -th atom of i -th fragment ($1 \leq j \leq n_i$) etc. Constrained and unconstrained forces and velocities can be related *via* geometric considerations by

the relations $\mathcal{F} = \mathbf{A}\mathbf{f}$ and $\mathbf{v} = \mathbf{B}\mathcal{V}$, where \mathbf{A} and \mathbf{B} are matrices depending on the molecular geometry and one can show easily by inspection that $\mathbf{A} = \mathbf{B}^{tr}$. It follows that $\Xi = \mathbf{B}^{tr}\xi\mathbf{B}$. For a system of linearly connected fragments it is relatively simple to evaluate matrix \mathbf{B} as a function of atomic positions \mathbf{r}_j^i . By assuming now a form for the friction tensor of non-constrained atoms, ξ , one can calculate the friction for the constrained atoms, Ξ . We may assume for simplicity the simplest model for non-interacting spheres in a fluid, namely that matrix ξ has only diagonal blocks of the form $\xi_0(T)\mathbf{1}_3$ where $\xi_0(T)$ is the translational friction of a sphere of radius R_0 at temperature T and given by the Stokes law:

$$\xi_0(T) = CR_0\eta(T)\pi \quad (2.12)$$

where $\eta(T)$ is the solvent viscosity at the given temperature T and C depends on hydrodynamic boundary conditions. The system friction is then given as $\Xi = \xi_0(T)\mathbf{B}^{tr}\mathbf{B}$. The diffusion tensor (which can be conveniently partitioned in translation, rotational, internal and mixed blocks) can now be obtained as the inverse of the friction tensor [182],[183]

$$\mathbf{D} = \begin{pmatrix} \mathbf{D}_{TT} & \mathbf{D}_{TR} & \mathbf{D}_{TI} \\ \mathbf{D}_{TR}^{tr} & \mathbf{D}_{RR} & \mathbf{D}_{RI} \\ \mathbf{D}_{TI}^{tr} & \mathbf{D}_{RI}^{tr} & \mathbf{D}_{II} \end{pmatrix} = k_B T \Xi^{-1} \quad (2.13)$$

and neglecting off-diagonal couplings, an estimate of the rotational diffusion tensor is given by $\mathbf{D}_{RR} \equiv \mathbf{D}$, which depends directly from the atomic coordinates, temperature, and the solvent viscosity. Finally, let us to evaluate matrix \mathbf{B} for the system of linearly connected fragments in Figure 2-3. If we indicated with \mathbf{r}_j^i the vector of the j -th atom of the i -th fragment in the MF, for the atoms that belong to the fragment v , the velocity is:

$$\mathbf{v}_j^v = \mathbf{V} + \boldsymbol{\omega} \times \mathbf{r}_j^v \quad (2.14)$$

while for all other atoms velocities are

$$\mathbf{v}_j^i = \mathbf{V} + \boldsymbol{\omega} \times \mathbf{r}_j^i + \sum_k \dot{\theta}_{\mathbf{u}_k} \times \mathbf{r}_{j,k}^i \mathbf{v}_j^i$$

$$= {}^T \mathbf{B}_j^i \mathbf{v} + {}^R \mathbf{B}_j^i \omega + \sum_k^I \mathbf{B}_{j,k}^i \dot{\theta} \quad (2.15)$$

where $\mathbf{r}_{j,k}^i$ is the difference between the vector of the j -th atom and the atom at the origin of the unit vector \mathbf{u}_k and the sum is taken over the angles that link the reference fragment v to the fragment i ; ${}^T \mathbf{B}_j^i = \mathbf{1}_3$, ${}^R \mathbf{B}_j^i = -r_j^{i \times}$, ${}^I \mathbf{B}_j^i = -\mathbf{r}_{j,k}^i \mathbf{u}_k$ or 0; and finally for vector \mathbf{r} , 3×3 matrix \mathbf{r}^\times is defined as:

$$\mathbf{r}^\times = \begin{bmatrix} 0 & r_z & -r_y \\ -r_z & 0 & r_x \\ r_y & -r_x & 0 \end{bmatrix} \quad (2.16)$$

which show the property $\mathbf{r}^\times = -(\mathbf{r}^\times)^{tr}$.

2.2.3 The model treatment

Approximate emission fluorescence

We shall start by introducing a reduced solvent variable $\tilde{x} = x/(F_{or}k_B T)^{1/2}$. The energy function for state n becomes

$$\frac{E_n}{k_B T} = \frac{\varepsilon_n - F_0 \mu_n^2 / 2}{k_B T} + \frac{1}{2}(\tilde{x} - \tilde{x}_n)^2 = \tilde{V}_n(\varphi) + \frac{1}{2}(\tilde{x} - \tilde{x}_n)^2 \quad (2.17)$$

where $\tilde{x}_n = x/(F_{or}/k_B T)^{1/2} \mu_n$. The emission fluorescence is given explicitly by Eq. 2.3 - where we remind now that $\mathbf{Q}=(\varphi, \tilde{x})$ - provided that numerical or analytical solution are obtained for the stationary populations $P_{st,n}$, which is obtained by solving Eq. 2.3 which takes the explicit form

$$- \left(\frac{1}{\tau_I} \frac{\partial}{\partial \varphi} P_{eq,n} \frac{\partial}{\partial \varphi} P_{eq,n}^{-1} + \frac{1}{\tau_S} \frac{\partial}{\partial \tilde{x}} P_{eq,n} \frac{\partial}{\partial \tilde{x}} P_{eq,n}^{-1} \right) P_{st,n} + \sum_{n'} k_{nn'} P_{st,n'} = S_n \quad (2.18)$$

Instead of resorting to an exact solution, we introduce the approximate *ansatz* $P_{st,n} \approx p_{st,n} G(\tilde{x} - \tilde{x}_{st,n})$, where $p_{st,n}(\varphi)$ and $\tilde{x}_{st,n}(\varphi)$ are functions, to be determined, of the torsional angle only and $G(\tilde{x}) = \exp(-\tilde{x}^2/2)/(2\pi)^{1/2}$, i.e. a Gaussian function of width equal to 1. Notice that $P_{eq,n} = p_n G(\tilde{x} - \tilde{x}_n)$, where p_n is the Boltzmann distribution

over \tilde{V}_n . The approximated emission fluorescence is then given by:

$$I(\omega) \propto \omega^3 \sum_n \int d\varphi k_n^{rad}(\varphi) p_{st,n}(\varphi) \int d\tilde{x} g[\omega - \Delta\omega_n(\varphi, \tilde{x})] G[\tilde{x} - \tilde{x}_{st,n}(\varphi)] \quad (2.19)$$

The integration with respect to the \tilde{x} variable can be carried on analytically, since it is easily reduced to the exponential of second degree polynomial in \tilde{x} . The resulting expression is

$$I(\omega) \propto \omega^3 \sum_n \int d\varphi k_n^{rad}(\varphi) p_{st,n}(\varphi) i_n(\omega, \varphi)$$

$$i_n(\omega, \varphi) = \exp \left\{ - \frac{[\omega - \omega_q(\Delta\tilde{x}_n \tilde{x}_{st,n} + \Delta\tilde{V}_n)]^2}{2(\omega_q^2 \Delta\tilde{x}_n^2 + \Omega^2)} \right\} / [2\pi(\omega_q^2 \Delta\tilde{x}_n^2 + \Omega^2)]^{1/2} \quad (2.20)$$

where $\omega_q = k_B T / \hbar$, $\Delta\tilde{x}_n = \tilde{x}_g - \tilde{x}_n$, $\Delta\tilde{V}_n = \tilde{V}_n - \tilde{V}_g$. The signal is given by a convolution, with respect to reduced stationary population $p_{st,n}(\varphi)$ and radiative coefficient $k_n^{rad}(\varphi)$ for each excited state n , of Gaussian functions $i_n(\omega, \varphi)$ centered in $\omega_q(\Delta\tilde{x}_n \tilde{x}_{st,n} + \Delta\tilde{V}_n)$ and with width $(\omega_q^2 \Delta\tilde{x}_n^2 + \Omega^2)^{1/2}$. Notice that solvent polarity enters mainly by defining the local emission center, for a given value of the torsional angle, in the function $i_n(\omega, \varphi)$, and secondarily by introducing an additional broadening to Ω of the order of $\omega_q \Delta\tilde{x}_n$.

Stationary populations

Functions $p_{st,n}(\varphi)$ and $\tilde{x}_n(\varphi)$ can be obtained by substituting the chosen *ansatz* form for $P_{st,n}$ in Eq. 2.4. We have yet to define the source function. A reasonable assumption is that only direct excitation of the TICT state is allowed [184],[185] and thus a simple choice is $S_n = \omega_S \delta_{n,TICT} P_{eq,TICT} = \omega_S \delta_{n,TICT} p_{TICT} G(\tilde{x} - \tilde{x}_{TICT})$, where ω_S is an arbitrary constant with the dimension of a frequency. The choice of this form for the source function depends on the consideration that the population is excited from the ground state to both excited state; owing to the large oscillator strength for the electronic excitation to TICT state, DMABN is easy to populate to the TICT state. So we consider this state the only populated state for approximation. Close expressions for $p_{st,n}(\varphi)$ and $\tilde{x}_n(\varphi)$ can now be obtained from Eq. 2.18 via a simple moment expansion.

If an average of Eq. 2.18 with respect to \tilde{x} is taken, the following equation is obtained

$$-\frac{1}{\tau_I} \frac{\partial}{\partial \varphi} \left[p_n \frac{\partial}{\partial \varphi} p_n^{-1} - (\tilde{x}_{st,n} - \tilde{x}_n) \frac{\partial \tilde{x}_n}{\partial \varphi} \right] p_{st,n} + \int_{n'} k_{nn'} p_{st,n'} = \omega_S \delta_{n,TICT} p_{TICT} \quad (2.21)$$

By multiplying Eq. 2.18 by \tilde{x} and then integrating in \tilde{x} one gets

$$\begin{aligned} & -\frac{1}{\tau_I} \frac{\partial}{\partial \varphi} \left\{ p_n \frac{\partial}{\partial \varphi} p_n^{-1} \tilde{x}_{st,n} + [\tilde{x}_{st,n}(\tilde{x}_{st,n} - \tilde{x}_n) - 1] \frac{\partial \tilde{x}_n}{\partial \varphi} \right\} p_{st,n} \\ & + \frac{1}{\tau_S} (\tilde{x}_{st,n} - \tilde{x}_n) p_{st,n} + \sum_{n'} k_{nn'} p_{st,n'} \tilde{x}_{st,n'} = \omega_S \delta_{n,TICT} p_{TICT} \tilde{x}_n \end{aligned} \quad (2.22)$$

Since $\tau_S \ll \tau_I$ a simplified expression is obtained by neglecting the first term in the r.h.s. of Eq. 2.22. Notice that since the emission signal is determined minus an arbitrary constant factor, we can choose conveniently to set $p_{st,n} \rightarrow \tau_I \omega_S p_{st,n}$. Eqns. 2.21 and 2.22 can then be written in their final form

$$\begin{aligned} & \rho (\tilde{x}_{st,n} - \tilde{x}_n) p_{st,n} + \sum_{n'} c_{nn'} p_{st,n'} \tilde{x}_{st,n'} = \delta_{n,TICT} p_{TICT} \tilde{x}_{TICT} \\ & - \frac{\partial}{\partial \varphi} \left[p_n \frac{\partial}{\partial \varphi} p_n^{-1} - (\tilde{x}_{st,n} - \tilde{x}_n) \frac{d\tilde{x}_n}{d\varphi} \right] p_{st,n} + \sum_{n'} c_{nn'} p_{st,n'} = \delta_{n,TICT} p_{TICT} \end{aligned} \quad (2.23)$$

where $c_{nn'} = \tau_I k_{nn'}$, $\rho = \tau_I / \tau_S$. Under the additional hypothesis that $\rho \gg c_{nn'}$ (i.e. $\tau_S \ll k^{nr}, k^{rad}$ meaning that solvent relaxation is considered fast also with respect to radiative and non radiative emission coefficients) the approximate solution $\tilde{x}_{st,LE} \approx \tilde{x}_{LE}$ and $\tilde{x}_{TICT} \approx \left(1 + \frac{1}{\rho} \frac{p_{TICT}}{p_{st,TICT}}\right) \tilde{x}_{TICT} \approx \tilde{x}_{TICT}$, if one neglects entirely the correction term $p_B / \rho p_{st,TICT}$, so that further simplified expressions for $p_{st,n}(\varphi)$ and $\tilde{x}_{st,n}(\varphi)$ are

$$\begin{aligned} & \tilde{x}_{st,n} = \tilde{x}_n \\ & - \frac{\partial}{\partial \varphi} p_n \frac{\partial}{\partial \varphi} p_n^{-1} p_{st,n} + \sum_{n'} c_{nn'} p_{st,n'} = \delta_{n,BPTICT} \end{aligned} \quad (2.24)$$

Eqns. 2.20 and 2.23, or 2.24, can be solved numerically. A finite difference scheme has been employed, on a regular grid of $2K + 1$ nodes $\varphi_k = \delta\varphi k$, with $k = -K, -K + 1, \dots, K - 1, K$. Discretization of Eq. 2.24 is straightforward and a standard linear methods can be employed to solve for the resulting linear system in the unknown $p_{st,n,k} = p_{st,n}(\varphi_k)$.

2.2.4 Parameters

Several theoretical investigations have been published in recent years for the interpretation of the fluorescence properties of DMABN. The reduced size of the molecule allow an investigation by *ab-initio* methods [26],[186], but semiempirical methods are still applied [187],[188]. Many theoretical investigations have been conducted for the ground state but few calculations have been described for the excited states that include the optimization of excited-state geometries [189]. The single-reference configuration interactions with single excitations (CIS) is frequently used [154],[190] but sometimes the order of the energies of the excited states is not reproduced correctly [191]. The complete active space self-consistent field (CASSCF) methods is a good approach to consider the non-dynamic electron correlation effects [192],[174]. CIS and CASSCF methods often given poor geometries for excited states because they not include the dynamical electron correlations [193] while the complete active space second-order perturbation theory (CASPT2) include the dynamic correlation effects that are important for obtaining a quantitative accordance with the energies. Density functional theory (DFT) based methods have proved to be a significant progress for the evaluation of excited state properties with the time dependent DFT (TD-DFT)[158], a combination of DFT with a single or multireference [194] configuration interactions. TD-DFT gives more accurate geometries and excitation energies than those of low-level *ab-initio* theories with a low computational cost equivalent to that of CIS. Recently, it was suggested that the poor behavior of charge transfer excitations by TD-DFT are solved by applying the long-range correction to the TD-DFT scheme [193]. We start by considering the PES and electric dipole moment for DMABN. Among computational methods apt to describe excited states, Time Dependent-Density Functional Theory (TD-DFT; for a survey of ground-state DFT see, for example, ref. [26]) is gaining more and more attention to study medium and large size molecules, thanks to its favorable balance between accuracy and computational demand. The recent implementation of TD-DFT analytical gradients [195] both *in vacuo* and in solution allows for the determination of excited state stationary points and properties (such as multipole moments); moreover, harmonic frequencies can be calculated by numerical differentiation of the analytic

gradients, and the subsequent vibrational analysis is providing encouraging results. The use of TD-DFT has been limited by some deficiencies in properly describing excited states involving charge separation or with contributions from double excitations [196],[197],[198],[199]. Recently, some interesting attempts to overcome these limitations have been proposed [198],[199],[200],[201],[202],[203],[204]. On the other hand, for

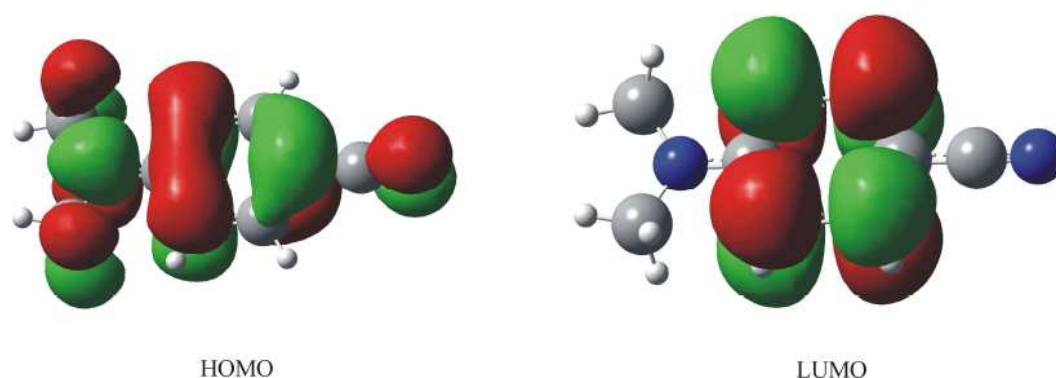


FIGURE 2-4: Schematic drawings of selected molecular orbitals (HOMO and LUMO) for DMABN at ground state geometry.

electronic transitions which involve only partial intramolecular charge transfer (TICT), the underestimate of excitation energies by TD-DFT, due to spurious self-interaction, may be controlled by the use of hybrid functionals. This is the case for DMABN, where the HOMO and LUMO molecular orbitals, involved in the TICT transition, partially overlap Figure 2-4. In the TICT state the HOMO is essentially a nitrogen p orbital describing the NMe_2 lone pair, while the LUMO is a π orbital which is delocalized over the aromatic ring and the nitrile group. Here are presented TD-DFT results for absorption energies for the two lowest states of DMABN at the geometry of the ground state minimum (C_{2v} symmetry) optimized at PBE0/6-31G(d) level of theory. The same hybrid functional [184] has been also employed for TD-DFT calculations, as it is known that the hybridization with Hartree-Fock exchange partly overcomes the self-interaction error. Despite the absence of adjustable parameters, when employed in TD-DFT calculations, PBE0 (TD-PBE0) has already provided excitation spectra in very good agreement with the available experimental results [205],[206]. Different basis sets have been tested: first, we used the Pople family of basis sets 6-31G [207], with different contraction schemes and the addition of polarization [208] and diffuse

functions [209] and then the aug-cc-pVDZ basis set. Results are collected in Table 2.1 and are compared with experimental data [185]. The analysis of the wave function reported in the last row of the Table 2.1 shows that the LE state in the full planar conformation is dominated by the HOMO \rightarrow LUMO+1 and HOMO-1 \rightarrow LUMO single excitations, where the involved orbitals are benzene ring π and π^* orbitals. Also the TICT state is dominated by a single excitation from the HOMO \rightarrow LUMO. The HOMO orbital includes a strong mixing with the N amino lone pair orbital. It is the excitation from this orbital that become the most important at the twisted conformation. At this conformation the lone pair orbital is no more mixed with the π system and, as a consequence, it is destabilized up to the HOMO level [154]. Gas-phase calculations for the TICT state provide differences from experimental values (ΔE) ranging between 0.29 (6-31G(d) basis set) and 0.14 eV (aug-cc-pVDZ). TD-DFT calculations, taken from literature [158], performed using B3LYP functional and TZVPP basis set provided $\Delta E=0.11$ eV. All TD-DFT excitation energies are close to their counterparts

	LE	TICT
Experimental [185]	4.25 (0.031) \pm 0.1	4.56 (0.680) \pm 0.1
TDDFT/6-31G	4.68 (0.0276)	4.85 (0.5546)
TDDFT/6-311+G(d,p)	4.49 (0.0338)	4.72 (0.5529)
TDDFT/aug-cc-pVTZ	4.45 (0.0319)	4.71 (0.5489)
Main contr.	HOMO \rightarrow LUMO+1	HOMO \rightarrow LUMO

TABLE 2.1: Absorption energies (in eV) for DMABN *in vacuo* at TD-DFT level employing PBE0 functional and different basis sets. Oscillatory strength is given in parenthesis. MO main contributions for each transition are also shown.

issuing from post-HF computations such as multireference perturbation configuration interaction (CIPSI [154], $\Delta E = 0.22$ eV), CASPT2/ANO(DZ) [210] ($\Delta E = -0.18$ eV) and STEOM-CCSD/cc-pVTZ [211]($\Delta E = 0.14$ eV). Moreover, the energy differences between LE and TICT states is also well reproduced by TD-DFT. After the choice of the best basis set (TD-DFT/6-31G) for the calculations of the parametes can be useful to consider a more accurate comparison with the experimental data. The Table 2.2 considers the comparison between experimental and calculated values of the energy and the dipole moment of DMABN *in vacuo*. All calculations have been performed by exploiting a development version of the Gaussian code [137]. As show in Figure 2-5.a the ground state g presents a valley along the torsional angle. The minimum is

	Twist angle (0°)		Twist angle (90°)	
	ΔE^a	μ^b	ΔE	μ^b
<i>g</i>	0	8.1(5-7)	0	6.0
LE	4.68 (4.25)	9.75 (6-11)	4.95	14.93
TICT	4.85 (4.56)	11.04 (11-17)	3.93	15.43 (14-20)

TABLE 2.2: Relative energy (in eV) and dipole moment (in D) of the ground state and the lower energy excited states of DMABN *in vacuo*. In parenthesis the experimental values. ^a from ref. [185]. ^b from ref. [212].

found at the full planar geometry. We consider the energy of this minimum as energy reference. The *g* state presents a maximum at 90° and the energetic barrier is 0.6 eV in accordance with the literature data [154]. During the evaluation of the energy the geometry has been kept frozen to that optimized for the ground state for every points and for both excited states. The only changing parameter is the torsional angle between the donor and the acceptor which has been varied from 0° to 180° in step of 10°. The first excited state, the LE state, shows a minimum energy as in the *g* state at the full planar geometry (4.68 eV). The TICT state presents a flat region (4.85 eV) around the planar conformation till the intersection region near 45°. From this point the energy of this state decreases till a minimum at 90° (3.95 eV). Figure 2-5.b describes the trend of the dipole moment for the ground state and for the two lowest energy excited states as a function of the torsional angle. The ground state dipole moment (in green) decreases with the increase of the torsional angle with a gap of -2.12 D from 0° to 90°. As for the energy calculations the torsional angle is varied with a step of 10° in the same range. The dipole moment of the TICT state increases with the torsional angle till a maximum at 90° with a of 15.5 D *in vacuo*.

Next we consider the diffusion coefficient associated to internal rotation, $D_{I,n} \approx D_I = 1/\tau_I$. Following the hydrodynamic approach [174] summarized in preview paragraph, we consider the molecule as a collection of identical spheres of radius R linked by rigid bonds immersed in a homogeneous fluid of viscosity $\eta(T)$. The roto-translational and internal friction and diffusion tensors are calculated as functions of the translational friction of a single free sphere, which at temperature T is obtained simply as $\xi(T) = CR\eta(T)\pi$, which depends on the boundary constant coefficient C and the effective atomic radius R . For the calculation we considered the value of 4 for C and

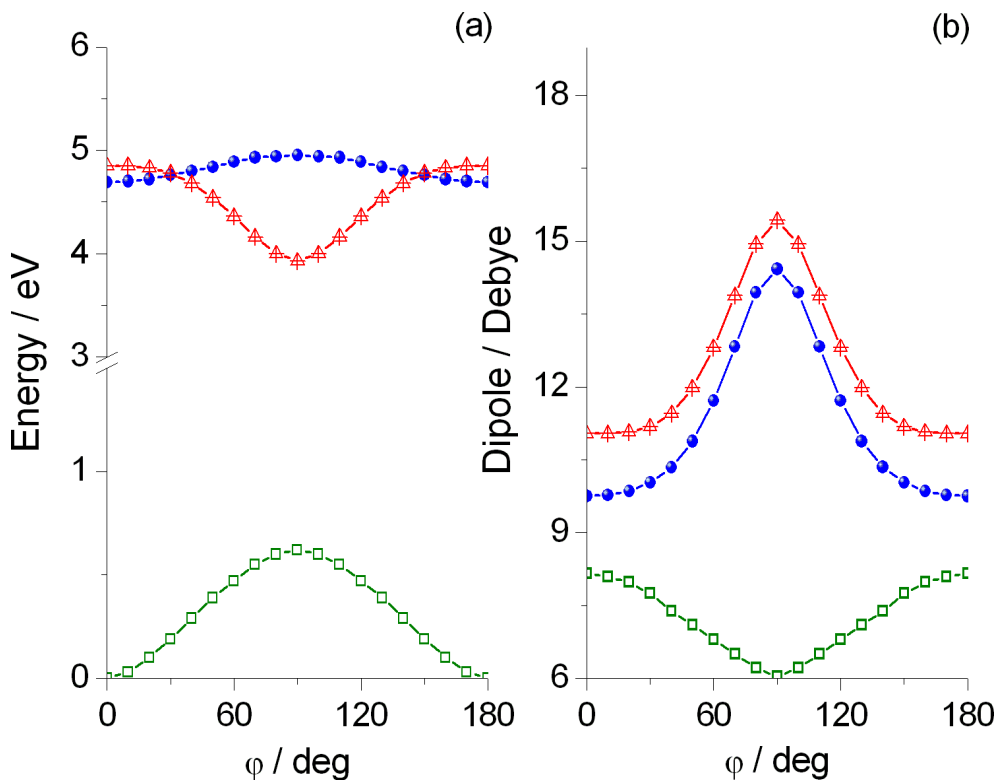


FIGURE 2-5: (a) Ground (g in green) and low-lying singlet excited states (LE state in blue and TICT state in red) potential energy surfaces (PES) of DMABN *in vacuo* as a function of the torsional angle (in degrees). The energy (in eV) is relative to the minimum of the ground state. (b) Ground and low-lying singlet excited states dipole moment curves of DMABN *in vacuo* as a function of the torsional angle (in degrees). Dipole moment are in debye.

a radius equal to 1.95 \AA . The Figure 2-6 considers the representation of DMABN in the hydrodynamic approach with a radius for spheres equal to R . Calculation of τ_I is relatively straightforward, and it can be further simplified if additional approximation are introduced. In Table 2.3 we report values for τ_I and the physical characteristic of the different solvents, namely *n*-hexane, cyclohexane, benzene, dibutyl ether, diethyl ether, *n*-butylchloride, acetonitrile and dimethylsulfoxide. Determination of molecular parameters $E_n(\varphi)$, $\mu_n(\varphi)$, τ_I and τ_S are therefore possible, although subject to severe approximation. In principle kinetic coefficients $k_{LE \rightarrow g}^{nr}$, $k_{TICT \rightarrow g}^{nr}$, $k_{TICT \rightarrow LE}^{nr}$, $k_{LE \rightarrow TICT}^{nr}$, $k_{LE \rightarrow g}^{rad}$, $k_{TICT \rightarrow g}^{rad}$, source function $S_n(\varphi, x)$ and intrinsic line shape $g_n(\omega)$ could be determined independently from quantum mechanical calculations. Here we shall choose a phenomenological approach, trying to model, in terms of a reduced number of free parameters, most of the expected features of these quantities [213]

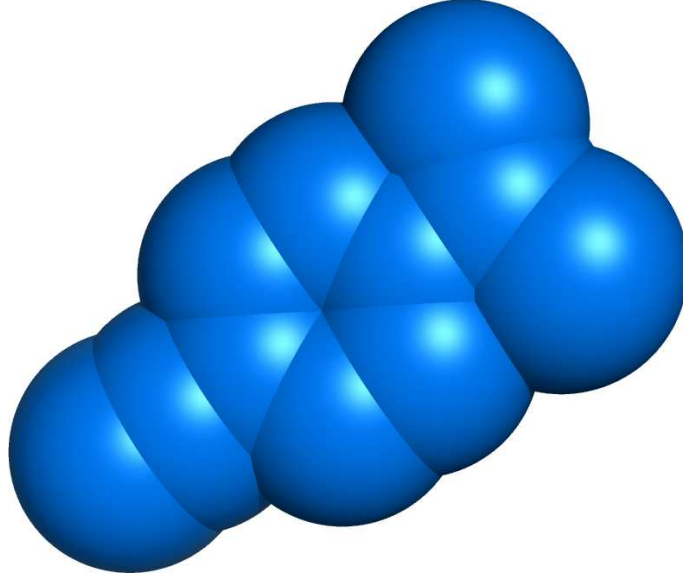


FIGURE 2-6: Schematic representation of the DMABN in the hydrodynamic approach.

within a TICT framework. To this purpose, we start by assuming simple functional forms for the kinetic coefficients, chosen to summarize known emission properties of DMABN: (i) $k_{LE \rightarrow TICT}^{nr}$, $k_{TICT \rightarrow g}^{nr}$ and $k_{TICT \rightarrow g}^{rad}$ are assumed to be monotonously increasing with increasing φ and to have a maximum at $\varphi \approx \pi/2$; (ii) $k_{TICT \rightarrow LE}^{nr}$, $k_{LE \rightarrow g}^{nr}$ and $k_{LE \rightarrow g}^{rad}$, are assumed to have a maximum at $\varphi \approx 0$ and to be monotonously decreasing with increasing φ ; (iii) only two effective solvent and temperature independent parameters k^{nr} and k^{rad} are introduced to measure radiative and non radiative emission strength, and a simple squared cosine/sine dependence upon φ is allowed. It follows that $k_{LE \rightarrow g}^{nr} \approx k^{nr} \cos^2 \varphi$, $k_{TICT \rightarrow g}^{nr} \approx k^{nr} \sin^2 \varphi$, $k_{LE \rightarrow TICT}^{nr} \approx k^{nr} \sin^2 \varphi$, $k_{TICT \rightarrow LE}^{nr} \approx k^{nr} \cos^2 \varphi$, $k_{LE \rightarrow g}^{rad} \approx k^{nr} \cos^2 \varphi$, $k_{TICT \rightarrow g}^{rad} \approx k^{nr} \sin^2 \varphi$. The matrix of coefficients $\mathbf{k} = \{k_{n,n'}\}$ in Eq. 2.3 takes the form

$$\mathbf{k} = \begin{pmatrix} k^{nr} \sin^2 \varphi + k \cos^2 \varphi & -k^{nr} \cos^2 \varphi \\ -k^{nr} \sin^2 \varphi & k^{nr} \cos^2 \varphi + k \sin^2 \varphi \end{pmatrix} \quad (2.25)$$

where $k = k^{nr} + k^{rad}$. The intrinsic line shape $g_n(\omega)$ is simply estimated as a Gaussian function with constant linewidth Ω , $g_n(\omega) \approx g(\omega) = \exp\left(-\frac{\omega^2}{2\Omega^2}\right) / (2\pi\Omega^2)^{1/2}$, while we postpone the definition of source function $S_n(\omega, x)$.

2.2.5 The simulated fluorescence spectra of DMABN

Summarizing, static properties $\varepsilon_n(\varphi)$, $\mu_n(\varphi)$ *in vacuo* are obtained from QM calculations; coarse correction to allow for solvent polar environment are taken into account at simplified Onsager level, with parameters $\epsilon_{0,\infty}$ (dielectric constants) and V (effective molecular volume); τ_I is estimated from hydrodynamic modeling and is directly linked to solvent viscosity η , τ_S available in the literature; parameters k^{nr} , k^{rad} and Ω are assumed to be solvent and temperature independent. We consider also two additional solvent-dependent corrective factors, to the PES for LE and TICT states, $e_{LE,TICT}^{corr}$. These are introduced to adjust absolute positions of the calculated spectra with respect

Solvent	Viscosity / Pa s	ϵ_0	ϵ_∞	τ_I / ps	e_{LE}^{corr}	e_{TICT}^{corr}
<i>n</i> -hexane [214]	0.29×10^{-3}	1.89	1.88	20.9	-0.46	0.28
Cyclohexane [214]	0.89×10^{-3}	2.22	2.03	63.7	-0.46	0.28
Benzene	0.6×10^{-3} [215]	2.27 [216]	2.24 [216]	42.7	-0.46	0.28
Dibutyl ether [214]	0.11×10^{-3}	3.10	1.96	8.11	-0.46	0.28
Diethyl ether [214]	0.22×10^{-3}	4.20	1.82	16.0	-0.28	0.28
<i>n</i> -butylchloride [214]	0.47×10^{-3}	9.60	1.97	33.4	0	0.28
Acetonitrile	0.34×10^{-3} [215]	35.94 [216]	1.80 [216]	24.2	0	0.2
Dimethylsulfoxide	1.99×10^{-3} [215]	46.45 [216]	2.18 [216]	141.8	0	0.13

TABLE 2.3: Physical characteristics and solvent dependent parameters for DMABN in *n*-hexane, cyclohexane, benzene, dibutyl ether, diethyl ether, *n*-butylchloride, acetonitrile and dimethylsulfoxide. The energy corrections are expressed in eV.

to experimental ones and they can be justified given the very simplified strategy adopted for estimating solvation energy corrections. We can now distinguish between a solvent independent parameter set and a solvent dependent parameter set. In the former set we number the effective molecular volume V , the average atomic radius R and boundary constant C for evaluation of τ_I , the amplitude of the elementary Gaussian band Ω and the cumulative non-radiative and radiative parameters k^{nr} , k^{rad} . The molecular volume is taken equal to 1.2×10^{-28} m³, while the effective radius for the calculation of τ_I is chosen equal to 1.95 Å and constant C as been taken equal to 6, corresponding to stick boundary conditions. The amplitude Ω has been chosen $\Omega = 0.5 \times 10^{14}$ s⁻¹. Finally k^{rad} is set to 50 ps while k^{nr} is taken equal to 0.5 ps. Parameters dependent from the solvent are summarized in Table 2.3, including the correction energies $e_{LE,TICT}^{corr}$. The values obtained for τ_I can be compared with known magnitudes of solvent relaxation

times [214],[215],[216]: for instance for benzene (low polarity) and acetonitrile (high polarity) we have $\tau_I= 42.7$ ps, $\tau_S= 2.2$ ps and $\tau_I= 24.2$ ps, $\tau_S= 0.26$ ps respectively, thus allowing a full justification of the time scale separation invoked previously to simplify the dynamic equations. Correction energies $e_{LE,TICT}^{corr}$ are essentially partitioned

Solvent	LE ^{exp} / s ⁻¹	TICT ^{exp} / s ⁻¹	LE ^{sim} / s ⁻¹	TICT ^{sim} / s ⁻¹
<i>n</i> -hexane	8.87×10^{14} [152]	//	8.96×10^{14}	//
Cyclohexane	8.78×10^{14} [217]	//	8.74×10^{14}	//
Benzene	8.65×10^{14} [217]	//	8.80×10^{14}	//
Dibutyl ether	8.61×10^{14} [152]	//	8.54×10^{14}	//
Diethyl ether	8.55×10^{14} [152]	//	8.56×10^{14}	//
<i>n</i> -butylchloride	8.50×10^{14} [152]	7.36×10^{14} [152]	8.80×10^{14}	7.54×10^{14}
Acetonitrile	8.30×10^{14} [218]	6.37×10^{14} [218]	8.52×10^{14}	6.32×10^{14}
Dimethylsulfoxide	8.37×10^{14} [219]	6.26×10^{14} [219]	8.64×10^{14}	6.24×10^{14}

TABLE 2.4: Experimental and simulated fluorescence maxima for LE and TICT bands in different solvents.

in two sets: low and intermediate polarity solvents, for which $e_{LE}^{corr} = -0.46$ eV, $e_{TICT}^{corr} = 0.28$ eV, and high polarity solvents for which correction energy are smaller in magnitude. This suggest that the rough estimate employed here for solvation energy based on Onsager theory is working, not unsurprisingly, only for highly polar environments, whereas is a mediocre choice for low-polarity media. The overall comparison of experimental and simulated data is shown in Figure 2-7, which displays solvatochromic effects calculated for the normalized fluorescence emission of DMABN at room temperature in the eight selected solvents of increasing polarity, namely *n*-hexane, cyclohexane, benzene, dibutyl ether, diethyl ether, *n*-butylchloride, acetonitrile and dimethylsulfoxide. The comparison shows that the model proposed is able to reproduce reasonably well the spectral position and shape of the emission spectra of DMABN, as it can also be seen quantitatively from Table 2.4. In particular the model reproduces the red shift expected for TICT excited states when the dielectric constant of the solvent increases. The combination of stochastic methods and QM calculation of PES/charge distributions for describing the static and dynamic properties of relatively complex molecules in polar solvents, like the one considered in this report, is potentially useful, based on a combination of continuum treatment (the solvent which is considered a continuous dielectric and/or hydrodynamic fluid) and detailed solute dynamics, but significantly

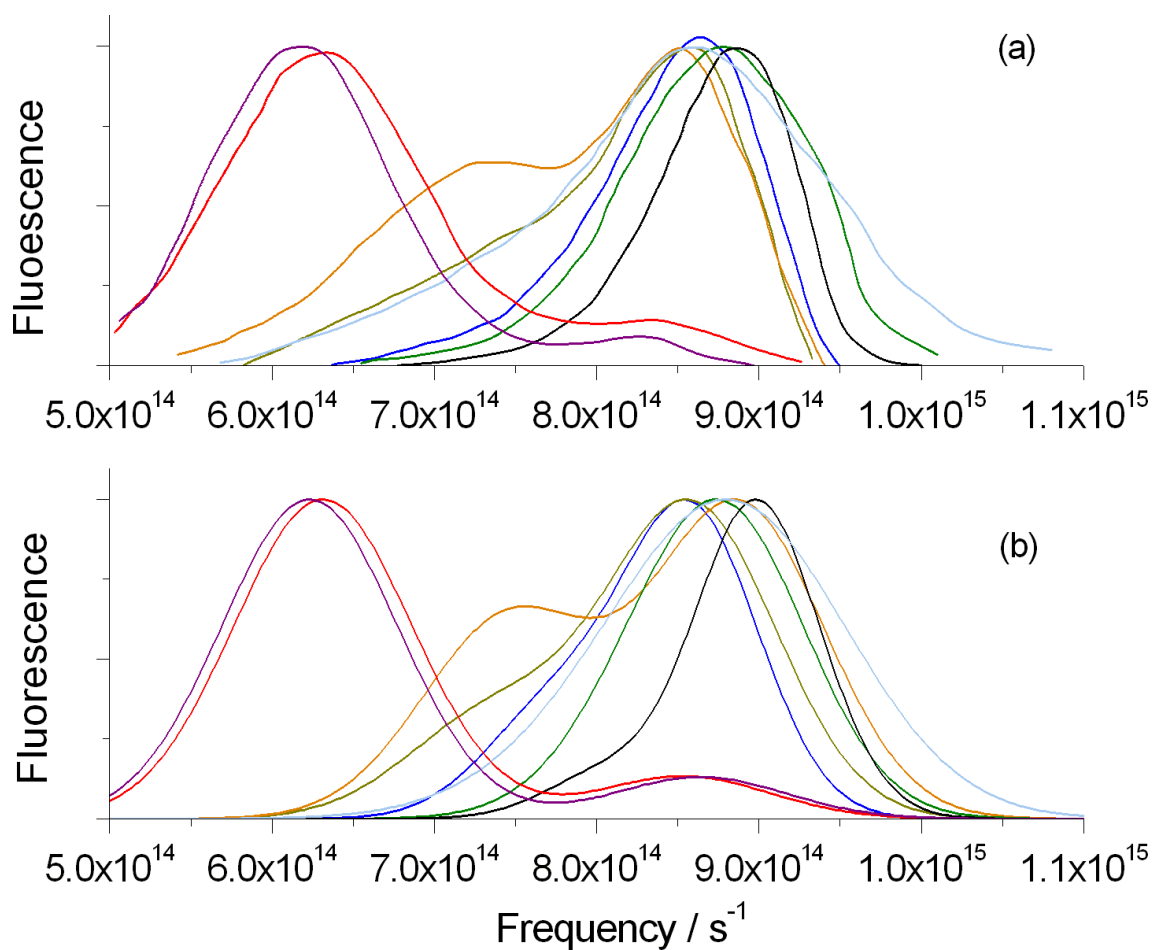


FIGURE 2-7: Experimental (a) and simulated (b) emission spectra for DMABN in: DMSO (purple), acetonitrile (red), *n*-butylchloride (orange), diethylether (dark yellow), dibutyl ether (blue), benzene (cyan), cyclohexane (olive) and *n*-hexane (black).

increasing the accuracy employed with respect to previous treatments [173] to define both geometric and dissipative parameters. However, before a real predictive value can be assured for the model in dealing with more complex systems, several improvements and integrations are needed.

2.3 Extension of the model to a DMABN derivative: DMABN-Crown5

We present an interpretation, based on a stochastic model approach, of the emission signal of a class of dimethylaminobenzonitrile derivatives. The study is prompted by

the interest in building relatively simple theoretical tools for understanding the static and dynamic properties of metal chelation-controlled fluorescent molecular systems, in the presence of internal flexibility and solvation effects, which can be employed as fluorescent sensors of metal ions. Since the seminal studies [148] of the dual fluorescent behavior of 4-(N,N-dimethylamino) benzonitrile (DMABN) in polar solvents this molecule has been the subject of several experimental [149],[150],[151] and theoretical studies [152],[153],[154],[155],[156],[217],[220],[221],[222],[223]. The emission spectrum of DMABN presents an anomalous emission in polar solvents, red-shifted with respect to the normal fluorescence band. This phenomenon is known as dual fluorescence and it has been observed in other electron donor-acceptor compounds. In low-polarity solvents only a band is usually observed (locally excited, LE or "normal band") at high frequency, while in highly polar solvents a second band is present at low frequency, usually interpreted as resulting from a twisted intramolecular charge transfer state (TICT). The unusual behavior of DMABN and of related compound is explained by the Grabowski model [152],[165] which links the intermolecular charge transfer process in the electronically-excited state to a twisting motion and orbital decoupling of the phenyl acceptor ring from the electron donor group. The charge separation is believed to be combined with a rotation of the amino group from the parallel (LE state) towards the perpendicular position (TICT state) with respect to the benzene ring. This twist leads to a decoupling of the amino and benzene parts of the molecule and it is accompanied by a charge transfer from donor to acceptor in the excited state. Recent studies have demonstrated that the dual fluorescence in DMABN and DMABN-derivatives arises from the two lowest singlet excited states, characterized by significantly different minimum energy structures. The LE state is the lowest excited singlet state of DMABN in the planar structure and is the origin of the "normal" band in the fluorescence spectrum, while the TICT state is the second excited singlet state and is the cause of the "anomalous" band in the spectrum of DMABN. It presents a strong minimum with a 90° twisted amino group conformation and an exceedingly high dipole moment. These two states have an intersection region [224] with strong vibronic coupling which allows for transitions between LE and TICT. A description of the excited states dynamics can be obtained by considering as relevant degree of freedom the angle between the

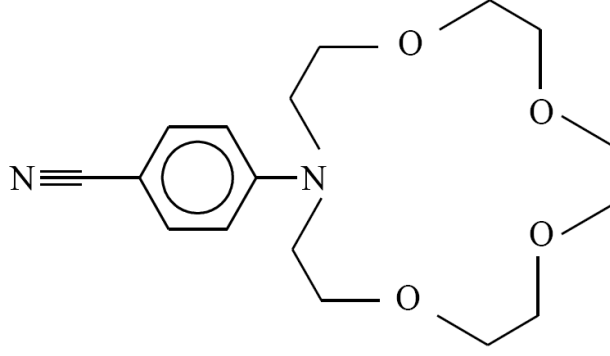
amino group and the aromatic plane and adopting a stochastic description for its time evolution [169],[170],[171],[172],[173] in order to describe the charge-transfer process of the excited state which accompanies torsional motion. The internal coordinate is coupled to a solvent polarization coordinate defined as the stochastic reaction field in an Onsager cavity [173]. The time evolution equation for the excited state population is determined by a Smoluchowski operator modified by inclusion of sink and source terms. The static emission spectra of DMABN in solvents with different polarity is obtained considered (i) the total energy of the system in the two excited states and (ii) the diffusion coefficients for the internal motion and for the solvent relaxation. Several molecules derived from DMABN exhibit also complex fluorescence in polar solvents, and several prototype systems with similar behavior have been studied [175],[176]. In DMABN-derivatives, inclusion of the aminic nitrogen atom in macrocyclic systems leads to more complex ground- and excited states behavior. The covalent attachment of the benzonitrile group to the aza group of a metal binding ionophore such as Cyclam creates a fluorescent ionophore DMABN-Cyclam [177],[178] that uniquely combines the characteristic fluorescence properties of DMABN with the metal binding properties of Cyclam. This molecule presents a triple fluorescence in ethanol that can be possibly interpreted as resulting from a LE state, a TICT state and an intramolecular exciplex (E) [179]. The LE band shows a nearly solvent-independent position while the other two bands present a strongly solvatochromic shift. The LE state emission at high frequency dominates the spectrum in non polar solvents as n-hexane while polar solvents stabilize the charge-transfer states at lower frequency. The E band is placed between the LE and the TICT bands and it presents a smaller solvatochromic effect than TICT. Letard et al. [180] reported the dual fluorescence of two compounds structurally similar to DMABN-Cyclam, 4-(1-aza-4,7,10-trioxacyclododecyl) benzonitrile (DMABN-Crown4 and 4-(1-aza-4,7,10,13-tetraoxacyclododecyl) benzonitrile (DMABN-Crown5). The fluorescence spectra of DMABN-Crown4 and DMABN-Crown5 show two bands in medium polarity solvents which can be interpreted as TICT and LE signals. The TICT/LE ratio increases with increasing solvent polarity. The relative intensity of the TICT band increases in going from DMABN-Crown4 to DMABN-Crown5. In polar solvents like acetonitrile or DMSO the emission spectrum is dominated by a single low

frequency band that shift towards higher frequencies when decreasing solvent polarity. TICT emission is observed even in non polar solvents and in general the TICT band is more pronounced and shifted to lower energy with respect to DMABN [152]. The changement of the characteristic fluorescence emission of DMABN with the concentration of metal cations has been investigated in a number of theoretical [225],[226] and experimental [227],[228],[229] studies. As a matter of fact fluorescent sensors in which reversible binding of a molecule or ion is accompanied by an emission shift are much sought after because they allow the measurement of the recognized species from the intensity ratio at two emission wavelengths with opposite substrate-sensitivity responses [230]. Unfortunately, on complexation by cations, the majority of the chromo and the fluoroionophores show hypsochromic shifts of the absorption spectra, while the emission spectra are only slightly blue-shifted as a result of the breaking of the cation-chromophore bond in the excited states. Fluorescent probes [228] with chemically tailored sensitivity can be obtained in principle by coupling a chromophore with two fluorescing excited states of considerably different charge-transfer character and a ionophore including the electron-donor substituent: the complexed cation is able to decrease the charge transfer process and hence the corresponding emission. The addition of alkali or alkaline-earth perchlorates to DMABN-Crown5 in acetonitrile solution shifts the absorption maximum to higher energies. The shift is strongly dependent on the characteristic properties of the cation. The hypsochromic shift induced by dications significantly exceed those for mono-cations of the same size. The large shift for Ca^{2+} in DMABN-Crown5 can be explained by the closer size compatibility with the crown ligand. The change in the absorption spectra for DMABN-Crown5, upon the complexation with cations, can be qualitatively interpreted as the stabilization of the amine lone pair by electrostatic interaction with the cation; cation complexation is expected to reduce or even suppress the charge transfer [227],[228]. The emission spectra of DMABN-Crown5- Ca^{2+} in acetonitrile [180] is composed of two bands. The high-frequency band is blue-shifted relative to that of the LE state of the free ligand. A higher hypsochromic shift is observed between the low-frequency band of the free and the complexed ligand. In the present work, we are particularly interested in defining a coarse-grained description of solvation dynamics to understand the main

effects of polar media on the observed emission fluorescence of DMABN-CrownN systems. A reliable model capable to describe the spectroscopic behavior of the metal free DMABN-CrownN system is a necessary step in the comprehension of this class of fluoro-ionophore. It should be stressed that we do not seek a truly comprehensive modeling approach which gives a detailed description of solvent local behavior at molecular level, nor we wish to explicitly take into account direct coupling between the solvent configurations and a quantum mechanical description of the solute molecule. Rather, we intend to achieve a relatively simple interpretation based on macroscopic solvent properties (dielectric constants and viscosity), keeping at a minimum the number of adjustable parameters. In order to do so, we shall employ an extension of the Nordio approach to TICT static and dynamic properties of DMABN [169], including a stochastic diffusive description of the molecule internal dynamics, an explicit evaluation of dissipative properties (diffusion tensor) from a simplified hydrodynamic description of the solute molecule and a simple characterization of solvent variables; the presence of a large relatively flexible crown group is also taken in account both from a static (considering more than one stable ring conformations) and dynamic point of view (including a strong-collision process or "hopping" motion among ring conformation), albeit in a very simplified way. Following Nordio *et al.* [169],[170],[171] our methodology is based on a three-step procedure, namely (i) the definition of potential energy surfaces for the ground state and the two lowest energy excited states of the solute molecules in vacuo, (ii) coupled with a description for the roto-translational and conformational dynamics, in the presence of a (iii) stochastic polarization coordinates representing the solvent relaxation. The model is limited to polar aprotic solvents, and is based on a very coarse description of solute-solvent interactions.

2.3.1 The model extension

We consider now the interpretation of static emission fluorescence of DMABN-Crown5. The molecular structure is sketched in Figure 2-8. The presence of a large relatively flexible crown group is taken in account (i) considering more than one stable ring conformations and (ii) including a strong-collision process or "hopping" motion among ring conformations, i.e. the internal dynamic of the donor ring is modeled by introduc-



(DMABN-Crown5)

FIGURE 2-8: Structure of 4-(1-aza-4,7,10,13-tetraoxacyclododecyl) benzonitrile (DMABN-Crown5).

ing a random-walk approximate description for the complex transition among different ring minima. We follow in general the methodology presented for DMABN with the extension of the model to a molecular system with more than one conformation in solution. We start from the definition of the generic emission signal as

$$I(\omega, t) \propto \omega^3 \int \mathbf{Q} \sum_{\sigma, n} k_{\sigma, n \rightarrow \sigma, g}^{rad}(\mathbf{Q}) g_{\sigma, n}[\omega - \Delta\omega_{\sigma, n}(\mathbf{Q})] P_{\sigma, n}(\mathbf{Q}, t) \quad (2.26)$$

The double index σ, n runs over all ring configurations (σ) and electronic states (n). All quantities retain the same meaning of their counterparts presented in the previews part of the work for the case of DMABN. The excited state populations $P_{\sigma, n}(\mathbf{Q}, t)$ are now described by a time evolution equation based on the hypothesis that electronic transitions do not change index σ , i.e. that the ring configuration is frozen during an electronic transition. Vice versa, rings minima are allowed to interconvert adiabatically, i.e. index n is not affected. The most general expression is then:

$$\begin{aligned} \frac{\partial}{\partial t} P_{\sigma, n}(\mathbf{Q}, t) = & -\hat{\Gamma}_{\sigma, n} P_{\sigma, n}(\mathbf{Q}, t) - \sum_{n'} k_{nn'}(\mathbf{Q}) P_{\sigma, n'}(\mathbf{Q}, t) + S_{\sigma, n}(\mathbf{Q}, t) \\ & - \sum_{\sigma'} \int d\mathbf{Q}' \left[P_{\sigma, n}(\mathbf{Q}, t) W_n(\sigma, \mathbf{Q} \rightarrow \sigma', \mathbf{Q}') - P_{\sigma', n}(\mathbf{Q}, t) W_n(\sigma', \mathbf{Q}' \rightarrow \sigma, \mathbf{Q}) \right] \quad (2.27) \end{aligned}$$

Kernel W_n is defined, for simplicity, as $W_n(\sigma, \mathbf{Q} \rightarrow \sigma', \mathbf{Q}') = \frac{1}{\tau_{rest}} P_{\sigma',n}(\mathbf{Q}') \delta(\varphi - \varphi')$, i.e. a single average frequency $1/\tau_{rest}$ for the jumping process from one minimum to another is considered, with imposed detailed balance, and with no change in the internal coordinate φ . We consider two diabatic states $n=LE, TICT$. In the case of a rigid

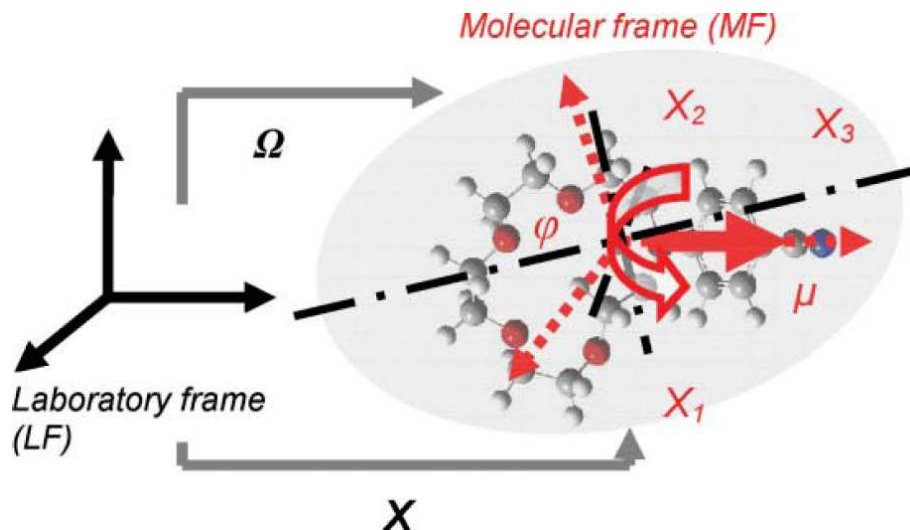


FIGURE 2-9: Relevant degrees of freedom for modeling DMABN-Crown5 fluorescence. Orientation is given by a set of Euler angles Ω ; relative orientation of donor-acceptor groups are described by the torsional angle φ ; a stochastic vector coordinate \mathbf{X} represents the solvent relaxation.

fluorescent systems (as for the DMABN model), a Brownian diffusion model includes explicitly the orientation of the solute Ω_{MF} . Additional internal degrees of freedom φ can be added to describe the dynamic evolution of dihedral angles. In Figure 2-9, a cartoon of the relevant degrees of freedom employed for interpreting dual fluorescence. In general, as for the DMABN model, the molecular orientation Ω_{MF} is coupled to the dynamic solvent vector variable \mathbf{X} and the internal conformational angle φ . In polar isotropic fluid, coupling with rotational coordinates can be averaged out, while only one component of the solvent polarization variable is tightly coupled with the molecular electric dipole. So, under the approximations (rotational isotropy, only one relevant component for dipole moment etc.), the energy for each state n and configuration σ is given by

$$\frac{E_{\sigma,n}}{k_B T} = \frac{\varepsilon_{\sigma,n} - F_0 \mu_{\sigma,n}^2 / 2}{k_B T} + \frac{1}{2} (\tilde{x} - \tilde{x}_{\sigma,n})^2 = \tilde{V}_{\sigma,n}(\varphi) + \frac{1}{2} (\tilde{x} - \tilde{x}_{\sigma,n})^2 \quad (2.28)$$

where $\tilde{x}_{\sigma,n} = (F_{or}/k_B T)^{1/2}$, $\varepsilon_{\sigma,n}$ is the *in-vacuo* energy of the n -th excited state and σ -th conformation depending upon the internal geometry; $\mu_{\sigma,n}$ is the electric dipole moment vector of the molecule in the n -th excited state and for the σ -th conformation. The term F_0 is defined in the general model described for DMABN. The stationary populations $P_{st,\sigma,n}$ is obtained by solving the equation

$$\begin{aligned}
& - \left(\frac{1}{\tau_{I,\sigma}} \frac{\partial}{\partial \varphi} P_{eq,\sigma,n} \frac{\partial}{\partial \varphi} P_{eq,\sigma,n}^{-1} + \frac{1}{\tau_S} \frac{\partial}{\partial \tilde{x}} P_{eq,\sigma,n} \frac{\partial}{\partial \tilde{x}} P_{eq,\sigma,n}^{-1} \right) P_{st,n} + \sum_{n'} k_{nn'} P_{st,\sigma,n'} \\
& + \frac{1}{\tau_{rest}} \sum_{\sigma'} \int d\tilde{x} \left[P_{st,\sigma,n}(\varphi, \tilde{x}) P_{eq,\sigma',n}(\varphi, \tilde{x}') - P_{st,\sigma',n}(\varphi, \tilde{x}') P_{eq,\sigma,n}(\varphi, \tilde{x}) \right] = S_{\sigma,n}
\end{aligned} \tag{2.29}$$

where $\tau_{I,\sigma}$ is obtained for configuration σ following the hydrodynamic model. After introducing the *ansatz* $P_{st,\sigma,n} \approx p_{st,\sigma,n} G(\tilde{n} - \tilde{x}_{st,\sigma,n})$, where $p_{st,\sigma,n}$ and $\tilde{x}_{st,\sigma,n}$ are functions, to be determined, of the torsional angle only and $G(\tilde{x}) = \exp(-\tilde{x}^2/2)/(2\pi)^{1/2}$, i.e. a Gaussian function of width equal to 1. Notice that $P_{eq,\sigma,n} = p_{\sigma,n} G(\tilde{x} - \tilde{x}_{\sigma,n})$, where is the Boltzmann distribution over $\tilde{V}_{\sigma,n}$. The integration with respect to the \tilde{x} variable can be carried out analytically in the expression for the stationary emission fluorescence:

$$\begin{aligned}
I(\omega) & \propto \omega^3 \sum_{\sigma,n} \int d\varphi k_{\sigma,n}^{rad}(\varphi) p_{st,\sigma,n}(\varphi) i_{\sigma,n}(\omega, \varphi) \\
i_{\sigma,n}(\omega, \varphi) & = \exp \left\{ - \frac{[\omega - \omega_q(\Delta\tilde{x}_{\sigma,n} \tilde{x}_{st,\sigma,n} + \Delta\tilde{V}_{\sigma,n})]^2}{2(\omega_q^2 \Delta\tilde{x}_{\sigma,n}^2 + \Omega^2)} \right\} \\
& / \left[2\pi(\omega_q^2 \Delta\tilde{x}_{\sigma,n}^2 + \Omega^2) \right]^{1/2}
\end{aligned} \tag{2.30}$$

Assuming that $\tau_S \ll \tau_{I,\sigma}, \tau_{rest}$ we can simplify Eq. 2.30 to obtain:

$$\begin{aligned}
& \rho_{\sigma}(\tilde{x}_{st,\sigma,n} - \tilde{x}_{\sigma,n}) p_{st,\sigma,n} + \sum_{n'} c_{\sigma,nn'} p_{st,\sigma,n'} \tilde{x}_{st,\sigma,n'} = \delta_{n,TICT} p_{\sigma,B} \tilde{x}_{\sigma,TICT} \\
& - \frac{\partial}{\partial \varphi} \left[p_{\sigma,n} \frac{\partial}{\partial \varphi} p_{\sigma,n}^{-1} - (\tilde{x}_{st,\sigma,n} - \tilde{x}_{\sigma,n}) \frac{d\tilde{x}_{\sigma,n}}{d\varphi} \right] p_{st,\sigma,n} \\
& + \frac{1}{\tau_{rest}} \sum_{\sigma'} (p_{st,\sigma,n} p_{eq,\sigma',n} - p_{st,\sigma',n} p_{eq,\sigma,n}) + \sum_{n'} c_{\sigma,nn'} p_{st,n'} = \delta_{n,TICT} p_{TICT}
\end{aligned} \tag{2.31}$$

where $c_{\sigma,nn'} = \tau_{I,\sigma}k_{nn'}$, $\rho_\sigma = \tau_{I,\sigma}/\tau_S$, and assuming that $\rho_\sigma \gg c_{\sigma,nn'}$

$$\begin{aligned}
\tilde{x}_{st,\sigma,n} &= \tilde{x}_{\sigma,n} \\
-\frac{\partial}{\partial\varphi}p_{\sigma,n}\frac{\partial}{\partial\varphi}p_{\sigma,n}^{-1}p_{st,\sigma,n} &+ \frac{1}{\tau_{rest}}\sum_{\sigma'}(p_{st,\sigma,n}p_{eq,\sigma',n} - p_{st,\sigma',n}p_{eq,\sigma,n}) \\
+ \sum_{n'}c_{\sigma,nn'}p_{st,\sigma,n'} &= \delta_{n,TICT}p_{\sigma,TICT}
\end{aligned} \tag{2.32}$$

2.3.2 Parameters

The optimized structure for the most stable conformations of the DMABN-Crown5 are obtained by QM calculations. The structures of the five conformers of DMABN-Crown5 have been optimized in the gas-phase at the PBE0/6-31G(d) level [184]. Schematic drawings of the geometrical structures of DMABN-Crown5 are in Figure 2-10. Vertical Excitation Energies (VEE) to the first and second excited states have been calculated by Time-Dependent density functional theory (TD-DFT), employing the PBE0 functional. The five most stable conformers have been selected as a representative set for the internal crown dynamics. The recent implementation of TD-DFT analytical gradients [195] both *in vacuo* and in solution allows for the determination of excited state stationary points and properties (such as multipole moments). The use of TD-DFT has been limited by some deficiencies in describing excited states involving charge separation or with contributions from double excitations [196],[197],[199]. Recently, some interesting attempts to overcome these limitations have been proposed [199],[200],[202]. Moreover, for electronic transitions which involve only partial intramolecular charge transfer (TICT), the underestimation of excitation energies by TD-DFT, due to spurious self-interaction, may be controlled by the use of hybrid functionals [205],[138]. The investigation of the PES for the ground and the excited states, mainly regarding dependence from the torsional angle φ has been performed on the optimized gas-phase structures of the ground state increasing φ by steps of 10 degrees. The computational procedure use for the calculations is equal to the procedure used for DMABN. The remaining internal coordinates are kept frozen at each step. At each geometry the dipole moment for *g*, LE and TICT states are computed, as well. All calculations have been performed by exploiting a development version of the Gaussian code [137]. Figure

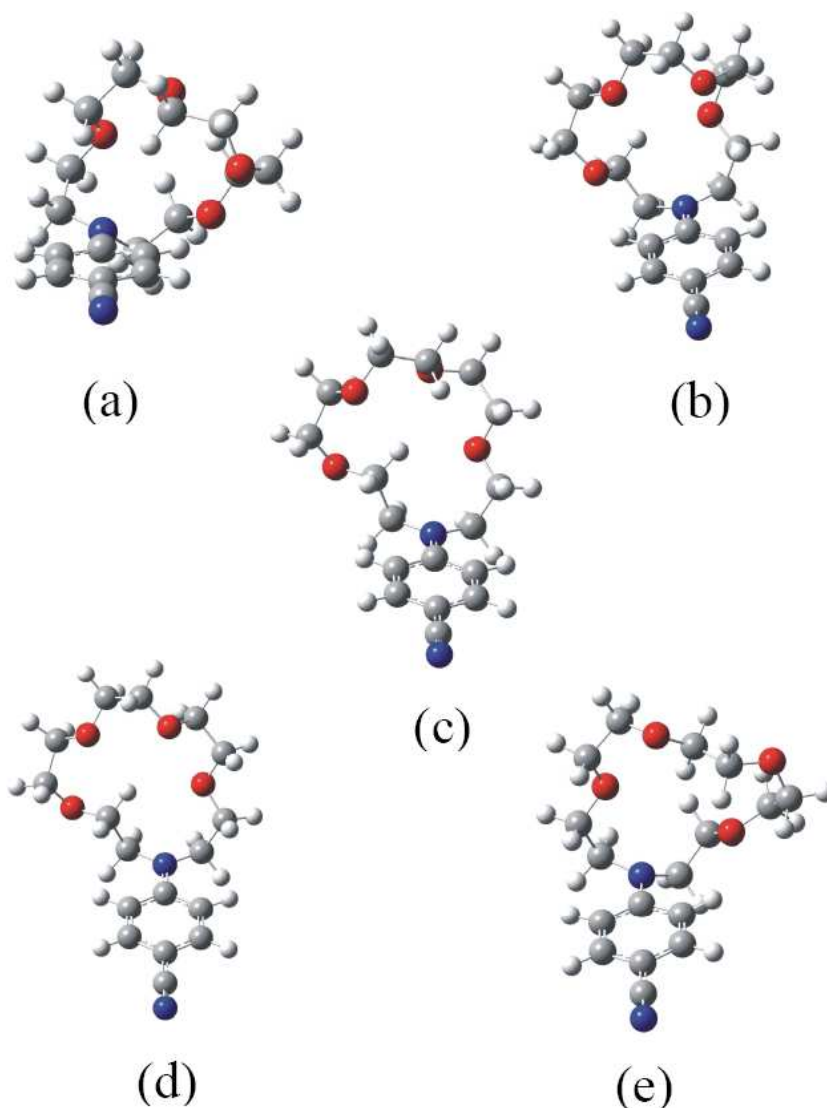


FIGURE 2-10: Structure of DMABN-Crown5 local minima.

2-11 shows a plot of the resulting potential energy curves and electric dipole moments as functions of the torsional angle φ specifying mutual orientation of the donor and acceptor group. During the evaluation of the energy the geometry is kept frozen to that optimized for the ground state for every points and for both excited states. The only changing parameter is the torsional angle. As show in Figure 2-11 the TICT state energy (left) of every conformations shows a strong minimum at 90° different for every conformations. We consider the minimum energy of the ground state as energy reference. In the right part we show the trend of the dipole moment for the ground state and for the excited states. In all conformations the dipole moment for the TICT state show

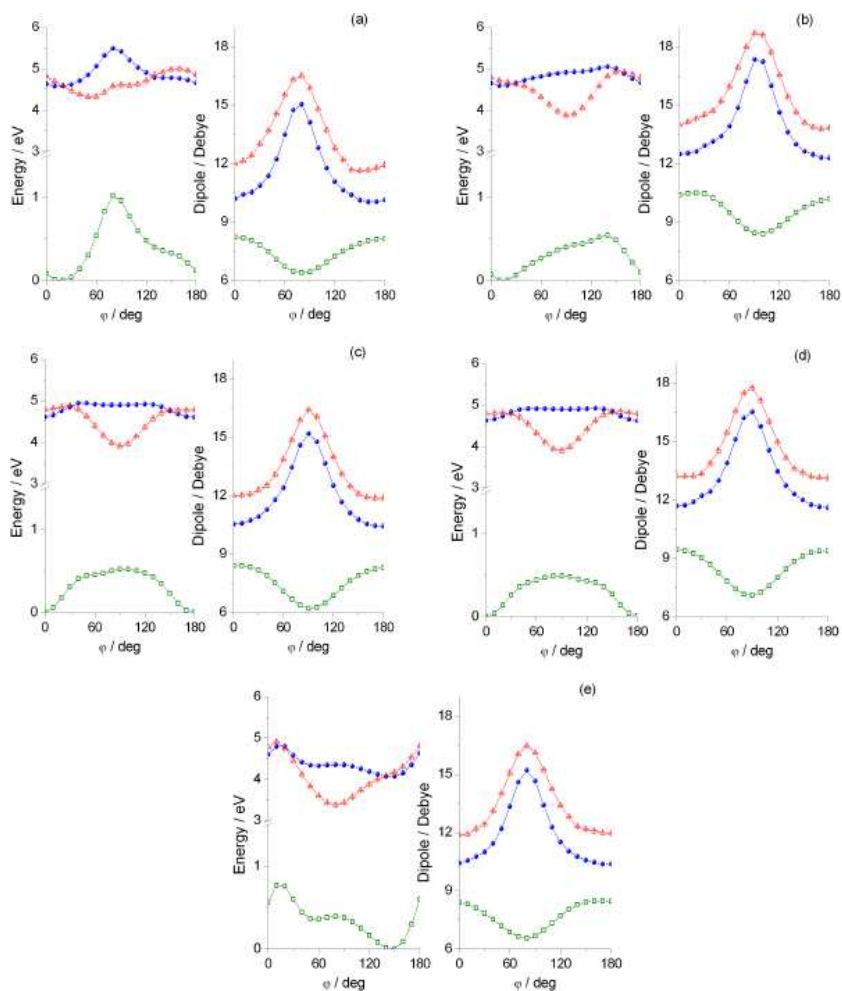


FIGURE 2-11: Potential energy surfaces (left) and dipole moments (right) for the five conformers (a)-(e) of DMABN-Crown5 as a function of the dihedral angle φ in the ground (green), LE (blue) and TICT (red) electronic state.

a maximum values for the perpendicular geometry. It is useful detail the attention on the characteristic of the five most stable conformers of DMABN-Crown5 summarized in Table 2.5. All the conformers show a higher value of the dipole moment of the TICT state respect to the LE state and in all cases this difference is over 1 D. At a torsional angle equal to 90° the TICT state is most stable respect to the LE state but the stabilization is different. The conformation (e) is the higher stabilized conformation and for this reason we choose this conformation for reproduce the emission fluorescence spectra in different solvent. If we consider the dynamics of the populations in the excited states and we permit a movement between the excited state of different conformations

		a	b	c	d	e
<i>g</i>	ΔE	0.96	0.41	0.52	0.49	0.38
	μ	7.17	9.82	9.32	8.99	9.20
LE	ΔE	5.42	4.91	4.89	4.9	4.35
	μ	14.10	18.61	18.56	16.51	17.58
TICT	ΔE	4.61	3.87	3.91	3.91	3.43
	μ	16.60	19.92	19.80	17.74	19.05
ΔE <i>vac.</i>		0.16	0.26	0.01	0	0.16

TABLE 2.5: Characteristic of the five most stable conformers of DMABN-Crown5 with a torsional angle equal to 90° . The structures are optimized in the gas-phase at the PBE0/6-31G(d). The energy are expressed in eV and the dipole moment in debye.

we observe that all the populations (at stationary time) converged in the excited state of the (e) conformer. So the important values in the Table 2.5 is the difference between the energy of the TICT state and the ground state. The (c) and (d) conformations have the lower relative energy and the shape of the PES and the dipole moments are identical to the DMABN but they are less stabilized in the excited state and for this reason they are not used for reproduced the emission fluorescence spectra. Another important ingredient in the model is the calculation of the diffusion coefficient associated to internal rotation $D_{I,\sigma}(\varphi) \approx D_I = \tau_I$. The evaluation of the diffusion parameters is obtained by an hydrodynamic approach [231] considering the internal degrees of freedom of the molecular system. We calculated a different diffusion coefficient for each conformer in each solvent, but for the spectra simulations we used a single average value for each different solvent. The value for the diffusion tensor are reported in Table 2.6. It is not a strange result that the value of the diffusion tensor for the different conformations in the same solvent is similar. A probably reason is that global shape of the molecule in solution it is not very different. From this consideration we choose a constat value for the volume of the molecule, too. The solvent relaxation diffusion D_S is obtained from dielectric constant in the simplifying hypothesis of a single solvent decay time $D_S/k_B T = F_{or}/\tau_S$ [170],[171],[172],[173]. Although the kinetic coefficients $k_{\sigma,LE \rightarrow \sigma,g}^{nr}$, $k_{\sigma,TICT \rightarrow \sigma,g}^{nr}$, $k_{\sigma,LE \rightarrow \sigma,B}^{nr}$, $k_{\sigma,TICT \rightarrow \sigma,TICT}^{nr}$, $k_{\sigma,LE \rightarrow \sigma,g}^{rad}$, $k_{\sigma,TICT \rightarrow \sigma,g}^{rad}$, source function $S_{\sigma,n}$ and intrinsic line shape $g_{\sigma,n}(\omega)$ could be, at least in principle, determined independently from quantum mechanical calculations, here we will follow a phenomenological approach, in terms of a reduced number of free parameters. To this purpose, we start

by assuming simple functional forms for the kinetic coefficients, chosen to reproduce known emission properties of DMABN: (i) $k_{LE \rightarrow TICT}^{nr}$, $k_{\sigma, TICT \rightarrow \sigma, g}^{nr}$ and $k_{\sigma, TICT \rightarrow \sigma, g}^{rad}$ are assumed to be monotonously increasing with increasing φ and to have a maximum at $\varphi \approx \pi/2$; (ii) $k_{\sigma, TICT \rightarrow \sigma, A}^{nr}$, $k_{\sigma, LE \rightarrow \sigma, g}^{nr}$ and $k_{\sigma, LE \rightarrow \sigma, g}^{rad}$, are assumed to have a maximum at $\varphi \approx 0$ and to be monotonously decreasing with increasing φ ; (iii) only two effective solvent and temperature independent parameters k^{nr} and k^{rad} are introduced to measure radiative and non radiative emission strength, and a simple squared cosine/sine dependence upon φ is allowed. It follows that $k_{\sigma, LE \rightarrow \sigma, g}^{nr} \approx k^{nr} \cos^2 \varphi$, $k_{\sigma, TICT \rightarrow \sigma, g}^{nr} \approx k^{nr} \sin^2 \varphi$, $k_{\sigma, LE \rightarrow \sigma, TICT}^{nr} \approx k^{nr} \sin^2 \varphi$, $k_{\sigma, TICT \rightarrow \sigma, LE}^{nr} \approx k^{nr} \cos^2 \varphi$, $k_{\sigma, LE \rightarrow \sigma, g}^{rad} \approx k^{rad} \cos^2 \varphi$, $k_{\sigma, TICT \rightarrow \sigma, g}^{nr} \approx k^{rad} \sin^2 \varphi$. We assume for simplicity that the radiative and non radiative coefficients are equal in every different conformations of DMABN-Crown5. The intrinsic line shape $g_{\sigma, n}(\omega)$ is simply estimated as a Gaussian function with constant linewidth Ω , $g_{\sigma, n}(\omega) \approx g(\omega) = \exp\left(-\frac{\omega^2}{2\Omega^2}\right) / (2\pi\omega^2)^{1/2}$.

2.3.3 The simulated fluorescence spectra of DMABN-Crown5

Emission spectra were measured with Perkin-Elmer LS50 spectrophotometer. Spectroscopic grade solvents were used, without further purification. DMABN-Crown5 was synthesized and purified according to the literature [180]. The model described in the preceding section is applied to the interpretation of the measured emission spectra. The *in vacuo* energy and electric dipole moment for each conformer are obtained by QM calculations, the diffusion coefficient is estimated from hydrodynamic model and the physical characteristic of the different solvent as the viscosity, the relaxation time and dielectric constant are available in the literature [215]. Parameters as k^{rad} , k^{nr} , Ω and τ_{rest} are assumed to be solvent, conformation and temperature independent. We consider also two additional corrective parameters to the PES for LE and TICT states, $e_{LE, TICT}^{corr}$, connected with the solvent. Parameters are summarized in Table 2.6. The molecular volume has been taken equal to $3.0 \times 10^{-28} \text{ m}^3$, while the effective radius for the calculation of has been chosen equal to $V = 1.95 \text{ \AA}$ and the boundary condition constant C as been taken equal to 4. The radiative and non-radiative coefficients have been estimated to be $k^{rad} = 14 \text{ ps}$ and $k^{nr} = 1 \text{ ps}$ respectively. The value of $\Omega = 0.5 \times 10^{14} \text{ s}^{-1}$ and $\tau_{rest} = 10 \text{ ps}$. The model results not very sensitive to the

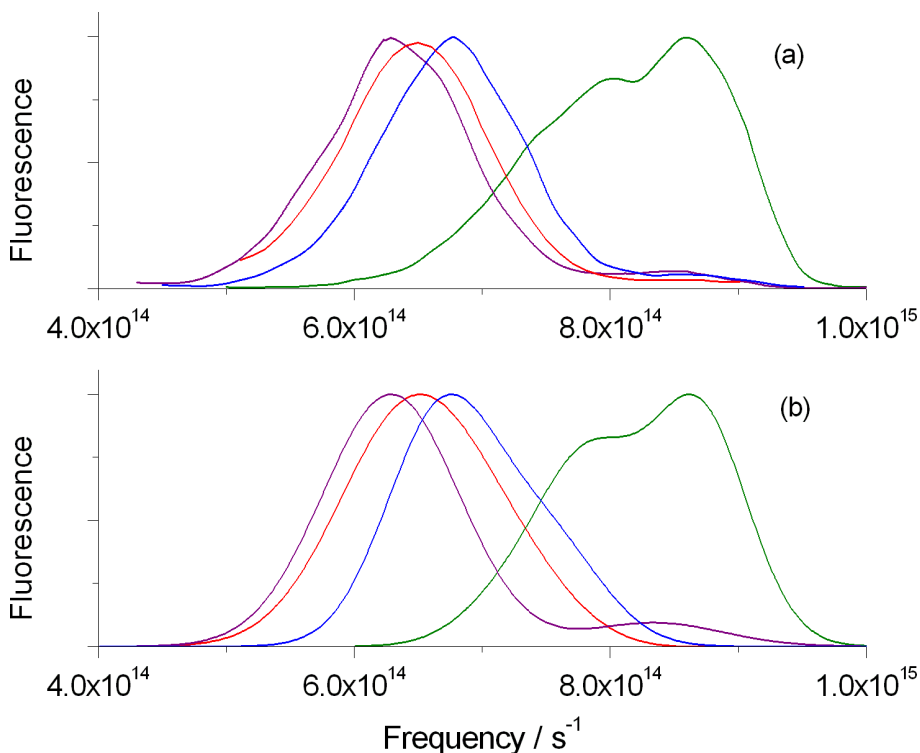


FIGURE 2-12: Experimental (a) and simulated (b) fluorescence emission spectra of DMABN-Crown5 in acetonitrile (red), DMSO (purple), dichloromethane (blue) and cyclohexane (olive).

value of τ_{rest} . The order of magnitude of the relaxation constant are in agreement with those estimated for similar derivatives of DMABN [228]. The internal flexibility of the crown ether has been taken into account by allowing in the simulations the presence and free inter-conversion between the five conformers of DMABN-Crown5 discussed above. We observed that one of the conformer [(e)] is significantly more stable in the excited state so in the stationary situation all the excited state populations converged to this conformer. So in a second step we tried to use in the simulations only the (e) conformer, obtaining the results reported in Figure 2-12 with the parameters in Table 2.6. In this way we have established, in agreement with the experimental evidence [152] that the two peaks in the cyclohexane spectra are originated by the TICT and the LE electronic states and that their explanation does not require the presence of different conformers in solution. Figure 2-12 shows solvatochromic effects calculated for the normalized fluorescence emission of DMABN-Crown5 at room temperature in the four selected solvents. As expected, the shift of the TICT band with respect to its

Solvent	Viscosity ^a / Pa s	ϵ_0^a	ϵ_∞^a	τ_S^a / ps	τ_I / ps	e_{LE}^{corr}	e_{TICT}^{corr}
Cyclohexane	0.89×10^{-3}	2.22	2.03	2.1	122.0	-0.31	0.13
Dichloromethane	0.41×10^{-3}	8.93	2.03	0.56	55.6	-0.64	0.10
Acetonitrile	0.34×10^{-3}	35.94	1.80	0.26	46.1	-0.56	0.20
Dimethylsulfoxide	1.99×10^{-3}	46.45	2.18	1.8	270.0	-0.21	0.03

TABLE 2.6: Physical characteristics and solvent dependent parameters for DMABN-Crown5 in cyclohexane, dichloromethane, acetonitrile and dimethylsulfoxide. The energy corrections are expressed in eV. ^a from [215].

locally excited, LE, counterpart increases with the solvent polarity. Furthermore, the positions and relative intensities of the computed TICT and LE bands are in agreement with the observed data. In particular our model is capable to reproduce the marked difference between the fluorescence spectra in cyclohexane and in all the other solvents. The model confirms that the LE peak does not shift with solvent polarity while the TICT peak shifts towards lower frequency as the dielectric constant of the solvent increases. A detailed comparison between the experimental and the simulation values for the fluorescence maxima reported in Table 2.7 convincingly shows that our model allows to reproduce in a correct way the shape and the position of the emission spectra of DMABN-Crown5. We try to reproduced the emission fluorescence spectrum

Solvent	LE ^{exp} / s ⁻¹	TICT ^{exp} / s ⁻¹	LE ^{sim} / s ⁻¹	TICT ^{sim} / s ⁻¹
Cyclohexane	8.56×10^{14}	8.05×10^{14}	8.60×10^{14}	7.99×10^{14}
Dichloromethane	//	6.77×10^{14}	//	6.76×10^{14}
Acetonitrile	//	6.50×10^{14}	//	6.52×10^{14}
Dimethylsulfoxide	//	6.29×10^{14}	//	6.28×10^{14}

TABLE 2.7: Experimental and simulated fluorescence maxima for LE and TICT bands in different solvents.

for a protic solvent, the *n*-octanol. The model reproduces with a good accordance the experimental position of emission maxima ($6.70 \times 10^{14} \text{ s}^{-1}$ the experimental value *versus* $6.65 \times 10^{14} \text{ s}^{-1}$ the calculated value) but the corrective parameters for energy, the radiative and non-radiative factor and Ω are altogether different from the other solvents. The explanation of this behavior is simply: a quantum mechanical treatment with implicit solvent does not permits to reproduce correctly the strong interaction of a protic solvent with the solute molecule.

2.4 Conclusions

The relationship between spectroscopic measurements and molecular properties can be gathered only indirectly, that is, structural and dynamic molecular characteristics can be inferred from the systematic application of modeling and numerical simulations to interpret experimental observables. A straightforward way to achieve this goal is the employment of spectroscopic evidence as "target" of a fitting procedure of molecular, mesoscopic and macroscopic parameters entering in the model. This strategy, based on the idea of a general fitting approach, can be very helpful in providing detailed characterization of molecular parameters. In this specific work we have developed a model capable to reproduce the overall shape and band positions in the emission spectrum of DMABN and DMABN-Crown5 as a function of solvent polarity. In the present approach, solvation coordinates are treated in a rather coarse way, and interaction with the solute is considered only via a simplified dipole-solvation polarization term; QM calculations are hardly refined and in particular, a limited description of internal degrees of freedom is assumed. Our main objective in this work has been to discuss the degree of advancement of the integrated computational approach to the interpretation of fluorescence emission of a prototype dual-fluorescence probe in solvated environments, *via* combination of advanced quantum mechanical approaches and stochastic modeling of relaxation processes. Specific stochastic variables can be employed for describing the instantaneous configuration of the local solvent structure and numerical solutions in semi-analytic form can be obtained in terms of correlation functions which are directly linked to the fluorescence signal. In the second part we try to understand the emission properties of the DMABN-Crown5. The knowledge of this kind of compounds is a necessary prerequisite to understand their behavior as fluoro-ionophores, which can be envisaged as their main application in the field of ion-sensing. The model is based on an integrated approach that combines stochastic methods and QM calculations. The static and dynamic properties of the molecule are obtained by a combination of a continuum treatment and a detailed solute dynamics. The integration of these building blocks can be used to define a robust computational approach for *ab-initio* prediction of emission spectroscopic properties. i.e. the combination of (i) quantum

mechanical calculations of structural parameters possibly including environmental and fast vibrational and librational averaging; (ii) direct feeding of calculated molecular parameters into dynamic description based on stochastic modeling. In particular, a diffusive approach is used to describe the charge-transfer dynamics of the excited state which accompanies torsional motion. The internal coordinate is coupled to a solvent polarization coordinate defined as the stochastic reaction field in an Onsager cavity. The time evolution equation for population is determined by a Smoluchowski operator modified by inclusion of sink and source terms, and leading to a standard operator for diffusion along the diabatic energy surface in the excited states. The total energy of the solute-solvent system in the excited states or in the ground state depends on the potential energy of the isolated molecule, on the dipole moments, on the diffusion coefficients that can be evaluated by an hydrodynamic model and on a diffusion coefficient for solvent coordinate related to the static and optical dielectric constants. The planar and perpendicular conformations are defined with respect to the dipole moment and static and dielectric constants. The sink term accounts for decay to the ground state and describes the continuous depletion of the excited state population due to non radiative and radiative decay. Lastly a pump term is included in the form of source defined as a peaked function around the planar conformation. Simple computational approximations lead to a semi-analytical treatment of the resulting equations, which reproduce correctly the static spectra at room temperature of DMABN-Crown5 in solvents with different polarity. Further integration of these building blocks can be used to define a general robust and reliable computational approach for *ab-initio* prediction of emission spectroscopic properties of organic molecules in solution.

Chapter 3

Ab-initio computational modeling of CW-ESR spectra of a double labeled peptide

3.1 Introduction

Optical spectroscopy has been enormously useful for exploring the energy levels and excitations of atomic systems at electron-volt energies. For understanding other kind of phenomena, if one would like information at milli-eV energies different form of spectroscopy become important. In this study we consider one spectroscopic methods know variously as electron paramagnetic resonance (EPR) or electron spin resonance (ESR). The technique depends on the fact that certain atomic systems have permanent magnetic moment. The link between theoretical predictive methodologies and ESR spectroscopy dates back to several decades, and it is due to a happy coincidence between experimental needs and available interpretative tools. On one side, the intrinsic resolution of the ESR spectra, together with the unique role played by paramagnetic probes in providing information about their environment, make in principle ESR one of the most powerful methods of investigation on the electron distribution in molecules, and on the properties of their environments. On the other side, ESR spectroscopy is intrinsically amenable to an advanced theoretical interpretation: the tools needed are

based on quantum chemistry, as far as the parameters of the spin Hamiltonian are concerned, and on statistical thermodynamics, for the spectral lineshapes. Nowadays, the introduction of the Density Functional Theory (DFT) has proved to be a turning point for the calculations of the spin Hamiltonian parameters [232],[233]. Reliable methods for the evaluation of hyperfine tensors are available for several cases and, particularly for radicals in solution, the agreement between experimental and calculated parameters of the spin Hamiltonian by DFT is outstanding [234],[235]. Moreover, because of its favorable time scale, ESR experiments can be highly sensitive to the details of the rotational and internal dynamics. In the so-called slow motional regime the spectral line shapes take on a complex form which is found to be sensitive to the microscopic details of the motional process. This is to be contrasted with the fast motional regime, where simple Lorentzian line shapes are observed, and only estimates of molecular parameters (e.g. diffusion tensor values) are obtained independently from the microscopic details of the molecular dynamics. The interpretation of slow motional spectra requires an analysis based upon sophisticated theory, and it is usually carried on via explicit modelization of the paramagnetic probe dynamics, as predicted for various Markovian models of reorientation. In order to extract useful dynamic information from ESR experiments, a slow motional theory based on the Stochastic Liouville Equation (SLE) has been developed, which shows that the more dramatic lineshape changes are particularly sensitive to microscopic details of the dynamics. The relationship between ESR spectroscopic measurements and molecular properties can be gathered only indirectly, that is, structural and dynamic molecular characteristics can only be inferred by the systematic application of modeling and numerical simulations to interpret experimental observables. A straightforward way to achieve this goal is the employment of spectroscopic evidence as the "target" of a fitting procedure of molecular, mesoscopic and macroscopic parameters entering the model. This strategy, based on the idea of a general fitting approach, can be very helpful in providing detailed characterization of structural parameters (e.g. intramolecular distances) and dissipative parameters (e.g. diffusion tensors). An intrinsic limitation of this approach is the difficulty of avoiding uncertainties due to multiple minima in the fitting procedure, and the difficulty, in many cases, to reconcile best-fitted parameters with more general approaches or

known physical trends (e.g. temperature dependence). A more refined methodology is based on an integrated computational strategy, i.e. the combination of (i) quantum mechanical (QM) calculations of structural parameters and magnetic tensors possibly including average interactions with the environment (by discrete-continuum solvent models) and short-time dynamical effects; (ii) direct feeding of calculated molecular parameters into dynamic models based on molecular dynamics, coarse grain dynamics, and, above all, stochastic modeling or a combination of the three. Fine-tuning of a limited set of molecular or mesoscopic parameters via limited fitting can still be employed. In particular, electron spin resonance measurements are highly informative and they are nowadays becoming particularly amenable to the integrated strategy, thanks to increasing experimental technological progress, advancement in computational methods, and refinement of available dynamics models. Nitroxide-derived paramagnetic probes allow in principle to detect several information contents at once: secondary structure information, inter-residual distances, if more than one spin probe is present, large amplitude protein motions from the overall ESR spectrum shape [236],[237],[238]. An *ab-initio* interpretation of ESR spectroscopy needs to take into account different aspects regarding the structural, dynamical and magnetic properties of the molecular system under investigation, and it requires, as input parameters, the known basic molecular information and solvent macroscopic parameters. The application of the stochastic Liouville equation formalism integrates the structural and dynamic ingredients to give directly the spectrum with minimal additional fitting procedures. In this method, the emphasis is on a relatively detailed treatment of the stochastic process, without, the restriction to fast motions. This equation is valid even for relatively slow random processes, and is therefore especially suitable for ESR, where the natural time scale is short so that the random processes are not usually fast on this time scale [239]. We apply this technique connected with an appropriate theoretical model to reproduce the ESR spectra of a small peptide. We want highlight the influence of the solvent on the magnetic properties.

3.2 A brief introduction to the ESR technique

Electron spin resonance spectroscopy deals with the interaction of electromagnetic radiation with the intrinsic magnetic moment of electrons arising from their spin. It is a sensitive method for probing the electronic and the molecular structure of paramagnetic sites because the energies of microwave induced transitions of unpaired electrons are modulated by interactions with nearby magnetic nuclei [240]. The phenomenon of electron ESR spectroscopy can be explained considering the behavior of a free electron. According with the quantum theory the electron has a spin which can be understood as an angular momentum leading to a magnetic moment. Consequently, the negative charge that the electron carries is also spinning and constitutes a circulating electric current. The circulating current induces a magnetic moment which, if the electron is subjected to a steady magnetic field, cause the electron to experience to torque tending to align the magnetic moment with the field. The energy of the system depends upon the projection of the spin vector along the magnetic field. Quantum theory stipulates that only two values are permitted for an electron, which means that the electron magnetic moment can only assume two projections onto the applied field. In the presence of a magnetic field the degenerate ground state splits according to the Zeeman Hamiltonian that depends on the external field, on the gyromagnetic tensor and projection of the spin vector. The energy levels of the magnetic system are influenced by surrounding atoms beside by the external magnetic field. For electrons bound into atoms, the ESR phenomena may not be observed at all, because electron spins pair off in atomic or molecular orbitals so that virtually no net spin magnetism is exhibited and the material is said to be diamagnetic. When an atom or molecule has an odd number of electrons, complete pairing is not possible and the material is said to be paramagnetic. In that case ESR can be observed. If the molecule contains nuclei with magnetic moment, such as protons, their interaction with the external field and the electronic magnetic moment will change the energy levels. This variation in energy is caused by the hyperfine coupling of the electron spin to nuclear spin I . Hyperfine interaction in the interaction between the magnetic moment of an electron with the magnetic moment of the nucleus in its vicinity. Nuclei individually associated with the

electron spin system often have a magnetic moment I which also has different allowed orientations $(2I + 1)$ in the magnetic field. The magnetic field associated with the nuclear moment can be add or subtract from the applied field experienced by the electron spin system associated with it. In the bulk sample some electrons will therefore be subject to an increased field and some to a reduce field. The hyperfine coupling constant varies with the nuclear species, and it is a measure of the strength of the interaction between the nuclear and the electronic spins. Its magnitude in a radical or radical ion reflects the extent of s character in its orbital because only the s -orbital has nonzero density at the nucleus. Two common mechanisms by which electrons and nuclei interact are Fermi-contact interaction and dipolar interaction. The former applies largely to the case of isotropic interactions (independent of sample orientation in a magnetic field) and the latter to the case of anisotropic interactions (spectra dependent on sample orientation in a magnetic field). For a large concentration of electronic spin, the electronic moments also interact appreciably with each other, and this can alter considerably the ESR spectra. The dipolar interaction induces a broadening of the resonance line, which increases with the concentration of dipole moments. The signal intensity in ESR depends on how much absorption of the microwave power takes place. This value will be the larger the greater is the difference between the populations of the two different electronic magnetic moment. The distribution follows the Boltzmann statistic.

ESR spectroscopy is used in various branches of science, such as chemistry and physics, for the detection and identification of free radicals and paramagnetic centers. ESR is a sensitive, specific method for studying both radicals formed in chemical reactions and the reactions themselves. Such radicals can be identified and studied by ESR. Organic and inorganic radicals can be detected in electrochemical systems and in materials exposed to UV light. In many cases, the reactions to make the radicals and the subsequent reactions of the radicals are of interest, while in other cases ESR is used to provide information on a radical's geometry and the orbital of the unpaired electron. Medical and biological applications of ESR also exist. Although radicals are very reactive, and so do not normally occur in high concentrations in biology, special reagents have been developed to spin-label molecules of interest. These

reagents are particularly useful in biological systems. Specially-designed nonreactive radical molecules can attach to specific sites in a biological cell, and ESR spectra can then give information on the environment of these so-called spin-label or spin-probes. ESR spectroscopy can only be applied to systems in which the balance between radical decay and radical formation keeps the free-radicals concentration above the detection limit of the spectrometer used. This can be a particularly severe problem in studying reactions in liquids. ESR also has been used by archaeologists for the dating of teeth. Radiation damage over long periods of time creates free radicals in tooth enamel, which can then be examined by ESR and, after proper calibration, dated.

3.3 *Ab-initio* modeling of a double spin labeled peptide in a polar solvent

Increasing the number of available experimental tools for determining secondary and tertiary structures of peptides and proteins is of fundamental importance. Nowadays, modern structural biology can count on sophisticated techniques such as NMR or X-ray crystallography which allow one to obtain the atomic resolution structure of peptides and proteins. However, a part of the structural information, such as conformational transitions, folding in real-time and, above all, detailed dynamic properties in solution, is still hardly accessible to these techniques. A promising approach to explore these aspects is the exploitation of the technique of site-directed spin labeling, SDSL [241],[242],[243],[244],[245],[246], combined with electron spin resonance (ESR) measurements, which often allows a resolution at the level of the peptide backbone fold [245]. Once incorporated the spin label into the protein, the ESR spectra and spin relaxation processes are dictated by molecular motion and local environment properties. Measurements of ESR spectroscopic observables can thus provide direct information on solvent accessibility, topography of the polypeptide chain [247], electrostatic potential at any surface site [248], dynamic of the side chain and the distance from an additional nitroxide [249]. The general strategy of SDSL requires the covalent attachment of a stable nitroxide free radical to a side-chain reactive amino acid (e.g. cysteine) at selected

sites in the polypeptide backbone. Several examples [250] of double or triple labeled proteins have been prepared by linking a nitroxide radical. More recently, in peptides the non-coded α -amino acid TOAC (2,2,6,6-tetramethylpiperidine-1-oxyl-4-amino-4-carboxylic acid) has been used, which acts as a rigidly attached spin label in any chosen position of the sequence [251],[252],[253]. TOAC is known to fold the peptide chain into a 3_{10} -(or α -) helical structure [254] because the piperidine ring is rigidly attached to the backbone quaternary -carbon [255]. In addition, it is stable under ordinary conditions, and provides a well-localized unpaired electron amenable to spectroscopic ESR signatures. TOAC belongs to the family of conformationally constrained, C^α -tetrasubstituted, α -amino acids, the prototype of which is α -aminoisobutyric acid (Aib)[256],[257]. Incorporating a member of this class of residues into the sequence allows a strict control of the peptide backbone conformation. In particular, peptides with two TOAC residues are used for obtaining, via ESR spectroscopy, structural parameters such as probe-probe distance, type of helical structure, coupling and dipolar interaction. Thus, TOAC double labeled systems allows to determine peptide geometry as a function of the solvent [258] and to distinguish between the strictly related 3_{10} - and α -helical structures [252],[253]. From the continuous wave electron spin resonance (CW-ESR) or electron-nuclear double resonance (ENDOR) spectra in SDSL it is possible to obtain both structural and dynamic information. If the motion of the labeled molecules is sufficiently fast, the structural information from the ESR spectrum is derived via simple fast-motional perturbative models, but in the so-called slow motion regime it is necessary to substantially improve the theoretical approach. This drawback is balanced by the obvious consideration that often slow motional regime spectra are highly informative since the spin relaxation system becomes intimately connected with the molecular motions. ESR spectroscopy in the slow-motional regime can be interpreted following the stochastic Liouville equation (SLE) developed by Freed and coworkers [259]. It has been shown recently that the SLE approach can be linked profitably with advanced density functional theory (DFT) evaluation of geometry and magnetic parameters of the radical in its environment [231]. Dissipative parameters, such as rotational diffusion tensors, can in turn be determined at a coarse-grained level using standard hydrodynamic arguments. The combination of the evaluation of struc-

tural properties based on quantum mechanical advanced methods with hydrodynamic modeling for dissipative properties, and, in the case of double labeled systems, determination of dipolar interaction based on the molecular structures beyond the point approximation, are the fundamental ingredients needed by the SLE to provide a fully integrated computational approach which gives the spectral profile in a truly *ab-initio* fashion. In this work we apply the integrated approach to interpret the CW-ESR spectra in acetonitrile (MeCN) of the double spin labeled peptide Fmoc-(Aib-Aib-TOAC)₂-Aib-OMe (**1**) (Fmoc, fluorenyl-9-methoxycarbonyl; OMe, methoxy), i.e. a heptapeptide characterized by two TOAC radicals at relative positions *i*, *i*+3 (Fig. 3-1). Terminally protected heptapeptides entirely formed by helicogenic C^α-tetrasubstituted

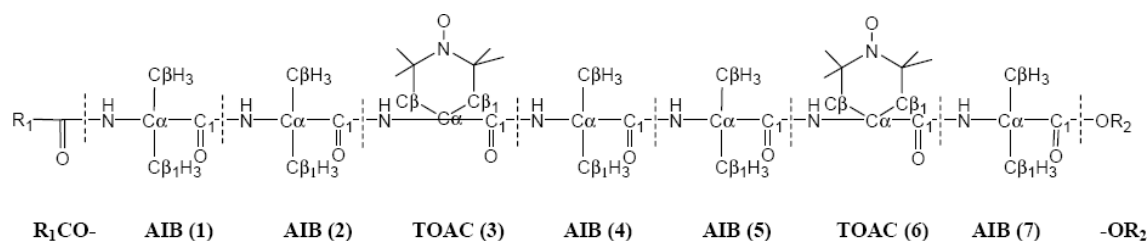


FIGURE 3-1: Chemical structure of Fmoc-(Aib-Aib-TOAC)₂-Aib-OMe (heptapeptide **1**).

α -amino acids, e.g. Aib and TOAC, are known to fold into a 3_{10} -helical structure of relevant stability [255],[256],[257]. Acetonitrile was chosen because of the low tendency to aggregation of the heptapeptide in this solvent at the concentration used for our experiments.

3.3.1 Peptide Synthesis, X-ray Diffraction and ESR Characterization

Peptide Synthesis

Heptapeptide **1** was synthesized step-by-step in solution using either the symmetrical anhydride method for the formation of the Aib-Aib bonds or the 1-(3-dimethylamino)propyl-3-ethylcarbodiimide/1-hydroxy-7-aza-1,2,3-benzotriazole method [260] for the formation of the TOAC-Aib and Aib-TOAC bonds. The chromatographically pure compound has a melting point of 171-173 °C (from ethyl acetate-petroleum ether); IR

(KBr) 3312, 1739, 1728, 1697, 1662, 1529 cm^{-1} ; mass spectrometry (ESI-TOF) $[\text{M}+\text{H}]^+$ 1074.6269 for a calculated molecular weight of 1073.6161.

X-ray Diffraction

Single crystals of heptapeptide **1** were grown by slow evaporation from a TFE (2,2,2-trifluoroethanol) solution. The asymmetric unit is composed of one peptide molecule and two co-crystallized TFE molecules. Formula $\text{C}_{60}\text{H}_{89}\text{F}_6\text{N}_9\text{O}_{14}$, $M = 1274.40$, monoclinic, space group $\text{P}2_1/c$, unit cell dimensions $a = 18.813(3) \text{ \AA}$, $b = 17.134(3) \text{ \AA}$, $c = 22.355(4) \text{ \AA}$, $\beta = 104.37(7)^\circ$; $V = 6981(2) \text{ \AA}^3$, $Z = 4$; $d_{\text{calc}} = 1.213 \text{ g cm}^{-3}$. Crystal size and color: $0.40 \times 0.20 \times 0.05 \text{ mm}^3$, orange. Absorption coefficient ($\text{CuK}\alpha$) = 0.817 mm^{-1} . Intensity data were collected at room temperature with $\text{CuK}\alpha$ radiation ($\lambda = 1.54178 \text{ \AA}$) using a Philips PW 1100 diffractometer in the $\theta - 2\theta$ scan mode up to $\theta = 54.2^\circ$ (0.95 \AA resolution). The crystal did not significantly diffract at higher resolution. The structure was solved by direct methods with the SIR 2002 program.³⁰ Refinement was carried out by least-squares procedures on F^2 , using all data, by application of the SHELXL 97 program. All non-hydrogen atoms were refined anisotropically. Restraints were applied to the anisotropic displacement parameters of the atoms of the two co-crystallized solvent molecules. Hydrogen atoms were calculated at idealized positions and refined using a riding model. The final R indices were $R_1 = 0.0890$, $wR_2 = 0.2241$ [$I > 2\sigma(I)$] and $R_1 = 0.1142$, $wR_2 = 0.2672$ (all data). Data / restraints / parameters: 8491 / 72 / 779. Goodness of fit on F^2 : 1.140. The largest peak and hole in the final difference Fourier map were 0.81 and -0.41 e \AA^{-3} , respectively. Crystallographic data (including atomic coordinates, bond distances, bond angles, torsion angles, intra- and intermolecular H-bonds parameters) may be found in the Supporting Information as a CIF file.

ESR Characterization

The X-band ESR spectra were recorded using an X-band (9.5 GHz) Bruker ER200D spectrometer. Temperature control was achieved using a Bruker BVT2000 nitrogen-flow system. For the ESR measurements a 10^{-4} M solution of the heptapeptide **1** in MeCN was prepared and put into ESR quartz tubes of 1 mm inner diameter. The

solution in the tubes was carefully degassed in a vacuum line by several pump-freeze-thaw cycles and finally sealed off. The high temperature (330 K) ESR spectrum of heptapeptide **1** in MeCN consists of five lines deriving from the hyperfine coupling of the unpaired electrons with two ^{14}N nuclei, as expected for a bis-nitroxide with an exchange interaction larger than the ^{14}N hyperfine coupling. The relative peak-to-peak intensities of the hyperfine components deviate from the 1:2:3:2:1 ratios corresponding to the degeneracy of the transitions for a two $I=1$ nuclear spins system. In particular, the heights of the second and fourth lines are lower. By lowering the temperature, the overall spectrum broadens and the variation in heights becomes more pronounced. A similar behavior was observed using other solvents, e.g. toluene and methanol.

3.3.2 The Stochastic Liouville Equation

The calculation of ESR observables can be in principle based on the complete solution of the Schrödinger equation for the system made of paramagnetic probe and explicit solvent molecules. The system can be described by a "complete" Hamiltonian which contains (i) electronic coordinates of the paramagnetic probe, (ii) nuclear coordinates and (iii) all degrees of freedom of all solvent molecules. The basic object of study, to which any spectroscopic observable can be linked, is given by the density matrix, which in turn is obtained from the Liouville equation. The integrated approach to modeling requires to take into account different aspects regarding the structural, dynamical and magnetic properties of the molecular system under investigation. All these aspects are taken into account by an integrated computational approach which requires, as input parameters, the known basic molecular information and solvent macroscopic parameters. The first important point for the develop of a model for the interpretation of the ESR spectra concerns the molecular motion and consequently the choice for the description of the spatial probability density that is connected with the equilibrium situation. In general we assumed that the important molecular motions are diffusive, rotational and Markovian. The last condition means that for every molecule the possibility to the orientation Ω_i , at time t_i depends only by the orientation Ω_{i-1} at time t_{i-1} . In this condition the time evolution of the rotational probability density, the Smoluchowski equation, for a generic stochastic process \mathbf{q} containing different rotational degrees of

freedom can be expressed as

$$\frac{\partial}{\partial t}P(\mathbf{q}, t) = -\hat{\Gamma}P(\mathbf{q}, t) \quad (3.1)$$

where $P(\mathbf{q}, t)$ is the probability density dependent on time for a stochastic process \mathbf{q} and $\hat{\Gamma}$ is the diffusive operator. The evolution of the probability density permits to obtain an equilibrium situation. We assume that the stationary state is obtained by the Boltzmann distribution.

$$P_{eq}(\mathbf{q}) = \frac{\exp[-V(\mathbf{q})/k_B T]}{\langle \exp[-V(\mathbf{q})/k_B T] \rangle} \quad (3.2)$$

where k_B is the Boltzmann constant, T is the temperature and V is a generic potential connected with the stochastic coordinates. With $\langle \dots \rangle$ we describe the integral over the stochastic coordinates \mathbf{q} . After the spatial part is necessary to define the magnetic part and the influence of the rotational motion on the magnetic part. For a *continuous wave electron spin resonance* (CW-ESR) the magnetic spin Hamiltonian \hat{H} for the particular case of two interacting paramagnetic residues includes Zeeman, hyperfine, exchange and dipolar interaction. It is possible to define the probability density spin operator and the time evolution of this operator is:

$$\frac{\partial \rho(t)}{\partial t} = -i [\hat{\Gamma}(t), \rho(t)] \quad (3.3)$$

The spin relaxation is caused by the motions in the chemical surrounding that influence the spin Hamiltonian. Solving for the density matrix allow in principle the direct evaluation of any molecular properties. However significant approximations are possible, which are basically rooted in time-scale separation arguments. The nuclear coordinates can be separated into fast probe vibrational coordinates and slow probe coordinates. Then the probe Hamiltonian is average on (i) femtoseconds and sub-picoseconds dynamics, pertaining to probe electronic coordinates and (ii) picoseconds dynamics, pertaining to probe internal vibrational degrees of freedom. The averaging on the electron coordinates is the usual implicit procedure for obtaining a spin Hamiltonian for the complete Hamiltonian of the radical. In the frame of Born-Oppenheimer approximation, the averaging on the picosecond dynamics of the nuclear coordinates allow to introduce in the calculation of magnetic parameters the effect of the vibrational motions. The modified time evolution equation for the density matrix can be efficiently

be interpreted within the framework of explicit stochastic modeling according to the the Stochastic Liouville Equation (SLE) that permits to coupled the coordinates describe with classical methods (rotational coordinates) with the quantistic coordinates (spin coordinates). The final application of SLE integrates the structural and dynamic ingredients to give directly the spectrum with minimal additional fitting procedures. We summarize the modeling approach as follows. Simulation of the ESR spectra is based on the implementation of the SLE which was introduced by Freed and coworkers [259],[261],[262]. If with \mathbf{Q} we consider the stochastic rotational and spin coordinates the SLE is defined as

$$\begin{aligned}\frac{\partial \rho(\mathbf{Q}, t)}{\partial t} &= -i \left[\hat{H}(\mathbf{Q}), \rho(\mathbf{Q}, t) \right] - \hat{\Gamma}(\mathbf{Q})\rho(\mathbf{Q}, t) \\ &= -i \left[\hat{H}^\times(\mathbf{Q}), \rho(\mathbf{Q}, t) \right] - \hat{\Gamma}(\mathbf{Q})\rho(\mathbf{Q}, t) = -\hat{L}(\mathbf{Q})\rho(\mathbf{Q}, t)\end{aligned}\quad (3.4)$$

describing the time evolution of the density matrix of the system, depending upon general stochastic coordinates \mathbf{Q} , controlled by the stochastic operator $\hat{\Gamma}$. Here \hat{H}^\times is the quantum Liouville operator, i.e. the commutator superoperator defined with respect to \hat{H} [259], the magnetic Hamiltonian of the system which includes Zeeman, hyperfine, exchange and dipolar interaction for the two TOAC residues:

$$\hat{H} = \frac{\beta_e}{\hbar} \sum_i \vec{B}_0 \cdot \mathbf{g}_i \cdot \hat{S}_i + \gamma_e \sum_i \hat{I}_i \cdot \mathbf{A}_i \cdot \hat{S}_i - 2\gamma_e J \hat{S}_1 \cdot \hat{S}_2 + \hat{S}_1 \cdot \mathbf{T} \cdot \hat{S}_2 \quad (3.5)$$

where the first term is the Zeeman interaction of each electron spin with magnetic field \vec{B}_0 , depending on the \mathbf{g}_i tensor; the second term is the hyperfine interaction of each ^{14}N / unpaired electron, defined with respect to hyperfine tensor \mathbf{A}_i ; the third and fourth term are the electron exchange and spin-spin dipolar terms, respectively. Here tensors \mathbf{g}_i , \mathbf{A}_i are diagonal in the same local frame $T_i\text{F}$ rigidly fixed on the i -th nitroxide; operators \hat{I}_i and \hat{S}_i are defined in the laboratory or inertial frame (LF). The system geometry is summarized in Fig. 3-2. The relative orientation of the molecular frame (MF), fixed rigidly on the peptide, with respect to the LF is described by the set of Euler angles Ω , while the local frames $T_i\text{F}$ are in turn defined with respect to MF by a set of angles Ω_i . The evaluation of all the magnetic tensors (which is not trivial for a system of the dimensions of the peptide under study in solution) is described in the

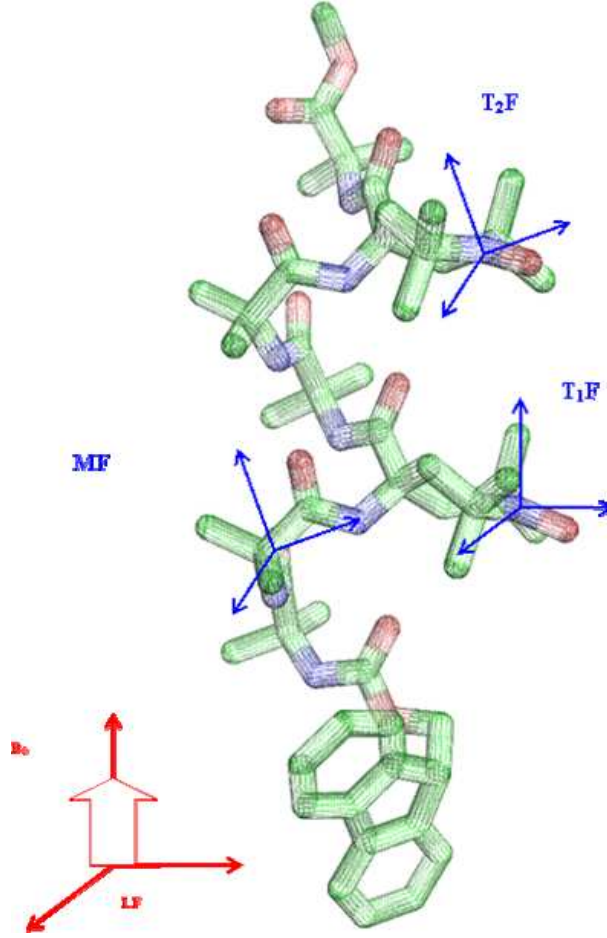


FIGURE 3-2: Reference frame employed in the Stochastic Liouville Equation (SLE).

next section. In general, several relaxation processes can be invoked, corresponding to different fast and slow degrees of freedom subject to Brownian motions and described by many-body Fokker-Planck operators. Here we adopt the simplest choice of considering as only relevant variables the orientation of MF in the LF, i.e. the Euler angles set, $Q=\Omega$. We shall also assume that the system reorients freely in space, subject to a simple diffusive motional regime, i.e.

$$\hat{\Gamma} = D_x \hat{J}_x^2 + D_y \hat{J}_y^2 + D_z \hat{J}_z^2 \quad (3.6)$$

where \hat{J}_i is the i -th component of the angular momentum operator in the molecular frame. Evaluation of the diffusion tensor principal values can be carried on based on a simple but effective hydrodynamic approach, which is summarized in a specific

section. The dependence of the superhamiltonian $i\hat{H}^\times$ from magnetic and orientational parameters is expressed in a spherical irreducible tensorial representation [259],[261]

$$\hat{H}^\times = \sum_{\mu} \sum_{l=0,2} \sum_{m,m'=-l}^l D_{mm'}^l(\Omega) F_{\mu,MF}^{(l,m')*} \hat{A}_{\mu,LF}^{(l,m)} \quad (3.7)$$

where μ runs over all possible interactions, $D_{mm'}^l(\Omega)$ is a generic Wigner matrix, $F_{\mu,MF}^{(l,m')*}$ is built from elements of \mathbf{g}_i , \mathbf{A}_i , J , and \mathbf{D} in the MF, is obtained from spin operators. The ESR spectrum is obtained as the Fourier-Laplace transform of the correlation function for the x -component of the magnetization, defined as $|v\rangle = (2I+1)^{-1}(|\hat{S}_{x,1}\rangle + |\hat{S}_{x,2}\rangle)$, where I is the nuclear spin. Following standard definitions [261] we obtain

$$G(\omega - \omega_0) = \frac{1}{\pi} \text{Re} \{ \langle v | [i(\omega - \omega_0) + (i\hat{H}^\times + \hat{\Gamma})]^{-1} | v P_{eq} \rangle \} \quad (3.8)$$

where $P_{eq} = 1/8\pi^2$ is the (isotropic) distribution in the space. Here ω is the sweep frequency, and $\omega_0 = g_0\beta_e B_0/\hbar = \gamma_e B_0$, and g_0 is the trace of each \mathbf{g}_i tensor divided by three, which is the same for the two electrons. The starting vector $|v\rangle$ is related to the allowed ESR transitions, and it is actually an operator acting on the electron spin degrees of freedom [261]. To summarize, the peptide is described as a diffusive rotor and the two TOAC probes are rigidly fixed. Parameters are the principal values of the diffusion tensor D_x , D_y , D_z ; principal values of \mathbf{g} and \mathbf{A} tensors, and Euler angles Ω_i specifying the orientation of magnetic local tensors with respect to MF; the exchange interaction J and the dipolar tensor \mathbf{T} .

3.3.3 Magnetic tensor

Usually, the spin-spin dipolar term is calculated by assuming that the two electrons are localized and placed at the center of the $N - O$ bond of the two TOAC residues. In this view, the two electrons are considered just as two point magnetic dipoles and the interaction term depends on the distance between the two localized electrons:

$$\mathbf{T} = \frac{\mu_0 g_e^2 \beta_e^2}{4\pi \hbar r^3} \left[\mathbf{1}_3 - \frac{3}{r^2} \begin{pmatrix} r_x^2 & r_x r_y & r_x r_z \\ r_y r_x & r_y^2 & r_y r_z \\ r_z r_x & r_z r_y & r_z^2 \end{pmatrix} \right] \quad (3.9)$$

where r is the distance between the two localized electrons, that is the distance between the centers of the N-O bonds of the two TOAC nitroxides. Obviously, this is only an approximation because the electrons are not fixed in one point of space but delocalized in a molecular orbital. A complete quantum mechanical computation starting from the computed spin density is available for small systems [280], but it is still lacking for large molecules. The dipolar tensor can be calculated as

$$\mathbf{T} = N^2 \langle \Psi'(1)\Psi''(2) - \Psi'(2)\Psi''(1) | \hat{\mathbf{T}} | \Psi'(1)\Psi''(2) - \Psi'(2)\Psi''(1) \rangle \quad (3.10)$$

where $\hat{\mathbf{T}}$ is the tensorial operator and its components are

$$\hat{T}_{\alpha,\beta} = \frac{r_{12}^2 \delta_{\alpha,\beta} - 3(\mathbf{r}_{12})_{\alpha}(\mathbf{r}_{12})_{\beta}}{r_{12}^5} \quad (3.11)$$

where $r_{12} = |\mathbf{r}_{12}| = |\mathbf{r}_1 - \mathbf{r}_2|$, is the vector between the two electrons, $\alpha, \beta = X, Y, Z$ and $(\mathbf{r}_{12})_{\alpha}$ is the component along of vector \mathbf{r}_{12} . The normalization constant can be found as $N = [2(1 - |S|^2)]^{-1/2}$ where $S = \langle \Psi' | \Psi'' \rangle$. The molecular orbitals are built

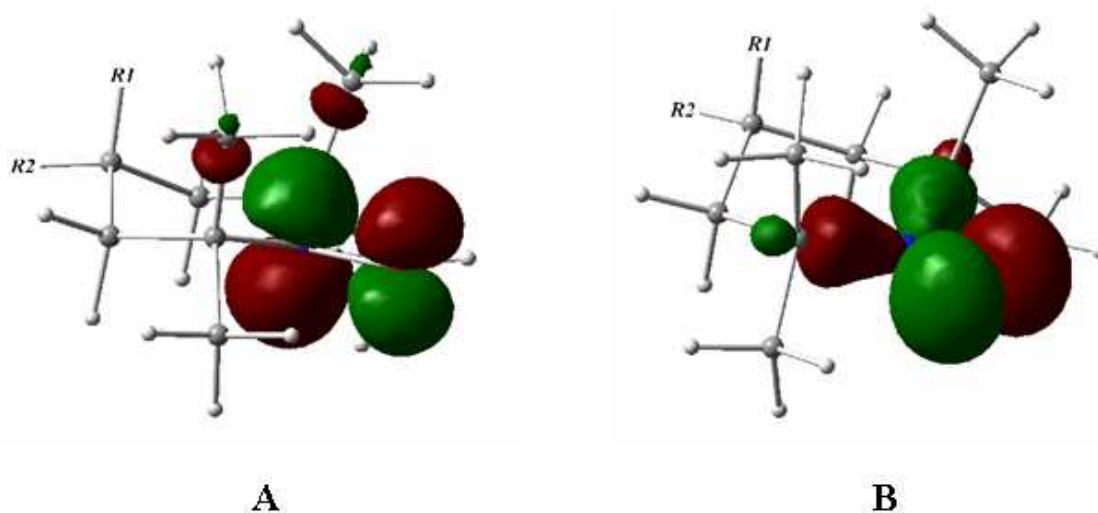


FIGURE 3-3: View of the π^* orbital containing the unpaired electron of TOAC radical. In particular we show a sketch of SOMO (A) and SOMO-1 (B) of TOAC (R1=-COOH, R2=-NH2).

starting from atomic orbitals that in general can be written as the linear combination $\Psi = N \sum_k c_k \phi_k$. In our case we resorted to the following computational strategy based on the well known localization of nitroxide SOMOs (π^* orbitals) on the NO moiety (Fig.

3-3)[269]. This strong localization suggests that, for not too short distances between NO moieties, a reliable approximation would be to fit the SOMO electron density by linear combinations (with equal contributions) of effective $2p_z$ atomic orbitals of nitrogen and oxygen [269],[281]:

$$\begin{aligned}\Psi' &= N' [\phi_{210}^{N_1}(\mathbf{r} - \mathbf{R}_{N_1}) - \phi_{210}^{O_1}(\mathbf{r} - \mathbf{R}_{O_1})] \\ \Psi'' &= N'' [\phi_{210}^{N_2}(\mathbf{r} - \mathbf{R}_{N_2}) - \phi_{210}^{O_2}(\mathbf{r} - \mathbf{R}_{O_2})]\end{aligned}\quad (3.12)$$

where Ψ' and Ψ'' are the molecular orbitals containing the electrons. Next we represent

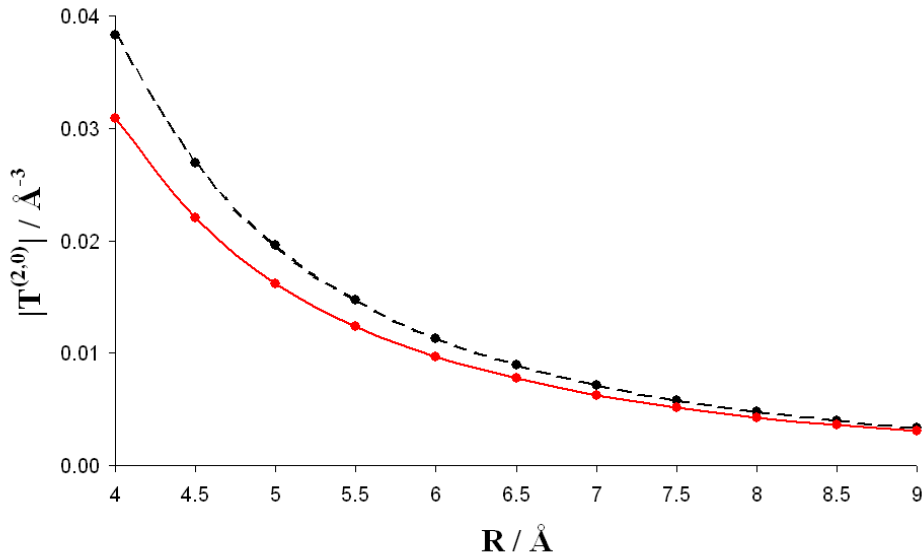


FIGURE 3-4: Trend in $|T^{(2,0)}|$ versus distance calculated with the approximated expression (dash line) and the exact treatment (solid line).

the AO's by Slater type orbitals (STO's) of the form $\phi_{210}(\mathbf{r}) = \sqrt{4/3}\alpha^5 r e^{-\alpha r} Y_{1,0}(\theta, \varphi)$ where $\alpha = Z_{eff}/2$ Hartree⁻¹ and Z_{eff} is the effective nuclear charge; standard Clementi-Raimondi values of $Z_{eff} = 3.83$ for nitrogen and $Z_{eff} = 4.45$ for oxygen were used. The dipolar tensor is calculated in the frame such that the z -axis is chosen to be parallel to the vector that pass through the centers of the two $N - O$ bonds, the x -axis is parallel to the $N - O$ bonds and the origin of the frame is placed in the middle point between the four atoms. The molecular geometry allows us to conclude that only the $T^{(2,0)}$ component contributes significantly to the dipolar tensor. Fig. 3-4 shows the trend

of $|T^{(2,0)}|$ (which is proportional to T_{ZZ} in Cartesian coordinates) versus the distance between the two TOAC nitroxides changes. As expected, at high distances the point approximation converges to the exact approach, while increasing differences are found when the distance is less than about 7 Å. A complete calculation of the magnetic tensor is reported in Appendix C.

3.3.4 Structure and diffusion properties

The optimized structure of heptapeptide **1** is obtained by DFT calculations [263],[264],[265],[266],[267] in a solvated environment (PCM). The hybrid counterpart PBE0 of the conventional functional PBE with the standard 6-31G(d) basis set is employed. The DFT

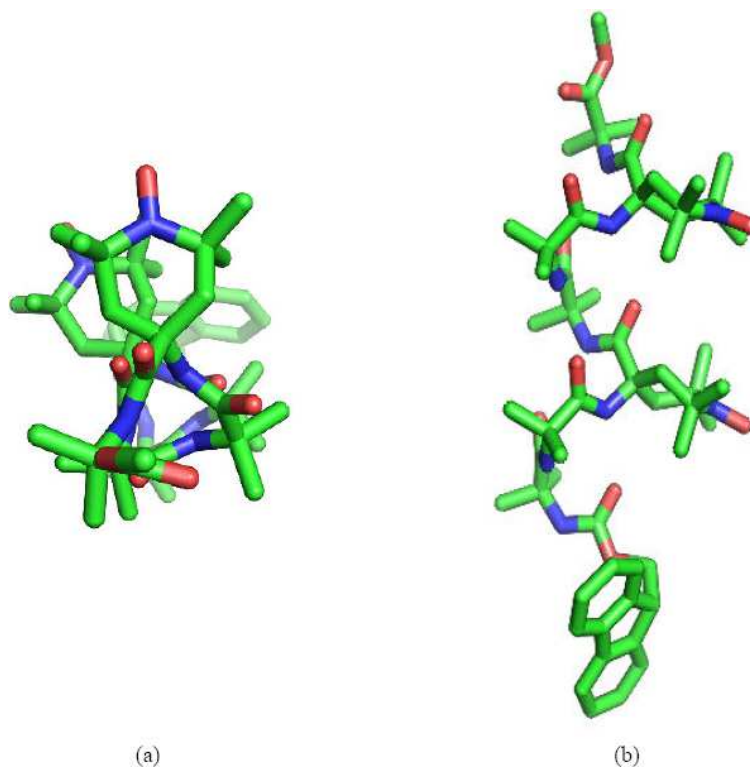


FIGURE 3-5: Optimize structure of heptapeptide **1**: (a) View along the helix axis (b) View orthogonal to the helix axis.

calculation provides four low-energy structures, as shown in Table 3.1, characterized by a backbone arranged into a 3_{10} -helix and different conformations and orientations for the rigid nitroxide (TOAC). The TOAC rigid side chain adopt different conformations:

boat conformation with axial placement of the α -amino group (dd), boat conformation with equatorial placement of the α -amino group (uu); different twist conformations (t_1t_1 and t_2t_2). We selected for further computations the conformer with the minimum

Structure	ΔE
t_1t_1	0.0
dd	2.0
t_2t_2	2.9
uu	6.1

TABLE 3.1: Relative stabilities (ΔE in kcal/mol) of the low-energy peptide conformations obtained by PBE0/6-31G* full geometry optimization.

relative energy, in which both TOAC residues are arranged in a twist structure [268] (Figure 3-5). Hyperfine and \mathbf{g} tensors have been computed by the same functional using the N06 basis set. While dipolar hyperfine terms and \mathbf{g} tensors are negligibly affected by local vibrational averaging effects, this is not the case for the isotropic hyperfine term especially concerning those large amplitude vibrations (here, out-of-plane bending) which modify hybridization at the radical center. As a consequence, vibrational averaging from the out-of-plane motion of the NO moiety has been evaluated using the general procedure for one-dimensional large amplitude motions developed and applied with remarkable success to a number of radicals [269]. The final values of the tensors are shown in Table 3.2. Despite ongoing progress,[269],[270],[271],[272] the quantitative agreement between computed and experimental values is not always sufficient for a fully satisfactory fitting of the spectrum, especially concerning isotropic hyperfine splitting (1/3 of the trace of the corresponding hyperfine tensors) [273],[274],[275]. In the present context, we allowed an adjustment of this term by ± 0.5 Gauss from the computed value in the simulation of the ESR spectrum. All these magnetic terms are local in nature, so that they are scarcely dependent on conformational modifications (e.g. passage from the 3_{10} - to the α -helix), unless they are accompanied by local effects (e.g. hydrogen bonds involving the nitroxide moieties or deformation of TOAC rings) [266]. The other magnetic terms (J and spin-spin dipolar interaction) have a long-range character and provide a signature of different helical structures. Although the computation of J is, in principle, quite straightforward by e.g. the so called broken symmetry approach [276],[277], currently available density functionals are not sufficiently reliable

Parameter	Value	Source
r_{12}	6.6 Å	PBE0/6-31G*
J	300 G	ref.[250]
\mathbf{D}	see text	hydrodynamic model
\mathbf{T}	see text	point dipole or QM
\mathbf{g}	2.009, 2.006, 2.003	PBE0/N06
\mathbf{A}	4.7, 4.8, 32.6 G	PBE0/N06

TABLE 3.2: Summary of the parameters employed in the simulations of the ESR spectra.

for the distances characterizing the system under investigation (7 Å) [278],[279]. While work is in progress in our laboratory to this end, we prefer to use an experimental estimate of J , also taking into account that the spectral patterns are rather insensitive to reasonable choices of this parameter. The evaluation of the *diffusion properties* of $\mathbf{1}$ was based on a hydrodynamic approach. As describe in the Chapter II the molecule is seen as an ensemble of N fragments, each constituted by a sphere (extended atom) representing atoms or group of atoms and immersed in a homogeneous isotropic fluid of known viscosity. By assuming a form for the friction tensor of non-constrained extended atoms, ξ , one can calculate the friction for the constrained atoms, Ξ . We may assume for simplicity the simplest model for non-interacting spheres in a fluid, namely that matrix ξ has only diagonal blocks of the form $\xi(T)\mathbf{1}_3$ where $\xi(T)$ is the translational friction of a sphere of radius R_0 at temperature T and given by the Stokes law $\xi(T) = CR\eta(T)\pi$, where $\eta(T)$ is the solvent viscosity at the given temperature T and C depends on hydrodynamic boundary conditions. The system friction is then given as $\Xi = \xi(T)\mathbf{B}^{tr}\mathbf{B}$, with \mathbf{B} a matrix depending on the molecular geometry. The diffusion tensor (which can be conveniently partitioned in translation, rotational, internal and mixed blocks) can now be obtained as the inverse of the friction tensor as in equation 2.13 and neglecting off-diagonal couplings, an estimate of the rotational diffusion tensor is given by $\mathbf{D}_{RR} \equiv \mathbf{D}$, which depends directly from the atomic coordinates, temperature, and the solvent viscosity. In our case we considered the peptide as a rigid body, i.e. without internal degrees of freedom, so the diffusion tensor becomes a 6×6 tensor made up by the translational, rotational and roto-translational part. Figure 3-6 summarizes how the molecule is sketched by this model, that is as a group of spheres rigidly attached constituting a unique body free to reorient in the isotropic medium.

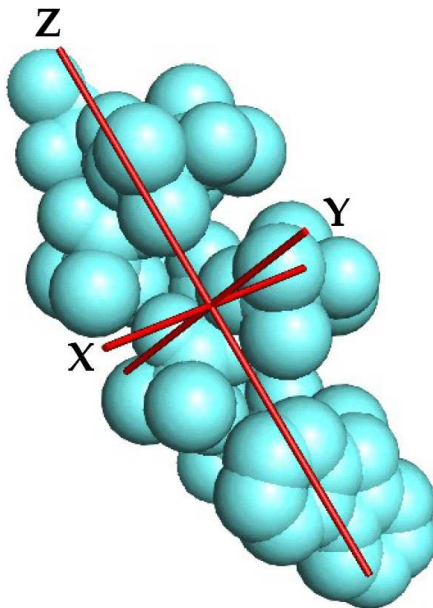


FIGURE 3-6: Representation of heptapeptide **1** used in the hydrodynamic model for the calculation of the diffusion tensor.

Size and shape of this body are related not only on the shape of the molecule, but also on the choice of the effective hydrodynamic radius associated with the extended atoms. We can write the diffusional tensor (already diagonalized in the MF) in the form $\mathbf{D}(T) = D(T)\mathbf{d}$ where $D(T) = k_B T / \xi(T)$ is the translational diffusional coefficient of a sphere of radius R at temperature T , and \mathbf{d} is a diagonal tensor depending only on the molecular geometry, with values $d_{XX} = 1.71 \times 10^{16}$, $d_{YY} = 1.83 \times 10^{16}$ and $d_{ZZ} = 5.75 \times 10^{16} \text{ m}^{-2}$. It is convenient to refer the temperature dependence to a standard state by defining $D(T) = D(T_0)\eta(T_0)/\eta(T)T/T_0$, where $D(T_0) = k_B/RC\pi T_0/\eta(T_0)$ is the translational diffusion coefficient for a sphere of radius R at reference temperature T_0 . The radius R was estimated to be 0.558 \AA , while constant C was chosen to be equal to 4 (for slip boundary conditions). We took as reference temperature [278] T_0 for which $\eta(T_0) = 260 \text{ \mu Pa s}$: the resulting value for $D(T_0)$ is $1.239 \times 10^{-8} \text{ m}^2 \text{ s}^{-1}$.

3.3.5 Results

Simulation of the ESR spectra requires the employment of a suite of integrated programs, each of them able to predict different parameters of the system under inves-

tigation: (i) DFT calculations are the basis of the entire simulation protocol because they provide all information that enter, as subsequent input, all of the remaining program codes. the final step (iv). The main information obtained from the DFT study are relative to structural properties of the molecule [266]. (ii) The calculation of the diffusion tensor is based on the geometry obtained from quantum mechanical (QM) calculations and the hydrodynamic model. Electronic information obtained from step (i) is fed to the dipolar interaction tensor evaluation procedure (iii). All data from (i)-(iii) enter, as input parameters, the program that calculates the ESR spectra based on the SLE which is the last effective step (iv). Table 3.2 summarizes all parameters

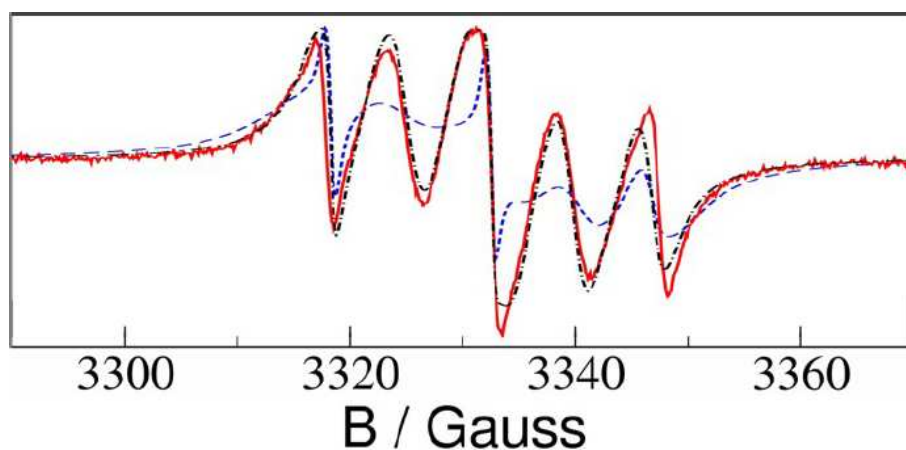


FIGURE 3-7: Comparison of the CW-ESR experimental spectrum of heptapeptide **1** (black line) at 310 K and the calculated spectra in the optimized 3_{10} -helix conformation (red line) and in a hypothetical α -helix structure (blue line).

employed in As an attempt to test the predictive power of our approach we performed a pure computational experiment by simulating the CW-ESR spectrum of heptapeptide **1** at a given temperature in the optimized 3_{10} -helix structure, employing the original parameters summarized in Table 3.2, without any adjustment. Next, we repeated the spectrum calculation employing a plausible α -helix conformation of the heptapeptide under the hypothesis that: (i) as an α -helix has more amino acids per turn (3.6) than a 3_{10} -helix (3.2)[254], it would appear shorter along the principal axis and "fatter" in the perpendicular direction, and (ii) in the α -helix the distance between the two TOAC nitroxide nitrogens at relative positions $i, i + 3$ would be higher than in the 3_{10} -helix (7.7 Å *versus* 6.9 Å)[253]. In Figure 3-7 the two simulated spectra, one of the real sys-

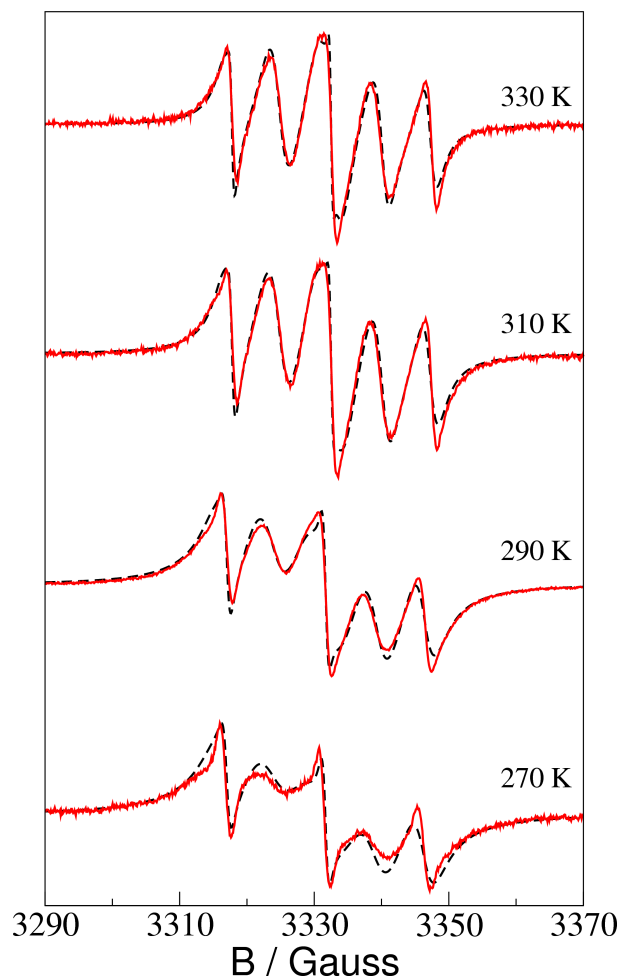


FIGURE 3-8: Experimental (solid line) and theoretical (dashed line) CW-ESR spectra of heptapeptide **1** in MeCN at temperatures 330, 310, 290 and 270 K.

tem at 310 K, the other of the "virtual" α -helical molecule at the same temperature, are shown together with the experimental spectrum. As the two simulated spectra are significantly different, it is clear that this computational experiment represents a strong indication of the sensitivity of our simulation procedure, which is able to discriminate between different helix conformations without employing any adjustable parameter, i.e. by predicting the spectrum solely based on the 3D-structure. Finally, we simulated and compared the spectra of the peptide dissolved in MeCN in the temperature range 270 K to 330 K. Figure 3-8 shows four theoretical spectra and their relative experimental counterparts. Two assumptions have been made. First, it was assumed the presence of a monoradical impurity that might arise from the reduction of one of the two nitroxide

functions. The estimated amount of the impurity is 2 %, a low but still appreciable percentage. Second, we allowed for a limited adjustment δA of the scalar component, $Tr(\mathbf{A})/3$, of the theoretical hyperfine tensor \mathbf{A} . The best agreement is obtained for $\delta A=0.3$ Gauss, which is well within the estimated uncertainty of 0.5 Gauss. The overall agreement between the theoretical and experimental CW-ESR spectra, in the considered range of temperature, is good. Only at the lowest temperature examined (270 K), the set of parameters employed in the simulations seems to be slightly less effective. It should be stressed that no internal dynamics model has been employed to describe collective motions in heptapeptide **1**, which has been treated, according to Eq. 3.6, as a simple Brownian rotator, with diffusive properties predicted only on the basis of fixed molecular shape and solvent viscosity. Nevertheless, a reasonable prediction of the change in linewidth and change of intensity is observed in the whole range of temperature considered, thus confirming that the molecular structure is essentially rigid in solution.

3.4 Unraveling solvent-driven equilibria between α and 3_{10} helices through an integrated computational approach

A better understanding of the properties and function of complex systems requires integrated strategies in which well defined models are investigated by both experimental and theoretical approaches. In the specific field of proteins, it is well recognized that polypeptides represent suitable models for a number of properties, and several experimental techniques have been systematically applied to their study. Unfortunately, interpretation of experimental results is not without ambiguities either because of the role of different environmental effects (e.g. crystal state for X-ray diffraction) or because the relationship between spectroscopic and structural/dynamics characteristics is only indirect. Here, theoretical approaches come into play provided that they are able to couple reliability and feasibility for large systems. Until quite recently, quantum mechanical (QM) computations of biomolecules were essentially restricted to the structural char-

acteristics of relatively small models in the gas phase. However, the development of powerful methods integrating the most recent models rooted into the density functional theory (DFT)[282] and discrete-continuum descriptions of solvent effects,[283] is paving the route toward the description of more realistic systems in their natural (aqueous) environment [284],[285],[286]. Direct comparison with experimental results then calls for the concomitant computation of reliable structural and spectroscopic parameters taking dynamical effects into the proper account [287],[288],[289],[138]. Although this is, in general, a quite ambitious long-term target, under some favorable circumstances we can already obtain remarkable results. In the particular case of electron spin resonance (ESR) spectroscopy, we have recently shown that proper use of different time scales can allow the complete a priori simulation of experimental spectra [231]. In particular, a new general computational approach combining QM calculations of structures and magnetic tensors with the treatment of rotational diffusion in solution by the Stochastic Liouville Equation (SLE) approach, leads to remarkable agreement between experimental and computed spectra for a number of test cases [290],[291]. Extension and validation of this approach to labeled biomolecules would then provide access to information of unprecedented richness and reliability by combining experimental and computational methodologies. Since peptides are well recognized models for studying stability and folding of helical regions of proteins, we decided to tackle the complete task of characterizing the solvent-driven equilibrium between different helical forms of a nitroxide doubly labeled peptide by characterizing at the same time its 3D-structure and complete ESR spectrum in different solvents and at different temperatures. It should be pointed out that the ESR spectral features do not depend only on the distance between the labels, but also on the relative orientations of the principal axes of the electron dipolar interaction tensor, the nitroxide label **A** tensor, the ^{14}N hyperfine tensors, and the diffusion tensor. Thus, agreement between experimental spectra and their counterparts issuing from QM structures and magnetic tensors through solution of the SLE represents a convincing demonstration of the correctness of the predicted structure. This approach is particularly interesting when different peptide conformations with slightly diverging energies (like e.g. 3_{10} - and α -helices) are available and the peptide can predominantly fold in one of them biased by a temperature and/or solvent

characteristics [292]. In the last decades, double spin labeling of peptides and proteins by stable nitroxide radicals has provided remarkable information: in particular, continuous wave (CW) and pulse [e.g. double quantum coherence (DQC) and PELDOR] ESR spectra of double spin labeled systems have been studied [246],[293],[294]. The sensitivity of DQC and PELDOR [295],[296] spectra allows the reliable determination of distances between labels in the range 1.6-6.0 nm in frozen solution, whereas shorter distances are not accessible because the electron dipolar interaction becomes too large and the presence of relevant scalar electron exchange interactions prevents the irradiation of a single electron spin, which is the prerequisite for their application [297]. On the other hand, when the spin labels are at short distances, the liquid solution CW-ESR spectrum could be very informative because its shape depends on several structural and dynamic parameters which characterize the double labeled peptide. We present the results of a CW-ESR investigation of the double spin labeled, terminally protected, (**1**) which is characterized by the presence of two TOAC nitroxide free radicals at relative positions i , $i + 3$ (Figure 3-1) in different solvents and at several temperatures. Aib [256],[257],[277] and TOAC [255],[298] are two strongly helicogenic, C $^{\alpha}$ -tetrasubstituted, α -aminoacids. The CW-ESR spectra have been compared with their theoretical counterparts pertaining to the deepest energy minima obtained by QM computations (3_{10} - and α -helix). It will be shown that in specific solvents the experimental spectra agree well with those expected for the 3_{10} -helix, in other solvents with those predicted for the α -helix, while for a final set of solvents with those associated with a mixture of α - and 3_{10} -helices with temperature-dependent relative percentages. The α - and 3_{10} -helices are two common polypeptide conformations [299],[254],[300],[301]. The former helix is a well-known secondary structural element in proteins. The 3_{10} -helix it not as widespread as the α -helix, but it is still rather frequently found in proteins, especially as N- or C-terminal extension of an α -helix. The 3_{10} -helices are usually quite short (about four residues in length) though 3_{10} -helices of 7-12 residues [257],[254],[302],[303] in length have been authenticated in proteins. The 3_{10} -helix differs in its hydrogen-boning pattern from the much more common α -helix: the carbonyl oxygen-to-amide hydrogen bonds are made between residues i and $i + 3$ in the former and between residues i and $i + 4$ in the latter. Changes in the backbone

dihedrals are less than 15° in the two helical conformations. The ideal 3_{10} -helix has one more intramolecular hydrogen bond than α -helix. 3_{10} -Helices have been proposed as intermediates in the folding/unfolding processes of α -helices [304] because there is a lower entropic penalty for the onset of the bend required for the formation of the intra-molecular $i \leftarrow i + 3$ versus $i \leftarrow i + 4$ hydrogen bonds. The relative stability in solution of these two ordered secondary structures depends on various factors. The major parameters are the peptide main-chain length, the amino acid sequence, the Aib content, and the solvent dielectric properties [257],[254],[302],[303], [305],[306], [307]. In polar environments, the α -helix is stabilized by its more favorable solute-solvent electrostatic interactions, and solute-solute steric interactions and solute-solute van der Waals interactions. In polar solvent, especially in water [308],[309],[310], it is possible to reduce some of the inherent strain of the 3_{10} -helix. Relatively short oligopeptides rich in Aib have been observed to largely prefer 3_{10} -helical structures in non-aqueous solutions [277],[254],[311]. It has been also suggested that the asymmetric geometry adopted by the Aib residue can favor the 3_{10} - over the α -helix [312].

3.4.1 Modeling

From the CW-ESR spectra it is possible to obtain both dynamic and structural information. In the case of fast motion of the labeled molecules the structural information can be derived from a fast-motional perturbative model. On the other hand, in the slow motion regime a more sophisticated theoretical approach is required, due to the profound effects that molecular motions exert on the spin relaxation processes. ESR spectroscopy in the slow-motion regime can be interpreted effectively within the SLE. A new integrated approach to the *ab-initio* modeling of CW-ESR presented elsewhere⁵ is composed by several ingredients: (i) state-of-the-art QM calculations providing the structural and local magnetic properties of the molecular system under investigation, (ii) calculation of dissipative parameters, such as rotational diffusion tensors, using standard hydrodynamic arguments, and (iii) in the case of multiply labeled systems, computation of the electron exchange and dipolar interactions. Let us point out in this connection that in conventional spectra simulation the two steps of guessing the magnetic parameters and of simulating the spectral profile are completely disentangled.

On the contrary, our approach requires self-consistency between magnetic and diffusive parameters, which are both related to the geometrical structure issuing from a priori geometry optimization or short-time dynamics. Simulation of the ESR spectra is based on the implementation of the SLE introduced by Freed and co-workers as previously described.

3.4.2 Structure, magnetic and diffusion properties

The structure of heptapeptide **1**, as determined by single crystal X-ray diffraction analysis, is illustrated in Figure 3-9. Relevant geometrical parameters are listed in Table

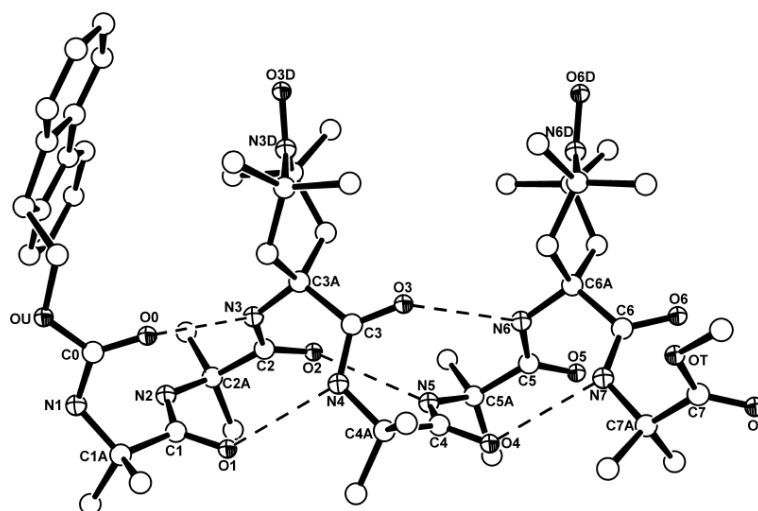


FIGURE 3-9: X-Ray diffraction structure of heptapeptide **1**. Intramolecular H-bonds are represented by dashed lines.

3.3. The peptide being achiral, and crystallizing in a centrosymmetric space group, molecules of both handedness are found in the crystals. A molecule of the right-handed screw sense has been chosen as the asymmetric unit. The peptide backbone is folded into a regular 3_{10} -helix, stabilized by five, consecutive, N-H \cdots O=C intramolecular hydrogen bonds of the $i + 3 \rightarrow i$ type. The C-terminal Aib(7) residue, external to the H-bonding pattern, adopts a helical conformation with a screw sense opposite to that of the preceding residues. The piperidinyl rings of the two TOAC residues are oriented roughly perpendicular to the helix axis and parallel to each other, the angle between normals to their average planes being $4.5(1)^\circ$. The angle between the

two N-O bonds is $10.9(4)^\circ$. The piperidinyl rings of both TOAC residues are found in the 6T_2 twist conformation (relative to the ring atom sequence $N^\delta - C^{\gamma 2} - C^{\beta 2} - C^\alpha - C^{\beta 1} - C^{\gamma 1}$, where $C^{\beta 1}$ refers to the *pro-S* C^β atom). For a statistical analysis of TOAC ring conformations in the crystal state see ref. [298]. The puckering parameters are the following: $Q_T = 0.595(4)$ Å, $\phi_2 = 92.3(4)^\circ$, $\theta_2 = 86.2(4)^\circ$ for TOAC(3), and $Q_T = 0.634(4)$ Å, $\phi_2 = 88.8(4)^\circ$, $\theta_2 = 90.1(3)^\circ$ for TOAC(6) [313]. The hydroxyl groups of the two co-crystallized TFE molecules are H-bonded to the nitroxide O and the carbonyl oxygen atom, respectively, of TOAC(6) within the same asymmetric unit. In the packing mode, peptide molecules are linked head-to-tail through an intermolecular H-bond between the N-H group of Aib(1) and the Aib(7) carbonyl oxygen atom of a $(x, y - 1, z)$ symmetry related molecule, giving rise to rows of molecules along the b direction. The availability of a relatively cheap QM approach able to reproduce the experimental trends would allow to gain further insight on the interplay of different factors in favoring different helical structures. In view of previous quite encouraging experiences [314],[315],[316] we have thus undertaken a systematic study of heptapeptide **1** by a DFT approach. The optimized structures have been obtained by PBE0/6-31G(d) calculations [184] in the gas-phase and in aqueous solution, using in the latter case the so-called polarizable continuum model (PCM)[283],[317] to represent bulk solvent effects (Figure 3-10). All energy minima obtained in the gas phase are characterized by

helix		N...N	O...O	TOAC3			TOAC6		
				NO	CNC	CNO...C	NO	CNC	CNO...C
3_{10}	gas phase	6.57	6.80	1.272	123.1	-177.9	1.273	123.0	-178.0
3_{10}	PCM/H ₂ O	6.51	6.74	1.273	123.0	-178.9	1.274	123.0	-179.2
α	PCM/H ₂ O	7.97	9.27	1.273	122.6	-179.1	1.273	122.5	-179.7
3_{10}	X-ray	6.57	6.80	1.272	123.1	-177.9	1.273	12.30	-178.0

TABLE 3.3: Comparison between the X-ray diffraction and computed geometrical parameters for heptapeptide **1** (distance in Å and angles in degrees. Estimated standard deviations for the crystallographically derived parameters are in the ranges 0.004-0.007 Å, 0.3-0.5° and 0.3-0.6° for bond distance, bond angles and torsional angles, respectively.

a 3_{10} -helical backbone with different conformations (chair or twist) of the rigid nitroxide ring, the absolute minimum corresponding to twist arrangements of both piperidine rings. All of the geometrical parameters of the absolute energy minimum issuing from QM computations are in remarkable agreement with those derived from the X-ray diffraction analysis of the same peptide (see Table 3.3), The Table 3.4 includes local

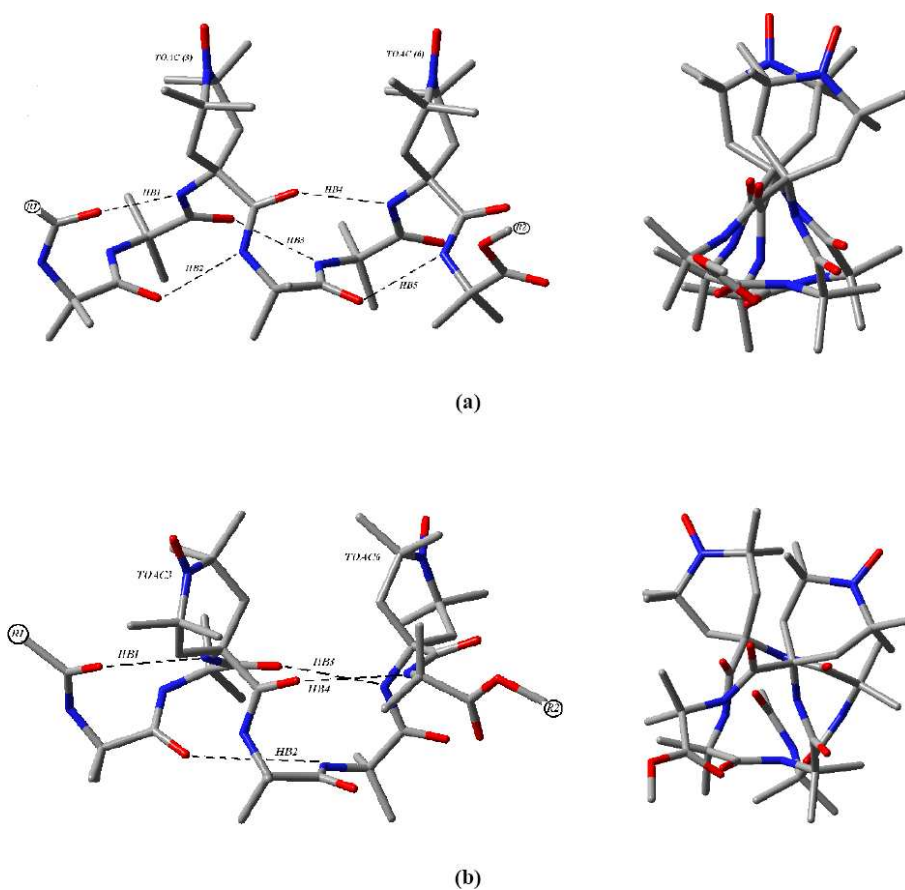


FIGURE 3-10: Optimized structure of heptapeptide 1: View along (right) and orthogonal (left) the helix axis of the (a) 3_{10} -helix and (b) α -helix secondary structure.

environment of the nitroxide moiety and the hydrogen bond network. The number of the hydrogen bonds is in accordance with the experiential data that relevance an higher number of hydrogen bonds in the 3_{10} -helix structure respect to the α -helix structure. This finding is quite interesting since the preferred conformation of the nitroxide ring depends on the backbone conformation: specifically, twist rings are favored by helical backbones, whereas chair rings are more stable for extended backbones or around turns [298],[266]. Furthermore, good match of the intermolecular distance between nitroxide groups is mandatory for the computation of reliable long-range J and spin-spin dipolar interactions. Starting from the structure optimized in the gas phase, two different energy minima are obtained in aqueous solution, corresponding to 3_{10} - and α -helical arrangements of the backbone (Figure 3-10). While the 3_{10} -helix is significantly more stable (by 2.1 kcal/mol), it is well known that current density functionals over-stabilize

helix		HB1	HB2	HB3	HB4	HB5
3_{10}	gas phase	2.02	2.11	2.05	2.12	2.06
3_{10}	PCM/H ₂ O	1.96	2.02	2.02	2.04	1.99
α	PCM/H ₂ O	1.97	2.13	2.18	2.19	-
3_{10}	X-ray	2.22	2.14	2.22	2.18	2.17

TABLE 3.4: Comparison between X-ray diffraction and computed geometrical parameters for **1** with a particular attention to the hydrogen bonds. Distance are in Å and the estimated standard deviation is in the range 0.004-0.007 Å.

the 3_{10} -helix with respect to the α -helix due to the lack of dispersion interactions. We have thus added these terms by the procedure and parameters recently optimized and validated by Grimme [318] and coded in the Gaussian package by one of us [263],[319]. It is remarkable that the α -helix now corresponds to the absolute energy minimum (more stable than the 3_{10} -helix by 3.0 kcal/mol) in aqueous solution, so that a transition between different helical forms is expected as a function of solvent polarity. The 3_{10} -helix differs in its intramolecular hydrogen-bonding pattern from the α -helix: the C=O \cdots H-N hydrogen bonds are seen between residues i and $i + 3$ in the former and between residues i and $i + 4$ in the latter helix. Differences in the backbone dihedrals ϕ and ψ are less than 15° for the two helical conformations. The 3_{10} -helix has one additional intramolecular hydrogen bond with respect to the α -helix (Table 3.4). Upon increasing the solvent dielectric, the effective strength of the extra hydrogen bond is reduced, and the closer non-bonded contacts in the 3_{10} -helix may disfavor this conformation. In polar environments, the α -helix is stabilized by its more favorable solute-solvent electrostatic interactions and intramolecular steric interactions. Lower polarity solvents are associated with an increased relative stability of the 3_{10} -helix that it is largely due to the additional intra-helical hydrogen bond characterizing this conformation. Although experimental evidence for such trends has been reported in previous works [257],[277] and will be confirmed in the following by simulation of ESR spectra, it is remarkable that a priori QM computations lead to the same conclusion. In the 3_{10} -helix the distance (d) between the nitroxide oxygen atoms of the two TOAC residues at relative positions i , $i + 3$ is about 6.5 Å, while in the α -helix this distance is significantly longer (8.0 Å). In general, the 3_{10} -helix exhibits $d(i, i + 3) < d(i, i + 4)$, whereas in the α -helix the opposite holds true. The experimentally observed peptide

helices are somewhat distorted from their ideal geometries, [254],[299] but the difference in the relative side-chain distances between the 3_{10} - and α -helices persists. The above 3D-structures have been next used to compute the magnetic tensors in different solvents, including in the case of chloroform and methanol, the solvent molecules forming hydrogen bonds with the nitroxide group. Typical optimized structures are shown in Figure 3-11. Let us recall that the orbitals determining the *magnetic properties* of

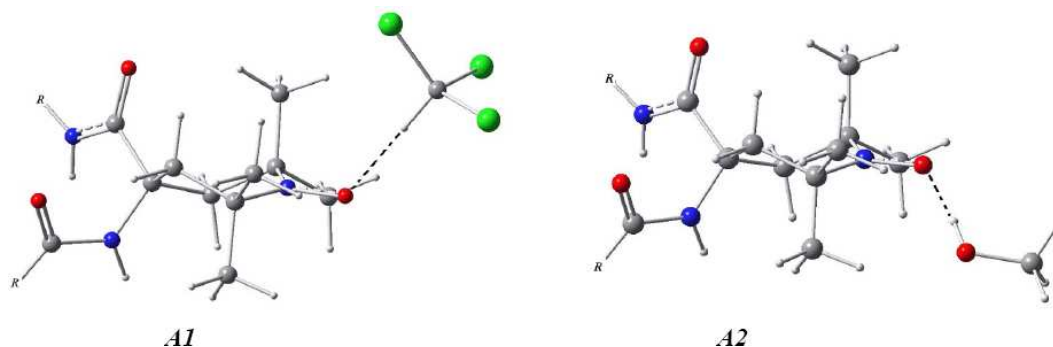


FIGURE 3-11: Structures of the TOAC-solvent complexes: twist conformation with CHCl_3 (**A1**); twist conformation with methanol (**A2**). R = peptide chain.

non conjugated nitroxides are strongly localized onto the NO moiety (Figure 3-3), so that the principal axes of both hyperfine and \mathbf{g} tensors are well aligned along the NO bond (by convention the x axis) and with the average direction of π -orbitals (z axis). The \mathbf{g} tensors computed by the last generation density functionals are usually in good agreement with the experiments and have been used without further corrections in the simulation of ESR spectra. Table 3.5 shows the values of the principal axes components reported in ppm units relatively to the free electron value in order to highlight the difference between the values in different solvents. The most important contribution to \mathbf{g} shifts comes from an electronic excitation from the SOMO-1 (an in plane lone pair, hereafter referred to as n) to the SOMO (an out of plane π^* orbital), both of which are sketched in Figure 3-3. The dependence of the \mathbf{g} tensor on solvent polarity is related to the selective stabilization of lone pair orbitals by polar solvents: this increases the $n \rightarrow \pi^*$ gap with the consequent reduction of \mathbf{g} tensor shifts (especially g_{xx}). Together with this purely electrostatic contribution, formation of solute-solvent H-bonds also concurs to the stabilization of lone pair orbitals and, once again, to a decrease of \mathbf{g}

	δg_{xx}	δg_{yy}	δg_{zz}
gas-phase	6829	3787	-262
toluene ($\epsilon=2.3$)	6674	3754	-262
chloroform ($\epsilon=4.9$)	6579 (6349)	3733 (3598)	-262 (-232)
methanol ($\epsilon=32$)	6472 (5912)	3709 (3580)	-262 (-253)
acetonitrile ($\epsilon=36$)	6470	3709	-262

TABLE 3.5: Gyromagnetic tensor (ppm) computed in different solvents. Value in parentheses are obtained including one specific solvent molecule for each NO moiety (see Figure 3-11).

tensor shifts. In any case, structural and solvent effects on \mathbf{g} are well within experimental uncertainty: thus, constant values of 2.009, 2.006, and 2.003 have been used in the fitting of all spectra for the principal axes of the \mathbf{g} tensor. The situation is more complex for nitrogen hyperfine tensors \mathbf{A} , which can be decomposed into two terms: the isotropic hyperfine term (a_{iso}) and dipolar contributions (\mathbf{B}). The results reported in Table 3.6 show that the \mathbf{B} tensor has the same behavior as the \mathbf{g} tensor and that, to a good approximation, its principal axes are parallel (B_{zz}) or perpendicular (B_{xx} , B_{yy}) to the NO π orbital with $B_{xx} \approx B_{yy}$. It is well known that accurate

	B_{xx}	B_{yy}	B_{zz}
gas-phase	-8.70	-8.465	17.16
toluene ($\epsilon=2.3$)	-8.92	-8.70	17.62
chloroform ($\epsilon=4.9$)	-9.05 (-9.38)	-8.85 (-9.24)	17.90 (18.62)
methanol ($\epsilon=32$)	-9.19 (-9.59)	-9.01 (-9.48)	18.20 (19.06)
acetonitrile ($\epsilon=36$)	-9.19	-9.02	18.21

TABLE 3.6: Dipolar hyperfine tensor (in Gauss) computed for heptapeptide **1** in different solvent. Value in parentheses are obtained including one specific solvent molecule for each nitroxide moiety (see Figure 3-11).

estimates of isotropic hyperfine couplings for nitroxides can be obtained only using very demanding theory levels, like, e.g. quadratic configuration interaction including single and double excitations (QCISD) with purposely tailored basis sets, possibly integrated into an ONIOM-like approach [266]. We have, however, recently developed a new basis set (N06) that, coupled to the PBE0 functional, promises to overcome this problem. Indeed, the computed a_{iso} for the closely related TEMPO (2,2,6,6-tetramethylpiperidine-N-oxyl) radical in cyclohexane (15.23) and in toluene (15.32) are in remarkable agreement with the experimental values (15.28 and 15.40 G, respectively) [320],[321]. The computed values for the chair conformation of TOAC are very

close, whereas significantly lower values (12.38 and 12.54 and G) are obtained for the twist structure. This is related to the different pyramidity around nitrogen: in particular, the nearly planar arrangement characterizing the twist structure leads to the lack of any contribution of nitrogen s orbitals to the orbital formally containing the unpaired electron with the consequent strong reduction of a_{iso} . However, vibrational averaging effects, which are essentially negligible for chair structures, cannot be neglected for the nearly planar nitroxide moieties characterizing twist structures. Without entering into a detailed description of the effective one-dimensional model we have used to estimate these effects,[277],[322],[323],[324] we just mention that a nearly constant vibrational correction of 1.7 Gauss is obtained for all twist structures. It is noteworthy that, after this correction, twist and chair conformations have comparable hyperfine couplings, which show, furthermore, a distinct solvent dependence (see Table 3.7). In particular,

	a_{iso}°	Δ_{vib}	Δ_{1s}	Best calc.	Best fit
gas-phase	12.2	1.7			
toluene ($\epsilon=2.3$)	12.6	1.7	-	14.3	14.5
chloroform ($\epsilon=4.9$)	12.8	1.7	0.58	15.1	15.0
methanol ($\epsilon=32$)	13.1	1.7	0.61	15.4	15.3
acetonitrile ($\epsilon=36$)	13.1	1.7	-	14.8	14.8

TABLE 3.7: Calculated nitrogen isotropic hyperfine coupling (in Gauss) for the optimized 3_{10} -helix of the heptapeptide **1** are compared with fitted values (best fit). The final calculated values (best calc.) include electronic values at the energy minimum (a_{iso}°), vibrational averaging (Δ_{vib}), and, for protic solvents, the contribution of a single explicit solvent molecule (Δ_{1s}). The last column reports the optimized values of the isotropic hyperfine coupling.

solvent polarity and formation of solute-solvent hydrogen bonds concur to the selective stabilization of the nitroxide resonance structure involving at the same time formal charge separation and increased spin density on nitrogen [269]. The final values selected for the different solvents are: 14.3 (toluene), 14.8 (acetonitrile), 15.0 (chloroform), and 15.3 Gauss (methanol), where 1 Gauss = 10^{-4} T. To fine-tune the simulated spectra we set $A_{XX} \approx A_{YY} = A_{\perp}$ and $A_{ZZ} = A_{\parallel}$ and then fit the isotropic value $a_{iso} = 2A_{\perp} + A_{\parallel}$ by keeping constant the anisotropy ratio $R = A_{\perp}/A_{\parallel} = 0.13$. Hyperfine and gyromagnetic tensors have a local character and are thus only marginally influenced by the long-range interactions modified by conformational changes (e.g transition from the 3_{10} - to the α -helix). The other magnetic terms (J and spin-spin dipolar interaction)

have a long-range character and can provide, in principle, a signature for the different helical structures. The J terms have been calculated from differences between triplet and singlet energies by the so-called broken-symmetry approach [277]. Although the computed J values are slightly different for the 3_{10} - and the α -helix (140.8 and 139.5 Gauss, respectively, at the PBE0/N06 level), this trend does not allow to gain further structural information, since (as we shall see) all values larger than 130 Gauss are compatible with experimental data. Usually, the spin-spin dipolar term is calculated by assuming that the two unpaired electrons are localized at the center of the NO bonds of the two TOAC residues. Then, the two electrons are considered just as two point magnetic dipoles and the interaction term depends on the distance between the two localized electrons. The considerations for the calculation of the dipolar interaction tensor for the α -helix are equal to the 3_{10} -helix. Figure 3-12 shows the trend of $|T^{(2,0)}|$ versus the distance between the two TOAC nitroxides and highlights the position of the 3_{10} -helix and the α -helix with respect to the distance between the TOAC residues. The difference between the point-dipole approximation and the quantum mechanical values of the dipolar tensor is higher in the 3_{10} -helix structure, in which the distance between the two nitroxides is lower if compared to that of the α -helix. The difference

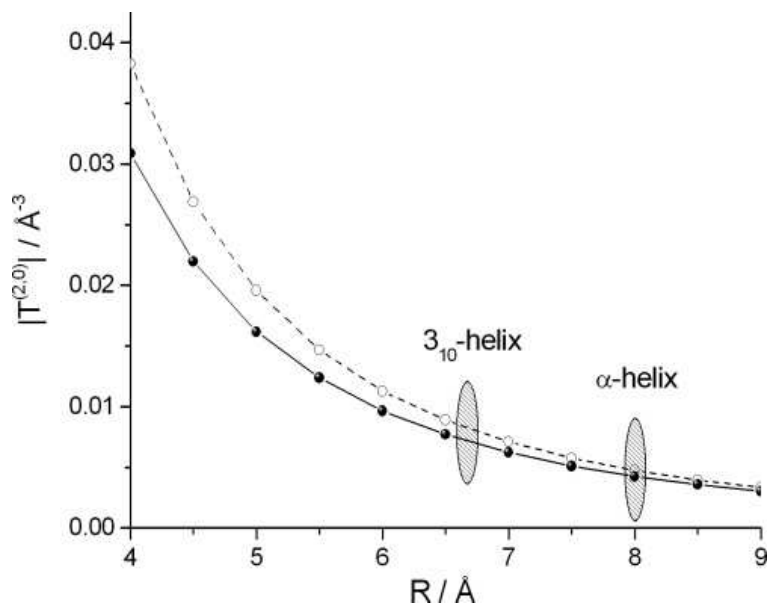


FIGURE 3-12: Trend of $|T^{(2,0)}|$ versus distance calculated with the point dipole (dashed line) and localized quantum mechanical (solid line) approaches.

between the point-dipole approximation and the quantum mechanical values of the dipolar tensor is higher in the 3_{10} -helix structure, in which the distance between the two nitroxides is lower if compared to that of the α -helix.

The rotational dynamics is controlled by the rotational diffusion tensor \mathbf{D} , which, in turn, can be evaluated from the molecular shape and macroscopic solvent properties [291]. In particular, evaluation of the *diffusion properties* of $\mathbf{1}$ is based on a hydrodynamic approach described in the Chapter II. We can write the rotational diffusional tensor (already diagonalized in the MF) in the form $\mathbf{D}(T) = D(T)\mathbf{d}$, where $D(T) = k_B T / \xi(T)$ is the translational diffusional coefficient of a sphere of radius R at temperature T , and \mathbf{d} is a diagonal tensor depending only on the molecular geometry, with values $d_{XX} = 1.71 \times 10^{16}$, $d_{YY} = 1.83 \times 10^{16}$ and $d_{ZZ} = 5.75 \times 10^{16} \text{ m}^{-2}$ for the 3_{10} -helix and $d_{XX} = 1.88 \times 10^{16}$, $d_{YY} = 2.01 \times 10^{16}$ and $d_{ZZ} = 4.91 \times 10^{16} \text{ m}^{-2}$ for the α -helix. The same procedure, previously employed [291] for the calculation of the diffusion tensor at different temperatures, and based on available viscosity data for the solvents considered [214], was used to calculate the temperature- and solvent-dependent rotational diffusion tensors. The larger difference between the value of the diffusion tensor for the 3_{10} -helix and the α -helix is computed for the ratio of the z component (d_{ZZ}) and the x component (d_{XX}) of the tensor. For all the temperatures and solvents investigated, this ratio is 3.36 for the 3_{10} -helix and 2.61 for the α -helix. These different values can be explained by simply considering the shape of the two secondary structures illustrated in Figure 3-10. A higher value of the ratio is related to a long and slim shape of the molecule (Figure 3-10.b) while a lower value indicates that the molecule is shorter and wider (Figure 3-10.a).

3.4.3 Results

Simulated spectra in different solvents exhibit different sensitivity with respect to the magnetic and diffusion calculated parameters. In particular, simulations, as expected, are not sensitive to changes in the electron exchange interaction J when $J > 130$ Gauss. The dependence on the values of the components of the diffusion tensor \mathbf{D} is more significant: variations within a 10 % range of the proposed values, calculated according to the hydrodynamic approach, cause a significant change in the intensity and

widths of the peaks. Moreover, the spectra dependence on the temperature is perfectly reproduced by the calculated \mathbf{D} tensor. Sensitivity upon the dipolar interaction tensor \mathbf{T} is also relevant. The spectrum is controlled by the dominant $T^{(2,0)}$ component, which causes noticeable variations when changed within 12%. An overestimation of \mathbf{T} , corresponding for instance to the adoption of the approximate point formulation, leads to an increase of the width and a decrease of the intensity of all peaks. Finally it is well known

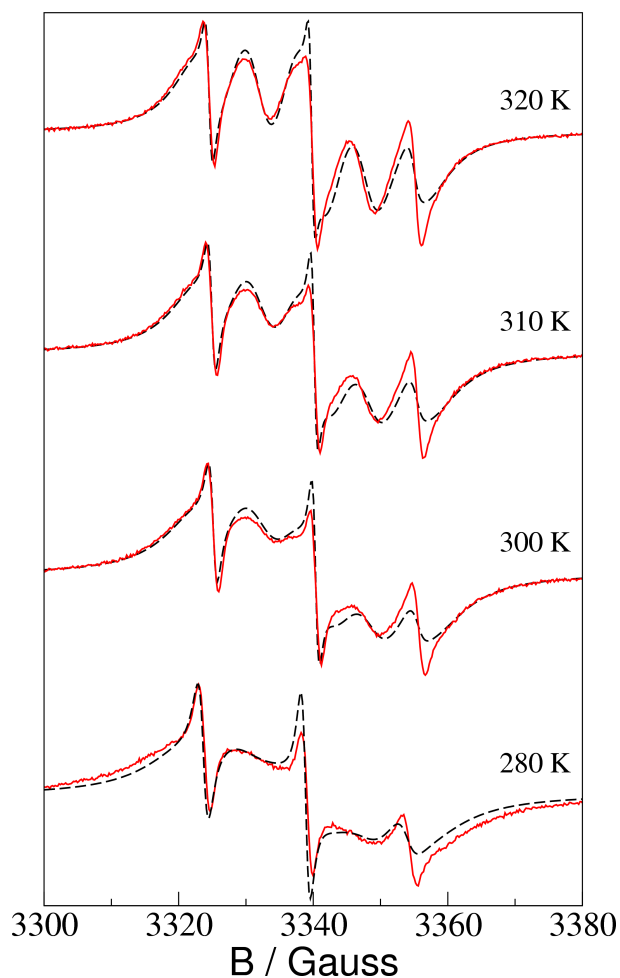


FIGURE 3-13: Experimental (solid line) and theoretical (dashed line) CW-ESR spectra of heptapeptide **1** in methanol at temperatures 320, 310, 300 and 280 K.

that the general dependence of CW-ESR spectra upon the \mathbf{g} and \mathbf{A} tensor component values and orientation Euler angles is highly pronounced and no significant adjustment is possible with respect to the calculated values which are in very good agreement with the experimental observations. The SLE computations were performed for four differ-

ent solvents: acetonitrile (MeCN), methanol, toluene and chloroform. It is worthwhile to remark that the overall computational protocol has been organized in a novel suite of computational codes which present significant advancements with respect to the existing packages for the interpretation of ESR spectra, namely the integration of the QM and stochastic dynamics parts, the extension to multiple radicals and nuclei and finally the increased computational efficiency based on a partial on-the-fly evaluation of matrix elements. For each solvent we examined different temperatures and at every step a different value of the diffusion tensor was employed owing to the temperature dependence of the viscosity. A common assumption for all solvents is the presence of a monoradical impurity that might arise from the reduction of one of the nitroxide functions. The estimated amount of the impurity is below 4 %, a low but still appreciable percentage. It is noteworthy that the optimized values of a_{iso} (the only adjustable parameters in our protocol) are very close to their QM counterparts for all solvents (see Table 3.7). Figure 3-8 collects four theoretical spectra for the heptapeptide **1** in MeCN and their experimental counterparts at four different temperatures: 330, 310, 290 and 270 K. From the simulations it appears that in this solvent only the 3_{10} -helix occurs, i.e. $p_{\alpha} = 0$, $p_{3_{10}} = 98$, $p_{mono} = 2$ % at all temperatures. Figure 3-13 shows five theoretical and experimental spectra in methanol solution in the temperature range 280 K to 320 K. The simulations, which consider that in solution is present only the α -helix, closely reproduce the experimental spectra, $p_{\alpha} = 97$, $p_{3_{10}} = 0$, $p_{mono} = 3$ % at all temperatures. Figure 3-14 collects the simulated and the experimental spectra for a toluene solution in the temperature range 270-350 K. At high temperatures (350, 340, 330, 320 K) the experimental spectra are well reproduced using comparable percentages of *alpha*-helix and 3_{10} -helix structures, $p_{\alpha} = 60$, $p_{3_{10}} = 38$, $p_{mono} = 2$ %. At lower temperatures (below 310 K) the experimental spectra are correctly reproduced by progressively increasing the α -helix percentage, with $p_{\alpha} = 75, 78, 92, 98$ % at 310, 300, 290, 280, 270 K (and constant $p_{mono} = 2$ %). Figure 3-15 shows the spectra for a chloroform solutions in the range 290 to 250 K. The experimental spectra are reproduced using only an α -helix structure, $p_{\alpha} = 96$, $p_{3_{10}} = 0$, $p_{mono} = 4$ % at all temperatures. From the available literature data [255] we could expect a high 3_{10} -helix percentage in solution induced by the low polarity of the solvent. However, QM computations show that quite stable

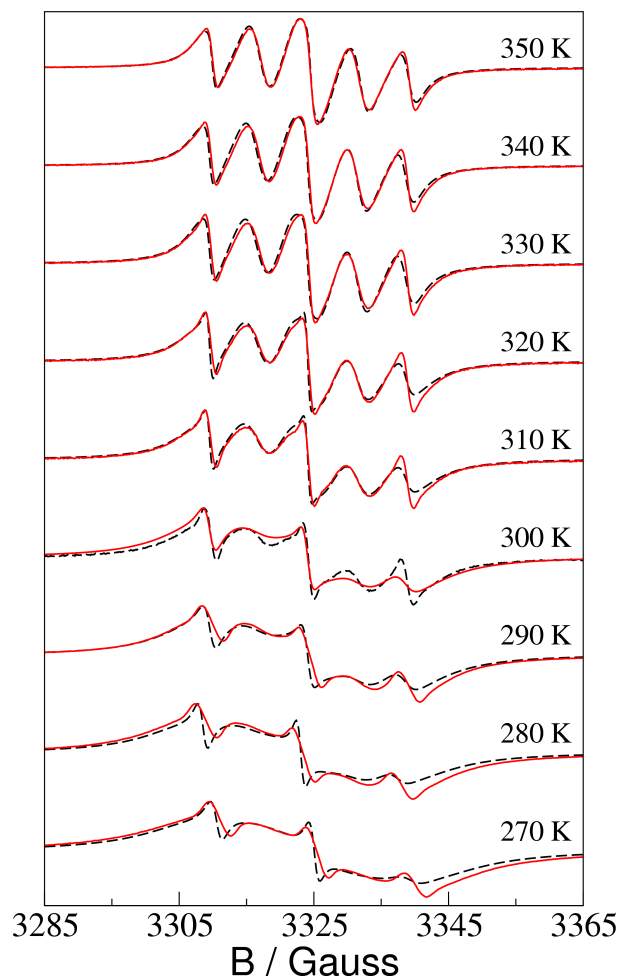


FIGURE 3-14: Experimental (solid line) and theoretical (dashed line) CW-ESR spectra of heptapeptide **1** in toluene at temperatures 350, 340, 330, 320, 310, 300, 290, 280 and 270 K.

hydrogen bonds can be formed between chloroform and both nitroxide and carbonyl groups (see e.g. Figure 3-11), which, in turn, could lead to a switch from the 3_{10} - to the α -helix [302],[303],[305]. The different behavior can be caused by the low range of temperature used in the experimental spectra. At low temperature the simulation points to an increasing presence of the α -helix structure. Examples of peptides possessing a main-chain length comparable to that of heptapeptide **1**, and largely [325] or even exclusively based upon C^α -tetrasubstituted amino acid residues, able to switch from the 3_{10} - to the α -helical conformation upon increasing medium polarity have been only recently reported. The simulated α and 3_{10} -helix CW-ESR spectra in the same solvent and at the same temperature is strong. The Figure 3-16 shows the experimen-

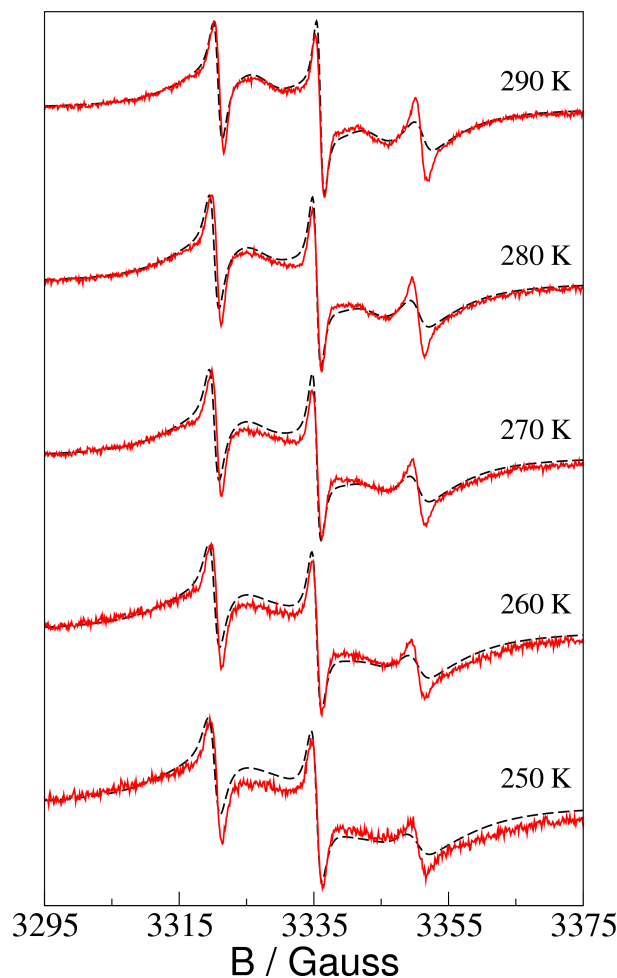


FIGURE 3-15: Experimental (solid line) and theoretical (dashed line) CW-ESR spectra of heptapeptide **1** in chloroform at temperatures 290, 280, 270, 260 and 250 K.

tal and the simulated α - and 3_{10} -helix CW-ESR spectra for two solvent at the same temperature. It is possible evidence that the difference between the simulate spectra of the two secondary structures. This evidence consolidates the results connects to the percentage of α or 3_{10} -helix effectively presents in the solution.

3.5 Conclusions

This part of the work want to emphasize the influence of the solvent on the magnetic properties connected to the CW-ESR spectra. We analyze the behavior of a small peptide in different solvent and at different temperatures. The first part of the work

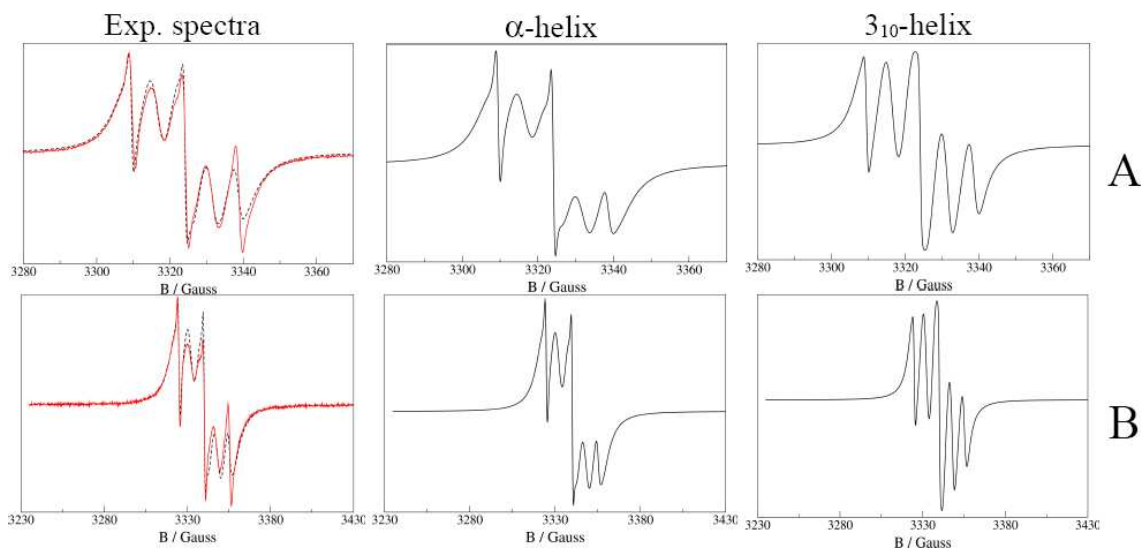


FIGURE 3-16: Experimental (left) and simulated α -helix (center) and 3_{10} (right) CW-ESR spectra of heptapeptide **1** in toluene (A) and methanol (B) at temperature 310 K.

evidence that the integrated approach to *ab-initio* prediction of CW-ESR spectra is able to assess the 3_{10} -helical and dynamic characteristics of the double spin labeled heptapeptide **1** entirely from computational models and direct comparison with the experimental data. The sensitivity of the integrated methodology to the overall molecular geometry is demonstrated by the significant change in the calculated spectrum for a hypothetical α -helix: the combination of a sophisticated *ab-initio* modeling and a relatively simple CW-ESR experimental measurement can be seen as a possible tool for characterizing peptide conformations. We suggest that prediction of trends in the CW-ESR spectra in increasingly slower motional regimes is a further capability of our integrated methodology combining the QM-DFT, SLE and hydrodynamic approaches. Some adjustment of computed magnetic tensors (here the trace of hyperfine tensor) is probably unavoidable for a quantitative fitting of experimental spectra, especially for large systems where only DFT approaches are feasible. However, the number of free parameters (if any) is limited enough that convergence to the true minimum can be granted. At the same time the allowed variation of parameters from their QM value is well within the difference between different structural models (e.g. 3_{10} or α -helix). Thus, pending further developments of DFT models, the integrated approach introduced in this study is already able to predict CW-ESR spectra of large molecular

systems in non-protic solvents starting only from the chemical structure of the solute and some macroscopic solvent properties. After a detailed study of the heptapeptide in a polar solvent (acetonitrile) at different temperature we develop the model considering that the small peptide, in other solvents, can assume other secondary structures. We consider four solvents: acetonitrile, methanol, toluene and chloroform. Some of these solvents present only a secondary structure (acetonitrile only the 3_{10} -helix and the methanol only the α -helix) while the toluene and the chloroform show the presence of both secondary structures. The model develops in the second part of this work reproduces the kind of secondary structure presents in solution and its percentage in connection with the variation of the temperature. In the second part we have reported a detailed analysis of the structural and magnetic properties of a double labeled peptide by an integrated computational and experimental strategy. From a chemical point of view, our results provide evidence on the property of Aib-rich peptides of changing their conformation from 3_{10} - to α -helix as a function of increasing polarity and hydrogen-bond donor capability of the solvent: α -helix in a protic solvent and at low temperature, whereas 3_{10} -helix in aprotic solvents. The X-ray diffractometric analysis reveals that the peptide assumes a 3_{10} -helical conformation in the crystal state. The 3_{10} -helix is very well reproduced by DFT computations in vacuo and in aqueous solution. Our computational results indicate that in aqueous solution the α -helical conformation becomes the deepest conformational minimum when dispersion interactions are taken into account. Computation of magnetic and diffusion tensors and their feeding in a general computational protocol based on the stochastic Liouville equation allowed us to reproduce in a remarkable way the ESR spectra in different solvents and at different temperatures without any adjustable parameter except the relative percentage of 3_{10} - and α -helices. The favorable scaling of our computational protocol with the dimensions of the system and its remarkable performances for both structural and magnetic properties might pave the route for systematic studies of spin labeled peptides and proteins. A schematic representation of the integrated approach to simulate the CW-ESR spectra in different solvents is reported in the Figure 3-17.

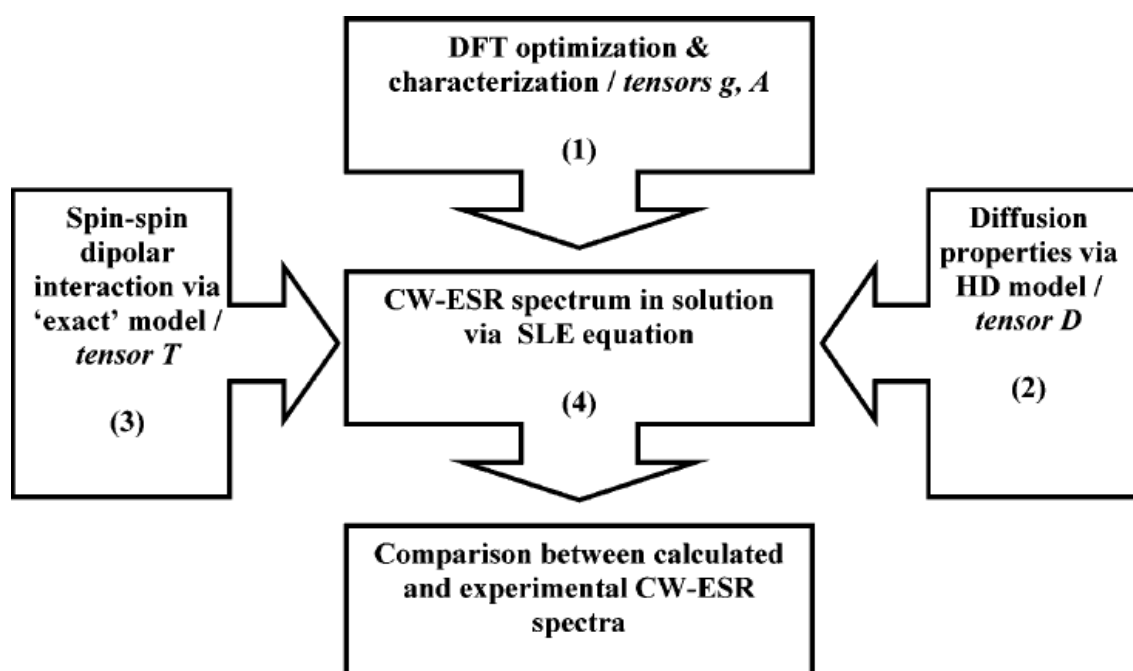


FIGURE 3-17: Chart of the integrated computational approach to the simulation of the CW-ESR spectra in solution. Steps (2) and (3) are based on the optimized geometry and electronic structure obtained in step (1).

Chapter 4

Evaluation of translational friction coefficients of macroscopic probes in Nematic Liquid Crystals

4.1 Introduction

This last Chapter considered the influence of the solvent on the rheological properties and apply a continuum approach to study a macroscopic object in an oriented phase: a nematic liquid crystals. The physic of the liquid crystal, and in particular the physics of colloidal dispersion in nematic liquid crystal, is a novel challenging type of soft matter. Nematic liquid crystals have been employed extensively in displays, and more recently in sensing technologies. In order to develop new applications for nematic-colloidal systems, a theoretical understanding of liquid crystal dynamics in the presence of colloidal particles is crucial. Dispersion of particles in a host medium are part of everyday life and for fundamental research [326]. There is in general a growing interest in suspension of particle in a nematic environment and there is underline by the high number of articles about the argument [327],[328],[329],[330]. Colloidal dispersions are particle size range from 10 nm to 100 nm that appear in food, in drugs, ink, paints and cosmetics so they are of considerable technological importance. In fundamental research they are an ideal systems to study Brownian motion and hydrodynamic interactions

[331], transition phase [332], and problems connect with the flocculation [333]. Early experiments started in 1970 when Brochard and de Gennes [334] studied a suspension of magnetic grains in nematic, then other experimental groups worked on silica spheres in nematic host [335], on latex particles in lyotropic liquid crystal [327] or water droplets [336]. Particles suspended in a fluid perform Brownian motion and their diffusion constant obeys the Stokes-Einstein relation [333]. A theoretical treatment of particles in anisotropic liquids has to deal with the dynamic equations of the Leslie-Ericksen equations, which couple the director field and the fluid velocity. In the 1961 Ericksen proceeded to generalize the static and theory of nematic in order to propose balance laws for their dynamical behavior [337]. Making use of these ideas Leslie formulated constitutive equations and complete the dynamic theory for nematic liquid crystals. This led to the celebrated Leslie-Ericksen dynamic theory for nematic liquid crystals. Due to their complexity, only few examples with an analytical solution exist, e.g. the flow between two parallel plates [338] or the back flow [339]. The solution to the Leslie-Ericksen equations are also of technological interest since they are necessary for determining the switching times of liquid-crystal display. In the past, several hydrodynamic and kinetic interpretations of experimental data on translation friction (or diffusion) coefficients of solutes in nematic solvents have been derived. Diogo [340] found analytical expressions for the friction acting on a spherical molecule in a nematic in the presence of an external field, under severe approximations. Franklin used [341] a modification of Kirkwood theory to relate translation parallel and perpendicular diffusion coefficients of probes in nematic to viscoelastic parameters, order parameter and molecular shape, deriving also an expression for rotation diffusion coefficients, and lately [342] employed hydrodynamic theory to interpret experimental findings of diffusion coefficients of molecular probes in PAA. Khare *et al.* [343] presented a kinetic treatment to study translation diffusion in nematic fluids, and compared their results with computer simulations. In this study, we shall attempt to study systematically the translational friction acting on macroscopic probes moving in nematic fluids, by solving numerically the constitutive hydrodynamic equations of nematics under some approximations. Experimental measures of translation diffusion coefficients of molecular probes in liquid crystals have been also obtained using several techniques. Poulin

et al. [327] measured translational diffusion of latex spheres with dynamic light scattering, Lettinga [344] used a digital microscopy to directly visualize the dynamics of fluorescently labeled *fd* virus in a nematic background of unlabeled *fd* virus, Yun and Fredrickson [345] measured translation diffusion of molecules tagged with ^{14}C radioactive isotopes by liquid scintillation counting in various liquid crystals, determining the parallel and perpendicular diffusion with respect to an applied magnetic field. Moseley and Lowenstein [346] [347], studied the diffusive motion of methane and chloroform molecules in liquid crystals. More generally Krüger [348] discussed several experimental techniques like NMR, MTR and QENS to measure diffusion coefficients in nematic and smectic phases, together with their theoretical interpretation. Recently, Spiegel *et al.* [349] employed forced Rayleigh scattering to study the diffusion of methyl-red in 5CB. In the study described in this work we shall describe numerically the translation of a spherical probe or ellipsoidal in nematic liquid crystals, solving the constitutive hydrodynamic equations of nematic fluids under the standard hypothesis of stationary Newtonian velocity. In particular, we shall present a qualitative analysis of the director field patterns created by the perturbation caused by the moving probe.

4.2 Nematic Liquid Crystals

There are three common states of matter that most people know about: solid, liquid, and gas. Liquid crystal is a fourth "state" that certain kinds of matter can enter into under the right conditions. The molecules in solids exhibit both positional and orientational order - in other words, the molecules are constrained to point only certain directions and to be only in certain positions with respect to each other. In liquids, the molecules do not have any positional or orientational order - the direction the molecules point and their positions are random. This fourth state of matter generally possess orientational or weak positional order and thus reveals several physical properties of crystals but flow like liquids. The liquid crystal phase exists between the solid and the liquid phase. If transitions between the phases are given by temperature, they are called thermotropic. In blends of different components phase transitions may also depend on concentration, and these liquid crystals are called lyotropic. While ther-

motropics are presently mostly used for technical applications, lyotropics are important for biological systems, e.g. membranes. These lyotropic liquid crystal substances are extremely important in display applications. There are several distinct kinds of liquid crystalline phases reported [350], and more phases are being discovered. The common characteristic of these phases is that they are stable in a temperature range which is between the temperature ranges where the isotropic liquid and the solid phase are stable. For this reason they are also referred to as mesophases, from the Greek word *mesos* meaning middle. Liquid crystals usually consist of steric "rod-" or "disk-like" organic molecules on the order of 20 Angstroms in length which tend to align themselves with a long range order due to anisotropic intermolecular forces. MBBA was the first room temperature liquid crystal synthesized in 1969, whereas 5CB was the first member of the optically and chemically stable cyanobiphenyls, one of the most applicable family of liquid crystals, discovered in 1973. Nematic liquid crystal in Figure 4-1 is a common type. It was Friedel [351] who first gave the name nematic from the

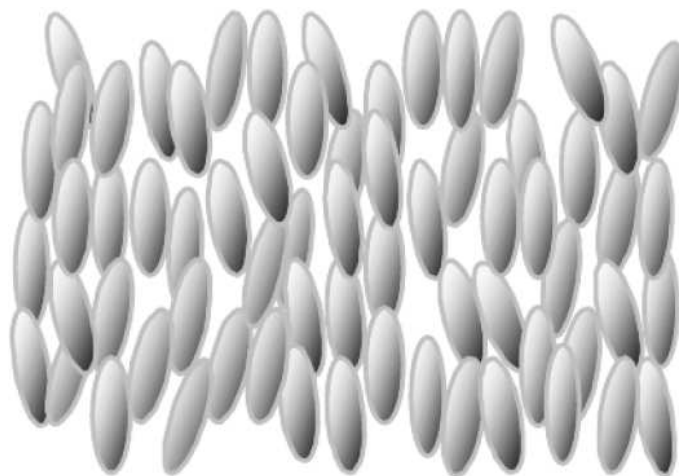


FIGURE 4-1: Pictorial representation of a nematic liquid crystal.

Greek word *nema*, meaning thread, because of the thread-like discontinuities which can be observed under the polarizing microscope for this phase. The nematic phase has the lowest ordering of all the mesophases and, if present, precedes the transition to the isotropic liquid which occurs at the clearing point. The molecules making up the nematic phase do not all point the same direction all the time but they tend to

orient on the average along a preferred direction within a large cluster of molecules, called the director \mathbf{n} . The ordering of the molecules in the nematic phase is completely described by the time or ensemble average of the orientation of a molecule-fixed axis system with respect to the director. The "amount" of order is measured by the order parameter of the liquid crystal, which can be found by averaging the function for all the molecules in the sample, where θ is the angle the long axis of the molecule makes with a particular direction. Averaging this function of $\cos^2\theta$ instead of just θ alone conveniently gives a value between 0 and 1 for the amount of orientational order. This order parameter is highly dependent on the temperature of the sample. As a result of orientational order, most physical properties of liquid crystals are anisotropic and must be described by second rank tensors. Examples are the heat diffusion, the magnetic susceptibility, the dielectric permittivity or optical birefringence. Additionally, there are new physical qualities, which do not appear in simple liquids as e.g. elastic or frictional torques (rotational viscosity) acting on static or dynamic director deformations, respectively. Orientational order and hence birefringence can be manipulated easily e.g. with the help of rather weak magnetic, electric or optical fields, leading to huge magneto-optical, electro-optical and opto-optical effects. Within a sufficiently large magnetic field, however, all the local directors will be either parallel or perpendicular to the magnetic field depending on the sign of the molecular magnetic susceptibility anisotropy of the molecules. Liquid crystal has a number of unique characteristics that makes it very useful in several applications. Most of these characteristics stem from the fact that liquid crystal is an anisotropic material, meaning that the properties of the material differ depending on what direction they are measured. Liquid crystal behaves differently depending on what direction electric or magnetic fields are applied relative to the director. The most successful application are liquid crystal displays well-known from wrist watches, pocket calculators or flat screens of laptop computer which take advantage of electro-optical effects. More recently, it turned out that orientational order can be also affected by optical fields leading to rather sensitive opto-optical effects and nonlinear optical properties, which are important e.g. for all-optical switching and other photonic devices in future optical information technologies.

4.3 The model

4.3.1 Isotropic fluid

It is convenient to first summarize the evaluation of translational friction coefficients for a moving probe in an *isotropic* (Navier-Stokes, NS) fluid under conditions of creeping flow [352]. In their most general form NS equations for an isotropic incompressible fluid describe the time evolution of and they describe the time evolution of fields $v_j(\mathbf{r}, t)$, components along the fixed axes of a laboratory frame $\mathbf{e}_1, \mathbf{e}_2, \mathbf{e}_3$ of the velocity field vector $\mathbf{v}(\mathbf{r}, t)$ in the space point \mathbf{r} of cartesian coordinates r_1, r_2, r_3 or polar coordinates r, θ, ϕ at time t . In the absence of external forces, NS equations read

$$\rho \frac{Dv_j}{Dt} = -\frac{\partial p}{\partial r_k} + \mu \nabla^2 v_j \quad (4.1)$$

where $p(\mathbf{r}, t)$ is the pressure, while μ is the dynamic viscosity; D/Dt is the material time derivative $D/Dt = \partial/\partial t + v_k \times \partial/\partial r_k$. Einstein's convention holds here and everywhere else in this paper unless otherwise stated. Let us now consider a fluid moving around a fixed spherical probe of radius R , with center in the lab frame origin, at a constant velocity along a chosen axis, e.g. \mathbf{e}_3 , which is equivalent to solve Eq. 4.1 for the boundary conditions $v_j = 0$ for $r = 0$, assuming stick conditions, and $v_j = V\delta_{j,3}$ for $r \rightarrow \infty$. This is tantamount to consider a sphere moving at constant velocity $-V$ along the \mathbf{e}_3 axis, with the fluid having the same velocity on the probe surface, and zero flow or velocity at $r \rightarrow \infty$ [353]. In conditions of creeping flow, or zero material derivative, the solution is analytic [353]

$$p = -\frac{3}{2}\mu V \frac{Rr_3}{r^3} \quad (4.2)$$

$$\frac{v_j}{V} = \left[1 - \frac{R}{4r} \left(\frac{R^2}{r^2} + 3 \right) \right] \delta_{j,3} + \frac{3Rr_j r_3}{4r^3} \left(\frac{R^2}{r^2} - 1 \right) \quad (4.3)$$

The force acting on the sphere can now be calculated as

$$F_i = - \int_S dS \sigma_{ij} m_j \quad (4.4)$$

where the integral is extended to the sphere surface and m_j is the j -th component in each surface point of the unitary normal vector \mathbf{m} ; σ_{ij} is the ij component of the *stress*

tensor σ , defined for a Newtonian fluid as

$$\sigma_{ij} = -p\delta_{ij} + \mu \left(\frac{\partial v_i}{\partial r_j} + \frac{\partial v_j}{\partial r_i} \right) \quad (4.5)$$

Integration of Eq. 4.4 is easily accomplished to give the only non-zero component along the axis of motion [352] $F_3 = 6 \pi \mu V R$, i.e. Stokes' law for the translation friction coefficient is found

$$\xi = 6\pi\mu R. \quad (4.6)$$

In the following, we shall discuss also ellipsoidal probes. Although slightly more complicated, the discussion of translational friction coefficients for ellipsoidal particles can be carried on analytically [354]. For an ellipsoidal probe of semi-axes a_1 , a_2 and a_3 , and axes aligned with lab frame axes, surrounded by a fluid described by boundary conditions $v_j = 0$ on the probe surface and $v_j = V\delta_{j,3}$ for $r \rightarrow \infty$, the stationary solution for the fluid velocity components is [354]:

$$v_j = A \frac{\partial^2 \Omega}{\partial r_3 \partial r_j} + B \left(r_3 \frac{\partial \chi}{\partial r_j} - \chi \delta_{j,3} \right) + V \delta_{j,3} \quad (4.7)$$

where Ω and χ are

$$\begin{aligned} \Omega &= \pi a_1 a_2 a_3 \int_l^\infty \left(\frac{r_1^2}{a_1^2 + \lambda} + \frac{r_2^2}{a_2^2 + \lambda} + \frac{r_3^2}{a_3^2 + \lambda} - 1 \right) \frac{d\lambda}{\Delta} \\ \chi &= a_1 a_2 a_3 \int_l^\infty \frac{d\lambda}{\Delta} \end{aligned} \quad (4.8)$$

here $\Delta = [(a_1^2 + \lambda) + (a_2^2 + \lambda) + (a_3^2 + \lambda)]^{1/2}$ and l is the positive solution of

$$\frac{r_1^2}{a_1^2 + l} + \frac{r_2^2}{a_2^2 + l} + \frac{r_3^2}{a_3^2 + l} = 1 \quad (4.9)$$

Parameters A and B are obtained imposing boundary conditions, i.e. again zero velocity on the probe surface

$$\begin{aligned} B &= \frac{V}{\chi_0 + \gamma_0 a_3^2} \\ A &= -\frac{B a_3^2}{2\pi} \end{aligned}$$

where χ_0 is obtained as χ for $l = 0$ and γ_0 is

$$\gamma_0 = a_1 a_2 a_3 \int_0^\infty \frac{d\lambda}{(a_3^2 + \lambda) \Delta} \quad (4.10)$$

Finally the pressure is obtained in the form:

$$p = 2B\mu \frac{\partial \chi}{\partial r_3} \quad (4.11)$$

The force acting on the probe can now be calculated, like in the spherical case, and a simple analytical form is obtained which is identical to spherical Stokes's law, but with an effective radius R_{eff}

$$R_{\text{eff}} = \frac{8a_1 a_2 a_3}{3(\chi_0 + \gamma_0 a_3^2)} \quad (4.12)$$

so that the stick friction coefficient calculated for an ellipsoidal probe in rectilinear motion in an isotropic fluid of viscosity μ is given by [354]

$$\xi_{\text{iso}} = 6\pi\mu R_{\text{eff}} \quad (4.13)$$

4.3.2 Leslie-Ericksen equations

The flow regimes of a nematic is more complex and more difficult to study than in an isotropic liquids. The translational motions are coupled to inner orientational motions of the molecules and, in most case, the flow disturb the alignment. Conversely, a change in the alignment (e.g by application of an external field) will induce a flow in the nematic. From a theoretical point of view the coupling between orientation and flow is a very delicate matter [350]. The problem has been analyzed essentially in two different way: (i) a macroscopic approach, based on classical mechanics, has been used by Leslie and Ericksen [355],[356],[357],[358] and (ii) a microscopic approach, based on a study of correlation functions, latest rewritten directly in macroscopic terms. So the two approach are essentially identical in contest. We describe the system under study in terms of Leslie-Ericksen equations (LE). The fist assumption of the hydrodynamic description of nematic fluids is that it is described by the fields $\mathbf{n}(\mathbf{r}, t)$, a unitary vector which specifies the director orientation in each point at a given time (local state of alignment) and $\mathbf{v}(\mathbf{r}, t)$, a velocity field giving the flow of matter. Constitutive Leslie-Ericksen equations describe the time evolution of the components n_j , v_j and of pressure p in the form (neglecting so-called inertial components in the director equation) [359].

For a nematic incompressible isothermal the LE equations can be expressed as:

$$\rho \frac{Dv_j}{Dt} = \frac{\partial \sigma_{ij}}{\partial r_j} \quad (4.14)$$

$$G_j + g_j + \frac{\partial \pi_{ij}}{\partial r_j} = 0 \quad (4.15)$$

where σ_{ij} is the stress tensor, ρ is the density, G_j is the j -th component of a generic external force (typically generated by an external electric or magnetic field), g_j is an internal force, derived from elastic and viscous contribution (see below), and π_{ij} is a tensor coming from purely elastic effects:

$$\pi_{ij} = \frac{\partial W}{\partial n_{j,i}} \quad (4.16)$$

where $n_{j,i}$ is the shorthand form for $\partial n_j / \partial r_i$, and W is the nematic elastic energy

$$W = \frac{1}{2} K_{11} (\nabla \cdot \mathbf{n})^2 + \frac{1}{2} K_{22} (\mathbf{n} \cdot \nabla \times \mathbf{n})^2 + \frac{1}{2} K_{33} (\mathbf{n} \times \nabla \times \mathbf{n})^2 \quad (4.17)$$

where K_{11} , K_{22} and K_{33} are elastic constants. Terms dependent upon viscous properties are the stress tensor components

$$\sigma_{ij} = -p\delta_{ij} - \pi_{ik} \frac{\partial n_k}{\partial r_j} + \sigma'_{ij} \quad (4.18)$$

here σ'_{ij} is the contribution to the stress tensor coming from purely viscous effects

$$\begin{aligned} \sigma'_{ij} = & \alpha_1 n_k n_p A_{kp} n_i n_j + \alpha_2 n_i N_j + \alpha_3 n_j N_i \\ & + \alpha_4 A_{ij} + \alpha_5 n_i n_k A_{kj} + \alpha_6 n_j n_k A_{ki} \end{aligned} \quad (4.19)$$

In Eq. 4.19, α_i are the well-known Leslie's coefficients, which characterize, together with elastic constants, the nematic fluid under investigation; matrix A_{ij} is simply

$$A_{ij} = \frac{1}{2} \left(\frac{\partial v_i}{\partial r_j} + \frac{\partial v_j}{\partial r_i} \right) \quad (4.20)$$

and vector N_i is

$$N_i = \frac{dn_i}{dt} - \omega_{ij} n_j \quad (4.21)$$

where ω_{ij} is

$$\omega_{ij} = \frac{1}{2} \left(\frac{\partial v_i}{\partial r_j} - \frac{\partial v_j}{\partial r_i} \right). \quad (4.22)$$

Finally the internal force is given by

$$g_i = \lambda_L n_i - \frac{\partial W}{\partial n_i} - \gamma_1 N_i - \gamma_2 A_{ij} n_j \quad (4.23)$$

where λ_L is a Lagrange multiplier related to the constraint on the director components $n_i n_i = 1$, and $\gamma_1 = \alpha_3 - \alpha_2$, $\gamma_2 = \alpha_3 + \alpha_2$. LE equation are easily reduced to NS equation by neglecting all viscous coefficients except α_4 , provided that μ is identified with $\alpha_4/2$. Computational solutions of LE equations are difficult, due to their intrinsical non-linear character. In the present case, one should consider the simultaneous solution of Eqns. 4.14 and 4.15, in order to account exactly for backflow effects due to the director re-orientation on the fluid velocity, i.e. on the time evolution of the velocity field. It is however reasonable, in a first approximation, at least for the case of creeping flow, to consider the velocity field as a stationary and Newtonian quantity. In the recent past, exact numerical calculations for the interpretation of magneto-rheological experiments [360],[361],[362],[363] have shown that in most cases the velocity field can indeed be approximated by the stationary solution of NS equations. We shall therefore assume that components v_k entering director equations are *known functions* given by Eqns. 4.3) and 4.7 for a sphere and an ellipsoid, respectively. Writing explicitly the director equations one gets

$$\frac{\partial n_i}{\partial t} = \frac{\lambda_L n_i}{\gamma_1} + \omega_{ik} n_k - \frac{\gamma_2}{\gamma_1} A_{ik} n_k - v_k \frac{\partial}{\partial r_k} n_i + \frac{K}{\gamma_1} \frac{\partial^2}{\partial r_k^2} n_i + \frac{\Delta \chi B_i B_k}{\mu_0 \gamma_1} n_k \quad (4.24)$$

where the additional spherical approximation of elastic energy ($K_1 = K_2 = K_3 = K$) has been assumed for simplicity. The external force has been explicitly written as the result of a magnetic field \mathbf{B} coupled with the director [350]. Eq. 4.24 is only subject to the unitary constraint on the director components and to boundary and initial conditions.

4.4 Computational methodology

Our strategy is then the following: first we solve numerically for the director components in time and space, then we substitute in Eq. 4.4 to calculate the force acting on

the probe and the friction coefficient. We start by scaling Eqns. 4.24, by introducing a convenient set of characteristic quantities $v_i^* = v_i/V$, $r_i^* = r_i/R_{\text{eff}}$ and $t^* = Vt/R_{\text{eff}}$: as a characteristic length we use the effective radius for an ellipsoidal particle, coinciding with radius R for a sphere. Scaled director equations are then

$$\frac{\partial n_i}{\partial t^*} = \lambda n_i + \omega_{ik}^* n_k - \gamma A_{ik}^* n_k - v_k^* \frac{\partial}{\partial r_k^*} n_i + k \frac{\partial^2}{\partial r_k^{*2}} n_i + \delta \frac{B_i B_k}{B^2} n_k \quad (4.25)$$

where only three parameters (plus the ratio of the imposed external magnetic field components, which is essentially a geometrical factor) are left: $\gamma = \gamma_2/\gamma_1$, $k = K/\gamma_1 R_{\text{eff}} V$ and $\delta = \Delta\chi R_{\text{eff}} B^2/\mu_0 \gamma_1 V$. The first parameter, γ , is related to viscous effects directly influencing the director time evolution, depending upon Leslie viscosities α_2 , α_3 : notice that an indirect influence comes also from α_4 which enters the analytical expressions of the Newtonian velocities employed in the present approximate treatment, while the remaining viscous coefficients α_5 , α_6 do not influence the director dynamics. The second parameter k is proportional to the average elastic constant, of the order of magnitude of 10^{-11} N, and can be assumed of relatively small importance. The last parameter δ is likely to be relevant since it defines the influence of the magnetic field on the director motion. It depends on the radius of the probe and on its velocity.

In order to define completely the probe-fluid interaction, we need to establish boundary conditions of the director components on the probe surface. It is interesting to note that in Eq. 4.4 only the behavior of the director field on the surface is present, so that the correction to the isotropic friction coefficient is straightforward once a condition of *strong anchoring*, i.e. of fixed director orientation on the probe surface, $[n_i(t) = n_i^0 \text{ on surface}]$, is assumed. We shall discuss this limit case below, which corresponds essentially to an infinite anchoring energy of the probe surface on the director. More interesting is the case of *weak anchoring*, which corresponds to negligible anchoring energy. In the following we shall mostly concentrate on this case, which can be defined formally by assuming zero normal derivatives ($\partial n_i(t)/\partial \mathbf{m}=0$) of the director components on the surface. Finally, we shall limit our investigation to a few geometrical set-ups, namely spherical probes or prolate/oblate ellipsoids with an axis coincident with the direction of motion (for sake of simplicity, assumed to be the laboratory frame axis \mathbf{e}_3) and a magnetic field directed either parallel to the axis of

motion and perpendicular, e.g. along \mathbf{e}_1 . In other words the factor $B_i B_k / B^2$ will be chosen equal $\delta_{i,3} \delta_{k,3}$ (parallel) or parallel to the axis of motion $\delta_{i,1} \delta_{k,1}$ (perpendicular). The numerical solution of Eq. 4.25 and integration of Eq. 4.4 can be accomplished by defining a suitable grid of points in space and adopting a finite difference scheme to propagate in time the director components n_i , starting from some suitable initial condition. In the following we shall assume that initially the director is everywhere aligned with the imposed magnetic field. The time evolution of the director components is obtained by using a simple explicit time scheme. Discretisation in space is accomplished by using an almost regular cylindrical grid (cfr. Fig. 4-2), i.e. a regular cylindrical grid in the bulk, defined by cylindrical coordinates r_i^* , ϕ_j , z_k or cartesian coordinates $r_i^* \cos \phi_j$, $r_i^* \sin \phi_j$, z_k and an irregular grid for for the probe surface, where the director is calculated directly in the points generated by the intersection of the bulk grid and the surface itself. Once the director components are calculated in all

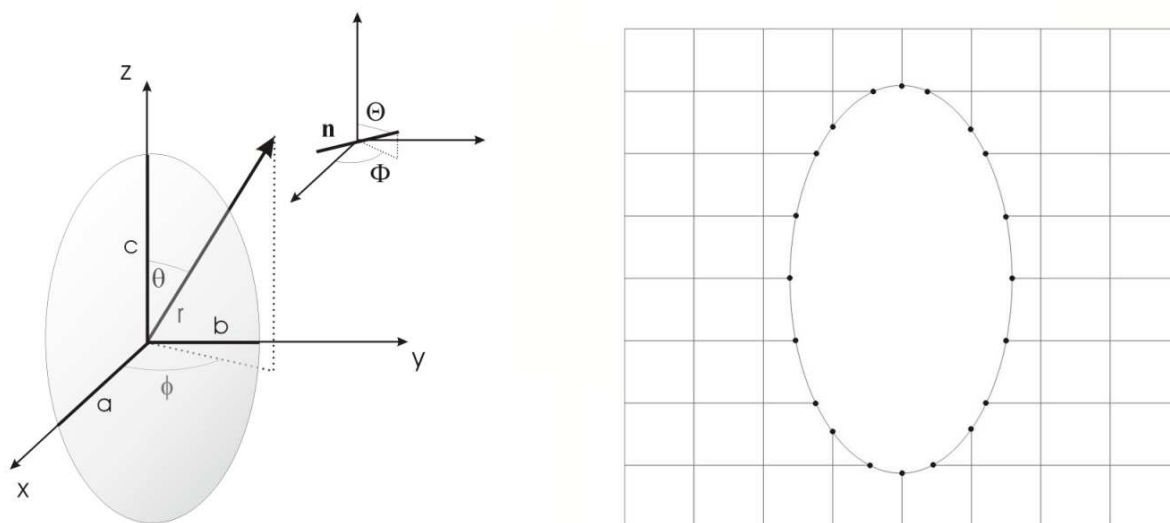


FIGURE 4-2: Polar coordinates for the position vector \mathbf{r} and for the director \mathbf{n} for the ellipsoidal case.

grid points at a given time, surface points only are employed to numerically integrate Eq. 4.4. We choose to solve for the director components in a finite cylindrical volume surrounding the probe. Naturally, other choices would have been possible, but in general they are much harder to implement and they do not improve significantly the

computational performances. For instance an adapted grid in ellipsoidal coordinates could have been used, which could have made easier accounting for points on the surface. However, the accuracy of the spatial derivatives calculated in non-Cartesian grids is usually less satisfactory. Implicit schemes in times could have been also employed, but we have found that a good accuracy of the numerical solution is assured nevertheless with an explicit scheme provided that smaller time steps are employed to assure stability. Periodic boundary conditions could have been implemented, but in practice in all the cases studied the influence of the probe motion on the director orientation is limited to a region two-three time larger than the probe dimension so that boundary spurious effects due to the finite volume are never observed, provided that a volume large enough is chosen: in our case we have simulated a cylindrical region with a radius ten times and height twenty times the probe radius, or effective radius in the case of ellipsoids. Calculation of the friction coefficient, based on Eq. 4.4, shows that friction is present only in the direction of motion of the probes, like in the isotropic fluid case. From Eq. 4.4, substituting the expression for the stress tensor of a nematic fluid, one can conveniently write the total friction acting on an ellipsoidal probe in rectilinear motion in a nematic fluid in the form

$$\xi_{\parallel,\perp} = \xi_{\text{iso}} c_{\parallel,\perp} \quad (4.26)$$

$$\xi_{\text{iso}} = 3\pi\alpha_4 R_{\text{eff}} \quad (4.27)$$

$$c = c_1 + c_2 + c_3 + 1 + c_5 + c_6 + c_{\text{el}} \quad (4.28)$$

where the isotropic term is simply obtained by Eq. 4.13 for $\mu = \alpha_4/2$, and the adimensional factors c_i come directly from the different terms entering the stress tensor σ_{ij} , and they are obtained numerically from Eq. 4.4: c is then a function of time, i.e. it is subject to change with the time evolution of the director configuration surrounding the probe, till a stationary configuration is reached. In all calculations, a grid of 75 (r_i^*) times 60 (ϕ_j) times 150 (z_k) points has been employed, with a time step equal to 0.0005 in scaled units.

4.5 Results

We discuss several sets of numerical and asymptotic results. First we shall present a simplified analysis for the case of a spherical probe in rectilinear motion in nematic MBBA, a well known liquid crystalline fluid. We assume an average elastic constant $K = 10^{-11}$ N; viscosity coefficients at 25° are reported in Table 4.1. Next we discuss a full solution for the case of spherical and ellipsoidal probes in MBBA, to underline the dependence of calculated friction upon the probe shape. Unless otherwise stated, we assume a unitary value for the ratio between the probe radius (or effective radius in the case of ellipsoidal probes) and velocity, and a value for the radius fixed to $100 \mu\text{m}$, and we study the director dynamics and friction coefficients by varying the scaled number δ . Finally, an analysis of simulations performed in other nematogens, namely PAA and 5CB, is provided.

$\alpha_i / \text{Pa s}$	MBBA [368]	PAA [369]	5CB [370]	E7
α_1	-0.0087	0.0043	-0.0066	0.006
α_2	-0.052	-0.0069	-0.07706	-0.013
α_3	-0.002	-0.0002	-0.0042	0.006
α_4	0.058	0.0068	0.0634	0.048
α_5	0.038	0.0047	0.0624	-0.045
α_6	-0.016	-0.0023	-0.0184	-0.026

TABLE 4.1: Leslie coefficients for three nematic liquid crystals phases.

4.5.1 Axially symmetric case

We start from a simple analytic calculation of the correction to the isotropic friction coefficient valid in the case of an axially symmetric system, by considering (i) a spherical probe, (ii) a director aligned with the direction of motion, i.e. $n_i = \delta_{i,3}$. This geometrical set-up will allow us to discuss simplified equations of motion for the director time evolution, and to illustrate anchoring effects. To simplify further the presentation, we shall neglect in this Section elastic and convective terms. We can write director components in the form $n_1 = \cos \Phi \sin \Theta$, $n_2 = \sin \Phi \sin \Theta$, $n_3 = \cos \Theta$. If r , ϕ and θ are polar coordinates in space, due to axial symmetry one has simply $\Phi = \phi$ and $\Theta = \Theta(\theta, r, t)$. By combining Eqns. 4.24, one can easily obtain an equation in the

unknown function Θ , which describes the time and space dependent angle between the local director and the symmetry axis:

$$\begin{aligned} \frac{\partial \Theta}{\partial t} &= \frac{1}{2} \left(r v_{\perp} - \frac{d v_{\parallel}}{d r} \right) \sin \theta - \frac{\gamma_2}{2 \gamma_1} \left[\left(r v_{\perp} + \frac{d v_{\parallel}}{d r} \right) \sin (\theta - 2 \Theta) + \right. \\ &\quad \left. + r^2 \frac{d v_{\perp}}{d r} \cos \theta \sin 2 (\theta - \Theta) \right] - \frac{\Delta \chi B^2}{2 \mu_0 \gamma_1} \sin 2 \Theta \end{aligned} \quad (4.29)$$

where the components of the Newtonian velocity field are written as $v_1 = v_{\perp} r_1 r_3$, $v_2 = v_{\perp} r_2 r_3$, $v_3 = v_{\perp} r_3^2 + v_{\parallel}$ and

$$v_{\perp} = \frac{3 R V}{4 r^3} \left(\frac{R^2}{r^2} - 1 \right) \quad (4.30)$$

$$v_{\parallel} = V \left[1 - \frac{R}{4 r} \left(\frac{R^2}{r^2} + 3 \right) \right] \quad (4.31)$$

On the probe surface, the scaled form of Eq. 4.29 assumes a particularly simple form:

$$\frac{\partial \Theta}{\partial t^*} = \frac{3}{4} \{ \sin \theta + \gamma [\sin (\theta - 2 \Theta) - \cos \theta \sin 2 (\theta - \Theta)] \} - \frac{1}{2} \delta \sin 2 \Theta \quad (4.32)$$

Calculation of corrective terms c_i is now relatively easy, and for completeness we report here the complete expressions. From Eq. 4.4 one gets

$$c_1 = \frac{\alpha_1}{\alpha_4} \int_0^{\pi} d \theta \sin \theta \cos \Theta \cos^2 (\theta - \Theta) [\cos \theta \cos (\theta - \Theta) - \cos \Theta] \quad (4.33)$$

$$c_2 = \frac{\alpha_2}{\alpha_4} \int_0^{\pi} d \theta \sin \theta \cos \Theta \sin (\theta - \Theta) \left(-\frac{1}{2} \sin \theta + \frac{2}{3} \frac{\partial \Theta}{\partial t} \right) \quad (4.34)$$

$$c_3 = \frac{\alpha_3}{\alpha_4} \int_0^{\pi} d \theta \sin \theta \sin \Theta \cos (\theta - \Theta) \left(\frac{1}{2} \sin \theta - \frac{1}{3} \frac{\partial \Theta}{\partial t} \right) \quad (4.35)$$

$$\begin{aligned} c_5 &= \frac{\alpha_5}{\alpha_4} \int_0^{\pi} d \theta \sin \theta \cos \Theta \left[\frac{1}{4} \sin 2 \theta \sin \Theta + \right. \\ &\quad \left. + \cos^2 \theta \cos \Theta - \frac{1}{2} \cos \Theta (1 + \cos^2 \theta) \right] \end{aligned} \quad (4.36)$$

$$\begin{aligned} c_6 &= \frac{\alpha_6}{\alpha_4} \int_0^{\pi} d \theta \sin \theta \cos (\theta - \Theta) \left[\sin \Theta \sin \theta \left(\cos^2 \theta - \frac{1}{2} \right) + \right. \\ &\quad \left. + \cos \Theta \cos \theta (\cos^2 \theta - 1) \right] \end{aligned} \quad (4.37)$$

We can further simplify our result assuming a fixed director orientation on the probe surface. This case can also be considered as the limit behavior of a spherical probe moving along the director axis of a nematic sample perfectly aligned (infinite magnetic

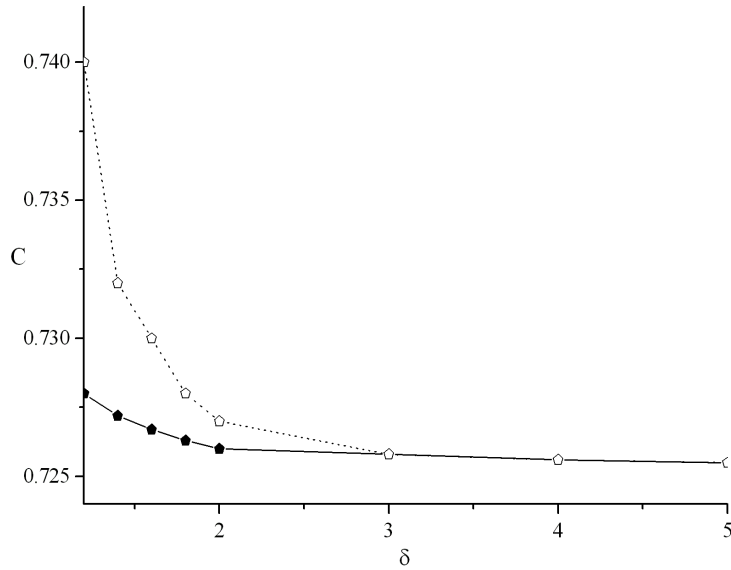


FIGURE 4-3: Adimensional Stokes coefficients versus δ parameter, for the case of a spherical probe in MBBA, calculated according to Eq. 4.32 for weak anchoring (dot line) and compared to the asymptotic value obtained from Eq. 4.38 (full line).

field or $\delta \rightarrow \infty$). The adimensional Stokes factor is obtained by putting $\Theta=0$ (perfect alignment) in the integral expressions of c_i ; one gets:

$$\alpha_4 c = \frac{4}{15}\alpha_1 + \frac{2}{3}\alpha_2 + 1 + \frac{2}{3}\alpha_5 + \frac{4}{15}\alpha_6 \quad (4.38)$$

In Fig. 4-3 we show the dependence of the adimensional coefficient as obtained from Eq. 4.32 and Eq. 4.38. Notice that the friction is significantly smaller (25 %) that in the isotropic case and that only for value of $\delta > 2$, typical of magnetic fields larger that 3 Tesla for the geometry considered here, the asymptotic expression 4.38 is acceptable.

4.5.2 Shape probe dependence

Let us now analyze the director behavior and friction coefficients for the case of a moving spherical probe in MBBA, predicted by the full solution of Eq. 4.25. We start by discussing the director behavior in time and space. In Fig. 4-4 the time evolution of the director field is represented for the case of the rectilinear motion of a spherical particle in MBBA along the external magnetic field (a) and perpendicular to

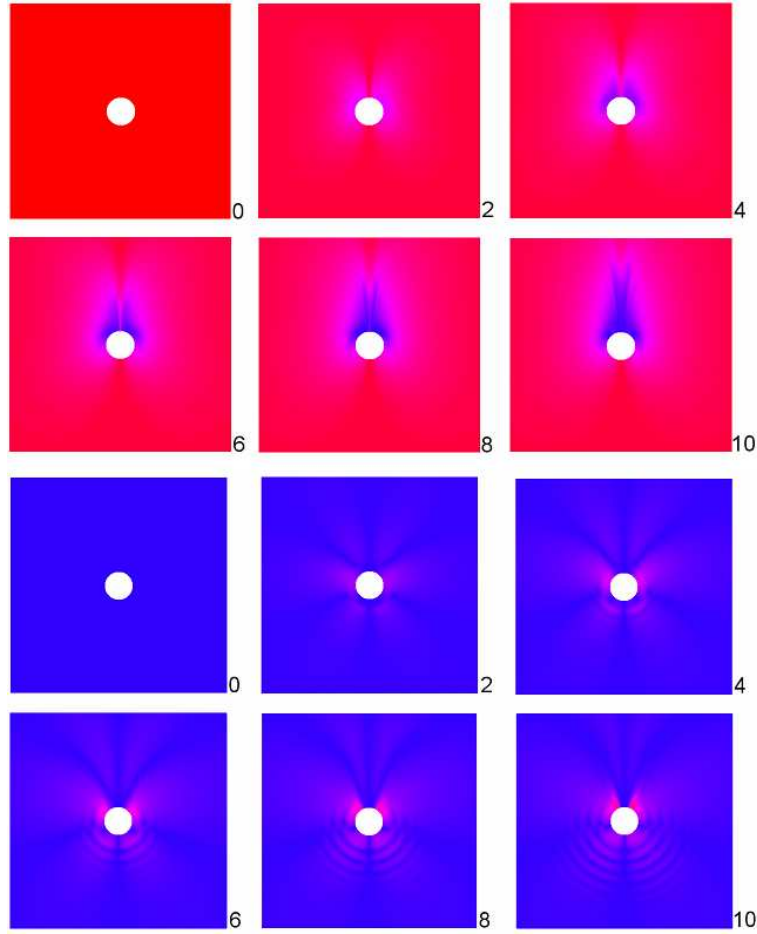


FIGURE 4-4: Time evolution of director field, for a spherical probe in MBBA, $R/V = 1$, $R = 100 \mu\text{m}$ and $\delta = 0.2$: direction of motion parallel to field (red) and perpendicular (blue).

the external magnetic field (b), for a value of $\delta = 0.2$. Here and in the following figures we adopt a color scale to represent the director angle with axis of motion \mathbf{e}_3 , in the plane $\mathbf{e}_1\mathbf{e}_3$. Notice that in the perpendicular case the system is not axially symmetric, so that a slight dependence of the director patterns is observed by changing the plane of section. The scale goes from blue (director aligned with the axis of motion) to red (director perpendicular to the axis of motion). Each snapshot shows the director pattern at a given scaled time: the probe is fixed in space and the fluid is moving from top to bottom. The initial state is chosen to be of perfectly alignment with the field in both cases. The first observation which can be made is that the disturbance in the director field is larger in the perpendicular case, while in the parallel case is limited to a close lateral area surrounding the probe. Several factors are influencing the director

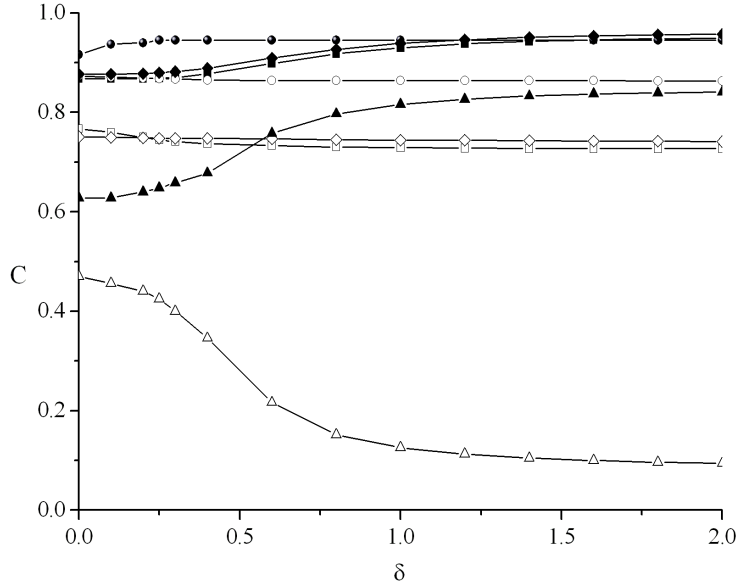


FIGURE 4-5: Stationary adimensional friction factor, in MBBA (squares), PAA (circles), 5CB (diamond) and E7 (triangle) for $\delta = 0.2$ for a sphere; empty symbols are for the case of parallel magnetic field and full symbols for the case of perpendicular magnetic field.

time evolution: for instance the magnetic torque tends to minimize the director motion, since the initial configuration is fully aligned (minimal magnetic free energy), while the fluid motion acts in a more complex way, although basically it favors alignment of the director along the direction of motion. From other calculation it is possible to observe that at low field the director is significantly modified from the initial configuration for the parallel and the perpendicular case. If we increase the intensity of the field, the perturbation induces by the particle decreases and the director remains parallel to the magnetic field. For this reason we choose a low value for the magnetic field. A stationary state is reached at slightly later times in the perpendicular case, thus causing a longer transition regime corresponding to a time dependent friction coefficient. In Fig. 4-5 we show the time evolution of the friction factors c_i with time for the motion of a spherical probe in the parallel (a) and perpendicular case (b). As expected, the elastic contribution is negligible compared to strictly viscous terms: c_2 , c_5 are the largest terms, although they are comparable in magnitude and opposite in sign; c_1 , c_3 and c_6 are negligible. A discussion in more general terms is hardly possible, since each factor has a complex dependence upon the set of viscous coefficients α_i , typical for

a particular liquid crystalline phase. We shall compare later the variation of friction coefficients in different liquid crystals. Notice that the overall time dependence of the single factors is more accentuated, whereas the total correction factor c reaches rapidly a stationary value. Next, let us consider the director field patterns which are

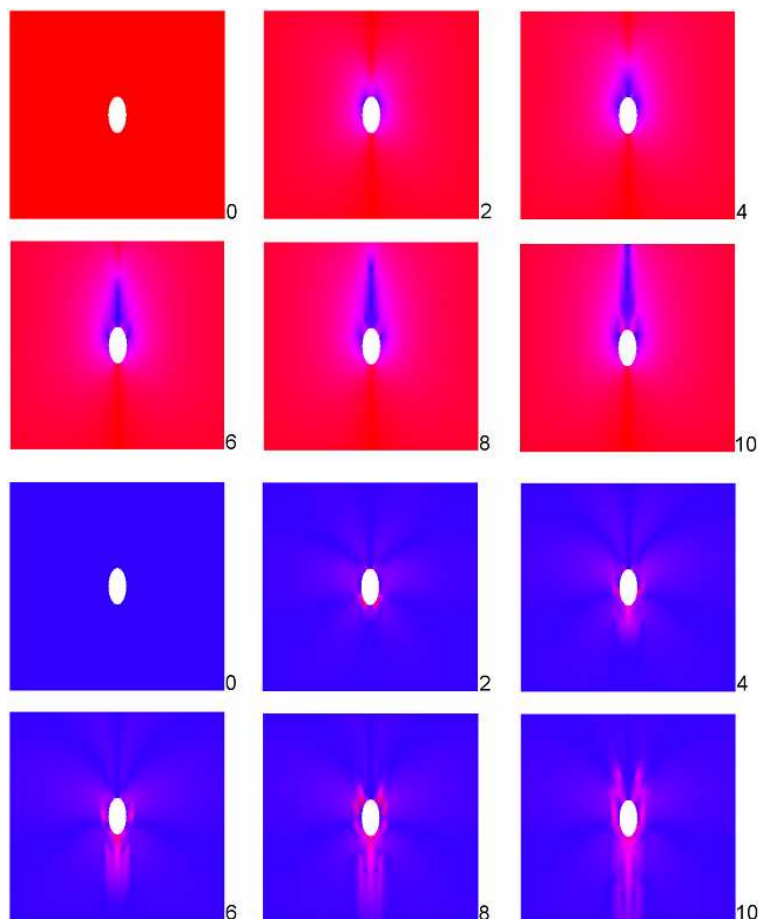


FIGURE 4-6: Time evolution of director field, for a prolate ellipsoidal probe in MBBA, $R_{\text{eff}}/V=1$, $R_{\text{eff}}=100 \mu\text{m}$ and $\delta=0.2$: direction of motion parallel to field (red) and perpendicular (blue).

created by a moving ellipsoidal particle. We consider here only rotation ellipsoids, defined by an effective radius $R_{\text{eff}}=100 \mu\text{m}$ and a ratio $R_{\text{eff}}/V=1$; we distinguish our discussion between prolate ellipsoid, i.e. having semiaxes $a_1 = a_2 < a_3$ and oblate ellipsoid, $a_1 = a_2 > a_3$. With respect to the spherical probe, the prolate ellipsoidal probe is responsible of a more localized disturbance of the director orientation in the front and rear regions, without perturbing significantly the lateral regions. Fig. 4-6. The perturbation caused by the probe motion propagates faster, and in general causes

the director to orient in a direction perpendicular to the probe direction of motion in the front region, whereas a tail with the director parallel to the velocity flux is always present in the rear region: this is true both for the case of orienting magnetic parallel to the probe velocity (a) and perpendicular (b). In the oblate ellipsoidal case, shown

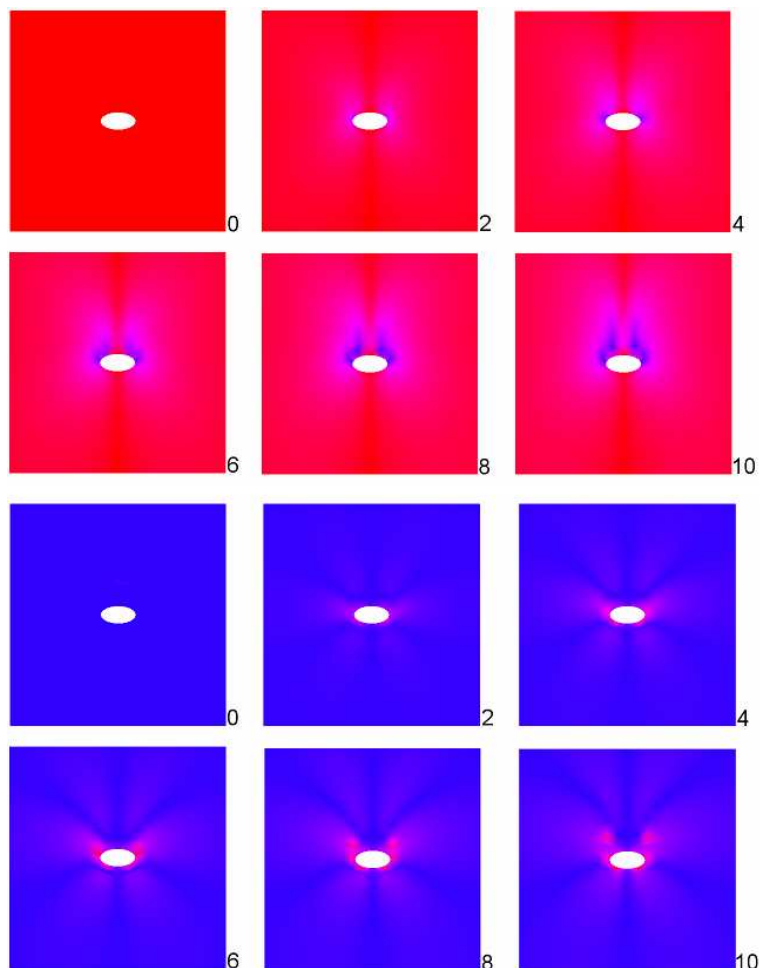


FIGURE 4-7: Time evolution of director field, for an oblate ellipsoidal probe in MBBA, $R_{\text{eff}}/V=1$, $R_{\text{eff}}=100 \mu\text{m}$ and $\delta=0.2$: direction of motion parallel to field (red) and perpendicular (blue).

in Fig. 4-7, the disturbance caused by the probe motion is more extended laterally and propagates slower than in the spherical case. The tail in the rear region is weak, especially for the case of magnetic field perpendicular to the direction of motion. The friction coefficients c_i and the total adimensional friction factor c can be calculated for the ellipsoidal probes exactly by the same procedure already employed for the spherical probe. The time dependence of the friction coefficients is analogous, and a stationary

value of c can be calculated. In general, the more prolate is the shape of the ellipsoidal probe, the more favored is the motion, i.e. the smaller is the friction coefficient c . In

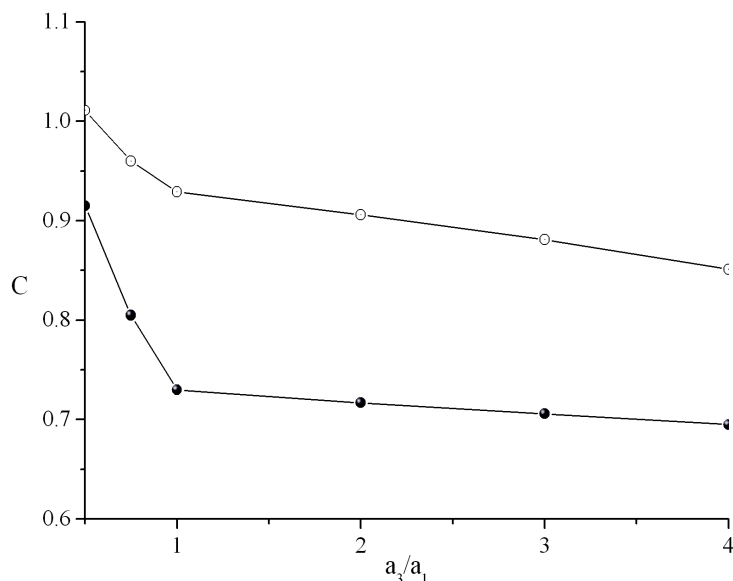


FIGURE 4-8: Stationary adimensional friction coefficient c of a ellipsoid moving in rectilinear motion in MBBA $R_{\text{eff}}/V = 1$, $R_{\text{eff}} = 100 \mu\text{m}$ and $\delta = 2$, as function of a_3/a_1 .

Fig. 4-8 we show the calculated stationary friction coefficient for $\delta = 2$, always for $R_{\text{eff}} = 100 \mu\text{m}$ and a ratio $R_{\text{eff}}/V = 1$, as a function of the ratio a_3/a_1 .

4.5.3 Viscoelastic parameters dependence

We can now consider the calculation of the stationary adimensional friction factor c in different liquid crystals, or more exactly in nematic liquid crystalline fluids described by different sets of viscous numbers α_i , reported in Table 4.1. For simplicity, we shall choose the same geometrical set-ups described in the previous section, namely a sphere, a prolate ellipsoid and an oblate ellipsoid with same effective radius of $100 \mu\text{m}$, unitary ratio between radius and velocity and $\delta = 0.2$. We also fix arbitrarily $K = 1 \times 10^{-11} \text{ N}$ for all cases considered. We organize our findings in Fig. 4-9, which is divided in three parts: sphere (a), prolate ellipsoid (b) and oblate ellipsoid (c). In all cases the friction factor is smaller than one, meaning that the overall friction correction is negative, i.e. the anisotropy of the nematic phase *favours* the probe

motion. This effect is accentuated when the direction of motion is parallel to the direction of the orienting magnetic field, whereas the correction is less important for perpendicular magnetic field. In general, the correction to the isotropic friction is not larger than 20 %. Both the spherical and prolate ellipsoidal probes cause a larger correction in the friction coefficients, while the oblate ellipsoidal probe does not have an anisotropic friction coefficient much different from the isotropic one, in accordance with the limited perturbation of the director configuration observed and discussed in the previous section.

4.5.4 Comparison with experimental data

The calculation of the translational friction coefficients is connected with the calculation of the perpendicular and parallel translational diffusion coefficients with the Stokes-Einstein Law [364]

$$\xi_{\parallel,\perp} 3\pi\alpha_4 c_{\parallel,\perp} R = \frac{k_B T}{D_{\parallel,\perp}} \quad (4.39)$$

The translational diffusion coefficients in thermotropic or lyotropic liquid crystals can be experimentally calculated using several techniques. These techniques can be applied to a large variety of systems that have great importance to biology, physics or technological applications. The systems under investigation in this work are colloidal dispersions particle in a size range from 50 nm to 100 μm that include spherical shape probe as latex particles [327], silica particles [335], FeSnO_3 [365] clusters or a silicon oil [366],[367], a copolymer of dymethylsiloxane and methylphenylsiloxane) or ellipsoidal probe as the *fd* virus [344]. In Table 4.2 we present the comparison between the experimental and the calculated translational diffusion coefficients for the systems in different nematic liquid crystals. The parallel diffusion coefficient for spherical systems (latex particles, silica particles, FeSnO_3 clusters and silicon oil) is obtained by the Eq. 4.39 where the temperature, c factor and depend on the nematic host. The effective radius of the system is reported in the relative articles. In Table 4.2 a value of 0.4 μm for the FeSnO_3 clusters but in the ref. [365] is radii in a range from 0.4 to 0.8 μm are presented; thus we estimate translational diffusion coefficients ranging from 3.9

System	Nematic	Radius	$D_{\parallel}^{calc.} / \text{m}^2 \text{s}^{-1}$	$D_{\parallel}^{exp.} / \text{m}^2 \text{s}^{-1}$
Latex particle [327]	CsPFO	60 nm	1.2×10^{-13}	1.15×10^{-13}
Silica particles [335]	5CB	92 nm	9.9×10^{-14}	8.8×10^{-14}
<i>fd</i> virus [344]	<i>fd</i> virus	173.6 nm	1.0×10^{-13}	1.3×10^{-13}
FeSnO ₃ [365]	EBBA	0.4 μm	3.9×10^{-14}	3.2×10^{-14}
Silicon oil [366]	5CB	0.55 μm	1.7×10^{-14}	1.1×10^{-14}
Silicon oil [367]	E7	1 μm	0.9×10^{-14}	0.8×10^{-14}

TABLE 4.2: Comparison between the calculated and experimental values for the translational diffusion coefficient for different chemical systems. A detailed description of the specific characteristic of the systems are reported in the text.

$\times 10^{-14}$ to $1.9 \times 10^{-14} \text{ m}^2 \text{ s}^{-1}$; the only experimental value reported is $3.2 \times 10^{-14} \text{ m}^2 \text{ s}^{-1}$. The *fd* virus have a length 880 nm with a diameter of 6.6 nm [344] and for this physical characteristic we calculated the effective radius with the Eq. 4.12 of a ellipsoidal probe with semiaxis $a_1 = a_2 = 6.6 \text{ nm}$ and $a_3 = 880 \text{ nm}$. The effective radius obtained by calculations is 173.6 nm. The last system reported in Table 4.2 is a silicon oil in E7 and the "experimental data" reported for the translational diffusion coefficient is a MD simulation [367] obtained from the Brownian trajectory of a 1 μm diameter droplet embedded in a nematic phase. In this simulation Loudet [367] works with a very dilute suspensions, with noninteracting quadrupoles. They analyze the Brownian fluctuations and determined the particle positions at regular time step. The self-diffusion coefficient of a random walker, in a nematic phase, has a rotational symmetry axis and the Brownian motion is governed by two independent diffusional coefficients, characterized by a diffusion along and perpendicular to the director. From the analysis of the Brownian fluctuations they derive these coefficients. The value obtained from the model is in accordance with the MD simulation too. In the range of dimension of the colloidal suspensions the methodology permits to obtained a good accordance between the experimental and the calculate data independently by the shape or the dimension of the probe or the kind of nematic used in the experiments.

4.6 Conclusions

To summarize, we have analyzed the dynamical behavior of low viscosity nematic liquid crystals in presence of micro-size probes. In particular, we study the translational fric-

tion coefficients of spherical and ellipsoidal probes moving in nematic liquid crystalline fluids, by solving numerically the constitutive hydrodynamic equations of nematics. The evaluation of the translational friction coefficients is based on a numerical solution of Leslie-Ericksen constitutive equations for the case of incompressible nematic fluids. The nematic medium is described by a vector field which specifies the director orientation in each point and by the velocity vector field. Simulation of director dynamics surrounding the moving probe are presented, and the dependence of translational diffusion upon liquid crystal viscoelastic parameters is discussed. The time evolution of director field, described by Leslie-Ericksen equations, is studied in the presence of an orienting magnetic field in two characteristic situations: director of motion parallel and perpendicular to field. A good accordance between experimental and calculated data has been obtained, independently from the shape or the dimension of the probe or the kind of nematic used in the experiments. Naturally, the computational prediction of the model becomes less favorable when the dimension of the probe is smaller (> 30 nm). Substantial departures from a continuum description have to be expected when probe dimensions are starting to be comparable with solvent molecular dimensions, and therefore purely hydrodynamic interpretations are less reliable. Nevertheless, the present methodology is able to describe friction properties of dispersed particles of micron dimensions, at the cost of a modest computational effort.

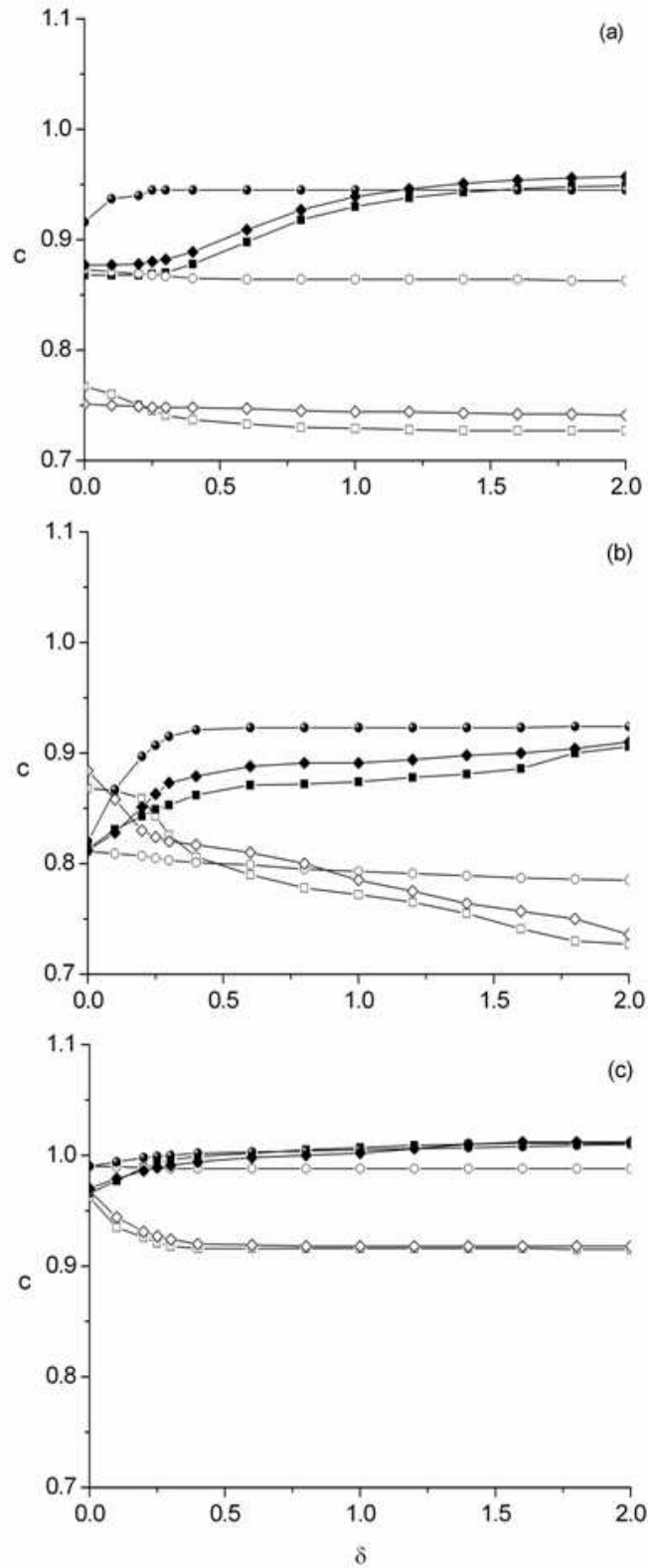


FIGURE 4-9: Stationary adimensional friction factor c , in MBBA (squares), PAA (circles), 5CB (diamonds) (cfr. Table 4.1), for $\delta=0.2$ for a sphere (a), a prolate ellipsoid (b) and an oblate ellipsoid (c); empty symbols are for cases of parallel magnetic field, full symbols for cases of perpendicular magnetic field.

Chapter 5

Conclusions

The relationship between spectroscopic measurements and molecular properties can be gathered only indirectly, that is, structural and dynamic molecular characteristics can be inferred by the systematic application of modeling and numerical simulations to interpret experimental observables. A straightforward way to achieve this goal is the employment of spectroscopic evidence as the "target" of a fitting procedure of molecular, mesoscopic and macroscopic parameters entering the model. A more refined methodology is based on the combination of quantum mechanical calculations of structural parameters possibly including environmental and fast vibrational and librational averaging, and direct feeding of calculated molecular parameters into dynamic models based on molecular dynamics, coarse grain dynamics, and above all stochastic modeling or a combination of the three. Our main objective in this work has been to discuss the degree of advancement of complementary integrated computational approaches to the interpretation of fluorescence emission of organic molecules in solvated environments, CW-ESR spectroscopy and rheological properties of ordered systems via combination of advanced quantum mechanical approaches, stochastic modeling of relaxation processes, and, in the last case, macroscopic models. In the first case we have shown that the model proposed is able to reproduce the spectral position and shape of the emission spectra. In particular the model reproduces the red shift expected for TICT excited states when the dielectric constant of the solvent increases. The combination of stochastic methods and QM calculation of PES/charge distributions for describing the static and dynamic properties of complex molecules in polar solvents

is based on a combination of continuum treatment (the solvent as a dielectric and/or hydrodynamic fluid) and detailed solute dynamics. Next, we have reported a detailed analysis of the structural and magnetic properties of a double labeled peptide by an integrated computational and experimental strategy. From a chemical point of view, our results provide evidence on the property of Aib-rich peptides of changing their conformation from 3_{10} - to α -helix as a function of increasing polarity and hydrogen-bond donor capability of the solvent: α -helix in a protic solvent and at low temperature, whereas 3_{10} -helix in aprotic solvents. Finally, the purpose of the last example has been to analyze the dynamical behavior of a low viscosity nematic liquid crystals in the presence of a micro-size spherical probe in rectilinear motion, by solving numerically, within clearly stated approximation valid in the case of micrometric objects immersed in a continuous anisotropic medium. To this aim, a very simple computational scheme has been employed based on a non-uniform spatial discretization and an explicit propagation in time.

Appendix A

The time dependent emission fluorescence signal

The emission spectrum $I(t)$ of an excited singlet state can be written as a double integral over all the ground and excited states configuration, where each conformation is represented by a point of phase space, which includes all relevant degrees of freedom of the molecule (e.g. space orientation of the molecular frame, conformational internal degrees of freedom, local solvent variables, etc.). The definition of the observable $I(t)$ is quite general. For the case of experiments performed in linearly polarized light, the signal is given, neglecting constant factors depending on the instrumental apparatus, by the expression

$$\begin{aligned} I(\omega_A, \omega_B, t) &= \int d\mathbf{Q}_0 d\mathbf{Q} [\mathbf{e}_A \cdot \boldsymbol{\mu}_A(\mathbf{Q}_0)]^2 g_A[\omega_A - \Delta\omega(\mathbf{Q}_0)] P^{(0)}(\mathbf{Q}_0) \\ &\times [\mathbf{e}_E \cdot \boldsymbol{\mu}_E(\mathbf{Q})]^2 g_E[\omega_E - \Delta\omega(\mathbf{Q})] P(\mathbf{Q}_0, \mathbf{Q}, t) \end{aligned} \quad (\text{A.1})$$

where \mathbf{Q}_0 and \mathbf{Q} represent a given configuration of the ground and the excited state respectively. Here $\mathbf{e}_{A,B}$ are the directions of the polarization vectors for the exciting and detected light, $\boldsymbol{\mu}_A(\mathbf{Q}_0)$ and $\boldsymbol{\mu}_B(\mathbf{Q})$ are the transition dipole moments; $\omega_{A,B}$ are the absorption and emission frequencies; $g_{A,B}$ are band-shape functions in absorption and emission, centered on the frequencies $\Delta\omega(\mathbf{Q}_0)$ and $\Delta\omega(\mathbf{Q})$, respectively, related to the difference in energy between the two states for a given point \mathbf{Q}_0 and \mathbf{Q} of the phase

space, $\Delta\lambda(\mathbf{Q}) = (E_1(\mathbf{q}) - E_0(\mathbf{Q}))/\hbar$

$$\Delta\lambda(\mathbf{Q}) = \frac{hc}{E_1(\mathbf{Q}) - E_0(\mathbf{Q})} \quad (\text{A.2})$$

The Eq. A.1 requires the knowledge of the Boltzmann equilibrium distribution for the ground state, $P^{(0)}(\mathbf{Q}_0)$, and the distribution at the time t for the excited state, $P(\mathbf{Q}_0, \mathbf{Q}, t)$. We now introduced the time evolution operator $\hat{\Gamma}$

$$\frac{\partial}{\partial t} P(\mathbf{Q}_0, \mathbf{Q}, t) = - [\hat{\Gamma} + f_B(\mathbf{Q})] P(\mathbf{Q}_0, \mathbf{Q}, t) + S(\mathbf{Q}_0, \mathbf{Q}, t) \quad (\text{A.3})$$

The time evolution includes a source term $S(\mathbf{Q}_0, \mathbf{Q}, t)$ and a sink term $f_B(\mathbf{Q})$. Considering the initial condition $P(\mathbf{Q}_0, \mathbf{Q}, t) = 0$ and obtain the formal solution

$$P(\mathbf{Q}_0, \mathbf{Q}, t) = \int_0^t d\tau \exp(-[\hat{\Gamma} + f_B(\mathbf{Q})]\tau) S(\mathbf{Q}_0, \mathbf{Q}, t - \tau) \quad (\text{A.4})$$

To solve the Eq. A.3 we consider some initial hypothesis: (i) the sink source $f_B(\mathbf{Q})$, responsible for the decay of the population of the excited state is taken as a simple exponential decay, (ii) the source function is chosen as the product of two Dirac delta functions in space and in time $S = \delta(\mathbf{Q}_0 - \mathbf{Q})\delta(t)$, (iii) the dependence of the band shape function, $g_A[\omega_A - \Delta\omega(\mathbf{Q}_0)]$ upon \mathbf{Q}_0 is neglected and (iv) we considered the conditions for depolarized light. From the Eq. A.1 we obtained

$$I(\omega, t) \propto \omega^3 \int d\mathbf{Q} k_B(\mathbf{Q}) g[\omega - \Delta\omega(\mathbf{Q})] P(\mathbf{Q}, t) \quad (\text{A.5})$$

where $k_B(\mathbf{Q})$ is the average emission factor that depends on the geometry of the excited state. The time dependent population $P(\mathbf{Q}, t)$ is defined as

$$P(\mathbf{Q}, t) = \int d\mathbf{Q}_0 P(\mathbf{Q}_0, \mathbf{Q}, t) P^{(0)}(\mathbf{Q}_0) \quad (\text{A.6})$$

and in the particular case in which S is defined as a Dirac function the Eq. A.6 became

$$P(\mathbf{Q}, t) = \{1 - \exp[\hat{\Gamma} + f_B] t\} P_{st}(\mathbf{Q}) \quad (\text{A.7})$$

where the stationary population $P_{st}(\mathbf{Q})$ for the excited state is calculable as

$$P_{st}(\mathbf{Q}) = (\hat{\Gamma} + f_B)^{-1} P^{(0)}(\mathbf{Q}) \quad (\text{A.8})$$

The Eq. A.5 is the general form of the Eq. 2.1 used in the model as definition of the time dependent emission fluorescence signal.

Appendix B

Analysis of the translational and rotational motions

All the equations in Chapter 2 describe a molecular system dependent on the torsional angle and on the solvent coordinates. In general the description of the system depend on a minimal set of coordinates that consider the internal geometry and the solvent degrees of freedom. For this model the set of coordinates that specify the total configuration of the molecular system is chosen as: the position of the molecule in the laboratory frame LF is given by a vector ${}^L\mathbf{r}$, a set of Euler angles $\boldsymbol{\Omega}_{MF} = \alpha, \beta, \gamma$ define the orientation respect to the molecular frame MF and the internal rotation φ define the torsional angle between the donor and the acceptor group. An additional set of variables, represented by the vector ${}^L\mathbf{X}$, defined in the LF, describe the local polarization of the solvent. The potential energy of the system is given

$$\begin{aligned} E_n({}^L\mathbf{r}, \boldsymbol{\Omega}_{MF}, \varphi, {}^L\mathbf{X}) &= \varepsilon_n({}^L\mathbf{r}, \boldsymbol{\Omega}_{MF}, \varphi) - \frac{1}{2}\mu_n({}^L\mathbf{r}, \boldsymbol{\Omega}_{MF}, \varphi)\mathbf{F}_\infty\mu_n({}^L\mathbf{r}, \boldsymbol{\Omega}_{MF}, \varphi) \\ &- \mu_n({}^L\mathbf{r}, \boldsymbol{\Omega}_{MF}, \varphi){}^L\mathbf{X} + \frac{1}{2}{}^L\mathbf{X} \cdot \mathbf{F}_{or}^{-1} \cdot {}^L\mathbf{X} \end{aligned} \quad (\text{B.1})$$

All the terms are already explained in the Chapter 2. The tensor $\mathbf{F}_{or}, \mathbf{F}_\infty$ and \mathbf{F}_0 are assumed as diagonal tensor in the LF. In an isotropic medium the tensors \mathbf{F} can be consider as scalar values, $\mathbf{F}_{or, \infty} = F_{or, \infty}\mathbf{1}$. With this consideration the PES in Eq. B.1 become the Eq. 2.5. As the PES the time evolution operator $\hat{\Gamma}$ can be defined respect

to the complete set of coordinates:

$$\begin{aligned}\hat{\Gamma}_n &= - \left(\frac{\partial}{\partial^L \mathbf{r}} \hat{\mathbf{M}} \frac{\partial}{\partial \varphi} \right)^{tr} \cdot {}^L \mathbf{D}_n \cdot P_{eq,n}(\mathbf{Q}) \begin{pmatrix} \frac{\partial}{\partial^L \mathbf{r}} \\ \hat{\mathbf{M}} \\ \frac{\partial}{\partial \varphi} \end{pmatrix} P_{eq,n}^{-1}(\mathbf{Q}) \\ &- \left(\frac{\partial}{\partial^L \mathbf{X}} \right)^{tr} \cdot \mathbf{D}_S \cdot P_{eq,n}(\mathbf{Q}) \left(\frac{\partial}{\partial^L \mathbf{X}} \right) P_{eq,n}^{-1}(\mathbf{Q})\end{aligned}\quad (\text{B.2})$$

The two tensors ${}^L \mathbf{D}_n$ and \mathbf{D}_S are associated to the translational, global rotational and internal rotational of the φ angle of the molecule and to the solvent polarization, respectively. Both tensors are defined in the LF. The diffusion tensor ${}^L \mathbf{D}_n$ is a matrix dependent on the translational, rotational and variation of the torsional angle:

$${}^L \mathbf{D}_n = \begin{pmatrix} {}^L \mathbf{D}_{TT,n} & {}^L \mathbf{D}_{TR,n} & {}^L \mathbf{D}_{TI,n} \\ {}^L \mathbf{D}_{TR,n}^{tr} & {}^L \mathbf{D}_{RR,n} & {}^L \mathbf{D}_{RI,n} \\ {}^L \mathbf{D}_{TI,n}^{tr} & {}^L \mathbf{D}_{RI,n}^{tr} & {}^L D_{II,n} \end{pmatrix}\quad (\text{B.3})$$

After this general definition of the static and the dynamic parts of the model we evidence the dependence on translation and rotational motions. In an isotropic medium the potential energy surface and the dynamics of the system are dependent on the molecular motions. If we focus the attention only on the translational motions we observed that the definition of the PES does not explicitly depend on the translational degrees of freedom: PES is invariant respect to ${}^L \mathbf{r}$. Considering this behavior it is possible to neglect in a complete way the dependence on the translational coordinates. We can neglect this dependence considering to develop the exponential operator in Eq. A.7 and integrating respect to the translational coordinates. So we obtain all the preview expressions but without translational terms. The new set of variable that describe the system is now $\mathbf{Q} = (\boldsymbol{\Omega}_{MF}, \varphi, {}^L \mathbf{X})$. In the new definition the diffusion tensor depends on the rotational terms and on the internal degrees of freedom:

$${}^L \mathbf{D}_n = \begin{pmatrix} {}^L \mathbf{D}_{RR,n} & {}^L \mathbf{D}_{RI,n} \\ {}^L \mathbf{D}_{RI,n}^{tr} & {}^L D_{II,n} \end{pmatrix}\quad (\text{B.4})$$

In the presence of magnetic or electric external non homogeneous fields or translational anisotropic fluid phases (smectic) it is necessary to consider the translational coordinates effects. It is possible to neglect the dependence on the rotational coordinates too

but the calculations are more complex. In the laboratory frame LF the model is apparently dependent on the rotational motion. If we consider a frame fixed on the molecule the dependence on the rotational motion is vanished. A frame fixed on the molecule (molecular frame MF) moves with the rotation hence it results invariant respect to the rotation. We redefine all the variables defined in the MF

$$\begin{aligned}
{}^L X_i &= \sum_j E_{ij} X_j \\
\frac{\partial}{\partial {}^L X_i} &= \sum_j E_{ji} \frac{\partial}{\partial X_j} \\
{}^L \hat{M}_i &= \sum_j E_{ij} \left[\hat{M}_i + (\hat{M}_i X_j) \frac{\partial}{\partial X_j} \right] = \sum_j E_{ij} \left[\hat{M}_i - X_{ij}^\times \frac{\partial}{\partial X_j} \right]
\end{aligned} \tag{B.5}$$

where the symbol X_i is the vectorial solvent coordinate in the MF. In the MF and considering the coupling with the isotropic medium the diffusion tensor become

$$\mathbf{D} = \begin{pmatrix} \mathbf{D}_{RR,n} & \mathbf{D}_{RI,n} & -\mathbf{D}_{RR,n} \mathbf{X}^\times \\ \mathbf{D}_{RI,n}^{tr} & D_{II,n} & -\mathbf{D}_{RI,n}^{tr} \mathbf{X}^\times \\ -(\mathbf{X}^\times)^{tr} \mathbf{D}_{RR,n} & -(\mathbf{X}^\times)^{tr} \mathbf{D}_{RI,n} & D_S \mathbf{1} \end{pmatrix} \tag{B.6}$$

The symbol \mathbf{a}^\times represents a matrix 3×3 connected with the generic vector \mathbf{a} and defined as

$$\mathbf{a}^\times = \begin{pmatrix} 0 & a_z & -a_y \\ -a_z & 0 & a_x \\ a_y & -a_x & 0 \end{pmatrix} \tag{B.7}$$

where x, y, z are the cartesian components of the position vector. Every element of the matrix is calculated as $a_{ij}^\times = \sum_k \epsilon_{ijk} a_k$ where ϵ is the tensor of Levi-Civita, equal to 0 if anyway indexes are equal, 1 for even permutation and -1 for odd permutation. In the molecular frame the rotation $\mathbf{\Omega}_{MF}$ is averaged on the coordinates so the potential energy surface and the diffusion tensor do not depend on $\mathbf{\Omega}_{MF}$. It is possible neglect the rotational coordinates and the new set become $\mathbf{Q} = (\varphi, \mathbf{X})$. The operator $\hat{\Gamma}_n$ is

$$\hat{\Gamma}_n = - \left[\frac{\partial}{\partial \varphi} \left(\frac{\partial}{\partial \mathbf{X}} \right)^{tr} \right] \left[\begin{array}{cc} D_{I,n}(\varphi) & -\mathbf{D}_{R,n}^{tr} \mathbf{X}^\times \\ -\mathbf{X}^{\times tr} \mathbf{D}_{R,n} & D_S \mathbf{1} \end{array} \right] P(\mathbf{Q}) \left[\begin{array}{c} \frac{\partial}{\partial \varphi} \\ \frac{\partial}{\partial \mathbf{X}} \end{array} \right] P(\mathbf{Q})^{-1} \tag{B.8}$$

At this point we consider the approximation that no significant coupling exists between internal and solvent degrees of freedom. The choice of a MF minimize the dynamic coupling between the φ angle and the solvent polarization \mathbf{X} . The tensor become

$$\mathbf{D} \approx \begin{pmatrix} D_{I,n}(\varphi) & \mathbf{0}^{tr} \\ \mathbf{0} & D_S \mathbf{1} \end{pmatrix} \quad (\text{B.9})$$

Substituting the approximate expression B.9 in the Eq. B.8 we obtained the Eq. 2.9 used for the calculation of the emission fluorescence spectra.

Appendix C

The dipole-dipole magnetic tensor

We assume that a vector in spherical coordinates is represented as \mathbf{r} , where r is the modulus of the vector, θ the angle between the vector and the z-axis of the reference frame and φ the angle between the projection of the vector on the xy-plane and the x-axis.¹ As mentioned before, Eq. 3.9 is an approximation because the two electrons are assumed to be fixed, while to take into account their delocalization over the molecular orbitals that they occupy one has to integrate over the electron coordinates. Calling Ψ' and Ψ'' the two molecular orbitals containing the electrons, the dipolar tensor can be calculated as

$$\mathbf{T} = N^2 \langle \Psi'(1)\Psi''(2) - \Psi'(2)\Psi''(1) | \hat{\mathbf{T}} | \Psi'(1)\Psi''(2) - \Psi'(2)\Psi''(1) \rangle \quad (\text{C.1})$$

where $\hat{\mathbf{T}}$ is the tensorial operator, the components of which are

$$\hat{T}_{\alpha,\beta} = \frac{r_{12}^2 \delta_{\alpha,\beta} - 3(\mathbf{r}_{12})_{\alpha}(\mathbf{r}_{12})_{\beta}}{r_{12}^5} \quad (\text{C.2})$$

where $r_{12} = |\mathbf{r}_{12}| = |\mathbf{r}_1 - \mathbf{r}_2|$, is the vector between the two electrons, $\alpha, \beta = X, Y, Z$ and $(\mathbf{r}_{12})_{\alpha}$ is the component along α of vector \mathbf{r}_{12} . The normalization constant can be easily found to be $N = [2(1 - |S|^2)]^{-1/2}$ with $S = \langle \Psi' | \Psi'' \rangle$. The molecular orbitals are built

¹This note is based on an original contribution by Mr. Mirco Zerbetto.

starting from atomic orbitals and in general can be written as the linear combination

$$\Psi = N \sum_k c_k \phi_k \quad (\text{C.3})$$

Given the frame respect to which the dipolar tensor is to be calculated one has to express all the orbitals in this frame. A way to do this, by keeping separated radial from angular coordinates, is to expand the orbital on a basis of spherical harmonics. In general one orbital is defined in a frame rotated by a set of Euler angles $\mathbf{\Omega}$ with respect to the frame where the tensor is to be calculated. Additionally, the center of the orbital frame (the nucleus) may be translated respect to the origin of the reference frame. Given the orbital $\phi_{NLM}(\mathbf{r}) = f_{NL}(r)Y_{LM}(\theta, \varphi)$, the effect of a rotation gives:

$$\hat{R}(\mathbf{\Omega})\phi_{NLM} = \sum_{K=-L}^L D_{MK}^L(\mathbf{\Omega})\phi_{NLK} \quad (\text{C.4})$$

where $D_{MK}^L(\mathbf{\Omega})$ is a rotation Wigner matrix. A vector $\mathbf{R} = (R, \Theta, \Phi)$ indicates the distance from the origin of the reference frame. It follows that

$$\phi_{NLM}(\mathbf{r} - \mathbf{R}) = \sum_{l=0}^{\infty} \sum_{m=-l}^l a_{l,m}(r, \mathbf{R})Y_{l,m}(\theta, \varphi) \quad (\text{C.5})$$

where the three quantum numbers N , L and M enter in the definition of the expansion coefficients. The formula clearly keeps separated radial from angular coordinates of the electron. One way to obtain the coefficients $a_{l,m}$ is to make use of the Fourier - transform convolution theorem [371],[372]. The coefficients can be expressed as

$$a_{l,m}(r, \mathbf{R}) = (-)^M \sum_{\lambda=|l-L|}^{(l+L)} \sqrt{\frac{[\lambda, l, L]}{4\pi}} \begin{pmatrix} \lambda & l & L \\ 0 & 0 & 0 \end{pmatrix} \cdot \begin{pmatrix} \lambda & l & L \\ m-M & -m & M \end{pmatrix} Y_{\lambda, m-M}(\Theta, \Phi) v_{l, \lambda, L}(r, T) \quad (\text{C.6})$$

Here $[n] = 2n + 1$ and

$$v_{l, \lambda, L}(r, R) = 4(-)^{(l-\lambda-L)/2} \int_0^{\infty} dr' r'^2 f(r') \int_{-\infty}^{\infty} dk k^2 j_{\lambda}(kR) j_l(kr) j_L(kr') \quad (\text{C.7})$$

with $j_n(x)$ a spherical Bessel function of integer index n . Expansion C.5 can be substituted into Eq. C.3 to obtain

$$\Psi = N \sum_{l=0}^{\infty} \sum_{m=-l}^l \left[\sum_k c_k a_{l,m}^k(r, \mathbf{R}_k) \right] Y_{l,m}(\theta, \varphi) = \sum_{l=0}^{\infty} \sum_{m=-l}^l A_{l,m}(r) Y_{l,m}(\theta, \varphi) \quad (\text{C.8})$$

Eq. 3.9 needs to be conveniently transformed to take into account rotational properties. First of all, the tensor $\hat{\mathbf{T}}$ can be expressed as irreducible spherical tensorial operator, $\hat{\mathbf{T}} = \hat{T}^{(0)} \oplus \hat{T}^{(1)} \oplus \hat{T}^{(2)}$ and the transformation from cartesian to spherical coordinates can be achieved by standard methods. Due to the fact that the dipolar tensor is traceless and symmetric, it can be seen that only the rank two operator is non zero, with components

$$\begin{aligned} \hat{T}^{(2,0)} &= \sqrt{\frac{3}{2}} \hat{T}_{ZZ} = \sqrt{\frac{3}{2}} \frac{1}{r_{12}^3} \left[1 - 3 \frac{(\mathbf{r}_{12})_Z^2}{r_{12}^2} \right] \\ \hat{T}^{(2,\pm 1)} &= \mp (\hat{T}_{XZ} \pm \hat{T}_{YZ}) = \pm \frac{3}{r_{12}^3} \left[\frac{(\mathbf{r}_{12})_X (\mathbf{r}_{12})_Z \pm i (\mathbf{r}_{12})_Y (\mathbf{r}_{12})_Z}{r_{12}^2} \right] \\ \hat{T}^{(2,\pm 2)} &= \frac{\hat{T}_{XX} - \hat{T}_{YY}}{2} \pm i \hat{T}_{XY} = -\frac{3}{r_{12}^3} \left[\frac{(\mathbf{r}_{12})_X^2 - (\mathbf{r}_{12})_Y^2}{2r_{12}^2} \pm i \frac{(\mathbf{r}_{12})_X (\mathbf{r}_{12})_Y}{r_{12}^2} \right] \end{aligned} \quad (\text{C.9})$$

By expressing the vector \mathbf{r}_{12} in spherical coordinates as

$$\begin{aligned} (\mathbf{r}_{12})_X &= r_{12} \sin(\theta_{12}) \cos(\varphi_{12}) \\ (\mathbf{r}_{12})_Y &= r_{12} \sin(\theta_{12}) \sin(\varphi_{12}) \\ (\mathbf{r}_{12})_Z &= r_{12} \cos(\theta_{12}) \end{aligned} \quad (\text{C.10})$$

where the two angles give the orientation of the vector that goes from the first electron to the second in the reference frame, one is able to re-write the spherical components of the tensor as

$$\begin{aligned} \hat{T}^{(2,0)} &= \sqrt{\frac{3}{2}} \frac{1}{r_{12}^3} \left[1 - 3 \cos^2(\theta_{12}) \right] = -\sqrt{\frac{24\pi}{5}} \frac{1}{r_{12}^3} Y_{2,0}(\theta_{12}, \varphi_{12}) \\ \hat{T}^{(2,\pm 1)} &= \pm \frac{3}{r_{12}^3} \sin(\theta_{12}) \cos(\theta_{12}) e^{\pm i\varphi_{12}} = -\sqrt{\frac{24\pi}{5}} \frac{1}{r_{12}^3} Y_{2,\pm 1}(\theta_{12}, \varphi_{12}) \end{aligned} \quad (\text{C.11})$$

$$\hat{T}^{(2,\pm 2)} = -\frac{3}{r_{12}^3} \sin^2(\theta_{12}) e^{\pm i2\varphi_{12}} = -\sqrt{\frac{24\pi}{5}} \frac{1}{r_{12}^3} Y_{2,\pm 2}(\theta_{12}, \varphi_{12}) \quad (\text{C.12})$$

For a vector $\mathbf{r} = |\mathbf{r}_1 - \mathbf{r}_2|$ it can be shown that subsists the expansion [373]

$$\begin{aligned} \frac{1}{r^{L+1}} Y_{L,M}(\theta, \varphi) &= \sqrt{\frac{4\pi}{(2L)!}} \sum_{l_1, l_2=0}^{\infty} (-)^{l_2} \sqrt{\frac{(2l_2)!}{(2l_1+1)!}} \frac{r_{<}^{l_1}}{r_{>}^{l_2+1}} \cdot \\ &\cdot [\mathbf{Y}_{l_1}(\theta_1, \varphi_1) \oplus \mathbf{Y}_{l_2}(\theta_2, \varphi_2)]_M^L \end{aligned} \quad (\text{C.13})$$

where $l_2 - l_1 = L$, $r_{<} = \min(r_1, r_2)$ and $r_{>} = \max(r_1, r_2)$. So every component of the dipolar tensor can be written as

$$\begin{aligned} \hat{T}^{(2,M)} &= -\sqrt{\frac{24\pi}{5}} \frac{1}{r_{12}^3} Y_{2,M}(\theta_{12}, \varphi_{12}) = \\ &= -\pi \sqrt{\frac{4}{5}} \sum_{l_1, l_2=0}^{\infty} (-)^{l_2} \sqrt{\frac{(2l_2)!}{(2l_1+1)!}} \frac{r_{<}^{l_1}}{r_{>}^{l_2+1}} [\mathbf{Y}_{l_1}(\theta_1, \varphi_1) \oplus \mathbf{Y}_{l_2}(\theta_2, \varphi_2)]_M^2 = \\ &= \sum_{l_1, l_2=0}^{\infty} d_{l_1, l_2}(\mathbf{r}_1, \mathbf{r}_2) [\mathbf{Y}_{l_1}(\theta_1, \varphi_1) \oplus \mathbf{Y}_{l_2}(\theta_2, \varphi_2)]_M^2 \end{aligned} \quad (\text{C.14})$$

where $l_2 - l_1 = 2$ and $[\mathbf{X}^{(l_1)} \oplus \mathbf{X}^{(l_2)}]_M^2$ is intended as the component M of the contraction of rank 2 of the two irreducible spherical tensors. If the tensors are spherical harmonics, this is called a bipolar harmonic. Expression C.14 shows that radial and spherical coordinates can be separated also for the tensor and only the two radial coordinates remain coupled, while the angular ones can be decoupled by noting that a bipolar harmonic can be rewritten as

$$\begin{aligned} [\mathbf{Y}_{l_1}(\theta_1, \varphi_1) \oplus \mathbf{Y}_{l_2}(\theta_2, \varphi_2)]_M^L &= \sum_{m_1=-l_1}^{l_1} \sum_{m_2=-l_2}^{l_2} (-)^{l_1-l_2+M} [L]^{1/2} \begin{pmatrix} l_1 & l_2 & L \\ m_1 & m_2 & -M \end{pmatrix} \\ &\cdot Y_{l_1, m_1}(\theta_1, \varphi_1) Y_{l_2, m_2}(\theta_2, \varphi_2) \end{aligned} \quad (\text{C.15})$$

Now, combining Eq. C.1, the expression for the molecular orbitals given in Eq. C.8 and the expansion of the different components of the tensor as in Eq. C.14 we can write

$$\begin{aligned} T^{(2,M)} &= \mathbf{N}^2 \sum_{l_1, l_2=0}^{\infty} \sum_{l_A, l_B, l_C, l_D} \sum_{m_A, m_B, m_C, m_D} \langle A'_{l_A, m_A}(r_1) A''_{l_B, m_B}(r_2) - A''_{l_A, m_A}(r_1) A'_{l_B, m_B}(r_2) | \\ &| d_{l_1, l_2} [A'_{l_A, m_A}(r_1) A''_{l_B, m_B}(r_2) - A''_{l_A, m_A}(r_1) A'_{l_B, m_B}(r_2)] \rangle \cdot \\ &\cdot \langle Y_{l_A, m_A}(\Omega_1) Y_{l_B, m_B}(\Omega_2) | [\mathbf{Y}_{l_1}(\theta_1, \varphi_1) \oplus \mathbf{Y}_{l_2}(\theta_2, \varphi_2)]_M^2 | Y_{l_C, m_C}(\Omega_1) Y_{l_D, m_D}(\Omega_2) \rangle = \end{aligned}$$

$$= \mathbf{N}^2 \sum_{l_1, l_2=0}^{\infty} \sum_{l_A, l_B, l_C, l_D} \sum_{m_A, m_B, m_C, m_D} I(r_1, r_2) \times I^{(2,M)}(\mathbf{\Omega}_1, \mathbf{\Omega}_2) \quad (\text{C.16})$$

So every component of the tensor is calculated as a series of integrals, each of whom is separated into an integral over only the radial coordinates of the two electrons and one over the angular coordinates. The first one is a complex function of the two radii and r_1 and r_2 , it is calculated numerically; the latter, is analytical and by expanding the bipolar harmonic (or equally by making use of the Wigner-Eckart theorem) one obtains

$$\begin{aligned} I^{(2,M)}(\mathbf{\Omega}_1, \mathbf{\Omega}_2) &= (-)^M \sqrt{5} \sum_{m_1, m_2} \begin{pmatrix} l_1 & l_2 & 2 \\ m_1 & m_2 & -M \end{pmatrix} \cdot \\ &\quad \cdot \langle Y_{l_A, m_A} | Y_{l_1, m_1} | Y_{l_C, m_C} \rangle \langle Y_{l_B, m_B} | Y_{l_2, m_2} | Y_{l_D, m_D} \rangle = \\ &= (-)^{M-m_A-m_B} \sqrt{5} \sqrt{\frac{[l_A, l_1, l_C, l_B, l_2, l_D]}{4\pi}} \sum_{m_1, m_2} \begin{pmatrix} l_1 & l_2 & 2 \\ m_1 & m_2 & -M \end{pmatrix} \cdot \\ &\quad \cdot \begin{pmatrix} l_A & l_1 & l_C \\ 0 & 0 & 0 \end{pmatrix} \begin{pmatrix} l_A & l_1 & l_C \\ -m_A & m_1 & m_C \end{pmatrix} \cdot \\ &\quad \cdot \begin{pmatrix} l_B & l_2 & l_D \\ 0 & 0 & 0 \end{pmatrix} \begin{pmatrix} l_B & l_2 & l_D \\ -m_B & m_2 & m_D \end{pmatrix} = \\ &= \delta_{M, m_A+m_B-m_C-m_D} (-)^{-m_C-m_D} \sqrt{5} \sqrt{\frac{[l_A, l_1, l_C, l_B, l_2, l_D]}{4\pi}} \cdot \\ &\quad \cdot \begin{pmatrix} l_1 & l_2 & 2 \\ m_A - m_C & m_B - m_D & -M \end{pmatrix} \begin{pmatrix} l_A & l_1 & l_C \\ 0 & 0 & 0 \end{pmatrix} \cdot \\ &\quad \cdot \begin{pmatrix} l_A & l_1 & l_C \\ -m_A & m_A - m_C & m_C \end{pmatrix} \begin{pmatrix} l_B & l_2 & l_D \\ 0 & 0 & 0 \end{pmatrix} \cdot \\ &\quad \cdot \begin{pmatrix} l_B & l_2 & l_D \\ -m_B & m_B - m_D & m_D \end{pmatrix} \end{aligned} \quad (\text{C.17})$$

Clearly, it is not necessary to calculate all the five components but only three are needed due to the property $T^{(2,M)} = (-)^M T^{(2,M)*}$. The procedure described here allows to calculate the dipolar interaction tensor starting from the electronic and structural information of the molecule, both obtainable directly from *ab-initio* calculations. Electronic information are used to identify atomic orbitals contributing to the forma-

tion of the two molecular orbitals occupied by the two unpaired electrons. Structural information is used to locate the various atoms (and so the various atomic orbitals) with respect to the origin of the reference frame in which the tensor is calculated. In our case, by examining the electron distribution of the unpaired electrons it is possible to state that substantially each electron, is delocalized in a π^* bond obtained by the linear combination of the two $2p_z$ orbitals of nitrogen and oxygen, so the two molecular orbitals are

$$\begin{aligned}\Psi' &= N' \left[\phi_{210}^{N_1}(\mathbf{r} - \mathbf{R}_{N_1}) - \phi_{210}^{O_1}(\mathbf{r} - \mathbf{R}_{O_1}) \right] \\ \Psi'' &= N'' \left[\phi_{210}^{N_2}(\mathbf{r} - \mathbf{R}_{N_2}) - \phi_{210}^{O_2}(\mathbf{r} - \mathbf{R}_{O_2}) \right]\end{aligned}\tag{C.18}$$

For the calculations we make the assumption that each electron is equally distributed between the oxygen and the nitrogen atoms. The atomic orbitals are STO of the form $\phi_{210}(\mathbf{r}) = \sqrt{\frac{4\alpha^5}{3}} r e^{-\alpha r} Y_{1,0}(\theta, \varphi)$ where $\alpha = Z_{eff}/2$ Hartree-1 and Z_{eff} if the effective nuclear charge; standard Clementi - Raimondi values of $Z_{eff}= 3.83$ for nitrogen and $Z_{eff}= 4.45$ for oxygen were used. The molecular geometry allows us to conclude that only the $T^{(2,0)}$ component contributes significantly to the dipolar tensor.

Bibliography

- [1] Orozco, M.; Alhambra, C.; Barril, X.; Lopez, J. M.; Busquets, M. A.; Lunque, F. J. *J. Mol. Model.* **1996**, *2*, 1.
- [2] Chong, D. P. *Recent Advanced in Density Functional Methods*, World Scientific **1997**.
- [3] Giesen, D. G.; Storer, J. W.; Cramer, C. J.; Truhlar, D. G. *J. Am. Chem. Soc.* **1995**, *117*, 1057.
- [4] Sahimi, M. *Heterogeneous Materials*, Springer **2003**.
- [5] Massova, I.; Kollman, P. A. *Persp. Drug Disc. Design* **2000**, *18*, 13.
- [6] Born, M. Z. *Phys.* **1920**, *1*, 45.
- [7] Kirkwood, J. G. *J. Che. Phys.* **1934**, *2*, 351.
- [8] Onsager, L. *J. Am. Chem. Soc.* **1936**, *58*, 1486.
- [9] Miertuš, S.; Tomasi, J. *J. Chem. Phys.* **1982**, *65*, 329.
- [10] Cramer, C. J. *Essentials of Computational Chemistry: Theories and Models*, John Wiley and Sons **2004**.
- [11] Smith, P. E.; Pettitt, B. M. *J. Phys. Chem.* **1994**, *98*, 9700.
- [12] Sutmann, G. *Quantum Simulations of Complex Many-Body Systems: From Theory to Algorithms*, Grotendorst J., Marx D., A. Muramatzu (Eds.), John von Neumann Institute for Computing, Jülich, NIC Series, vol. 10, 211, **2002**.

- [13] Allen, M. P. *Computational Soft Matter: From Synthetic Polymers to Proteins*, NIC Series, **2004**, 23, 1.
- [14] Hinchliffe, A. *Chemical Modelling: Applications and Theory*, Royal Society of Chemistry **2000**.
- [15] Hohenberg, P.; Kohn, W. *Phys. Rev.* **1964**, 136, B864.
- [16] Labanowski, J. K.; Andzelm, J. W. *Density functional Methods in Chemistry*, Springer-Verlag New York, New York **1991**.
- [17] Thomas, L. H. *Proc. Cambridge Phil. Soc.* **1927**, 23, 542.
- [18] Fermi, E. *Physik* **1928**, 48, 73.
- [19] Jones, R. O.; Gunnansson, O. *Rev. Mod. Phys.* **1989**, 61, 689.
- [20] Slater, J. C. *Quantum Theory of Matter*, McGraw Hill, New York, **1968**.
- [21] March, N. H. *Adv. Phys.* **1957**, 6, 1.
- [22] Dirac, P. A. M. *Proc. Cambridge Phil. Soc.* **1930**, 26, 376.
- [23] Chakraborty, A. *Molecular Modeling and Theory in Chemical Engineering*, Academic Press, Elsevier **2001**.
- [24] Kohn, W.; Sham, L. J. *Phys. Rev. A* **1965**, 140, 1133.
- [25] Marquez, M. A. L.; Gross, E. K. U. *Annu. Rev. Phys. Chem.* **2004**, 55, 427.
- [26] Parr, R. G.; Yang, W. *Density Functional Theory of Atoms and Molecules*, Oxford University Press: Oxford **1989**.
- [27] Seminario, J.; Politzer, P.; *Modern Density Functional Theory-A Tool for Chemistry, Theoretical and Computational Chemistry, Volume 2*, Elsevier, Amsterdam **1995**.
- [28] Ziegler, T. *Chem. Rev.* **1991**, 91, 651.

- [29] Bartolotti, L. J. *Reviews in Computational Chemistry, Volume VII*, Lipkowitz K. B. and Boyd D. B. Editors, VCH Publishers, New York **1996**.
- [30] St-Amant, A. *Reviews in Computational Chemistry, Volume VII*, Lipkowitz K. B. and Boyd D. B. Editors, VCH Publishers, New York **1996**.
- [31] Autschbach, J. *Structr. Bond.* **2004**, *112*, 1.
- [32] Rosa, A.; Ricciardi, G.; Gritsenko, O.; Baerends, E. J. *Structr. Bond.* **2004**, *112*, 49.
- [33] Kaltsoyannis, N.; McGrady, J. E. *Principles and Applications of Density Functional Theory in Inorganic Chemistry*, Springer **2004**.
- [34] Li, S.; Liu, W. K. *Meshfree Particle Methods*, Springer, **2004**.
- [35] www.charmm.org
- [36] www.amber.scripps.edu
- [37] Marx, D.; Hutter, J. *Modern Methods and Algorithms of Quantum Chemistry*, J. Grotendorst (Ed.), John von Neumann Institute for Computing, Jülich, NIC Series, vol. 1, 301, **2000**.
- [38] Car, R.; Parrinello, M. *Phys. Rev. Lett.* **1985**, *55*, 2471.
- [39] Martin, R. M. *Electronic Structure: Basic Theory and Practical Methods*, Cambridge University Press **2004**.
- [40] Gao, J. *Methods and applications of combined quantum mechanical and molecular mechanical potentials*, p.119-185 in *Reviews in Computational Chemistry* **1996**, *7*, 119.
- [41] Ho, L. L.; MacKerel, A. D. *J. Phys. Chem.* **1996**, *100*, 4466.
- [42] Hartsough, D. S.; Merz, K. M. *J. Phys. Chem.* **1995**, *99*, 11266.
- [43] Lyne, P. D.; Mulholland, A. J.; Richards, W. G. *J. Am. Chem. Soc.* **1995**, *117*, 11345.

- [44] Li, H.; Hains, A. W.; Everts, J. E.; Robertson, A. D.; Jensen, J. H. *J. Phys. Chem. B* **2002**, *106*, 3486.
- [45] Thompson, M. A. *J. Am. Chem. Soc.* **1995**, *117*, 11341.
- [46] Matsubara, T.; Maseras, F.; Koga, N.; Morokuma, K. *J. Phys. Chem.* **1996**, *100*, 2573.
- [47] Gao, J. *J. Phys. Chem.* **1992**, *96*, 537.
- [48] Gao, J. *J. Am. Chem. Soc.* **1994**, *116*, 9324.
- [49] Liu, H.; Muller-Plathe, F.; van Gunsteren, W. F. *J. Chem. Phys.* **1995**, *102*, 1722.
- [50] Bash, P. A.; Field, M. J.; Davenport, R. C.; Petsko, G. A.; Ringe, D.; Karplus, M. *Biochemistry* **1991**, *30*, 5826.
- [51] Warshel, A.; Levitt, M. *J. Mol. Biol.* **1976**, *100*, 13213.
- [52] Singh, U. C.; Kollman, P. A. *J. Comput. Chem.* **1986**, *7*, 718.
- [53] Aqvist, J.; Warshel, A. *Chem. Rev.* **1993**, *93*, 2523.
- [54] Cramer, C. J.; Truhlar, D. G. *Chem. Rev.* **1999**, *99*, 2161.
- [55] Tomasi, J.; Persico, M. *Chem. Rev.* **1994**, *94*, 2027.
- [56] Amovilli, C.; Mennucci, B. *J. Phys. Chem. B* **1997**, *101*, 1051.
- [57] Cui, Q. *J. Chem. Phys.* **2002**, *117*, 4720.
- [58] Bondi, A. *J. Phys. Chem.* **1964**, *229*, 244.
- [59] Tomasi, J.; Cammi, R.; Mennucci, B.; Cappelli, C.; Corni, S. *Phys. Chem. Chem. Phys.* **2002**, *4*, 5697.
- [60] Cancès, E.; Mennucci, B.; Tomasi, J. *J. Chem. Phys.* **1997**, *107*, 3032.
- [61] Tomasi, J.; Mennucci, B.; Cammi, R. *Chem. Rev.* **2005**, *105*, 2999.

- [62] Hoogerbrugge, P. J.; Koelman, J. M. V. A. *Europhys. Lett.* **1992**, *19*, 155.
- [63] Español, P.; Warren, P. *Europhys. Lett.* **1995**, *30*, 191.
- [64] Español, P. *Phys. Rev. E* **1995**, *52*, 1734.
- [65] Marsh, C.; Backx, G.; Ernst, M. H. *Europhys. Lett.* **1997**, *38*, 411.
- [66] Marsh, C.; Backx, G.; Ernst, M. H. *Phys. Rev. E* **1997**, *56*, 1976.
- [67] Ripoll, M.; Ernst, M. H.; Español, P. *J. Chem. Phys.* **2001**, *115*, 7271.
- [68] Romanovsky, Y. M.; Ebeling, W.; Schimansky-Geier, L. *Stochastic Dynamics of Reacting Biomolecules*, World Scientific **2002**.
- [69] Kijima, M. *Markov Processes for Stochastic Modeling*, CRC Press **1997**.
- [70] Waldron, J. T.; Kalmykov, Y. P.; Coffey, W. *The Langevin Equation: With Applications in Physics, Chemistry and Electrical Engineering*, World Scientific Series in Contemporary Chemical Physics, vol. 10, **1996**.
- [71] Dattagupta, S.; Puri, S. *Dissipative Phenomena in Condensed Matter: Some Applications*, Springer **2004**.
- [72] Kadanoff, L. P. *Statistical Physics: Statics, Dynamics and Renormalization*, World Scientific **2000**.
- [73] Risken, H. *The Fokker-Planck Equation: Methods of Solution and Applications*, Springer **1996**.
- [74] Feng, X.; Thompson, W. H. *J. Phys. Chem. C* **2007**, 10.1021/jp074516h.
- [75] Hinch, E. J. *J. Fluid Mech. Dig. Arch.* **1975**, *72*, 499.
- [76] de Baas, A. F. *Quart. J. Roy. Meteor. Soc.* **1986**, *112*, 165.
- [77] Namsrai, K. H.; Hulree, Njamtsereen, N. *Int. J. Mod. Phys. A* **1992**, *7*, 2661.
- [78] Oppenheim, I.; Orsky, A. *J. Stat. Phys.* **2005**, *65*, 859.

- [79] Trigger, S. A.; Ebeling, A. M.; Ignatov, A. M.; Tkachenko, I. M. *Contrib. Plasma Phys.* **2003**, *43*, 377.
- [80] Kühn, O.; Yi, Z.; Feng, S.; Yijing, Y. *J. Chem. Phys.* **2000**, *12*, 6104.
- [81] Trigger, S. A. *Phys. Rev. E* **2003**, *67*, 046403.
- [82] Kou, S. C.; Xie, X. S. *Phys. Rev. Lett.* **2004**, *93*, 180603.
- [83] Nykypanchuk, D.; Strey, H. H.; Hoagland, D. A. *Science* **2002**, *297*, 987.
- [84] Leimkuhler, B. *New Algorithms for Macromolecular Simulation*, Springer **2006**.
- [85] Warwicker, J.; Watson, H. C. *J. Mol. Biol.* **1982**, *157*, 671.
- [86] Parker, D. F. *Fields, Flows, and Waves: An Introduction to Continuum Models*, Springer **2003**.
- [87] Roux, B.; Simonson, T. *Biophys. Chem.* **1999**, *78*, 1.
- [88] Feig, M.; Brooks, C. L. *Curr. Opin. Struct. Biol.* **2004**, *14*, 217.
- [89] Rinaldi, D.; Rivail, J. L. *Theor. Chim. Acta* **1973**, *32*, 57.
- [90] Still, W. C.; Tempczyk, A.; Hawley, R. C.; Hendrickson, T. *J. Am. Chem. Soc.* **1990**, *112*, 6127.
- [91] Onufriev, A.; Bashford, D.; Case, D. A. *J. Comp. Chem.* **2002**, *23*, 1297.
- [92] Rapp, C.; Friesner, R. *Proteins Struct. Funct. Genet.* **1999**, *35*, 173.
- [93] Wang, T.; Wade, R. *Proteins Struct. Funct. Genet.* **2003**, *50*, 158.
- [94] Xia, B.; Tsui, V.; Case, D.; Dyson, H.; Wright, P. *J. Biomol. NMR* **2002**, *22*, 317.
- [95] Nymeyer, H.; Garcia, A. E. *Proc. Natl. Acad. Sci.* **2003**, *1000*, 13934.
- [96] Ferrara, P.; Apostolakis, J.; Caffisch, A. *Proteins Struct. Funct. Genet.* **2002**, *46*, 24.

- [97] Jean-Charles, A.; Nicholls, A.; Sharp, K.; Honig, B.; Tempczyk, A.; Hendrickson, T.; Still, W. C. *J. Am. Chem. Soc.* **1991**, *113*, 1454.
- [98] Alkorta, I.; Villar, H.; Perez, J. J. *J. Comp. Chem.* **1993**, *14*, 620.
- [99] Misra, V. K.; Sharp, K.; Friedman, N. A.; Honig, B. *J. Mol. Biol.* **1994**, *238*, 245.
- [100] Lucy, L. B. *Astron. J.* **1977**, *82*, 1013.
- [101] Monaghan, J. J. *Ann. Rev. Astron. Astrophys.* **1992**, *30*, 543.
- [102] Liu, G. R.; Liu, M. B. *Smoothed particle hydrodynamics: a meshfree particle method*, World Scientific **2003**.
- [103] Español, P.; Revenga, M. *Phys. Rev. E* **2003**, *67*, 026705.
- [104] Caricato, M.; Mennucci, B.; Tomasi, J. *J. Chem. Phys.* **2005**, *122*, 154501.
- [105] Tellung, A. *Physica* **1953**, *19*, 217.
- [106] Turski, L. A. *Physica* **1972**, *57*, 432.
- [107] Dzyaloshinskii, I. E.; Volovick, G. E. *Ann. Phys.* **1980**, *125*, 67.
- [108] van Saarloos, W.; Bedeaux, D.; Mazur, P. *Physica A* **1981**, *107*, 435.
- [109] Öttinger, H. C.; Grmela, M. *Phys. Rev. E* **1997**, *56*, 6633.
- [110] Grmela, M. *Phys. Lett.* **2002**, *296*, 97.
- [111] Nguyen, S.; Turski, L. A. *Physica A* **1999**, *272*, 48.
- [112] Nguyen, S.; Turski, L. A. *J. Phys. A: Math. Gen.* **2001**, *34*, 9281.
- [113] Anthony, K. H. *J. Non-Newton. Fluid.* **2001**, *92*, 291.
- [114] Muschik, W.; Papenfuss, C.; Ehrentraut, H. *J. Non-Newton. Fluid.* **2001**, *96*, 255.
- [115] Landau, L. D.; Lifshitz, E. M. *Physique Statistique*, Mir **1984**.

- [116] Forster, D.; Nelson, D. R.; Stephen, M. J. *Phys. Rev. Lett.* **1976**, *36*, 867.
- [117] Forster, D.; Nelson, D. R.; Stephen, M. J. *Phys. Rev. A* **16**, 732 (1977).
- [118] Grabert, H.; Green, M. S. *Phys. Rev. A* **1979**, *19*, 1747.
- [119] Grabert, H.; Graham, R.; Green, M. S. *Phys. Rev. A* **1980**, *21*, 2176.
- [120] Enz, C. P. *Physica A* **1977**, *89*, 1.
- [121] Enz, C. P. *Physica A* **1978**, *94*, 20.
- [122] Enz, C. P.; Turski, L. *Physica A* **1979**, *96*, 369.
- [123] van Saarloos, W.; Bedeaux, D.; Mazur, P. *Physica A* **1982**, *110*, 147.
- [124] Das, S.; Mazenko, G. F. *Phys. Rev. A* **1986**, *34*, 2265.
- [125] Kim, B.; Mazenko, G. F. *J. Stat. Phys.* **1991**, *64*, 631.
- [126] Eyink, G. L.; Lebowitz, J. L.; Spohn, H. *J. Stat. Phys.* **1996**, *65*, 385.
- [127] Mazur, P. *Physica A* **1998**, *261*, 451.
- [128] Rubi, J. M.; Mazur, P. *Physica A* **2000**, *276*, 477.
- [129] Grabert, H. *Projection Operator Techniques in Nonequilibrium Statistical Mechanics*, Springer, Berlin **1982**.
- [130] Zubarev, D. N.; Morozov, V. G. *Physica A* **1983**, *20*, 411.
- [131] Espanõl, P. *Physica A* **1998**, *248*, 77.
- [132] Backer, N. A. *Curr. Opin. Struct. Biol.* **2005**, *15*, 137.
- [133] Lin, J. H.; Backer, N. A.; McCammon, J. A. *Biophys. J.* **2002**, *83*, 1374.
- [134] Edwards, S.; Corry, B.; Kuyucak, S.; Chung, S. H. *Biophys. J.* **2002**, *83*, 1348.
- [135] Sheinerman, F. B.; Brooks, C. L. *Proc. Natl. Acad. Sci. USA* **1998**, *95*, 1562.
- [136] Sheinerman, F. B.; Brooks, C. L. *J. Mol. Biol.* **1998**, *278*, 439.

- [137] Gaussian 03, Revision C.02, Frisch, M. J.; et all. Gaussian, Inc.: Pittsburgh, PA, **2003**.
- [138] Barone, V.; Polimeno, A. *Chem. Soc. Rev.* **2007**, *36*, 1724.
- [139] Valeur, B.; Brochon, J. C. *New Trends in Fluorescence Spectroscopy: Applications to Chemical and Life Sciences*, Springer **2001**.
- [140] Bakalova, S.; Kaneti, J. *Spectrochim. Acta Part A* **2000**, *56*, 1443.
- [141] Tatchen, J.; Marion, C. M. *Phys. Chem. Chem. Phys.* **2006**, *8*, 2133.
- [142] Lukes, V.; Aquino, A.; Lischka, H. *J. Phys. Chem. A* **2005**, *109*, 10232.
- [143] Baraldi, I.; Brancolini, G.; Momicchioli, F.; Ponterini, G.; Vanossi, D. *Chem. Phys.* **2003**, *288*, 309.
- [144] Chen, R.; Huang, Z.; Lui, H.; Hamzavi, I.; McLean, D. I.; Xie, S.; Zeng, H. *J. Photochem. Photobiol. B: Biol.* **2007**, *86*, 219.
- [145] Churmakov, D. Y.; Meglinski, I. V.; Piletsky, S. A.; Greenhalgh, D. A. *J. Phys. D: Appl. Phys.* **2003**, *36*, 1722.
- [146] Gomez, J. A.; Thompson, W. H. *J. Phys. Chem. B* **2004**, *108*, 20144.
- [147] Bhattacharyya, K.; Chowdhury, M. *Chem. Rev.* **1993**, *93*, 507.
- [148] Lippert, E.; Lüder, W.; Moll, F.; Nagele, H.; Boos, H.; Prigge, H.; Siebold-Blankenstein, I. *Angew. Chem.* **1961**, *73*, 695.
- [149] Van Der Auweraer, M.; Vannerem, A.; De Schryver, F. C. *J. Mol. Struct.* **1982**, *84*, 343.
- [150] Sobolewski, A. L.; Domcke, W. *Chem. Phys. Lett.* **1996**, *250*, 428.
- [151] Kim, H. J.; Hynes, J. T. *Photochem. Photobiol. A:Chem* **1997**, *105*, 337.
- [152] Grabowski, Z. R.; Rotkiewicz, K.; Rettig, W. *Chem. Rev.* **2003**, *103*, 3899.

- [153] Schamschule, R.; Parusel, A. B. J., Köhler, G. *J. Mol. Struct. (Theochem)* **1997**, *419*, 161.
- [154] Mennucci, B.; Toniolo, A.; Tomasi, J. *J. Am. Chem. Soc.* **2000**, *122*, 10621.
- [155] Suldholt, W.; Sobolewski, A. L.; Domcke, W. *Chem. Phys.* **1999**, *204*, 9.
- [156] Nordio, P. L.; Polimeno, A.; Barbon, A. *Polish. J. Chem.* **1993**, *67*, 1397.
- [157] Kasha, M. *Discuss. Faraday Soc.* **1950**, *9*, 14.
- [158] Rappoport, D.; Furche, F. *J. Am. Chem. Soc.* **2004**, *126*, 1277.
- [159] Rattig, W.; Baumann, W. *Photoche. Photophys.* **1992**, *6*, 79.
- [160] Al-Hassan, K. A.; Khanfer, M. F. *J. Fluoresc.* **1998**, *8*, 139.
- [161] LaClair, J. J. *Angew. Chem., Int. Ed.* **1998**, *37*, 325.
- [162] LaClair, J. J. *Angew. Chem., Int. Ed.* **1999**, *38*, 3045.
- [163] Bautista, J. A.; Connors, R. E.; Raju, B. B.; Hiller, R. G.; Sharples, F. P.; Gosztola, D.; Wasielewski, M. R.; Frank, H. A. *J. Phys. Chem. B* **1999**, *103*, 8751.
- [164] Zigmantas, D.; Hiller, R. G.; Yarysev, A.; Sundström, V.; Polivka, T. *J. Phys. Chem. B* **2003**, *107*, 5339.
- [165] Grabowski, Z. R. *Pure Appl. Chem.* **1992**, *64*, 1249.
- [166] Nakashima, N.; Inoue, H.; Mataga, N.; Yamanaka, Y. *Bull. Chem. Soc. Jpn.* **1973**, *46*, 2288.
- [167] Kosower, E. M.; Dodiuk, H. *J. Am. Chem. Soc.* **1976**, *98*, 924.
- [168] Chandross, E. A.; Thomas, H. T. *Chem. Phys. Lett.* **1971**, *9*, 397.
- [169] Nordio, P. L.; Polimeno, A. *Mol. Phys.* **1992**, *75*, 1203.
- [170] Polimeno, A.; Saielli, G.; Nordio, P. L. *Chem. Phys.* **1998**, *235*, 313.

- [171] Moro, G. J.; Nordio, P. L.; Polimeno, A. *Chem. Phys.* **1989**, *68*, 1131.
- [172] Giacometti, G.; Moro, G. J.; Nordio, P. L.; Polimeno, A. *J. Mol. Liq.* **1989**, *42*, 19.
- [173] Polimeno, A.; Barbon, A.; Nordio, P. L.; Rettig, W. *J. Phys. Chem.* **1994**, *98*, 12158.
- [174] Xu, X.; Cao, Z.; Zhang, Q. *J. Chem. Phys.* **2005**, *122*, 194395.
- [175] Van Der Auweraer, M.; Grabowski, Z. R.; Rettig, W. *J. Phys. Chem.* **1991**, *95*, 2083.
- [176] Von Der Haar, T.; Hebecker, A.; Il'chev, Y.; Jiang, Y. B.; Köhne, W.; Zachariasse, K. A. *Recl. Trav. Chim. Pays-Bas* **1995**, *114*, 430.
- [177] Collins, G. E.; Choi, L. S.; Callahan, J. H. *J. Am. Chem. Soc.* **1998**, *120*, 1474.
- [178] Choi, L. S.; Collins, G. E. *Chem. Comm.* **1998**, *8*, 893.
- [179] De Lange, M. M. C.; Leeson, D. T.; Van Kuijk, K. A. B.; Huizer, A. H.; Varma, C. A. G. O. *Chem. Phys.* **1993**, *177*, 43.
- [180] Letard, J. F.; Delmond, S.; Lapouyade, R.; Braun, D.; Rettig, W.; Kressler, M. *Recl. Trav. Chim. Pays-Bas* **1995**, *14*, 517.
- [181] Zare, R. N. *Angular Momentum: Understanding Spatial Aspect in Chemistry and Physics*, John Wiley and Sons, New York **1988**.
- [182] Moro, G. *Chem. Phys.* **1987**, *118*, 167.
- [183] Moro, G. *Chem. Phys.* **1987**, *118*, 181.
- [184] Adamo, C.; Barone, V. *J. Chem. Phys.* **1999**, *110*, 6158.
- [185] Bulliard, C.; Allan, M.; Wirtz, G.; Haselbach, E.; Zachariasse, K. A. *J. Phys. Chem. A* **1999**, *103*, 7766.
- [186] Quinones, E.; Ishikawa, Y.; Leszczynski, J. *J. Mol. Struct. (Theochem)* **2000**, *529*, 127.

- [187] Purkayastha, P.; Bhattacharyya, P. K.; Bera, S. C.; Chattopadhyay, N. *Phys. Chem. Chem. Phys.* **1999**, *105*, 4182.
- [188] Tomin, V. I.; Brozis, M. *Optic. Spectr.* **2005**, *100*, 546.
- [189] Parusel, A. B. J.; Rettig, W.; Sudholt, W. J. *J. Phys. Chem. A* **2002**, *106*, 804.
- [190] Lommatzsch, U.; Brutschy, B. *Chem. Phys.* **1998**, *234*, 35.
- [191] Foreman, J. B.; Head-Gordon, M.; Pople, J. A.; Frisch, M. J. *J. Phys. Chem.* **1992**, *96*, 135.
- [192] Cogan, S.; Zilberg, S.; Haas, Y. *J. Am. Chem. Soc.* **2006**, *128*, 3335.
- [193] Chiba, M.; Tsuneda, T.; Hirao, K. *J. Chem. Phys.* **2007**, *126*, 034504.
- [194] Parusel, A. B. J. *Phys. Chem. Chem. Phys.* **2000**, *2*, 5545.
- [195] Scalmani, G.; Frisch, M. J.; Mennucci, B.; Tomasi, J.; Cammi, R.; Barone, V. *J. Chem. Phys.* **2006**, *124*, 094107/1.
- [196] Wanko, M.; Garavelli, M.; Bernardi, F.; Niehaus, T. A.; Frauenheim, T.; Elstner, M. *J. Chem. Phys.* **2004**, *120*, 1674.
- [197] Tozer, D. J.; Amos, R. D.; Handy, N. C.; Roos, B. O.; Serrano-Andres, L. *Mol. Phys.* **1999**, *97*, 859.
- [198] Dreuw, A.; Weisman, J. L.; Head-Gordon, M. *J. Chem. Phys.* **2003**, *119*, 2943.
- [199] Dreuw, A.; Head-Gordon, M. *J. Am. Chem. Soc.* **2004**, *126*, 4007.
- [200] Burkow, K.; Werschnik, J.; Gross, E. K. U. *J. Chem. Phys.* **2005**, *123*, 622006.
- [201] Gritsenko, O.; Baerends, E. J. *J. Chem. Phys.* **2004**, *121*, 655.
- [202] Tawada, Y.; Tsuneda, T.; Yanagisawa, S.; Yanai, T.; Hirao, K. *J. Chem. Phys.* **2004**, *120*, 8425.
- [203] Maitra, N. T.; Zhang, F.; Cave, R. J.; Burke, K. *J. Chem. Phys.* **2004**, *120*, 5932.

- [204] Maitra, N. T. *J. Chem. Phys.* **2005**, *122*, 234104.
- [205] Adamo, C.; Scuseria, G. E.; Barone, V. *J. Chem. Phys.* **2000**, *111*, 2889.
- [206] Improta, R.; Barone, V. *J. Am. Chem. Soc.* **2004**, *126*, 14320.
- [207] Frisch, M. J.; Pople, J. A.; Binkley, J. S. *J. Chem. Phys.* **1984**, *80*, 3265.
- [208] Dunning, T. H. Jr *J. Chem. Phys.* **1989**, *90*, 1007.
- [209] Petersson, G. A.; Al-Laham, M. A. *J. Chem. Phys.* **1991**, *94*, 6081.
- [210] Serrano-Andres, L.; Merchán, M.; Roos, B. O.; Lindh, R. *J. Am. Chem. Soc.* **1995**, *117*, 3198.
- [211] Parusel, A. B. J.; Köhler, G.; Nooijen, M. *J. Phys. Chem. A* **1999**, *103*, 4056.
- [212] Jamorski, C.; Foresman, J. B.; Thilgen, C.; Lüthi, H. P. *J. Chem. Phys.* **2002**, *116*, 8761.
- [213] Lippert, E.; Rettig, W.; Bonačić-Koutecký, V.; Heisel, F.; Míche, J. A. *Adv. Chem. Phys.* **1987**, *68*, 1.
- [214] *Handbook of Chemistry and Physics*, 64 th Edition; CRC Press, Boca Raton, Florida **1983**.
- [215] Horng, M. L.; Gardecki, J. A.; Papazyan, A.; Maroncelli, M. *J. Phys. Chem.* **1995**, *99*, 17311.
- [216] Horng, M. L.; Dahl, K.; Jones, G.; Maroncelli, M. *Chem. Phys. Lett.* **1999**, *315*, 363.
- [217] Schuddeboom, W.; Jonker, S. A.; Warman, J. M.; Leinhos, U.; Kühnle, W.; Zachariasse, K. A. *J. Phys. Chem.* **1992**, *96*, 10809.
- [218] Murali, S.; Kharlanov, V.; Rettig, W.; Tolmachev, A. I.; Kropachev, A. V. *J. Phys. Chem. A* **2005**, *109*, 6420.
- [219] Haidekker, M. A.; Brady, T. P.; Lichlyter, D.; Theodorakis, E. A. *Bioorg. Chem.* **2005**, *33*, 415.

- [220] Leinhos, U.; Kühnle, W.; Zachariasse, K. A. *J. Phys. Chem.* **1991**, *95*, 2013.
- [221] Parusel, A. B. J.; Köhler, G.; Grimme, S. *J. Phys. Chem. A* **1998**, *102*, 6207.
- [222] Broo, A.; Zerner, M. C. *Theor. Chim. Acta* **1995**, *90*, 383.
- [223] Broo, A.; Zerner, M. C. *Chem. Phys. Lett.* **1994**, *227*, 551.
- [224] Fuß, W.; Pushpa, K. K.; Rettig, W.; Schmid, W. E.; Trushin, S. A. *Photochem. Photobiol. Sci.* **2002**, *1*, 255.
- [225] Freidzon, A. Ya.; Bagatur'yants, A. A.; Gromov, S. P.; Alfimov, M. V. *Russ. Chem. Bull. Int. Ed.* **2003**, *52*, 2646.
- [226] Avakyan, V. G.; Gromov, S. P.; Vedernikov, A. I.; Dmitrieva, S. M.; Alfimov, M. V. *Russ. Chem. Bull. Int. Ed.* **2004**, *53*, 24.
- [227] Löhr, H. G.; Vögtle, F. *Acc. Chem. Res.* **1985**, *18*, 65.
- [228] Dumon, P.; Jousauskas, G.; Dupuy, F.; Pee, Ph.; Rulliere, C.; Letard, J. F.; Lapoyade, R. *J. Phys. Chem.* **1994**, *98*, 10391.
- [229] Collins, G. E.; Choi, L. S. *Chem. Comm.* **1997**, *12*, 1135.
- [230] Czarnik, A. M. *Fluorescence Chemosensor for Ions and Molecule Recognition*, vol. 538, ACS Books: Washington DC **1993**.
- [231] Barone, V.; Polimeno, A. *Phys. Chem. Chem. Phys.* **2006**, *8*, 4609.
- [232] Barone, V. *J. Chem. Phys.* **1994**, *101*, 6834.
- [233] Barone, V. *J. Chem. Phys.* **1994**, *101*, 10666.
- [234] Malkina, O. L.; Vaara, J.; Schimmelpfenning, J. B.; Munzarova, M. L.; Malkin, V. G.; Kaupp, M. J. *J. Am. Chem. Soc.* **2000**, *122*, 9206.
- [235] Neese, F. *J. Chem. Phys.* **2001**, *115*, 11080.
- [236] Van Doorslaer, S.; Vinck, E. *Phys. Chem. Chem. Phys.* **2007**, *9*, 4620.

- [237] White, G. F.; Ottignon, L.; Georgiuiu, T.; Kleanthous, C.; Moore, G. R.; Thomson, A. J.; Oganessian, V. S. *J. Mag. Res.* **2007**, *185*, 191.
- [238] Jeschke, G.; Polyhach, Y. *Phys. Chem. Chem. Phys.* **2007**, *9*, 1895.
- [239] Gamliel, D.; Levanon, H. *Stochastic Processes in Magnetic Resonance*, World Scientific, **1995**.
- [240] Berliner, L. J. *Biological Magnetic resonance: The Next Millenium*, Springer **1998**.
- [241] Langen, R.; Oh, K. J.; Cascio, D.; Hubbell, W. L. *Biochemistry* **2000**, *59*, 8396.
- [242] Mchaourab, H. S.; Lietzow, M. A.; Hideg, K.; Hubbell, W. L. *Biochemistry* **1996**, *35*, 7692.
- [243] Hubbell, W. L.; Cafiso, D. S.; Altenbach, C. *Nat. Struct. Biol.* **2000**, *7*, 735.
- [244] Koteiche, H. A.; Berengian, A. R.; Mchaourab, H. S. *Biochemistry* **1998**, *37*, 12681.
- [245] Hubbell, W. L.; Altenbach, C. *Curr. Opt. Struct. Biol.* **1994**, *4*, 566.
- [246] Hubbell, W. L.; Mchaourab, H. S.; Altenbach, C.; Lietzow, M. A. *Structure* **1996**, *4*, 779.
- [247] Altenbach, C.; Marti, T.; Khorana, H. G.; Hubbell, W. L. *Science* **1990**, *248*, 1088.
- [248] Shin, Y.-K.; Hubbell, W. L. *Biophys. J.* **1992**, *61*, 1443.
- [249] Anthony-Cahill, S. J.; Benfield, P. A.; Fairman, R.; Wasserman, Z. R.; Brenner, S. L.; Stafford, W. F.; Altenbach, C.; Hubbell, W. L.; De Grado, W. F. *Science* **1992**, *255*, 979.
- [250] Kokorin, A. I. *Appl. Magn. Res.* **2004**, *26*, 253.
- [251] Sartori, E.; Corvaja, C.; Oancea, S.; Formaggio, F.; Crisma, M.; Toniolo, C. *ChemPhysChem.* **2005**, *6*, 1472.

- [252] Hanson, P.; Martinez, G.; Millhauser, G.; Formaggio, F.; Crisma, M.; Toniolo, C.; Vita, C. *J. Am. Chem. Soc.* **1996**, *118*, 271.
- [253] Hanson, P.; Millhauser, G.; Formaggio, F.; Crisma, M.; Toniolo, C.; *J. Am. Chem. Soc.* **1996**, *118*, 7618.
- [254] Toniolo, C.; Benedetti, E. *Trends Biochem. Sci.* **1991**, *16*, 350.
- [255] Toniolo, C.; Crisma, M.; Formaggio, F. *Biopolymers* **1998**, *47*, 153.
- [256] Karle, I. L.; Balaram, P. *Biochemistry* **1990**, *29*, 6747.
- [257] Toniolo, C.; Crisma, M.; Formaggio, F.; Peggion, C. *Biopolymers* **2001**, *60*, 396.
- [258] Flippen-Anderson, J. L.; George, C.; Valle, G.; Valente, E.; Bianco, A.; Formaggio, F.; Crisma, M.; Toniolo, C. *Int. J. Pept. Protein Res.* **1996**, *47*, 231.
- [259] Polimeno, A.; Freed, J. H. *J. Phys. Chem.* **1995**, *99*, 10995.
- [260] Carpino, L. A. *J. Am. Chem. Soc.* **1993**, *115*, 4397.
- [261] Schneider, D. J.; Freed, J. H. *Adv. Chem. Phys.* **1989**, *73*, 487.
- [262] Meirovitch, E.; Igner, D.; Igner, E.; Moro, G.; Freed, J. H. *J. Chem. Phys.* **1982**, *77*, 3915.
- [263] Ciofini, I.; Barone, V.; Adamo, C. *J. Chem. Phys.* **2004**, *121*, 6710.
- [264] Improta, R.; Barone, V. *J. Comp. Chem.* **2004**, *25*, 1333.
- [265] Cossi, M.; Scalmani, G.; Rega, N.; Barone, V. *J. Comp. Chem.* **2003**, *24*, 669.
- [266] D'Amore, M.; Improta, R.; Barone, V. *J. Phys. Chem. A* **2003**, *107*, 6264.
- [267] Improta, R.; Antonello, S.; Formaggio, F.; Maran, F.; Rega, N.; Barone, V. *J. Phys. Chem. B* **2005**, *109*, 1023.
- [268] Marsh, D. *J. Magn. Spectr.* **2006**, *180*, 305.
- [269] Improta, R.; Barone, V. *Chem. Rev.* **2004**, *104*, 1231.

- [270] O'Malley, P. J. *J. Phys. Chem. B* **2002**, *106*, 12331.
- [271] Mattar, S. M. *J. Phys. Chem. B* **2004**, *108*, 9449.
- [272] Hermosilla, L.; Calle, P.; Garcia de la Vega, J. M.; Siero, C. *J. Phys. Chem. A* **2005**, *109*, 1114.
- [273] Gauld, J. W.; Eriksson, L. A.; Radom, L. *J. Phys. Chem. A* **1997**, *101*, 1352.
- [274] Munzarova, M.; Kaupp, M. *J. Phys. Chem. A* **1999**, *103*, 9966.
- [275] Al Derzi, A. T.; Fan, S.; Bartlett, R. J. *J. Phys. Chem. A* **2003**, *107*, 6656.
- [276] Bencini, A.; Totti, F.; Daul, C. A.; Doclo, K.; Fantucci, P.; Barone, V. *Inorg. Chem.* **1997**, *36*, 5022.
- [277] Improta, R.; Barone, V.; Kudin, K.; Scuseria, G. E. *J. Am. Chem. Soc.* **2002**, *124*, 113.
- [278] Yawada, Y.; Tsuneda, T.; Yanagisawa, S.; Yanai, T.; Hirao, K. *J. Chem. Phys.* **2004**, *120*, 8425.
- [279] Kamiya, M.; Sekino, H.; Tsuneda, T.; Hirao, K. *J. Chem. Phys.* **2005**, *122*, 234111.
- [280] Reviakine, R.; Arbuznikov, A. V.; Tremblay, J. C.; Remenyi, C.; Malkina, O. L.; Malkin, V. G.; Kaupp, M. *J. Chem. Phys.* **2006**, *125*, 054110.
- [281] Zheludev, A.; Barone, V.; Bonnet, M.; Delley, B.; Grand, A.; Ressouche, E.; Rey, P.; Subra, R.; Schweizer, J. *J. Am. Chem. Soc.* **1994**, *116*, 2019.
- [282] Koch, W.; Holthousen, W. C. A. *Chemist's Guide to Density Functional Theory*, Wiley-VCH: Weinheim **2000**.
- [283] Tomasi, J.; Mannucci, B.; Cammi, R. *Chem. Rev.* **2005**, *105*, 2999.
- [284] Brancato, G.; Rega, N.; Barone, V. *J. Chem. Phys.* **2006**, *125*, 164515.
- [285] Gustavson, T.; Banyasz, A.; Lazzarotto, E.; Markovitsi, D.; Scalmani, G.; Frisch, M.; Improta, R.; Barone, V. *J. Am. Chem. Soc.* **2006**, *128*, 607.

- [286] Improta, R.; Santoro, F.; Barone, V. *Theor. Chem. Acc.* **2007**, *117*, 1073.
- [287] Improta, R.; Barone, V.; Santoro, F. *Angew. Chem. Int. Ed.* **2007**, *46*, 405.
- [288] Santoro, F.; Improta, R.; Lami, A.; Bloino, J.; Barone, V. *J. Chem. Phys.* **2007**, *126*, 084509.
- [289] Brancato, G.; Rega, N.; Barone, V. *Theor. Chem. Acc.* **2007**, *117*, 1001.
- [290] Barone, V.; Brustolon, M.; Cimino, P.; Polimeno, A.; Zerbetto, M.; Zoleo, A. *J. Am. Chem. Soc.* **2006**, *128*, 15865.
- [291] Zerbetto, M.; Carlotto, S.; Polimeno, A.; Corvaja, C.; Franco, L.; Toniolo, C.; Formaggio, F.; Barone, V.; Cimino, P. *J. Chem. Phys. B* **2007**, *111*, 2668.
- [292] Carlotto, S.; Cimino, P.; Zerbetto, M.; Franco, L.; Corvaja, C.; Crisma, M.; Formaggio, F.; Toniolo, C.; Polimeno, A.; Barone, V.; *J. Am. Chem. Soc.* **2007**, *129*, 11248.
- [293] Stainhoff, H. J. *Frontiers in Bioscience* **2002**, *7*, 97.
- [294] Eaton, S. S.; Eaton, G. R. *Biological Magnetic Resonance*, Berliner, L. J., Eaton, S. S., Eaton, G. R., Eds.; Kluwer Academic/Plenum Publishers: New York **2000**, vol. *19*, pp 2-28.
- [295] Tsvetkov, Yu. D. *Biological Magnetic Resonance*, Berliner, L. J., Eaton, S. S., Eaton, G. R., Eds.; Kluwer Academic/Plenum Publishers: New York **2004**, vol. *21*, pp 385-433.
- [296] Jeske, G.; Pannier, M.; Spiess, H. W. *Biological Magnetic Resonance*, Berliner, L. J., Eaton, S. S., Eaton, G. R., Eds.; Kluwer Academic/Plenum Publishers: New York **2000**, vol. *19*, pp 493-512.
- [297] Borbat, P. P.; Freed, J. F. *Biological Magnetic Resonance*, Berliner, L. J., Eaton, S. S., Eaton, G. R., Eds.; Kluwer Academic/Plenum Publishers: New York **2000**, vol. *19*, pp 383-460.

- [298] Crisma, M.; Deschamps, J. R.; George, C.; Flippen-Anderson, J. L.; Kaptein, B.; Broxterman, Q. B.; Moretto, A.; Oancea, S.; Jost, M.; Formaggio, F.; Toniolo, C. *J. Pept. Res.* **2005**, *65*, 564.
- [299] Barlow, D. J.; Thornton, J. M. *J. Mol. Biol.* **1988**, *201*, 601.
- [300] Armen, R., Alonso, D. O. V.; Daggett, V. *Protein Sci.* **2003**, *12*, 1145.
- [301] Bolin, K. A.; Millhauser, G. L. *Acc. Chem. Res.* **1999**, *32*, 1027.
- [302] Smythe, M. L.; Huston, S. E.; Marshall, G. R. *J. Am. Chem. Soc.* **1995**, *117*, 5445.
- [303] Smythe, M. L.; Nakaie, C. R.; Marshall, G. R. *J. Am. Chem. Soc.* **1995**, *117*, 10555.
- [304] Millhauser, G. L. *Biochemistry* **1995**, *34*, 3873.
- [305] Marshall, G. R., Hodgkin, E. E.; Langs, D. A.; Smith, G. D.; Zabrocki, J.; Leplawy, M. T. *Proc. Natl. Acad. Sci. USA* **1990**, *87*, 487.
- [306] Smythe, M. L.; Huston, S. E., Marshall, G. R. *J. Am. Chem. Soc.* **1993**, *115*, 11594.
- [307] Fiori, W. R.; Mück, S. M.; Millhauser, G. L. *Biochemistry* **1993**, *32*, 11957.
- [308] Marqusee, S.; Robbins, V. H.; Baldwin, R. L. *Proc. Natl. Acad. Sci. USA* **1989**, *86*, 5286.
- [309] Karle, I. L.; Sukmar, M. K.; Balaram, P. *Proc. Natl. Acad. Sci. USA* **1986**, *83*, 9284.
- [310] Karle, I. L.; Flippen-Anderson, J.; Uma, K.; Balaram, P. *Proc. Natl. Acad. Sci. USA* **1988**, *85*, 299.
- [311] Zhang, L.; Hermans, J. *J. Am. Chem. Soc.* **1994**, *116*, 11915.
- [312] Paterson, Y., Rumsey, S.; Benedetti, E.; Nemethy, G.; Scheraga, H. A. *J. Am. Chem. Soc.* **1981**, *103*, 2947.

- [313] Cremer, D.; Pople, J. A. *J. Am. Chem. Soc.* **1975**, *97*, 1354.
- [314] Improta, R.; Benzi, C.; Barone, V. *J. Am. Chem. Soc.* **2001**, *123*, 12568.
- [315] Improta, R., Mele, F.; Crescenzi, O.; Benzi, C.; Barone, V. *J. Am. Chem. Soc.* **2002**, *124*, 7857.
- [316] Langella, E.; Improta, R.; Barone, V. *J. Am. Chem. Soc.* **2002**, *124*, 11531.
- [317] Cossi, M.; Scalmani, G.; Rega, N.; Barone, V. *J. Chem. Phys.* **2002**, *117*, 43.
- [318] Grimme, S. *J. Comput. Chem.* **2004**, *25*, 1463.
- [319] Barone, V.; Carbonniere, P.; Pouchan, C. *J. Chem. Phys.* **2005**, *122*, 224308.
- [320] Lucarini, M.; Pedulli, G. F. *Phys. Rep.* **2001**, *351*, 387.
- [321] Aurich, H. G.; Hahn, K.; Stork, K.; Weiss, W. *Tetrahedron* **1977**, *33*, 369.
- [322] Barone, V. *J. Phys. Chem.* **1995**, *99*, 11659.
- [323] Barone, V.; Subra, R. *J. Chem. Phys.* **1996**, *104*, 2630.
- [324] Barone, V. *Chem. Phys. Lett.* **1996**, *262*, 201.
- [325] Bellanda, M.; Mammi, S.; Geremia, S.; Demitri, N.; Randaccio, L.; Broxterman, Q. B.; Kaptein, B.; Pengo, P.; Pasquato, L.; Scrimin, P. *Chem.-Eur. J.* **2007**, *13*, 407.
- [326] Stark, H. *Phys. Rep.* **2001**, *351*, 387.
- [327] Poulin, P.; Raghunathan, V. A.; Richetti, P.; Roux, D. *J. Phys. II* **1994**, *4*, 1557.
- [328] Terentien, E. M. *Phys. Rev. E* **1995**, *51*, 1330.
- [329] Stark, H. *Eur. Phys. J. B* **1999**, *10*, 311.
- [330] Loudet, J. C.; Barois, P.; Poulin, P. *Nature* **2000**, *407*, 611.
- [331] Klein, R. *Interacting Brownian Particles-The dynamics of Colloidal Suspension in the Physycs of Complex Systems*, edited F. Mallamace and H. E. Stanley, IOS Press, Amsterdam **1997**.

- [332] Sanyal, S.; Sood, A. K.; Ramkumar, S.; Ramaswamy, S.; Kumar, N. *Phys. Rev. Lett.* **1994**, *72*, 2963.
- [333] Russel, W. B.; Saville, D. A.; Schowalter, W. R. *Colloidal Dispersions*, Cambridge University Press, Cambridge **1995**.
- [334] Brochard, F.; de Gennes, P. G. *J. Phys. (Paris)* **1970**, *31*, 691.
- [335] Böttger, A.; Frenkel, D.; van de Riet, E. *Liq. Cryst.* **1987**, *2*, 539.
- [336] Poulin, Stark, H.; Lubensky, T. C.; Weitz, D. A. *Science* **1997**, *257*, 1770.
- [337] Stewart, I. W. *The Static and the Dynamic Continuum Theory of Liquid Crystals*, CRC Press **2004**.
- [338] Currie, P. K. *J. Phys. (France)* **1979**, *501*, 40.
- [339] Pieranski, P.; Brochard, F.; Guyon, E. *J. Phys. (France)* **1973**, *34*, 35.
- [340] Diogo, A.C. *Mol. Cryst. Liq. Cryst.* **1983**, *30*, 153.
- [341] Franklin, W. *Mol. Cryst. Liq. Cryst.* **1971**, *14*, 227.
- [342] Franklin, W. *Phys. Rev. A* **1975**, *11*, 2156.
- [343] Khare, A. A., Kofke, D. A., Evans, G. T. *Mol. Phys.* **1997**, *91*, 993.
- [344] Lettinga, M. P.; Barry, E.; Dogic, Z. *Europhys. Lett.* **2005**, *71*, 692.
- [345] Yun, C. K., Frerickson, A. G. *Mol. Cryst. Liq. Cryst.* **1971**, *12*, 73.
- [346] Moseley, M. E.; Loewenstein, A. *Mol. Cryst. Liq. Cryst.* **1982**, *90*, 117.
- [347] Moseley, M. E.; Loewenstein, A. *Mol. Cryst. Liq. Cryst.* **1983**, *95*, 51.
- [348] Krüger, G. J. *Phys. Rep.* **1982**, *82*, 229.
- [349] Spiegel, D. R.; Thompson, A. L.; Campbell, W. C. *J. Chem. Phys.* **2001**, *114*, 3842.

- [350] de Gennes, P. G.; Prost, J. *The Physics of Liquid Crystals*, Oxford University Press **1993**.
- [351] Friedel, G. *Ann. Phys.* **1922**, *18*, 273.
- [352] Bird, R. B.; Stewart, W E.; Lightfoot, E. N. *Transport Phenomena*, Wiley **1960**.
- [353] Currie, I. G. *Fundamental Mechanic of Fluids*, McGraw-Hill **1993**.
- [354] Lamb, H. *Hydrodynamics*, Dover **1945**.
- [355] Leslie, F. M. *Qaunt. J. Mech. Appl. Math.* **1966**, *19*, 357.
- [356] Leslie, F. M. *Adv. Liq. Cryst.* **1979**, *4*, 1.
- [357] Ericksen, J. L. *Trans. Soc. Rheol.* **1961**, *5*, 23.
- [358] Ericksen, J. L. *Adv. Liq. Cryst.* **1976**, *2*, 233.
- [359] Polimeno, A.; Orian, L.; Martins, A. F.; Gomes, A. E. *Phys. Rev. E* **2000**, *62*, 2288.
- [360] Polimeno, A.; Orian, L.; Nordio, P. L.; Martins, A. F. *Mol. Cryst. Liq. Cryst.* **1999**, *336*, 17.
- [361] Polimeno, A.; Martins, A. F.; Nordio, P. L. *Mol. Cryst. Liq. Cryst.* **1999**, *328*, 541.
- [362] Polimeno, A.; Martins, A. F. *Liq. Cryst.* **1998**, *25*, 545.
- [363] Martins, A. F.; Gomes, A. E.; Orian, L.; Polimeno, A. *Mol. Cryst. Liq. Cryst.* **2000**, *351*, 135.
- [364] Einstein, A. *Investigation on the Theory of the Brownian Movement*, R. Furth **1956**.
- [365] Bhide, V. G.; Kandpal, M. C. *Phys. Rev. B* **1979**, *20*, 85.
- [366] Stark, H.; Ventzki, D. *Phys. Rev. E* **2001**, *64*, 031711.

- [367] Loudet, J. C.; Hanusse, P.; Poulin, P. *Science* **2004**, *306*, 1525.
- [368] Martins, A. F. *Private Communication*.
- [369] Tseng, H. C.; Silver, D. L.; Finlayson, B. A. *Phys. Fluids* **1972**, *15*, 1213.
- [370] Borzsonyi, T.; Buka, A.; Krekhov, P. A.; Kramer, L. *Phys. Rev. E* **1998**, *58*, 7419.
- [371] Silverstone, H. J.; Moats, R. K. *Phys. Rev. A* **1977**, *4*, 1731.
- [372] Silverstone, H. J. *J. Chem. Phys.* **1967**, *47*, 537.
- [373] Varshalovich, D. S.; Moskalev, N. A.; Khersonskii, W. K. *Quantum Theory of Angular Momentum*, World Scientific **1988**.

Publications

- Zerbetto, M.; Carlotto, S.; Polimeno, A.; Corvaja, C.; Franco, L.; Toniolo, C.; Formaggio, F.; Barone, V.; Cimino, P. *J. Chem. Phys. B* **2007**, *111*, 2668.
- Carlotto, S.; Cimino, P.; Zerbetto, M.; Franco, L.; Corvaja, C.; Crisma, M.; Formaggio, F.; Toniolo, C.; Polimeno, A.; Barone, V.; *J. Am. Chem. Soc.* **2007**, *129*, 11248.
- Polimeno, A.; Carlotto, S., *Theor. Chem. Acc.* **2007**, in press.
- Carlotto, S.; Polimeno, A.; Ferrante, C.; Benzi, C.; Barone, V., *J. Chem. Phys. B* **2007**, submitted.
- Carlotto, S.; Benzi, C.; Ricco, R.; Ferrante, C.; Maggini, M.; Polimeno, A.; Barone, V., *J. Chem. Phys. B* **2007**, submitted.
- Carlotto, S.; Polimeno, A. *J. Phys. Chem.* **2007**, submitted.
- Polimeno, A.; Carlotto, S. *On a hydrodynamic approach to solvation effects in apolar media*, in preparation.

Acknowledgments

The three years of my PhD are concluded. I would like to thank my parents, Patrizia and Rolando, my brother Marco and the rest of my family for their continued love and support throughout my entire life and my university career. I would like to express my sincere thanks to them and all they had done for me.

My sincerest thanks and appreciation goes to my supervisor prof. Antonino Polimeno. Thank you for his advice, invaluable time and input. Additional thanks to the Direttore della Scuola di Dottorato, prof. Maurizio Casarin for all help throughout my Ph.D.

My thanks to my friends and colleagues for the great time I had in our group. I enjoyed the atmosphere, their friendship, and their support. My thanks to Mirco, "Maestro" Fabio, Mirko, Elisabetta, Inge, Matteo, Andrea and Barbara.

I would also like to acknowledge the prof. Vincenzo Barone and his group at the University "Federico II" of Napoli, Caterina and Paola in particular, for the collaborations in these years. My thanks to prof. Michele Maggini and prof. Claudio Toniolo at the University of Padova for the synthesis respectively of the optical and the paramagnetic probe. My thanks to prof.ssa Camilla Ferrante, , prof. Carlo Corvaja, Dr. Lorenzo Franco at the University of Padova for the characterization of the molecules.

My thanks to my housemates Emma, Betty, Vale and Lorenzo for creating a nice home environment in which to live.

I would also like to give a huge thank to the new friends of the Tsuki Kage Dojo for the fantastic welcome in their "world".

And now I wish to say an enormous thank you to Marzio. Thank you to your love, friendship, patience and encouragement. Thank you to gift me a pair of wings.

